Subwavelength Sensing Using Nonlinear Feedback in a Wave-Chaotic Cavity

by

Seth D. Cohen

Department of Physics
Duke University

Date: _____

Approved:

_____
Daniel J. Gauthier, Supervisor

_____
Harold Baranger

_____
Robert Behringer

_____
Ashutosh Kowtal

_____
Joshua Socolar

Dissertation submitted in partial fulfillment of the
requirements for the degree of Doctor of Philosophy
in the Department of Physics
in the Graduate School of
Duke University

2013

Report Documentation Page

Form Approved
OMB No. 0704-0188

1. REPORT DATE	2. REPORT TYPE	3. DATES COVERED
2013		**00-00-2013 to 00-00-2013**

4. TITLE AND SUBTITLE	5a. CONTRACT NUMBER
Subwavelength Sensing Using Nonlinear Feedback in a Wave-Chaotic Cavity	5b. GRANT NUMBER
	5c. PROGRAM ELEMENT NUMBER
6. AUTHOR(S)	5d. PROJECT NUMBER
	5e. TASK NUMBER
	5f. WORK UNIT NUMBER
7. PERFORMING ORGANIZATION NAME(S) AND ADDRESS(ES) **Duke University ,Department of Physics,Durham,NC,27708**	8. PERFORMING ORGANIZATION REPORT NUMBER
9. SPONSORING/MONITORING AGENCY NAME(S) AND ADDRESS(ES)	10. SPONSOR/MONITOR'S ACRONYM(S)
	11. SPONSOR/MONITOR'S REPORT NUMBER(S)

12. DISTRIBUTION/AVAILABILITY STATEMENT
Approved for public release; distribution unlimited

13. SUPPLEMENTARY NOTES

14. ABSTRACT

Typical imaging systems rely on the interactions of matter with electromagnetic radiation which can lead to scattered waves that are radiated away from the imaging area. The goal such an imaging device is to collect these radiated waves and focus them onto a measurement detector that is sensitive to the wave?s properties such as wavelength (or color) and intensity. The detector?s measurements of the scattered fields are then used to reconstruct spatial information about the original matter such as its shape or location. However, when a scattered wave is collected by the imaging device, it diffracts and interferes with itself. The resulting interference pattern can blur spatial information of the reconstructed image. This leads to a so-called diffraction limit, which describes the minimum sizes of spatial features on a scatterer that can be resolved using conventional imaging techniques. The diffraction limit scales with the wavelength of the illuminating field, where the limit for conventional imaging with visible light is approximately 200 nm. Investigating subwavelength objects (<) requires more advanced measurement techniques, and improving the resolving capabilities of imaging devices continues to be an active area of research. Here, I describe a new sensing technique for resolving the position of a subwavelength scatterer (<) with vastly subwavelength resolution (<<). My approach combines two separate fields of scientific inquiry: time-delayed nonlinear feedback and wave chaos. In typical time-delayed nonlinear feedback systems, the output of a nonlinear device is delayed and fed back to its input. In my experiment, the output of a radio-frequency (15 cm) nonlinear circuit is injected into a complex scattering environment known as a wave-chaotic cavity. Inside the cavity, the field interacts with a subwavelength dielectric object from all sides, and a portion of the scattered waves are coupled out of the cavity, amplified, and fed back to the input of the nonlinear circuit. The resulting closed-feedback loop generates its own radio-frequency illumination field (> 1 GHz), which contains multiple wavelengths and is sensitive to location of the scattering object. Using the dynamical changes in the illumination field, I demonstrate subwavelength position-sensing of the scatterer?s location in the cavity with a two-dimensional average resolution of 0.5 mm (=300) given by the RMS error of the position sensing and an upper bound on the resolution given by the maximum observed error (2.1 mm =70). This novel method demonstrates that the dynamical changes of a feedback oscillator can be exploited for resolving subwavelength spatial features. Unlike conventional imaging techniques, it uses a single scalar measurement of the scattered

15. SUBJECT TERMS

16. SECURITY CLASSIFICATION OF:			17. LIMITATION OF ABSTRACT	18. NUMBER OF PAGES	19a. NAME OF RESPONSIBLE PERSON
a. REPORT	b. ABSTRACT	c. THIS PAGE			
unclassified	**unclassified**	**unclassified**	**Same as Report (SAR)**	**291**	

ABSTRACT

Subwavelength Sensing Using Nonlinear Feedback in a Wave-Chaotic Cavity

by

Seth D. Cohen

Department of Physics
Duke University

Date: _____

Approved:

_____
Daniel J. Gauthier, Supervisor

_____
Harold Baranger

_____
Robert Behringer

_____
Ashutosh Kowtal

_____
Joshua Socolar

An abstract of a dissertation submitted in partial fulfillment of the
requirements for the degree of Doctor of Philosophy
in the Department of Physics
in the Graduate School of
Duke University

2013

Abstract

Typical imaging systems rely on the interactions of matter with electromagnetic radiation, which can lead to scattered waves that are radiated away from the imaging area. The goal such an imaging device is to collect these radiated waves and focus them onto a measurement detector that is sensitive to the wave's properties such as wavelength (or color) and intensity. The detector's measurements of the scattered fields are then used to reconstruct spatial information about the original matter such as its shape or location. However, when a scattered wave is collected by the imaging device, it diffracts and interferes with itself. The resulting interference pattern can blur spatial information of the reconstructed image. This leads to a so-called diffraction limit, which describes the minimum sizes of spatial features on a scatterer that can be resolved using conventional imaging techniques. The diffraction limit scales with the wavelength λ of the illuminating field, where the limit for conventional imaging with visible light is approximately 200 nm. Investigating subwavelength objects ($< \lambda$) requires more advanced measurement techniques, and improving the resolving capabilities of imaging devices continues to be an active area of research.

Here, I describe a new sensing technique for resolving the position of a subwavelength scatterer ($< \lambda$) with vastly subwavelength resolution ($<< \lambda$). My approach combines two separate fields of scientific inquiry: time-delayed nonlinear feedback and wave chaos. In typical time-delayed nonlinear feedback systems, the output of a nonlinear device is delayed and fed back to its input. In my experiment, the output of a radio-frequency ($\lambda \sim 15$ cm) nonlinear circuit is injected into a complex scattering environment known as a wave-chaotic cavity. Inside the cavity, the field interacts with a subwavelength dielectric object from all sides, and a portion of the scattered waves are coupled out of the cavity, amplified, and fed back to the

input of the nonlinear circuit. The resulting closed-feedback loop generates its own radio-frequency illumination field (> 1 GHz), which contains multiple wavelengths and is sensitive to location of the scattering object. Using the dynamical changes in the illumination field, I demonstrate subwavelength position-sensing of the scatterer's location in the cavity with a two-dimensional average resolution of 0.5 mm ($\sim \lambda/300$) given by the RMS error of the position sensing and an upper bound on the resolution given by the maximum observed error (2.1 mm $\sim \lambda/70$).

This novel method demonstrates that the dynamical changes of a feedback oscillator can be exploited for resolving subwavelength spatial features. Unlike conventional imaging techniques, it uses a single scalar measurement of the scattered field and takes advantage of a complex scattering environment. Furthermore, this work demonstrates the first application of quasiperiodic dynamics (oscillations with incommensurate frequencies) from a nonlinear system. Using the key ingredients from my radio-frequency system, I extend my method to an experiment that uses optical frequencies ($\lambda \sim 1550$ nm) to demonstrate subwavelength sensing in two dimensions with a resolution of approximately 10 nm. Because this new sensing technique can be adapted to multiple experiments over vastly different length scales, it represents a potential platform for creating a new class subwavelength imaging devices.

Contents

List of Tables

List of Figures

Acknowledgements

The work in this thesis not only demonstrates my research accomplishments, but also represents the personal and professional support of my mentors, colleagues, friends, and family. Without these named contributors, I would not be the person or scientist that I am today.

I would first like to thank my adviser, Dr. Daniel J. Gauthier, whose mentorship throughout the years has sharpened my research, scientific writing, and public speaking skills. To me, his confidence and problem solving skills in the laboratory represent standards that all graduate students should strive to achieve.

Secondly, I would like to thank two post-doctoral research scientists who gave me countless hours of their time. In the beginning of my research career, Dr. Hugo Leonardo Davi de Souza Cavalcante personally taught me the foundations of nonlinear dynamics research, and in my final years at Duke, Dr. Damien Rontani was a knowledgeable and invaluable resource. Damien was also an immense help in editing the content of this dissertation.

During my time in the Duke Physics Department, I was lucky enough to be able to work with other graduate students who also specialized in the field of nonlinear dynamics: Kristine Callan, David Rosin, and Zheng Gao. Though we all worked on separate projects, our meetings provided me with insight into my projects and for that I am thankful. I would also like to thank all of the other graduate students in my research group who were constantly sharing ideas, journal articles, and constructive criticism: Joel Greenberg, Yunhui (Rena) Zhu, Hannah Guilbert, Bonnie Schmittberger, Meizhen Shi, and Margaret Shea. I wish all of them good luck in their future careers.

I have also been fortunate enough to work with G. Martin Hall, a Duke Physics

alumnus who now works the private company Propagation Research Associates. His advice helped to shape my research from an applied point-of-view.

In addition, my high school teachers in physics, calculus, and chemistry: Scott Durkee, Alice Murphy, and Maureen Boino deserve recognition. Looking back, the education from these inspirational instructors at Pittsfield High School became contributing factors to my successes at Duke.

My parents, Robert and Marcy Cohen, gave me endless support and encouragement to pursue all of my passions. They have forever instilled in me that "you cannot fail if you try your hardest", and their generosity in providing the means to higher education will always be remembered. I vow to offer my future children this gift.

My wife, Caroline, has supported me throughout graduate school. Her sense of humor and optimism were nourishment during difficult times and her nutritional advice and recipes continue to be nourishment during hungry times.

In addition to these people, I would like to acknowledge the financial support of the U. S. Office of Naval Research for affording me the opportunity to work on grant number N000015-07-0734 for *Exploiting nonlinear dynamics in novel sensor systems*. I would also like to mention the support provided by the U.S. Army Research Office grant number W31P4Q-11-C-0279 for studying a *Low-Cost Chaos Based Radar*.

Lastly, I would like to thank the members of my committee for our discussions and for taking the time to consider this work.

Chapter 1

Introduction

This dissertation represents the cumulative results of my investigations into a new method for sensing the position of a scatterer using electromagnetic radiation as an illumination source. In particular, I have developed a novel experiment that combines the dynamics of a time-delayed nonlinear feedback system with the complex scattering environment of a wave-chaotic cavity. This combination provides a new technique for resolving spatial information about a scatterer that is smaller than the wavelength of the illuminating field. Unlike typical imaging systems, this experiment exploits the sensitivity of a dynamical state in a time-evolving system. Overall, this unique subwavelength resolving system is the first step towards realizing a new super-resolved microscope for imaging spatial information with a nanometer resolution.

For decades, scientists have worked to create images of the world's microscopic phenomena to help our understanding of their underlying structures and functions. What are the limitations on creating such images? One major constraint is diffraction, which can blur the spatial information in an image, limiting its resolution based on the wavelength λ of the illumination source [1]. For example, images formed from visible light ($\lambda \sim 400-700$ nm) are typically limited to a resolution of approximately 200 nm [2]. Resolving spatial information below this limit requires new techniques, and to this day, scientists continue to search for ways to circumvent diffraction for imaging.

In this chapter, I first review the building blocks of a standard imaging system and the limit of its resolution due to diffraction. Then, using two examples from the

literature, I review specific imaging techniques that can resolve spatial information below the diffraction limit. Following these examples, I introduce my new experimental system and its sensing mode-of-operation for imaging the two-dimensional (2D) position of a subwavelength scatterer ($< \lambda$) with vastly subwavelength resolution ($<< \lambda$). Lastly, I give a brief summary of the main results for each of the remaining chapters.

1.1 Imaging and the Diffraction Limit

The main components for constructing an image are: (i) an illumination source, (ii) an object of interest that scatters light, (iii) an imaging system, and (iv) a detector [3]. As illustrated in Fig. 1.1a, the illumination source radiates an electromagnetic (EM) field that interacts with a scatterer through absorption or scattering from differences in its index of refraction relative to free space. The scattered radiation forms wavefronts (WF) that propagate to the imaging system, where a hole with a diameter D, known as an aperture, contains a lens that focuses the collected radiation onto an array detector comprised of light-sensitive pixels. Each pixel generates a voltage that is proportional to the incident light intensity, and we can construct an image of the scatterer through post-processing [1, 3].

However, because of the wave-like nature of the EM radiation, the light collected through the aperture diffracts. For a distant point-like source or scatterer, this can create a diffraction pattern on the detector, as illustrated in Fig. 1.1b. This diffraction pattern contains a primary intensity maxima with weaker secondary maxima and the resulting image shows a circular diffraction pattern similar to the one shown in Fig. 1.1b, where the width of the pattern depends on the relative sizes of λ and D [3].

This diffraction pattern creates problems for resolving small scattering features.

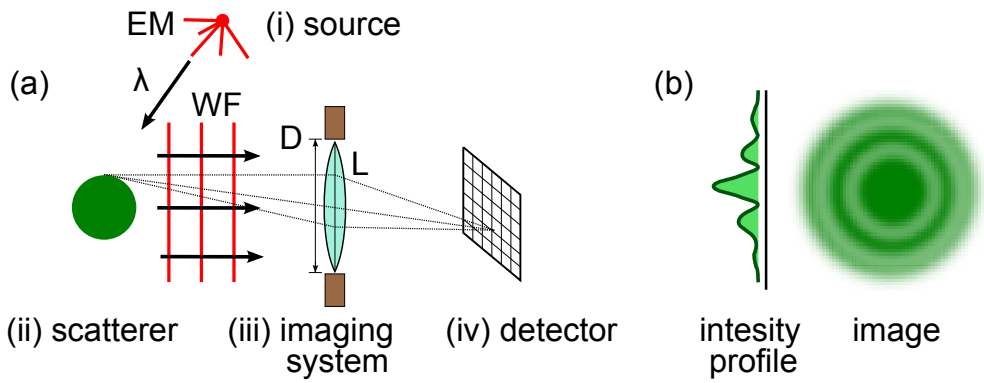

Figure 1.1: **Typical imaging system** (a) consisting of a (i) a source that produces electromagnetic radiation of wavelength λ, (ii) a scatterer that reflects the incident radiation as wavefronts (WF), (iii) an imaging system with a circular aperture of diameter D and lens (L), and (iv) an array detector with light sensitive pixels. (b) For a point-like scatterer, the intensity profile of the light on the detector shows oscillations with primary and secondary maxima and the resulting image or (diffraction pattern) is blurred with concentric rings.

As an example, consider the case of two distant point-like scatterers, shown in Fig. 1.2a, that are separated by a distance y and are a distance $x >> \lambda$ from the imaging system with a circular aperture. The ability to resolve both of these scatterers depends on a criterion first established by Lord Rayleigh in 1871 that states: the spatial features of a scatterer (or multiple scatterers) can only be resolved if the angular separation θ between these features satisfies

$$\sin(\theta_{\text{min}}) > 1.22\frac{\lambda}{D}, \tag{1.1}$$

where the factor of 1.22 comes from the calculation of the light distribution for all points of a wavefront at the circular aperture of the imaging system [1]. As shown in Fig. 1.2b, for $\theta > \theta_{\text{min}}$, the image shows diffraction patterns from the two scatterers that are well resolved. However, for $\theta = \theta_{\text{min}}$, the diffraction patterns begin to overlap and for $\theta < \theta_{\text{min}}$, the two patterns are no longer distinguishable from one

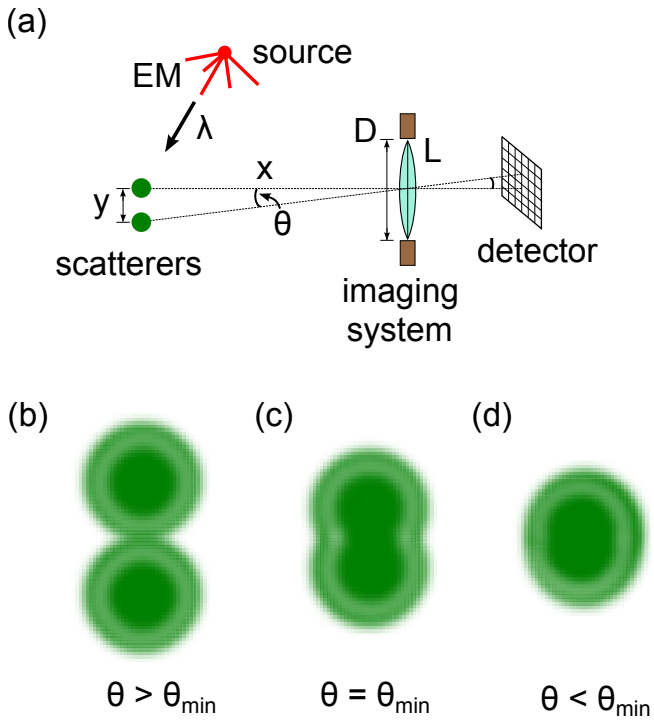

Figure 1.2: **Limitations of imaging due to diffraction.** (a) The incident EM radiation of wavelength λ from a source interacts with two point-light scatterers that are separated by a distance y. An imaging system with a circular aperture of diameter D (and lens L) and an array detector is placed a distance x from the scatterers, forming a scattering angle defined by θ. (b) For $\theta > \theta_{\text{min}}$, the diffraction patterns of from the scatterers are well resolved, (c) for $\theta = \theta_{\text{min}}$, the diffraction patterns are partially resolved, and (d) for $\theta < \theta_{\text{min}}$, the patterns are indistinguishable, where θ_{min} is defined by Eq. (1.1).

another [3]. Thus, the Rayleigh criterion summarizes the diffraction limit of optical devices with circular apertures, such as microscopes, telescopes, and cameras.

As a of the consequence of Eq. (1.1), consider the following example. For an camera with $\lambda = 500$ nm and a circular aperture with $D = 25$ mm, two point-like spatial features that are placed near the focal point of the camera's lens $f = 50$ mm can only be resolved if they are spaced approximately by a minimum distance $y_{\text{min}} = 1.2\ \mu$m. Therefore, in this example, nanometer-sized spatial features cannot be resolved [4]. The Rayleigh criterion, which has now been known for over a

century, is typically taught at universities in the introductory undergraduate physics courses, giving students a foundation for understanding the resolving capabilities of basic optical imaging devices [1, 3].

However, diffraction does not fundamentally limit our the ability to create images, and vastly subwavelength features can be resolved with the addition of more advanced measurement techniques [5].

1.2 Resolving Subwavelength Features

One of the simplest imaging devices that resolves spatial features below the diffraction limit is an interferometer [6], shown in Fig. 1.3a. An interferometer uses a monochromatic, coherent light source (the phase of the light is constant in time) of wavelength λ that is split along two separate optical paths, an imaging and a reference arm of lengths L_1 and L_2, respectively. At the end of the imaging arm is a near flat scattering surface and at the end of the reference arm is a flat mirror. The light from the surface and the mirror are reflected back and recombined along a common path to form an interference-pattern on an array detector [7].

In the figure, a scattering angle θ defines the tilt of the scattering surface along the imaging arm. For a scattering angle $\theta = \theta_1 \neq 0$, the interference pattern on the detector is given by image-1 in Fig. 1.3b. At each point in the pattern, the brightness is proportional to the incident intensity. The stripes of constant intensity are known as *interference fringes*, where the parallel pattern is caused from the misalignment of reflected waves from the scattering surface relative to the light from the reference arm [7].

The separation between these fringes changes as a function of the scattering angle θ [7, 8]. For example, given a scattering angle $\theta_2 < \theta_1$, the interference

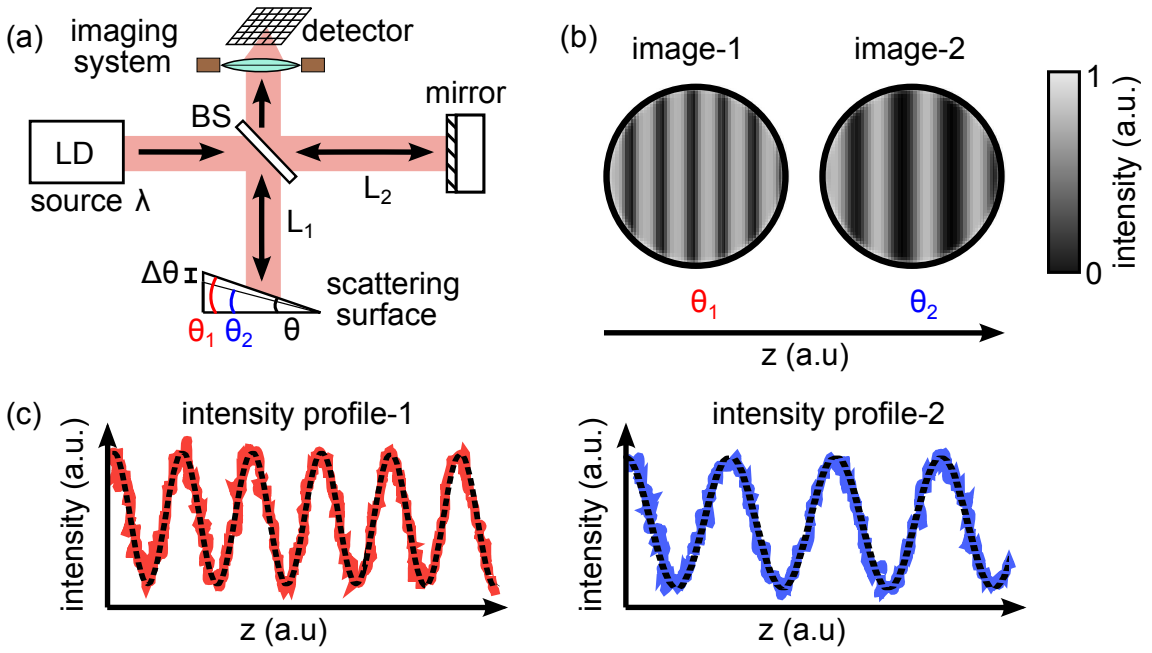

Figure 1.3: **Resolving subwavelength features using interferometry.** Coherent light of wavelength λ from a laser-diode (LD) source is separated using a beam splitter (BS) along two paths, an imaging arm of length L_1 with a reflecting scattering surface and a reference arm of length L_2 with a mirror. The reflected light from each path is focused through the circular aperture of an imaging system and forms an interference pattern on an array detector. (b) Interference patterns of image-1 and image-2 for the scattering angles θ_1 and θ_2, respectively. (c) Cross sections of the interference patterns along the z direction give intensity profile-1 (red) and intensity profile-2 (blue), which are fitted with periodic functions of frequencies f_1 and f_2 (black dashed-curves), respectively, where $f_1 > f_2$.

fringes shift further apart, as shown by the interference pattern in image-2 of Fig. 1.3b. This shift $\Delta\theta = |\theta_2 - \theta_1|$ is representative of a subwavelength change ($< \lambda$) to the features of the scattering surface, and by tracking the relative spacings of the interferences fringes, near-flat surface topologies can be resolved below the diffraction limit.

Experimentally, there are several ways to measure the spacings of these interference fringes. The simplest technique is to count the number of fringes in the interference pattern, but this method is limited to a resolution of $\sim \lambda/4$ [7]. An

enhanced resolution can be achieved by examining the cross-section of the interference pattern's intensity profile. In Fig. 1.3c, the cross sections of the interference patterns for image-1 and image-2 are plotted as intensity profile-1 and intensity profile-2 as a function of z. Note that the intensity fluctuates due to experimental noise in the imaging system and detector. Using a numerical fit of a periodic function to the data, the fringe spacing can be quantified by the frequency f of oscillation in the intensity profile. In addition, using a similar technique that tracks the relative phase of the interference fringes, this type of interferometer can be used to measure changes in the distance L_1 relative to L_2. However, the ability to quantify vastly subwavelength features ($<< \lambda$) using these fringes depends on the system's signal-to-noise ratio (SNR), which will be discussed in detail in the next subsection.

There are also built-in limitations in an interferometer's operation that such it can only image relatively flat surfaces [7]. However, even with this limitation, this type of interferometer, which appears in standard optics textbooks [6], is still considered to be a state-of-the art method for imaging surface profiles below the diffraction limit. For example, Agilent Technologies currently sells a high-resolution interferometer system (10716A) with a resolution of $\sim \lambda/2,000$.

A more recent development in subwavelength imaging technique was published in 2006, when researchers demonstrated a novel method for imaging nanoscale biological structures using visible light [9]. This technique, known as stochastic optical reconstruction microscopy (STORM), circumvents diffraction using fluorescent molecules that blink [10–13]. As depicted in Fig. 1.4a, a nanoscale biological structure is stained with fluorescent photo-switching molecules. These particular green fluorescent protein (GFP) molecules fluoresce green light ($\lambda \sim 500$ nm) when excited and act as fluorescent tags along the structure, where a nearby imaging system focuses the incident light onto an array detector.

In this imaging modality, each fluorescent molecule serves as a point-like source and scatterer. This can be an issue if two neighboring molecules, A and B in Fig. 1.4b, which are spaced by $\sim$ 10 nm [11], fluoresce simultaneously. In this case, similar to Fig. 1.2b, the diffraction patterns of the collected light from both A and B overlap and become difficult to distinguish from one another, as shown in Fig. 1.4c.

To overcome the diffraction limit, STORM uses an innovative measurement technique. Rather than excite all of the fluorescent molecules simultaneously, a weak excitation is used such that each molecule blinks stochastically [11]. In this stochastic mode-of-operation, the fluorescent tags blink on and off at random times, as illustrated in Fig 1.4d. In the figure, the average light intensities from molecules A and B are plotted as a function of time, and due to the stochastic nature of the photo-switching [11], there are times when molecule A fluoresces and molecule B does not (and vice versa). During these times, separate diffraction patterns for A and B can be isolated, as shown in Figs. 1.4e-f. The centroids of these separated diffraction patterns can be localized using a numerical fit of their respective intensity profiles, where the SNR of each intensity profile determines the resolution of the centroid localization (discussed in detail in the next subsection).

Using post-processing, the centroids of all the individual intensity profiles are located in both the x and y directions to reconstruct the protein's structure (see Fig. 1.4g) with a resolution $\sim$ 10 nm ($\lambda/50$) [11]. Based on the success of this method, new types of photo-switching molecules are currently being developed [14]. Thus, similar to interferometry, a specific type of intensity measurement combined with a numerical fitting procedure enhances the resolving power of STORM well below the diffraction limit.

However, STORM also has limitations. In particular, the photo-switching molecules can only be used to tag certain biological structures, limiting the types of samples

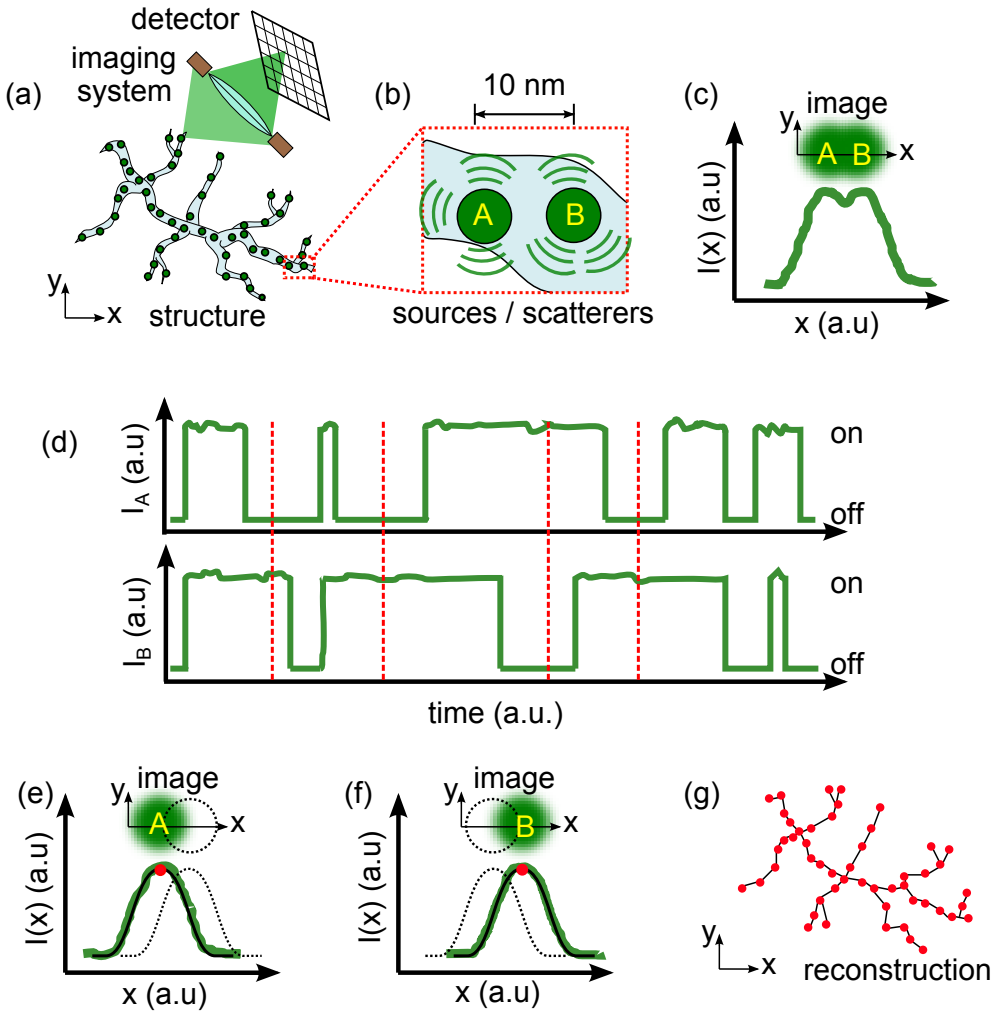

Figure 1.4: **Stochastic optical reconstruction microscopy.** (a) A structure labeled with photo-switching tags emits light that is focused by an imaging system onto an array detector. (b) Tags A and B, separated by $\sim$ 10 nm, fluoresce simultaneously. (c) Image and intensity profile in the x direction from A and B when they fluoresce at the same time. (d) Average intensities, I_A and I_B from A and B, respectively, as a function of time. High intensity indicates an "on" state when the tag fluoresces, and low intensity indicates an "off" state. Red dotted lines mark times when only one of the two tags is "on". (e) Intensity profile of A (green) while B is "off" (black dotted-line). (f) Intensity profile of B (green) while A is "off" (black dotted-line). Numerical fits of the intensity profiles (black solid lines) give measures of the centroids in each profile (red dots). (g) The centroids in the x and y directions are used to reconstruct an image of the structure.

that can be imaged. Another limitation is the acquisition time of STORM, which can take several minutes to collect light from all of the fluorescent tags. Decreasing the acquisition time means less collected light and, as a result, a smaller SNR [11].

1.2.1 Signal-to-Noise Ratio

This now begs the question: we know the imaging mechanisms of both interferometry and STORM, but what limits their resolutions? Or, in other words, if diffraction is no longer a factor in their imaging, why don't these methods have perfect resolutions? One answer lies in the ability to create a good numerical fit to the collected data, which is determined by the data SNR. Fitting data with a high SNR means that the information collected from the fit is more accurate. However, no signal has an infinite SNR, and thus the data and its fit can only give approximations of the scattering features.

A typical procedure for improving a system's SNR is to collect repeated measurements and average them together. The standard deviation of a noise level σ_{noise} of a repeated measurement scales as

$$\sigma_{\text{noise}} \propto \frac{1}{\sqrt{N}}, \tag{1.2}$$

where N is the number of measurements. As an exmaple, for STORM, N represents the number of photons collected in an intensity profile [15].

As mentioned earlier, for an interferometer, the SNR is determined by fluctuations in the system such as the detector's output voltages. Another example includes fluctuations of the refractive index of air with temperature, which cause changes in the reference and imaging arm lengths that can be larger than the detected changes $\Delta\theta$ or ΔL_1, limiting the system's resolution [7]. This is especially true for a weak

reflected signal from the scattering surface.

To combat these effects, there have been several techniques developed for improving the SNR of an interferometer. For example, one method is known as phase compensation interferometry, where a feedback mechanism is used between the detector and a piezoelectric transducer that controls the reference arm length L_2 (from Fig. 1.3a). This mechanism is used to keep the detected intensity profile constant, and by doing so, the feedback signal becomes a very sensitive measure of small changes along the imaging arm [7]. In addition, heterodyne interferometry uses an acousto-optic modulator to shift the frequency of the light along the reference arm, introducing a beat-frequency into the interference pattern which can be tracked with a lock-in detector to enhance the SNR a low amplitude reflected signal [7].

For STORM, the main limiting factor in its resolving capabilities is the system's contrast (signal to background noise) between the photo-switching "on" and "off" states [5]. Typically in experiments, the background noise can also influenced by other extraneous light sources [6]. Collecting more photons from a single fluorescent molecule can increase the SNR of the localization measurements [15]. In addition, coupling STORM with other sub-diffraction imaging techniques can also further enhance the system's SNR [15].

STORM represents one of the new imaging modalities for circumventing diffraction, and, along with it, are several other techniques that continue to revolutionize imaging capabilities. Before moving on to the next section, these other recently-discovered sub-diffraction imaging techniques deserve mentioning. For example, super-lenses made from negative-index media [16, 17] allow for the propagation of a wave's near field, which contains subwavelength scattering information but normally decays quickly, into its far-field, thus giving access to subwavelength features.

In addition, super-oscillations [18], which are a subwavelength phenomenon of interferences patterns, can give rise to enhanced subwavelength interference patterns in the focal plane of imaging system. Other techniques for accessing subwavelength information use nano-structures with surface plasmons for creating sub-diffraction focused imaging spots [19, 20]. With only a handful of techniques for resolving subwavelength information, each with its own advantages and limitations, the continued research of this field is important for the further development of imaging science.

1.3 A New Approach: Overview of Thesis

In this thesis, I present a novel method for sensing changes in the position of subwavelength scatterer with vastly subwavelength resolution. My technique, which represents the first step towards realizing a new class of imaging devices, is unique because:

- Its illuminating field, which contains multiple wavelengths, is self-generated through a feedback mechanism and changes depending on the scatter's location.
- The system does not require an array detector with separate pixels to localize the scatterer. Instead, a scalar measurement of the illuminating field, which can be performed with a single pixel detector at an arbitrary location, is used to resolve subwavelength position changes.
- For the first time, this sensing system combines two previously studied, separate fields of science: time-delayed nonlinear feedback and wave chaos.

- This method represents the first application of quasiperiodic dynamics (oscillations with incommensurate frequencies) for sensing purposes.

- The mechanism for sensing subwavelength changes gives rise to an easily detected signal, which can be measured without the need of a high-resolution sampling device, keeping the cost of the system low with a small amount of stored data.

The basic setup for my system is shown in Fig. 1.5a. An EM radiation source is coupled into a 2D structure known as a wave-chaotic cavity. The boundary of this structure is such that the EM radiation floods the cavity, filling it with scattered waves. A more detailed explanation of wave-chaotic cavities is given in Ch. 2. Inside the cavity is also a subwavelength dielectric scatterer that interacts with wavefronts from nearly all directions due to the complex scattering pattern of the injected EM waves. A portion of this radiation is then coupled out of the cavity to a detector that both processes the signal and drives the EM source. Thus, my system circulates EM energy through the cavity in a closed feedback loop.

Based on the nonlinear properties of the combined detector and source, this type of energy-circulating device is known as a time-delayed nonlinear feedback system (see Ch. 2 for more details). An interesting result of this nonlinear feedback is that the circulated EM energy can have a time varying, oscillatory intensity. These oscillations are self-generated and stable; no other excitation source is necessary. An example of the oscillatory field $E(t)$ is given in Fig. 1.5a, where $E(t)$ oscillates while its intensity profile modulates slowly in time. Furthermore, due to the constant circulation and finite propagation time of the EM radiation through the system, the overall feedback loop stores a large amount of energy, allowing access to precise measurements with a high SNR. The resulting intensity oscillations are also sensi-

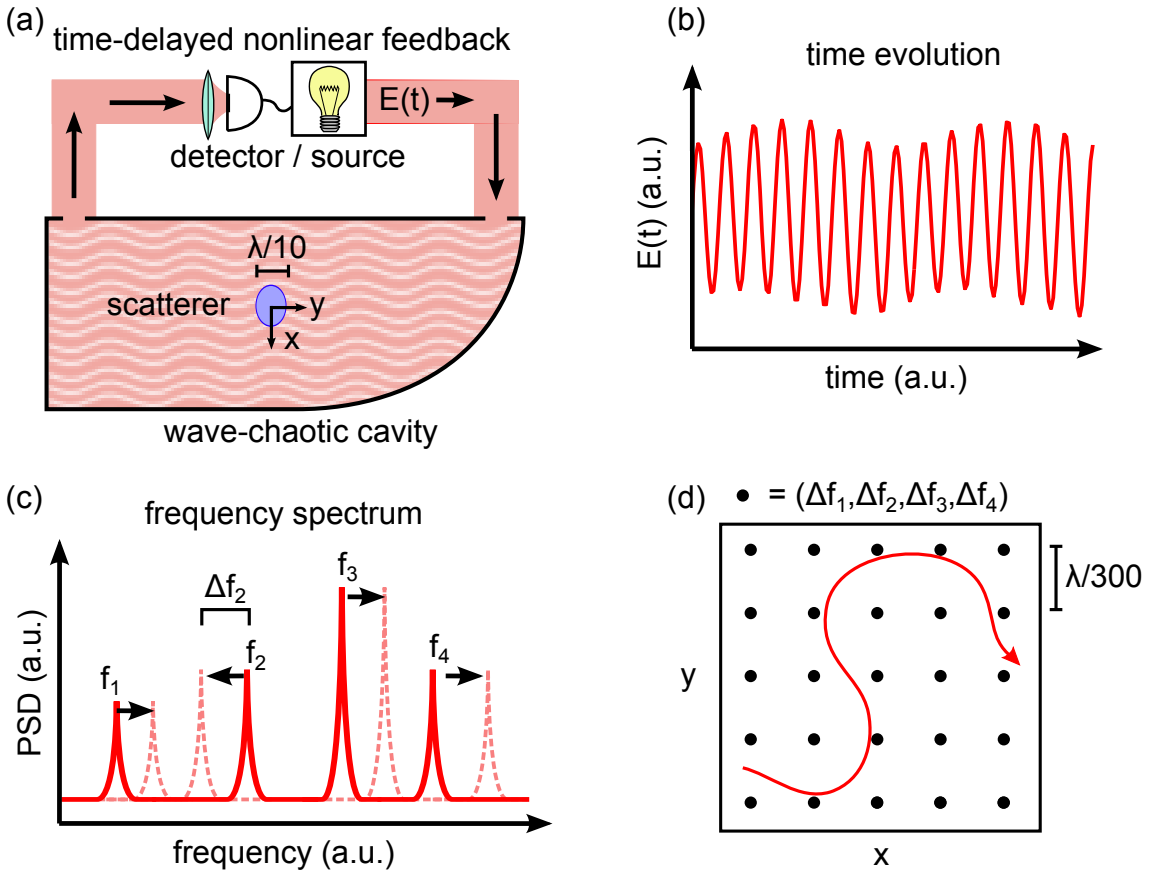

Figure 1.5: **Time delayed nonlinear feedback through a wave-chaotic cavity.** (a) A source floods EM raditation into a wave-chaotic cavity, where it scatters and diffracts off of a subwavelength object ($\sim\lambda/10$), exits the cavity to a detector, and recirculates through the feedback loop. (b) The measured EM radiation as a function of time. (c) The power spectral density of the detected field $E(t)$ with primary frequencies that shift as a function of scatterer position. (d) Calibration grid (black dots) for interpolating and tracking the scatterer's location (red curve) in a 2D plane (x, y) with subwavelength resolution.

tive to the scatterer's location and change as a function of its position. Thus, this feedback system represents a new type of dynamically-sensitive illumination source.

This system's design is tailored to determine the position of the subwavelength scatterer inside of a 2D area of the cavity with a subwavelength resolution. The localization is achieved through measurements of the frequency content of the oscillations that propagate through the feedback loop. As shown in Fig. 1.5c, a typ-

ical frequency spectrum of the field shows several dominant frequencies f_i for a fixed scatterer position. As the scatterer moves, these frequencies shift by Δf_i, and calibrated measurements of these frequency shifts are mapped out in a grid with subwavelength spacing ($\lambda/300$), as shown in Fig. 1.5d. In the figure, each black dot represents a unique measurement of frequency shifts $(\Delta f_1, \Delta f_2, \Delta f_3, \Delta f_4)$. After the calibration, I measure the system's frequency shifts as the scatterer moves throughout the 2D grid along an arbitrary path and use the calibration points to interpolate the scatterer's movements and reconstruct its path with a 1D resolution of $\sim \lambda/10,000$ and a 2D resolution of $\sim \lambda/300$.

Similar to interferometry and STORM, I use a numerical fit of the detected signal in order to enhance the overall resolution of the system. The oscillations in Fig. 1.5b are fit with the function

$$E(t) = \sum_{i=1}^{N} c_i \sin(2\pi f_i t + \phi), \tag{1.3}$$

where c_i and f_i are constant fitting coefficients, ϕ is an offset phase, and N is the total number of dominant frequencies. By tracking the changes to f_i in each fit, I am able to measure small frequency shifts $\Delta f_i << f_i$, yielding an enhanced subwavelength sensitivity to the scatterer's location. Lastly, I choose to observe $E(t)$ after a large accumulated ϕ such that small frequency shifts are easily detectable with minimal data on a digital oscilloscope. The full details of these results and my acquisition methods are presented in Ch. 3 and Appendix A.

This new imaging modality also has limitations. First and foremost, I have only demonstrated a proof-of-concept for the application of this system using radio-frequency (RF) EM radiation ($\lambda \sim 15$ cm), and it is currently limited to imaging the location of only a single, dielectric scatterer in a small 2D area. In addition, by

flooding the wave-chaotic cavity with EM waves, the interference patterns of the scattered radiation are extremely complex and sensitive. Thus, due to this sensitivity (which works as advantage for imaging), the scatterer's properties (size, shape, orientation, dielectric constant, etc.) must be fixed between the system's calibration and measurements; changing to a different scatterer requires a new calibration grid. Even with these limitations, the system's resolving capabilities are still promising for future subwavelength microscopy applications.

I published the original concept and results for this imaging system in Physical Review Letters [21], where it is highlighted as an *Editor's Selection*. Since its publication, I have continued my investigations of the experimental results and discovered the following: methods for modeling the dynamics of the system (Ch. 4), new theories for interpreting the experimental results (Ch. 5), and new experiments in both the RF and optical frequency domain that show the potential universality of this work (Ch. 6-7).

1.3.1 Chapter Summaries and Main Results

Overall, the thesis is divided into two main sections: (i) an experimental section made up of Chs. $2-3$, which details my apparatus, techniques, and observations, and (ii) a theoretical section made up of Chs. $4-6$ that investigates different models to explain the observed phenomena. In particular, from all my experimental observations, I focus my modeling efforts on understanding the sensing mechanism which uses quasiperiodic dynamics. This sensing mechanism has not previously been investigated, and there is currently no theory to explain my observations. Thus, modeling and understanding the quasiperiodic sensing mechanism is the primary topic discussed throughout the second half of this dissertation. Specifically, I

provide a model with sufficient ingredients to reproduce qualitatively the dynamics, a technique for predicting the quasiperiodic frequencies, and a simplified system to understand how the quasiperiodic frequencies shift. As support of my theoretical investigations, I also implement experimentally a simple system in Ch. 6 that provides additional insight into the necessary ingredients quasiperiodic sensing.

More specifically, in Ch. 2, I detail the two main components of the sensing system: a time-delayed nonlinear feedback system (Fig. 1.6a) and a wave-chaotic cavity (Fig. 1.6b). The nonlinear feedback system uses a nonlinear circuit to create an approximately piecewise-linear (and hence nonlinear) relationship between its input and output voltages. In a closed feedback loop configuration, the circuit's output is amplified, delayed, and reinjected at its input, and this system can self-oscillate at high frequencies ($\sim$ 1 GHz) with dynamics that range from narrow-band periodic oscillations to broad-band chaos. The second component of the imaging system is a wave-chaotic cavity, which is an approximately 2D scattering environment with densely and irregularly spaced resonances over a broad frequency range (10 MHz $< f <$ 10 GHz). Based on the spacing of these resonances, the cavity is classified as chaotic both with and without a dielectric scatterer. Using the pulse-response of the cavity, which is a time-domain representation of the resonances, I demonstrate a method for sensing the presence and position of the scatterer along a path in 1D using a correlation measure between different pulse responses. The subwavelength resolution of this 1D method ($\sim \lambda/600$) serves as a reference for comparing the results of Ch. 3.

Chapter 3 focuses on the core results for subwavelength sensing in the full experimental setup, the cavity-feedback system, shown in Fig. 1.7a. By translating the scatterer in the cavity-feedback system, I show that the dynamics of the illuminating field can change depending on its location. These qualitative changes yield

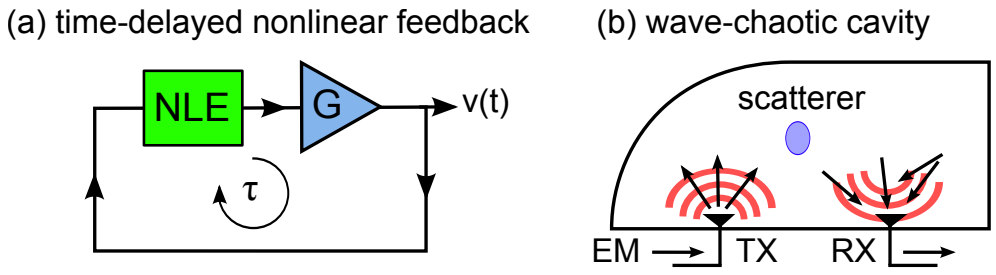

Figure 1.6: **Main components of the imaging system.** (a) Time-delayed nonlinear feedback system. The output of a nonlinear element (NLE) is amplified with gain G and time-delayed by a fixed amount τ. The delayed signal is reinjected into the NLE to form a closed feedback loop. In the experimental system, the NLE is a transistor-based nonlinear circuit and the output of the system is measured as a time varying voltage v(t). (b) Wave-chaotic cavity. The 2D structure is an aluminum, quarter-stadium shape with transmitting (TX) and receiving (RX) antennas to couple EM radiation in and out of the cavity, respectively. The injected radiation interacts with the scatterer inside the cavity through reflection and absorption.

an extremely sensitive and history-dependent method for detecting and reporting changes in its position. Then, using different dynamical regimes (chaos, periodicity, and quasiperiodicity), I illustrate the potential for detecting quantitatively the position of the scatterer with subwavelength resolution. In the broad-band chaotic regime, the oscillations surrounding large-amplitude spikes in the dynamics show sensitivity to the scatterer's position, which can be quantified to yield a 1D resolution of $\sim \lambda/1,200$. In the narrow-band periodic regime, the frequency of oscillation shows a sensitivity to the scatterer's position, which can be recorded and fitted with a function to yield an improved 1D resolution of $\sim \lambda/20,000$.

Lastly, in order to realize a 2D imaging method, I measure simultaneously the multiple frequencies of the system's quasiperiodic dynamics, shown in Fig. 1.7b, as a function of scatterer's position. The frequencies in the quasiperiodic spectrum, shown in Fig. 1.7c, shift independently, thus providing a unique map to the scatterer's 2D position (x, y). After an initial calibration, I test the quasiperiodic imaging

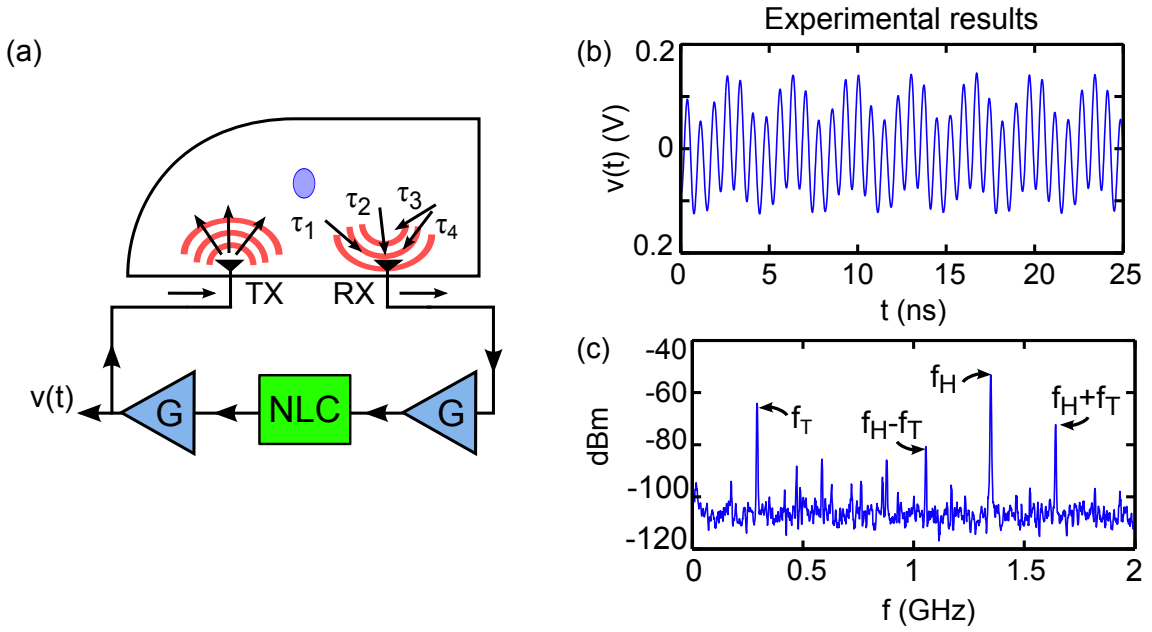

Figure 1.7: **Full experimental setup** (a) showing the combination of the time-delayed nonlinear feedback system with the wave-chaotic cavity to form the cavity-feedback system. The propagation delays of a scattered signal in the cavity τ_i through the cavity are the time delays of the nonlinear feedback system. The time-evolving voltage v(t) represents a measurement of the EM oscillations in the feedback loop. The nonlinear element of the feedback loop is a nonlinear circuit (NLC) whose input and output are amplified. (b) Experimental time series of the quasiperiodic oscillations of v(t) while the scatterer's position is fixed. (c) Experimental power spectral density (PSD) of the quasiperiodicity with primary frequencies f_{H}, f_{T}, and linear combinations $f_{\mathrm{H}} \pm f_{\mathrm{T}}$.

system experimentally by tracking the scatterer's position along a path in 2D. Overall, the quasiperiodicity provides an average 1D resolution of $\sim \lambda/10,000$ and an average 2D resolution of $\sim \lambda/300$.

To better understand the details of the quasiperiodic dynamics of the cavity-feedback system, I combine separate models for the nonlinear circuit and the wave-chaotic cavity in Ch. 4. The modeling strategy is depicted in Fig. 1.8a. In the model, the output of the nonlinear circuit is split into many paths, each with time-delay τ_i and gain coefficient g_i, which are then summed, amplified, and reinjected into the

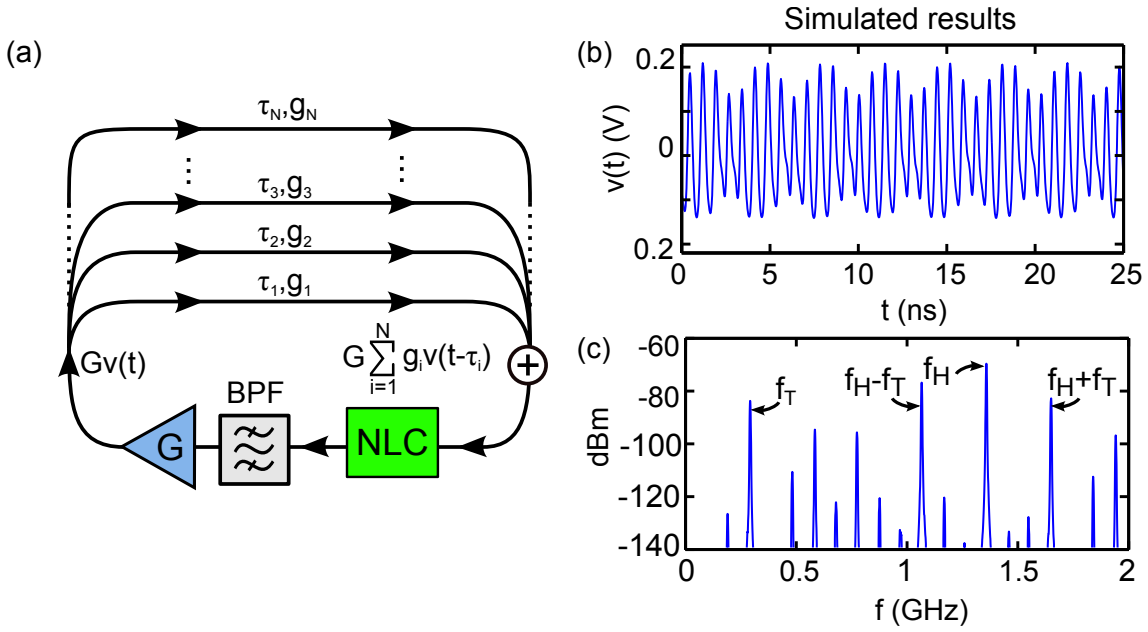

Figure 1.8: **Cavity-feedback system model.** (a) Pictorial representation of the model. The output voltage of the nonlinear circuit passes through a band-pass filter (BPF) with output v(t) that is amplified with gain G, split among (τ_i, g_i), summed, and reinjected into the NLC. (b) Simulated time series of the quasiperiodic oscillations of v(t) while the scatterer's position is fixed. (c) Simulated power spectral density (PSD) of the quasiperiodicity with primary frequencies f_{H}, f_{T}, and linear combinations $f_{\mathrm{H}} \pm f_{\mathrm{T}}$.

nonlinear circuit to form the closed feedback loop. The model for the nonlinear circuit includes non-ideal high-frequency effects and the model of the wave-chaotic cavity is simulated as a convolution with the delay-gain distribution (τ_i, g_i) of the system (measured using the finite bandwidth pulse response of the cavity). In addition, a band-pass filter with gain is used to model the remaining components in the feedback loop of the system. As shown in Figs. 1.8b-c, the resulting oscillations of the full model are quasiperiodic with a comparable frequency distribution to that of Figs. 1.7b-c. With the experimental dynamics as a comparison, I demonstrate that the full model for the system is capable of reproducing numerically the approximate quasiperiodic dynamics from the experiment.

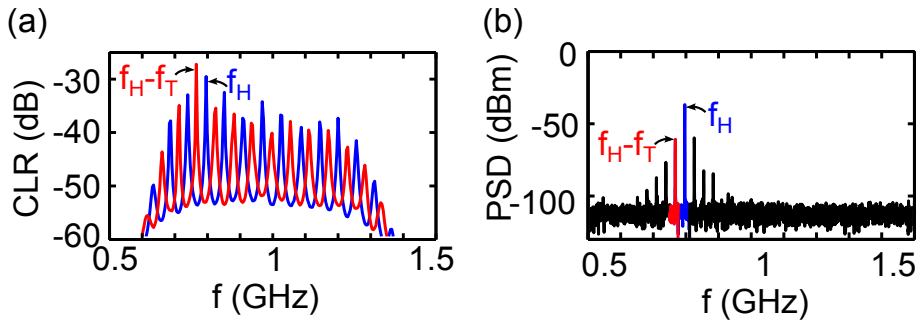

Figure 1.9: **Closed-loop resonances** (CLR) of the nonlinear feedback system with a single time delay showing (a) the predicted values for $f_{\mathrm{H}} \sim 796$ MHz and $f_{\mathrm{H}} - f_{\mathrm{T}} \sim 766$ MHz. The blue and red resonances are measured for specific configurations of the nonlinear circuit based on the theory. (b) Power spectral density (PSD) of the quasiperiodic signal with actual $f_{\mathrm{H}} \sim 797$ MHz and $f_{\mathrm{H}} - f_{\mathrm{T}} \sim 767$ MHz labeled in blue and red, respectively.

In Ch. 5, I simplify the model of the cavity-feedback system to the general form of a band-pass filter with time-delayed nonlinear feedback. This allows me to derive analytical expressions to predict the numerical values of the quasiperiodic frequencies in the dynamics. The results of these analytical expressions are also the closed-loop transfer functions of the feedback system with linearized feedback. Using new methods that I developed for measuring these closed-loop transfer functions, namely the resonance (R) method, the shifted-resonance (SR) method, and the amplitude-modulation (AM) method, I show that the frequencies of quasiperiodicity can be predicted in simulations with randomly chosen delay-gain distributions. Furthermore, as shown in Fig. 1.9a, for specific parameter configurations of the nonlinear circuit, the largest resonance peaks of closed-loop transfer functions in the experimental system give estimations for the quasiperiodic frequency spectrum shown in Fig. 1.9b. Therefore, using my derivations from the simplified model yields new experimental measures that help to explain the origins of the quasiperiodicity in the cavity-feedback system.

In Ch. 6, I simplify my quasiperiodic sensing technique down to its most essential components: a band-pass-filtered, time-delayed, nonlinear feedback system with two independent feedback loops, as shown in Fig. 1.10. The goal of this chapter is to study experimentally and analytically the frequency shifts of quasiperiodicity using known changes to the delay-gain distribution. These changes take the form of time-delay shifts that are controlled using two separate variable delay-lines in the dual-delay setup. In the experiment, I demonstrate that the quasiperiodic frequency shifts of the two-delay system can also be used to form a unique map to reconstruct the values of the time-delay shifts. This two-delay system therefore behaves similarly to the full cavity-feedback system. Using the simplified model for the nonlinear feedback system, I derive analytical expressions for the frequency shifts in the quasiperiodic dynamics as a function of small delay changes. The results of these derivations also yield an expression that can be used to test for the existence of a unique map between the quasiperiodic frequency shifts and the values of the system's delays. These theories are applied using simulations and experimental results. To conclude, I revisit the cavity-feedback system dynamics and discuss the implications of these theories with respect to the original results from Ch. 3.

Finally, in Ch. 7, I summarize my contributions and discuss the future applications of my work. Using the ideas from Ch. 1-2, I also comment on the potential of these results with respect to other types of nonlinear feedback systems and wave-chaotic cavities. Specifically, I propose a future study in the quasiperiodic dynamics of a semiconductor laser with time-delayed feedback for realizing a new, all-optical 2D subwavelength position sensor. Preliminary experimental analysis of this system is conducted using the setup shown in Fig. 1.11 with nanometer-resolving capabilities for sensing and imaging applications.

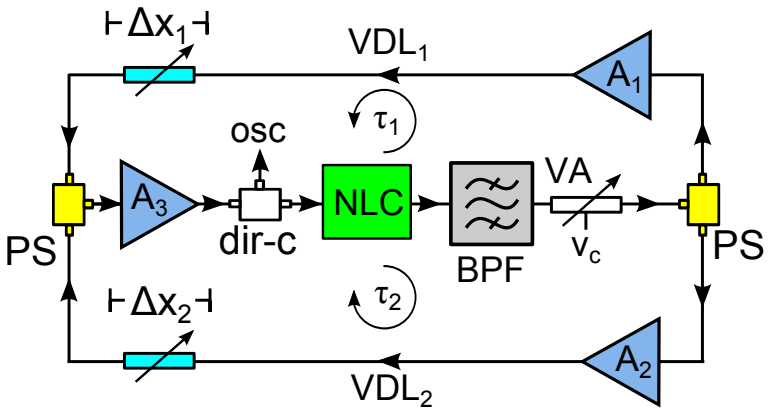

Figure 1.10: **Two-delay nonlinear feedback system** with time delays τ_1 and τ_2. The dual-delay nonlinear system uses a nonlinear circuit (NLC), power splitters (PS), a variable attenuator (VA) with control voltage v_c, amplifiers A_i, two variable delay lines (VDLs), a band-pass filter (BPF), and a directional coupler (dir-c) in its feedback, where the feedback signal is measured using an oscilloscope (osc). The values of the time-delays τ_1 and τ_2 are adjusted using coaxial waveguides of tunable lengths Δx_1 and Δx_2, respectively.

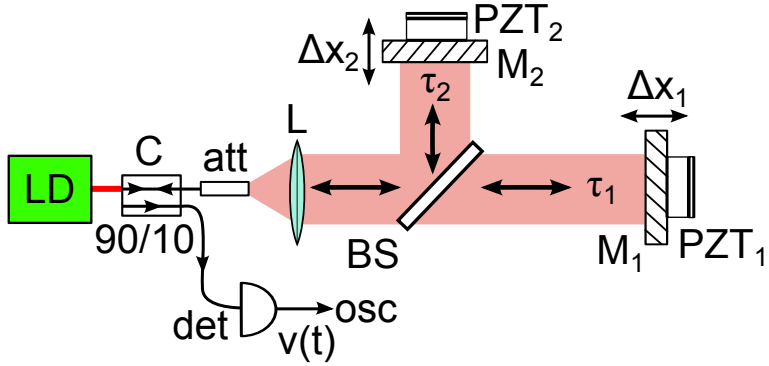

Figure 1.11: **Two-delay all-optical feedback system for subwavelength sensing.** The output of a laser diode (LD) passes through a collimating lens (L) in free space, separates using a beam splitter (BS), is time-delayed along two separate paths with propagation delays τ_1 and τ_2, and feeds back to itself. Mirrors M_1 and M_2 at the end of these paths are attached to piezoelectric transducers PZT_1 and PZT_2 to make small adjustments to τ_1 and τ_2 by changing the relative locations Δx_1 and Δx_2, respectively. Using an attenuator (att) and a 90/10 coupler (C), the feedback gain is controlled and the feedback signal is routed to a photodetector (det) and an oscilloscope (osc).

Chapter 2

Time-delayed Nonlinear Feedback Systems and Wave-Chaotic Cavities

In this dissertation, I describe a a novel method for imaging the position and relative movements of a subwavelength object with subwavelength resolution. This new experiment combines concepts from two existing fields of scientific inquiry: time-delayed nonlinear feedback systems and wave chaos. In this chapter, I first briefly review time-delayed nonlinear feedback systems and demonstrate an experimental example. Then, I introduce the concept of wave-chaos and illustrate the characterization and properties of my experimental wave-chaotic cavity. Both sections include a brief literature review of the imaging applications for each topic. This chapter provides a basic foundation for understanding the dynamical behaviors and properties associated with time-delayed nonlinear feedback systems and wave-chaotic cavities as these two topics will be combined later to form my imaging system.

The experimental and numerical results of this chapter were obtained with the help of several individuals. The nonlinear circuit featured throughout this dissertation was designed by Zheng Gao based on Ref. [22]. Hugo Cavalcante helped with the construction of wave-chaotic cavity and the design of the experimental procedure for acquiring the pulse responses of the system. Furthermore, numerical simulations were performed with the help of Damien Rontani. Lastly, the analysis of my data benefited from discussions with Daniel Gauthier and Damien Rontani.

2.1 Time-delayed Nonlinear Feedback Systems

The study of time-evolving systems is a research topic that branches out across various areas of science including physics, chemistry, and biology [23–25]. Specifically, research involving nonlinear systems, also known as nonlinear dynamics, has improved our understanding of many of the world's complex systems ranging from weather patterns [26] to atomic interactions [27] and genetic networks [28]. In addition, harnessing the dynamics of engineered nonlinear systems has led to technological advances including high-speed electronic [22] and opto-electronic oscillators [29] and, in particular, new methods for using a laser for imaging [30]. Due to the richness of phenomena observed in nonlinear dynamical systems, this field continues to be an active area of research.

A subset of nonlinear dynamical systems are those with time-delayed feedback, where information about the system in the past is coupled into the dynamics of the present. They are encountered in nature [25, 28] and in man-made experiments studied in laboratories [29]. In particular, time-delayed feedback can arise in high-speed electronic and optical systems where the propagation delays of signals can be comparable to the time scales of the dynamics [31]. A common time-delayed nonlinear feedback system contains a nonlinear element whose output state variable $x(t)$ is amplified and coupled back to its input through a single feedback loop that delays the signal by a fixed amount τ [32], as shown schematically in Fig. 2.1. The time-evolution of this system can be represented typically by

$$\dot{x}(t) = F[x(t), x(t-\tau)], \tag{2.1}$$

where F is a nonlinear function. Thus, the temporal evolution of such a system is determined by the value of x at time t as well as at time $t-\tau$.

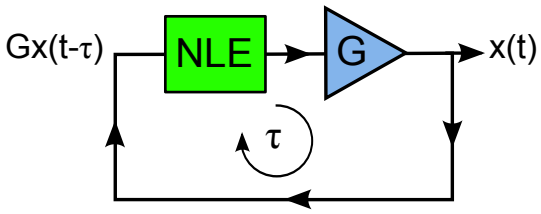

Figure 2.1: **Time-delayed nonlinear feedback system.** (a) General time-delayed nonlinear feedback system with a nonlinear element (NLE), net time delay τ, gain G, and state variable $x(t)$.

For a dynamical system, the dimensionality M of the its phase space is equal to the number of independent variables that defines its initial state (at time $t = 0$) [33]. For non-delayed systems, the initial value of each independent variable is necessary to predict the system's dynamics. However, for Eq. (2.1), an infinite number of initial values are necessary to specify the starting state of the system. As time progresses from $t = 0$, the delayed variable $x(t-\tau)$ must be specified for all values of $t \in [-\tau, 0]$. Thus, for Eq. (2.1), the dimensionality of its phase space is, surprisingly, infinite [33].

The dynamics of $x(t)$ moves throughout phase space and converges to a attracting set of trajectories known as an attractor. An attractor represents the trajectories or solutions that initial system states asymptotically approach and remain once there [34]. In other words, an attractor is a region of phase space with a flow that attracts all other phase space points from within a certain distance or basin of attraction. In time-delayed nonlinear feedback systems, the consequences of an infinite phase space can lead to high-dimensional attractors and, as a result, the emergence of complex dynamical behaviors [35].

As demonstrated in the next subsection, these dynamical behaviors include: steady-state dynamics, periodic oscillations, quasiperiodicity, and chaos. In steady-state, the system's dynamics are constant in time, whereas, with periodic oscilla-

tions, the system produces an oscillatory signal that repeats in time and is typically characterized by one or more commensurate frequencies in its spectrum. On the other hand, quasiperiodicity, which is also an oscillatory signal, does not repeat in time due to the fact that its frequency content is comprised of several incommensurate frequencies [23]. Lastly, time-delayed nonlinear feedback systems can generate broadband signals with many different frequencies known as chaos.

Chaos, which was first discovered by Edward Lorenz in 1963 [26], is a deterministic, non-repeating signal that is characterized by a sensitivity to initial conditions, leading to an exponential divergence of trajectories along the system's attractor. For a continuous-time system to produce chaotic dynamics, it must have a nonlinearity and a phase space dimensionality $M \geq 3$ [23, 34]. Though Eq. (2.1) is simple in its form, it satisfies both of these criteria and can be used for generating many varieties of dynamical behaviors including chaos [22, 36, 37].

Systems that obey Eq. (2.1) have been designed in the laboratory using optical and electronic components. In the following subsection, I present a time-delayed nonlinear feedback system using a specific nonlinear electronic circuit with a feedback loop to produce ultra-high-frequency dynamics (30 MHz $-$ 3 GHz). This nonlinear circuit will be used later as an essential component in my subwavelength imaging system.

2.1.1 Experimental Electronic System Using a Single Time-Delayed Nonlinear Feedback Loop

The nonlinear circuit used in my experiments is based on a design that was first introduced by Illing *et al.* [22]. This circuit, which lies at the heart of my time-delayed nonlinear feedback system, is constructed on a printed circuit board using

a high-speed transistor (BFP620) and several passive electronic components (resistors, capacitors, inductors), as shown in Figs. 2.2a-b. The circuit board is made of a dielectric material known as FR4 ($\epsilon \sim 4.5$) and copper to conduct voltages throughout the circuit and serve as a ground plane. In the figure, the transistor, which serves as the main nonlinear element (NLE) of the circuit, is circled to highlight its location. The purpose of the nonlinear circuit (NLC) is to process or detect a time-varying input voltage v_{in} and to produce a a modified output voltage v_{out}.

The circuit diagram for the NLC in Fig. 2.2c helps to illustrate its function. In the schematic, a supply voltage V_{CC} powers the transistor, where the resistor R_2 and inductor L_2 help prevent high-frequency signals from coupling to the power supply. For input voltages below the transistor's operating threshold $v_T \sim 0.7$ V, the transistor is non-conducting and the output current of the device is given by the voltage drop across the resistor labeled R_{NL}. For input voltages above v_T, the transistor is in an active state and the output current is the difference between the voltage drop across R_{NL} and the circuit's current flowing through the transistor and resistor R_1 to ground [22]. The output capacitor C_2 blocks the direct current component of the input signals and the supply voltage such that v_{out} is an alternating current (ac) coupled signal. Lastly, to raise low amplitude input voltages near the transistor's threshold, a bias voltage v_b is added to v_{in} such that the true input voltage of the device is $v_{in} + v_b$. When powered and driven with an oscillatory signal, the nonlinear circuit continuously switches the transistor on and off, performing effectively a nonlinear operation on v_{in}.

To demonstrate the basic functional operation of this nonlinear circuit, I characterize the output voltage v_{out} as a function of an input sinusoidal driving signal v_{in}. Using a driving signal at frequency $f = 270$ MHz and $v_b = 0.7$ V, I plot the waveform v_{in} versus v_{out} in Fig. 2.2d. For voltages below v_T, the nonlinear aspects of the

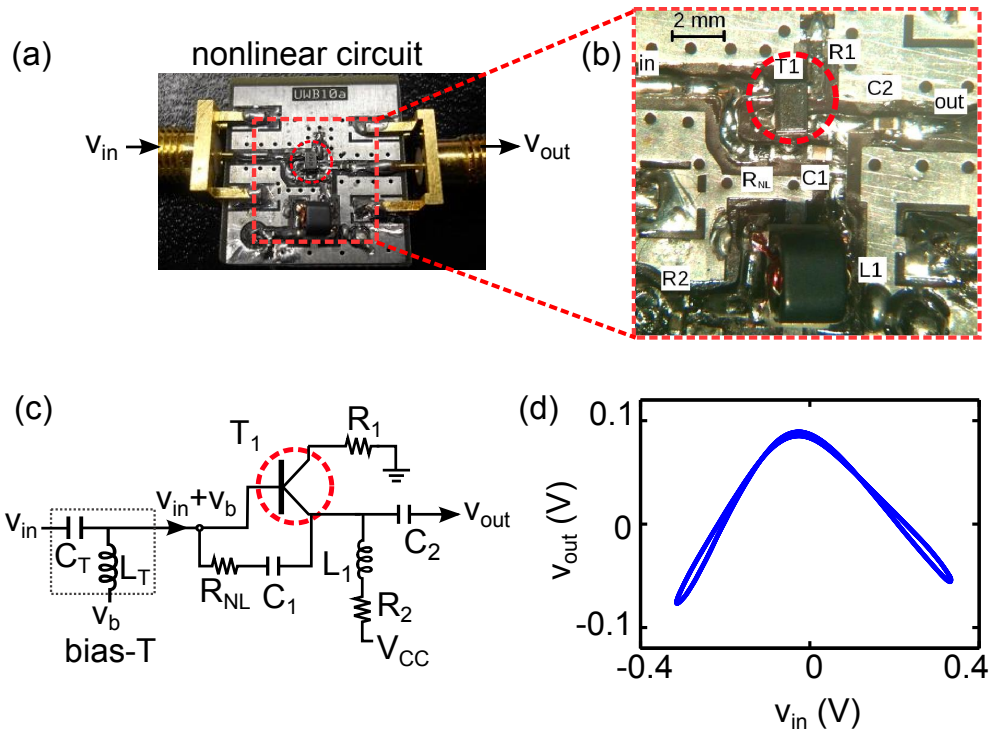

Figure 2.2: **Nonlinear circuit**. (a) Photograph of the circuit board showing its input and output connectors for voltages v_{in} and v_{out}, respectively. (b) Zoom of the nonlinear circuit indicating the relative locations of the transistor, supply voltage $V_{CC} = 1.6$ V and the passive components: $R_{NL} = 30\ \Omega$, $C_1 = 47$ nF, $L_1 = 1\ \mu$H, $R_1 = 5.1\ \Omega$, $R_2 = 68\ \Omega$, and $C_2 = 0.1\ \mu$F. The capacitor C_T and inductor L_T represent the bias-T (grey dotted box) that adds the voltages v_{in} and v_b. In (a), (b), and (c), the transistor is highlighted with a red-dotted circle. (d) Tent-like nonlinear operation of the circuit between the voltages v_{in} and v_{out}, where v_{in} is generated using a signal generator (Agilent E8267D) and v_{out} is measured on an oscilloscope (DSO80804A with noise floor standard deviation $\sigma \sim 1.2$ mV).

circuit remain inactive and the circuit produces a linear input-output relation. For voltages above v_T, the nonlinear circuit induces an anti-linear input-output relation. Thus, this transistor-based circuit behaves like a piecewise-linear (PWL) function

$$F_{\text{PWL}}(v_{in}) = v_{out} \sim \begin{cases} A_0 + A_1 v_{in}, & \text{if } v_{in} \leq v_T \\ B_0 + B_1 v_{in}, & \text{if } v_{in} > v_T \end{cases}, \tag{2.2}$$

where A_0 and B_0 are constant coefficients and $A_1 < 0$ and $B_1 > 0$ are slopes of opposite signs. The tent-like shape between the NLC input and output voltages is similar to circuit operation proposed in Ref. [22].

It is important to acknowledge that this characterization of the NLC is not exhaustive. In particular, there are several non-ideal filtering properties that are associated with its operation at high-frequencies ($f > 500$ MHz) that are not shown here. At this point, I simply want to establish that the circuit behaves in a deterministic, nonlinear fashion. This assumes that the non-ideal aspects of the circuit are not essential for demonstrating its role in the dynamics of a time-delayed nonlinear feedback system. For the full details of its higher-frequency mode-of-operation, see Chapter 4, where an in-depth characterization is performed and a model is developed specifically to include these non-ideal effects. In addition, for a more comprehensive comparison of this particular NLC with the circuit from Ref. [22], refer to Appendix B.

In a time-delayed feedback loop, the output of the NLC is delayed and injected at its input using a coaxial cable. As shown in Fig. 2.3, several linear electronic components are also included between its input and output. First, the output of the nonlinear circuit v_{out} passes through a variable attenuator (VA) that controls the net gain of the entire feedback loop using a control voltage v_c. Then, due to the inherent losses as it propagates through the coaxial cable, v_{out} is amplified by the amplifier A_1. Next, v_{out} is band-pass filtered (BPF) so that a certain frequency band ($f^{(-)} < f < f^{(+)}$) is selected and limits the overall system's bandwidth, following the design in Ref. [22]. The output voltage of the BPF $v(t)$ is measured using a directional coupler (dir-c) and a high-speed oscilloscope (osc). Lastly, prior to the input of the nonlinear circuit, $v(t)$ is amplifed again by A_2 for additional gain and then added to v_B. Thus, the schematic in Fig. 2.3 represents a band-pass filtered

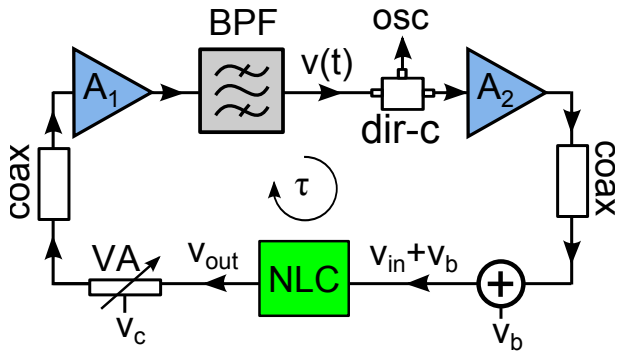

Figure 2.3: **Ultra-high-frequency system.** The nonlinear circuit (NLC) drives a variable attenuator (VA, Mini-Circuits ZX73-2500+) with a control voltage (v_c), the amplifier A_1 (Mini-Circuits ZX60-3018G+), a band-pass filter (BPF, Mini-Circuits ZBFV-925+), a directional coupler (dir-c, Mini-Circuits ZX30-9-4+), the amplifier A_2 (comprised of two amplifiers in series: Mini-Circuits ZX60-3018G+ and Picosecond Pulse Labs 5828-108), and a bias-T (Mini-Circuits ZFBT-6G+) with bias voltage v_b. Coaxial cables (coax) connect these components and act as a propagation delay. The net time-delay of a signal through the feedback loop is τ.

system with time-delayed nonlinear feedback.

To demonstrate the various dynamical states of the system, I vary the net gain G of the feedback loop using the control voltage v_c of the VA [22]. For low (high) values of the v_c, the attenuation of the VA is high (low) and thus G is low (high). The voltage v_c, which is used to tune the feedback dynamics, is known as the system's *bifurcation parameter*.

Using this bifurcation parameter, I examine the dynamics of the system with increasing values of v_c. As shown in Fig. 4.17a, for $v_c < 2.6$ V, the nonlinear feedback system shows the steady-state dynamics $v(t) \sim 0$ V. The frequency spectrum of the steady-state is plotted in Fig. 4.17b, which shows the power spectral density (PSD) of the noise-floor in the system (small narrow spikes in the spectrum are caused by the internal electronics of our oscilloscope and ambient RF noise in the room). A 2D projection of the phase-space representation of the steady-state dynamics is plotted in Fig. 4.17c using a time-delayed embedding to reconstruct the system's

dynamical trajectories [38]. As shown in the figure, the steady-state is represented by a single fixed-point in phase space.

For control voltages 2.6 V $\leq v_c <$ 3.5 V, the output voltage $v(t)$ changes to periodic oscillations (Fig. 4.17c) at a single frequency $f_H \sim 797$ MHz (Fig. 4.17e). The change to periodic dynamics from a steady-state is typically known as a *Hopf bifurcation*, which always has an associated *Hopf frequency* f_H [23]. A detailed description for this type of Hopf bifurcation is provided in Chapter 5. The phase space projection of the periodic $v(t)$ is plotted in Fig. 4.17f. In this case, the system's trajectories form a limit-cycle [23].

For control voltages 3.5 V $\leq v_c <$ 4.3 V, the output voltage $v(t)$ changes to quasiperiodic oscillations (Fig. 4.17g) with the addition of a new frequency $f_T \sim 30$ MHz and the mixed frequencies $f_H \pm k f_T$ (Fig. 4.17h), where k represents an integer harmonic number. Similar to a Hopf bifurcation, the change to quasiperiodic dynamics from a periodic state is typically known as a *torus bifucation* with an associated *torus frequency* f_T [23]. A detailed description for this type of torus bifurcation is also provided in Ch. 5. The torus bifurcation is named based on the phase space representation of the resulting quasiperiodic dynamics. As shown in Fig. 4.17i, the 2D projection of the dynamical trajectories for this state forms a torus.

Lastly, for control voltages 4.3 V $\leq v_c <$ 5.2 V, the output voltage $v(t)$ changes to a non-repeating oscillation (Fig. 4.17j) with a broadband frequency spectrum (Fig. 4.17k). In addition, the phase-space projection (Fig. 4.17l) reveals a complex structure with trajectories that fill more regions of phase space (as compared to periodicity or quasiperiodicity). Thus, based on the complex characteristics of this waveform, I conjecture that this dynamical state of $v(t)$ is chaotic. To verify that this type of dynamical behavior is not just due to electrical noise, I present a simple model of the dynamics in the next subsection to verify that similar chaotic-like

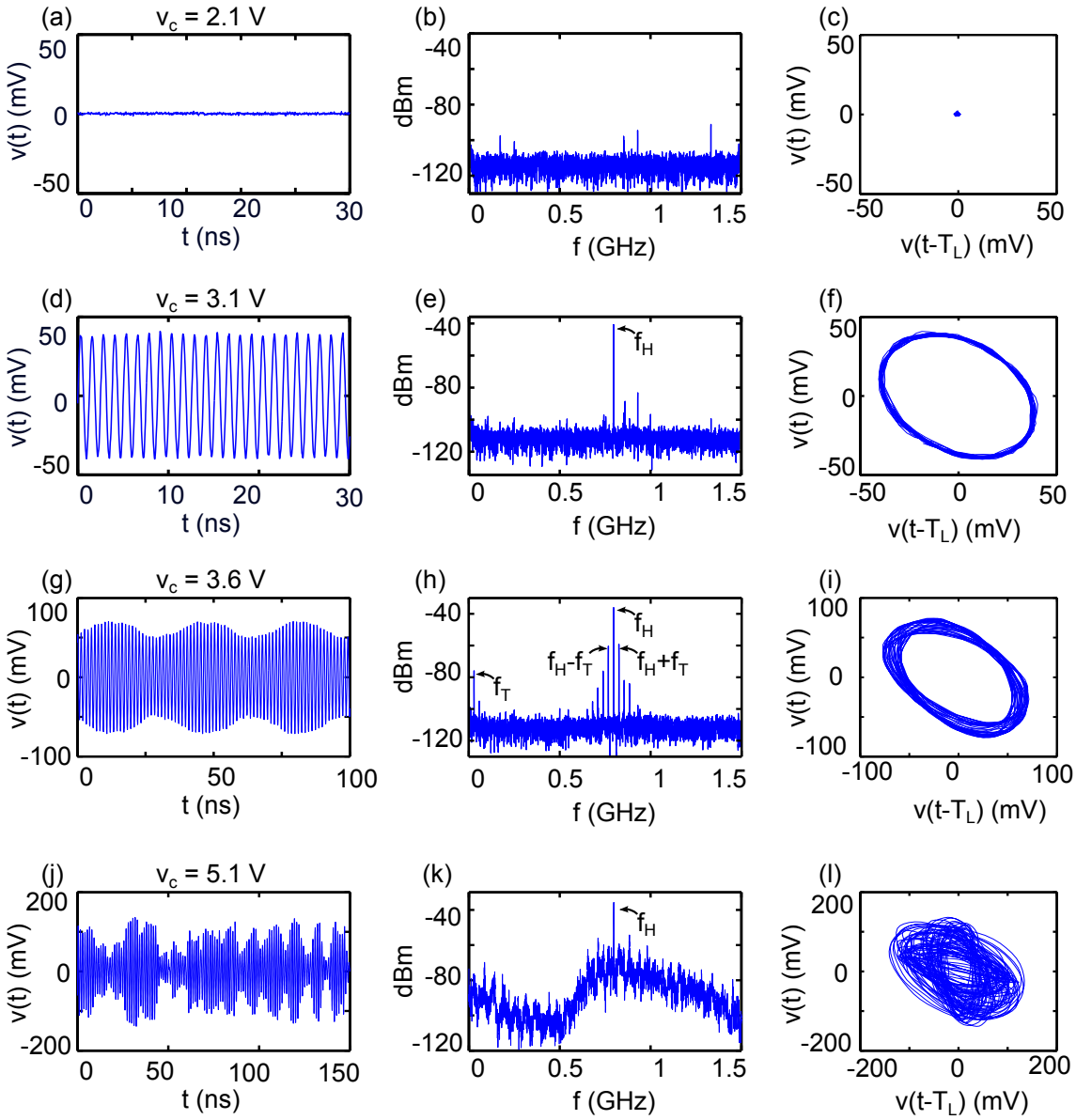

Figure 2.4: **Single-loop experimental dynamics**. (a) Steady-state temporal evolution, (b) Power spectral density (PSD), and (c) phase-space projection (PSP) of $v(t)$ for $v_c = 1.2$ V. (a) Periodic temporal evolution, (b) PSD, and (c) PSP of $v(t)$ for $v_c = 3.0$ V. (a) Quasiperiodic temporal evolution, (b) PSD, and (c) PSP of $v(t)$ for $v_c = 4.1$ V. (a) Chaotic temporal evolution, (b) PSD, and (c) PSP of $v(t)$ for $v_c = 5.2$ V. Each PSP uses a delayed version $v(t - T_L)$ where $T_L = 10.5$ ns is a lag time.

waveforms can be achieved in noise-free simulations.

Before moving on to the next subsection, I present a plot that summarizes the

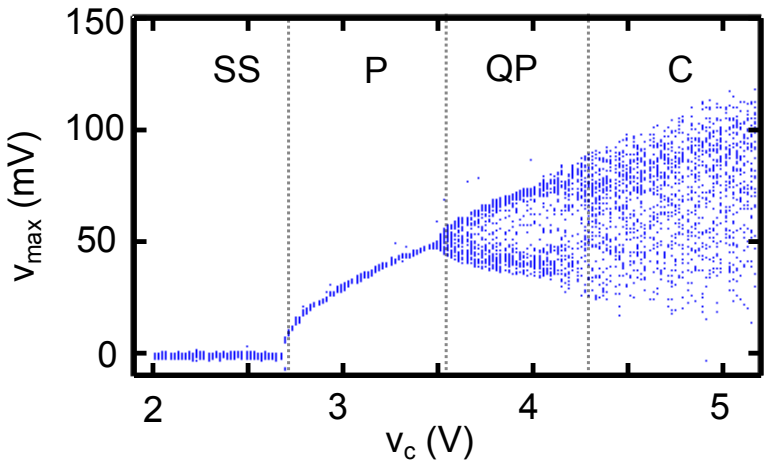

Figure 2.5: **Single-loop bifurcation diagram.** The local maxima v_{max} plotted as a function of the control voltage v_c. Vertical grey dashed lines separate steady-state (SS), periodic (P), quasiperiodic (QP), and chaotic (C) regions of the dynamics. For these measurements, the discretization error of v_{max} from the digital oscilloscope is approximately 100 μV, the noise floor standard deviation is approximately 1.2 mV, and the control voltage v_c is varied in steps of 20 ± 2 mV.

dynamical behaviors of the nonlinear feedback system as a function of v_c. This type of plot, known as a *bifurcation diagram*, is shown in Fig. 2.5. In the figure, for each value of v_c, I plot the local maxima of $v(t)$ and label the various dynamical regions as steady-state (SS), periodic (P), quasiperiodic (QP), and chaotic (C). For the SS region, the density of local maxima are concentrated at $v_{max} \sim 0$. Once the region of periodicity appears, v_{max} follows the amplitudes of the periodic oscillations, scaling as $v_{max} \sim \sqrt{v_c - v_c^*}$, where v_c^* is the critical value of the control voltage for which the Hopf bifurcation occurs. This scaling of v_{max} is typical of a specific type of Hopf bifurcation known as a *super-critical* Hopf bifurcation [23]. In the QP region, the density of v_{max} spreads until the bifurcation to chaos, where the spread in the local maxima is at its greatest.

In the next subsection, I present a simple model for the single-loop, time-delayed nonlinear feedback system using the mathematical representations from Ref. [22].

Though this model is not a complete description of our NLC, it serves as one of the main building blocks for interpreting the dynamics of the full feedback system in the chapters to come.

2.1.2 Simple Model

This subsection is divided into three main parts. First, I introduce a function that is representative of the piecewise-linear operations performed by the nonlinear circuit. Then, using a differential equation that describes a band-pass filter, I combine band-pass filtered, time-delayed feedback and this nonlinear function to realize a simple model for the single-loop system.

As an approximation for the input-output function of the nonlinear circuit, Illing *et al.* use the function [22]

$$\mathrm{v_{out}} = F(\mathrm{v_{in}}) = \mathrm{v_o} - \sqrt{F_1(\mathrm{v_{in}} + \mathrm{v_b})^2 + a_\mathrm{o}^2}, \tag{2.3}$$

where $\mathrm{v_{in}}$ and $\mathrm{v_{out}}$ are the input and output voltages of the nonlinear circuit, respectively, $\mathrm{v_b}$ is the additive input bias voltage, a_o is a constant that controls the sharpness of the tent-like function, $\mathrm{v_T}$ is the transistor threshold, and F_1 is the piecewise-linear function [22]

$$F_1(\mathrm{v_{in}} + \mathrm{v_b}) = \begin{cases} A_\mathrm{L}(\mathrm{v_{in}} + \mathrm{v_b} - \mathrm{v_T}), & \text{if } \mathrm{v_{in}} + \mathrm{v_b} \leq \mathrm{v_T} \\ A_\mathrm{R}(\mathrm{v_{in}} + \mathrm{v_b} - \mathrm{v_T}), & \text{if } \mathrm{v_{in}} + \mathrm{v_b} > \mathrm{v_T} \end{cases}. \tag{2.4}$$

For input voltages less than $\mathrm{v_T}$, the nonlinear function is approximately linear with slope A_L, and for input voltages greater than $\mathrm{v_T}$, the nonlinear function is approximately anti-linear (negative slope) with slope A_R. For non-zero values of a_o, the transition between these two regions in smooth and the maximum output of $F(\mathrm{v})$

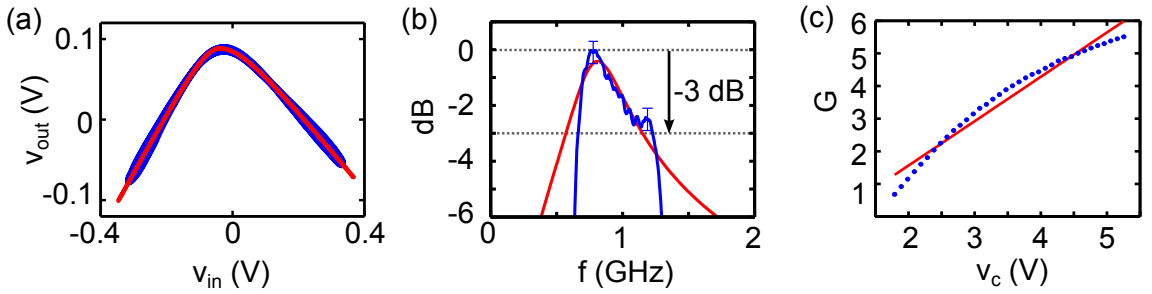

Figure 2.6: **Model parameters.** (a) Numerical fitting of the nonlinear function $F(\mathrm{v})$ (red curve) to the experimental nonlinearity of the nonlinear circuit (blue curve). (b) Bandwidth of experimental system (blue curve) used for determining the model parameters $f^{(+)}$ and $f^{(-)}$ of the fitted transfer function magnitude $|H_{\mathrm{BP}}(f)|$ (red curve). The error bar indicates the accuracy of ±0.4 dB for the spectrum analyzer (Agilent E4440A), and the resolution of the frequency sweep is approximately 4 MHz. (c) Linear fit (red curve) of the experimental gain G as a function the control voltage $\mathrm{v_c}$. The error bars for each measurement of G represent the fluctuations in the measured waveforms but do not extend beyond the data points, and the control voltage $\mathrm{v_c}$ is varied in steps of 100 ± 2 mV.

is determined by $\mathrm{v_o}$. But, the value of $\mathrm{v_o}$ is arbitrary in this model because the ac-coupled output of the nonlinear circuit will always have a time-average of 0 V. Using this model function, I fit the experimentally measured nonlinearity of the circuit with Eqs. (2.3)-(2.4) using a least-square regression algorithm. The numerical fit, shown in Fig. 2.6, yields the parameters $A_{\mathrm{L}} = 0.76 \pm 0.01$, $A_{\mathrm{R}} = 0.50 \pm 0.01$, $a_{\mathrm{o}} = 0.05 \pm 0.01$ V, and $\mathrm{v_T} = 0.71 \pm 0.01$ V (these errors represent the 90% confidence intervals of the parameters of the fit). Thus, Eqs. (2.3)- (2.4) display a qualitatively similar piecewise-linear operation to the experimental nonlinear circuit.

In their original work, Illing *et al.* studied the dynamical behaviors of the nonlinear circuit in a band-pass filtered feedback system. In the frequency domain, the net filtering of the feedback loop is approximated as a band-pass filter with transfer function $H_{\mathrm{BP}}(f)$. To model the filtering effects of the feedback loop, Illing *et al.* use

the transfer function for a two-pole band-pass filter

$$H_{\mathrm{BP}}(f) = \frac{1}{1 + 2\pi i f/\Delta + \omega_{\mathrm{o}}^2/(2\pi i f \Delta)}. \tag{2.5}$$

where $\Delta = 2\pi(f^{(+)} - f^{(-)})$, $\omega_{\mathrm{o}} = 2\pi\sqrt{f^{(+)}f^{(-)}}$, and $f^{(+,-)}$ are the upper and lower cutoff frequencies of the band-pass filter (at a -3 dB power loss), respectively [22]. Using the experimentally measured bandwidth of the feedback loop, shown in Fig. 2.1, $|H_{\mathrm{BP}}(f)|$ is fit to the data within a vertical window between -3 dB $< |H_{\mathrm{BP}}(f)| < 0$ dB. The numerical fit yields the parameters $f^{(-)} = 647 \pm 10$ MHz and $f^{(+)} = 989 \pm 10$ MHz (these errors represent the 90% confidence intervals of the parameters of the fit, and the maximum difference between the bandwidth and the fit within the 3 dB interval is $\sim$ 2 dB at $f \sim 67$ MHz, which is one source of error). Thus, the central frequency of the bandpass filter is $\omega_{\mathrm{o}}/(2\pi) \sim 800$ MHz. Fitting a larger window of the experimentally measured bandwidth, which behaves differently from an ideal band-pass filter, skews the fitting parameters to non-physical values.

In the time-domain, the band-pass filter with time-delayed nonlinear feedback can be represented by the delay differential equation (DDE) [22]

$$\frac{\dot{\mathrm{v}}(t)}{\Delta} + \mathrm{v}(t) + \frac{\omega_{\mathrm{o}}^2}{\Delta}\int_{-\infty}^{t} \mathrm{v}(t')\,\mathrm{d}t' = F(G\mathrm{v}(t-\tau) + \mathrm{v}_{\mathrm{B}}), \tag{2.6}$$

where G is the net gain of the feedback loop and τ is the feedback-loop delay. The experimentally measured time delay is $\tau \sim 14.5$ ns. To match the range of gain values used in the experiment, the net gain G of the experimental feedback loop is plotted as a function of v_{c} in Fig. 2.6c. For a given v_{c}, the gain is measured using a sinusoidal driving voltage at frequency $f = 800$ MHz (to avoid filtering from the

band-pass filter) and computing $G = A_{\text{out}}/A_{\text{in}}$, where A_{in} and A_{out} are the amplitudes of the input and output waveforms of the feedback loop, respectively. Note that this measurement is made without the nonlinear circuit present in the feedback loop. In Fig. 2.6c, the experimental values of G follow an approximately linear function of v_c, ranging from $1.2 < G < 6$ with a slope of $1.3\ \text{V}^{-1} \pm 0.2$ (within a 90% confidence interval of the fit). Thus, a linear sweep of G in the model will approximate the effect of tuning the bifurcation parameter v_c.

Lastly, with this model, the ac-coupled output of the nonlinear circuit is not modeled directly because the band-pass filter in the feedback loop, which includes a high-pass cutoff frequency $f^{(-)} > 0$, accounts for this effect. As I will show, for the purposes of this numerical experiment, Eq. (6.3) is sufficient for describing qualitatively the single-loop dynamics.

To simulate the system, I use an Adams-Bashforth algorithm to integrate numerically Eq. (6.3) and solve for the temporal evolution of $v(t)$ for increasing G values. To demonstrate the qualitative similarities of these simulations to the experiment, typical steady-state, periodic, quasiperiodic, and chaotic time series produced by the model are plotted in Fig. 4.19. This figure mimics the format of Fig. 4.17 for an easy comparison and shows that the model is also capable of producing similar power spectral densities and phase-space projections. In particular, shown in Figs. 4.19e,h, the simulated values of the Hopf and torus frequencies, $f_{\text{H}} = 760$ MHz and $f_{\text{T}} = 36$ MHz, show near agreement with the experimental frequencies (discrepancies in the values of these frequencies can be attributed to the approximations made in the model by assuming a simple function for the NLC and an ideal band-pass filter for the bandwidth of the feedback loop).

Furthermore, using the local maxima v_{max} of the time series from the model, I plot a simulated bifurcation diagram in Fig. 2.8. Comparing this figure to the

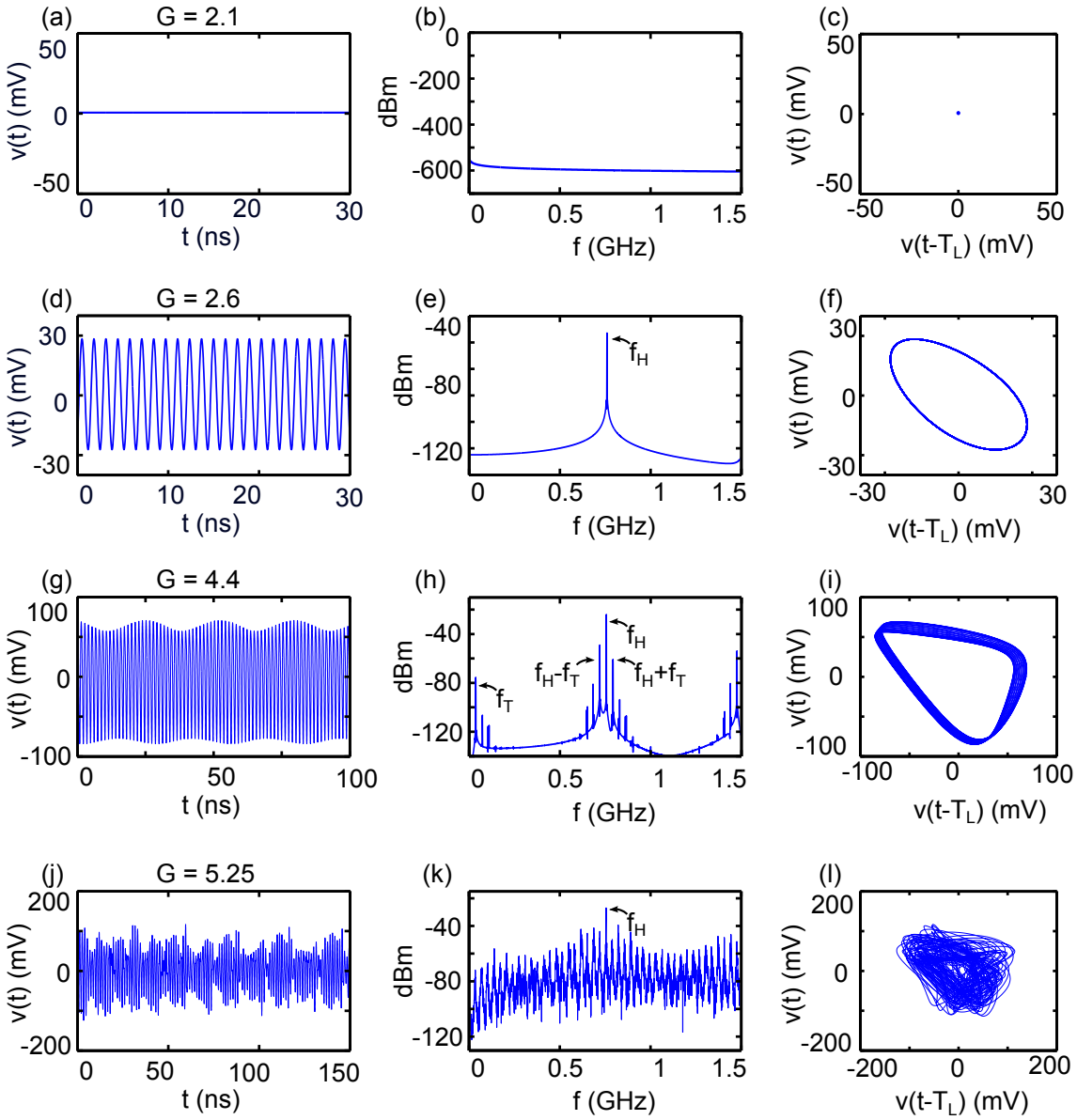

Figure 2.7: **Observed single-loop simulated dynamics.** (a) Steady-state temporal evolution, (b) Power spectral density (PSD), and (c) phase-space projection (PSP) of $v(t)$ for $v_c = 1.2$ V. (a) Periodic temporal evolution, (b) PSD, and (c) PSP of $v(t)$ for $v_c = 3.0$ V. (a) Quasiperiodic temporal evolution, (b) PSD, and (c) PSP of $v(t)$ for $v_c = 4.1$ V. (a) Chaotic temporal evolution, (b) PSD, and (c) PSP of $v(t)$ for $v_c = 5.2$ V. Each PSS uses a delayed version $v(t - T_L)$ where $T_L = 9.7$ ns is a lag time.

experimental bifurcation diagram, the simulated steady-state (SS), periodic (P), quasiperiodic (QP), and chaotic (C) dynamics appear in similar succession with

qualitatively similar values in the local maxima. Also, the initial scaling of the periodic amplitudes and the initial spreading of the quasiperiodic amplitudes match those from the experiment. However, it is clear from the simulated bifurcation diagram that the region of periodicity in the simple model is larger than that of the experiment. In addition, the simulated transition from quasiperiodicity to chaos shows new structures. Thus, based on their bifurcation diagram, Eqs. (2.3)-(6.3) represent a simple model for simulating a time-delayed nonlinear feedback system that reproduces qualitative features from the single-loop experimental system.

The bifurcation diagrams from both the model and experiment also highlight the sensitivity of the dynamics in this time-delayed nonlinear feedback system to the feedback-loop gain G. As G changes continuously, the amplitude of $v(t)$ can shift, showing quantitative dynamical changes, or the state of $v(t)$ can change, illustrating qualitative dynamical changes.

In addition to the feedback loop gain, researchers have also shown that the dy-

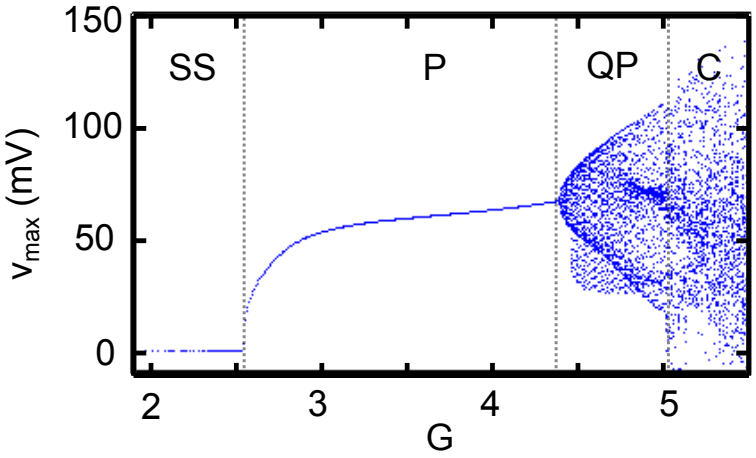

Figure 2.8: **Simulated bifurcation diagram.** The simulated local maxima v_{max} plotted as a function of the feedback loop gain G. Vertical grey dashed lines separate steady-state (SS), periodic (P), quasiperiodic (QP), and chaotic (C) regions of the dynamics.

namics of time-delayed nonlinear feedback systems are sensitive to changes in the feedback time delay τ [22]. In this case, changes to τ can alter the frequencies of oscillation in periodic and quasiperiodic dynamics (f_H and f_T) [32, 39, 40] as well as cause bifurcations [41]. The sensitivity to τ is discussed in more detail in Ch. 6. Furthermore, changes to the dynamics based on perturbations to the feedback parameters have lead to interesting applications of time-delayed nonlinear feedback systems in both imaging and sensing.

In the next subsection, I present a brief literature review of the applications of time-delayed nonlinear feedback systems using the sensitivity of their dynamics to perturbations in each of the system's feedback parameters.

2.1.3 Applications of Time-Delayed Nonlinear Feedback Systems in Subwavelength Imaging and Sensing

The sensitivity to feedback parameter changes in time-delayed nonlinear feedback systems has been used to create new sensor technologies. A well-known example is the laser-feedback interferometer (LFI) [30] or optical-feedback interferometry (OFI), which is depicted in Fig. 2.9a. LFI uses a laser diode (LD) as the system's nonlinearity; the output light from the LD is reflected off of a surface and fed back to the laser cavity [30]. Thus, the round trip propagation of an optical signal leaving and entering the laser cavity represents a time-delayed nonlinear feedback loop with time delay τ. Depending on the distance from the laser output to the scattering surface, the time delay of the feedback loop can change, causing a shift in the steady-state optical intensity of the feedback system. The light emitted by the LD is also monitored by a photodetector (PD), which generates a steady-state voltage v_s that is proportional to the laser intensity. As depicted in Fig. 2.9, by tracking the

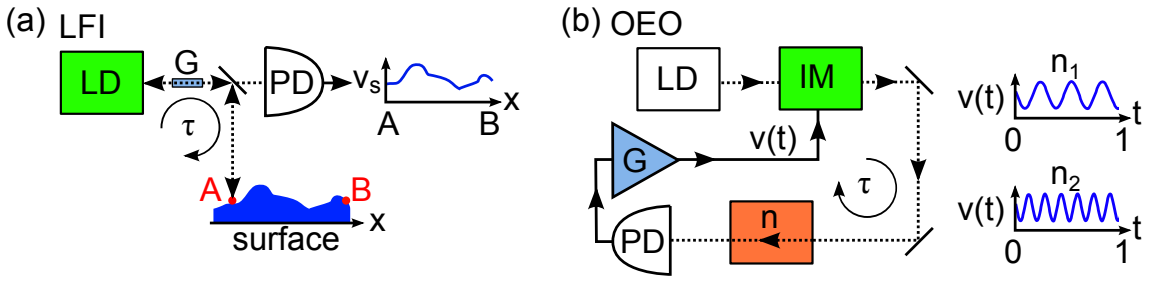

Figure 2.9: **Time-delayed nonlinear feedback sensors.** (a) Laser feedback interferometry (LFI) system. The gain of the feedback loop G is determined by an attenuator at the output of the LD. As the point of reflection on the surface scans from A to B, the time-delay τ of the nonlinear feedback system changes such that v_s reveals the surface profile when plotted as a function of x. (b) Index of refraction sensor using an opto-electronic oscillator (OEO) with a LD, interference modulator (IM), and photodetector (PD). The gain of the feedback loop is determined by an amplifier (G). As the index of refraction changes from n_1 to n_2, the net delay τ of the nonlinear feedback loop decreases ($n_2 < n_1$) and thus the frequency of oscillation in $v(t)$ increases. The position x and time t are in arbitrary units.

dynamical shifts of the steady-state intensity while scanning the point of reflection from $A \rightarrow B$, LFI can reconstruct the surface profile with a 5 nm resolution, which is approximately $\sim \lambda/130$ when $\lambda = 1550$ nm [42].

Another similar sensor has been demonstrated in a time-delayed nonlinear feedback system known as an opto-electronic oscillator (OEO). In this system, depicted in Fig. 2.9b, the light emitted by a LD drives an interference modulator (IM), which serves as the system's nonlinearity. Placed in the optical path of the feedback, a scatterer with refractive index n alters the τ and G of the feedback. The resulting detected signal is amplified and fed back to the IM as a periodic oscillatory voltage $v(t)$. It has been demonstrated that the frequency of the periodic $v(t)$ shifts due to changes in τ that are proportional to n [39]. As depicted in the example in Fig. 2.9b, for $n_2 < n_1$, the net delay τ decreases and thus the relative frequency of oscillation in $v(t)$ increases [39]. These types of changes to n can be used for subwavelength imaging because a change $\Delta n = |n_2 - n_1|$ is proportional to a time-

delay shift $\Delta\tau = \Delta x/\mathrm{c}$, where $\Delta x << \lambda$ represents a (potential) subwavelength distance change. Thus, similar to LFI, the OEO uses perturbations to the feedback parameters for sensing. An advantage of both the LFI and OEO sensors is that the changes to the system are easily detectable due to relatively simple dynamical states (simple compared to quasiperiodicity and chaos).

In addition to steady-state and periodic dynamical states, chaos can also be used for sensing purposes [43]. Using time series analysis, small changes to a chaotic attractor have been used to detect small parameter perturbations in a nonlinear system [44]. Applications include detecting damage to a structure that is embedded in the chaotic nonlinear feedback system [45]. However, these methods involve large data storage and have only been proven to work for low-dimensional chaotic attractors, and it remains an interesting and open problem to find simple, robust sensing applications of time-delayed nonlinear feedback systems that take advantage of complex dynamical states other than periodic or steady-state dynamics.

As I will show later, my full-feedback imaging system demonstrates the first application of quasiperiodic dynamics for imaging the position of a subwavelength object in 2D. Similar to the above-mentioned applications of time-delayed nonlinear feedback systems, my imaging system works by exploiting the sensitivity of its dynamics to changes in its feedback parameters. However, my system differs from these applications because of the addition of a wave-chaotic cavity in its feedback loop. This additional component creates a 2D scattering environment that is embedded in the feedback of the time-delay system. Furthermore, this scattering environment is tailored to exhibit a property known as wave chaos, which gives rise to an enhanced complexity to the interference patterns inside of the cavity.

2.2 Wave-Chaotic Cavities

In order to explain wave chaos in cavities, I will first review ray chaos in 2D billiards. Ray chaos describes the trajectories of a two, identical, non-interacting particles with similar initial conditions (position and momentum) that propagate inside of a billiard and bounce off of the hard boundaries elastically, as shown in Figs. 2.10a-b. For the billiard in Fig. 2.10a, the two particles' trajectories remain close after many bounces. However, for the billiard in Fig. 2.10b, the two particles' trajectories diverge, demonstrating a sensitivity to initial conditions. This effect, which is appears in certain billiard geometries, is known as ray chaos [46, 47]. Ray chaos has been studied in many geometries ranging from deformed circular billiards [48] to stadium [49] and quarter-stadium shaped billiards [50] like the one shown in Fig. 2.10b. In addition to the sensitivity to initial conditions, a particle in a ray chaotic billiard visits every possible position within the boundary from every possible direction, thus filling the position and momentum phase space of the system ergodically [46, 51].

To explain wave chaos, consider the 2D billiards as the boundaries of 2D microwave cavities. The trajectories of the particles in Figs. 2.10a-b become the propagation of waves that scatter and interfere, as depicted in Figs. 2.10c-d. The wave-chaotic cavity in Fig. 2.10d contains a complex interference pattern and a large number of irregularly spaced frequency resonances (as illustrated in Fig. 2.10f) when compared to the interference pattern and resonances in Figs. 2.10c,e. In addition, similar to the ergodicity of ray chaotic systems, the interference patterns of wave-chaotic cavities fill the cavity more densely when compared to regular (non-chaotic) cavities [46]. The spatial modes of a regular cavity are less dense than those of a wave-chaotic cavity. Also, the resonances of the regular cavity tend to be

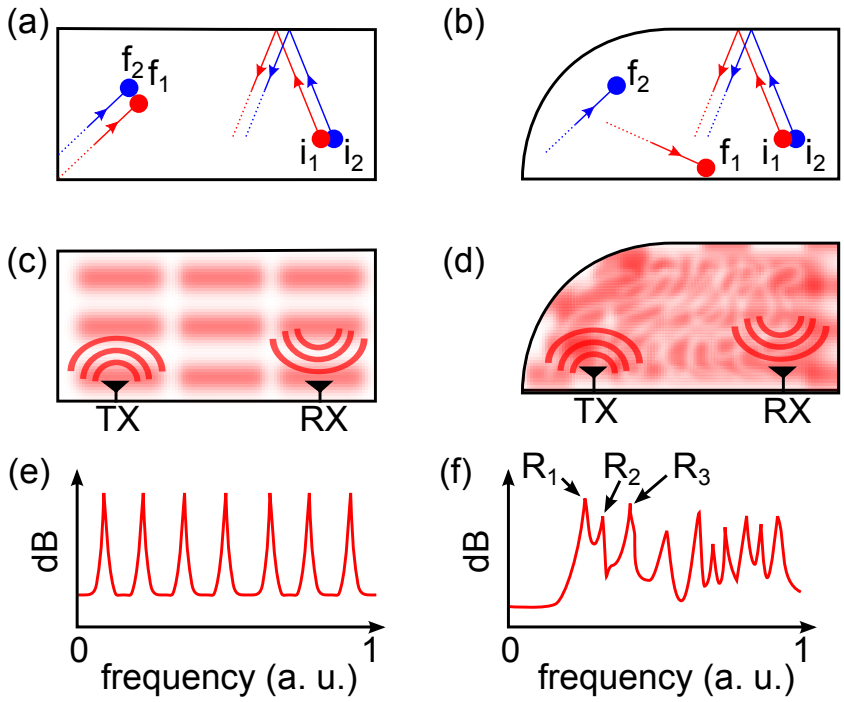

Figure 2.10: **Ray and wave chaos.** (a) Rectangular and (b) quarter-stadium (QS) 2D billiards with identical particles (red and blue) and their trajectories from initial positions i_1 and i_2 to final positions f_1 and f_2. Illustrations of the interference patterns from the (c) rectangular and (d) QS cavity. The rectangular cavity contains large nodes or blind spots, indicated in white, when compared to the complex interference pattern in the QS cavity. (e)-(f) Typical frequency resonances of a rectangular and QS wave-chaotic cavities, respectively. The frequency is given in arbitrary units (a. u.).

more symmetric and can cluster to the boundary of the cavity. This is one advantage of a wave-chaotic cavity; the spatial modes cover more regions of the cavity's interior. The complex standing-wave patterns of a wave-chaotic cavity can also change dramatically due to perturbations to its boundary [51, 52] or interior [53, 54].

It should be noted that wave chaos is only truly defined for classical dynamics with rays. Based on experimental observations over the past few decades, researchers conjecture that there is a correlation between the nearest-neighbor-spacing statistics (NNSS) of a cavity's resonances and the level of wave chaos in the cavity

[52, 55, 56]. Therefore, in this section, I present a foundation for understanding the NNSS of a cavity and the types of statistics that are correlated with wave chaos. These techniques will later be used to conjecture the presence of wave chaos in my experimental cavity. As depicted in Fig. 2.10f, the resonances of the wave-chaotic cavity are labeled R_n to help illustrate this procedure. For each pair of neighboring resonances R_n and R_{n+1}, the normalized resonance spacing is calculated

$$s_n = \frac{R_{n+1} - R_n}{\frac{1}{N}\sum_{n=1}^{N-1}(R_{n+1} - R_n)}, \tag{2.7}$$

where N is the number of resonances and s_n is the n^{th} spacing [46, 52]. As it turns out, the density of the resonances is the same for a regular and a wave-chaotic cavity [46]. However, the NNSS of the resonances is different. It is conjectured that, for a wave-chaotic cavity, the probability distribution of s_n follows a Wigner distribution, given by

$$P_{\text{w}}(s) = \frac{\pi}{2} s e^{-\pi s^2/4}. \tag{2.8}$$

For a regular cavity, the probability distribution of s_n follows a Poisson distribution that reads

$$P_{\text{p}}(s) = e^{-s}. \tag{2.9}$$

For a detailed explanation of the origin of these distributions, see Refs. [46, 57]. As shown in Fig. 2.11a, the Poisson distribution $P_{\text{p}}(s)$ has a maximum as $s \to 0$ while the Wigner distribution $P_{\text{w}}(s) \to 0$ as $s \to 0$.

Though $P_{\text{p}}(s)$ and $P_{\text{w}}(s)$ are correct for characterizing wave chaos, the NNSS of these distributions is dependent on a histogram bin size of s_n [56]. Thus, it is more useful to use a cumulative measure that is independent of the bin size. A cumulative density function (CDF) for the Poisson and Wigner probability distributions can be

represented as [52]

$$I_{\mathrm{p,w}}(s) = \int P_{\mathrm{p,w}}(s')\,\mathrm{d}s'. \tag{2.10}$$

Examples of these cumulative probability distributions $I_{\mathrm{p,w}}(s)$ are depicted in Fig. 2.11b. Thus, for a regular and wave-chaotic cavity, the cumulative resonance spacing s follows $I_{\mathrm{p}}(s)$ and $I_{\mathrm{w}}(s)$, respectively.

However, it has been shown in both experiments and simulations that typical resonance-spacing distributions are actually a superposition of both the Poisson and Wigner distributions [56], demonstrating that a real-world cavity can have a mixture of regularity and wave chaos. Thus, to measure the degree of chaos in the cavity, or *chaoticity*, researchers use the Brody CDF to account for the balance between Poisson and Wigner distributions. This CDF is given by [56]

$$I_{\mathrm{b}}(b,s) = (1-b)I_{\mathrm{p}}(s) - bI_{\mathrm{w}}(s), \tag{2.11}$$

where b is a fixed parameter that can range from 0 to 1. For $b = 0$, $I_{\mathrm{b}}(b,s) \to I_{\mathrm{p}}(s)$, which indicates that the cavity is purely regular, and for $b = 1$, $I_{\mathrm{b}}(b,s) \to I_{\mathrm{w}}(s)$,

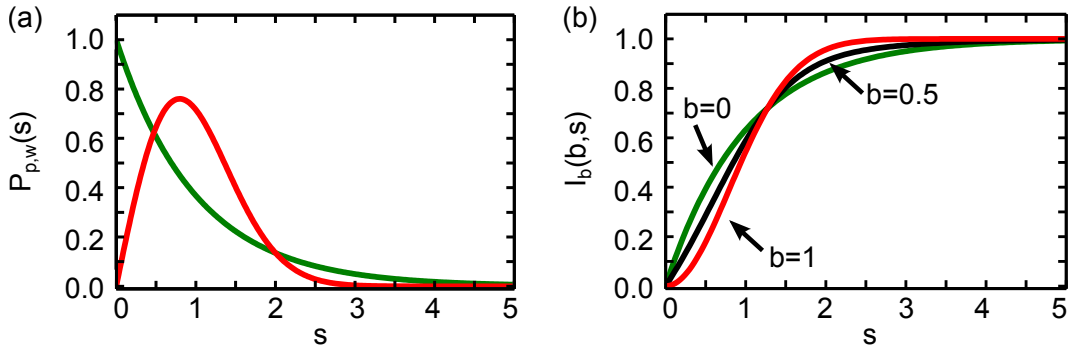

Figure 2.11: **Probability distributions.** (a) The Poisson (green curve, $P_{\mathrm{p}}(s)$) and Wigner (red dashed-curve, $P_{\mathrm{w}}(s)$) probability distributions. (b) The cumulative Poisson (green curve, $I_{\mathrm{b}}(0,s) = I_{\mathrm{p}}(s)$), Wigner (red curve, $I_{\mathrm{b}}(1,s) = I_{\mathrm{w}}(s)$), and Brody (black curve, $I_{\mathrm{b}}(0.5,s)$) probability distributions.

which indicates that the cavity is purely wave-chaotic. For a comparison to these types of distributions, I also plot the Brody distribution $I_{\mathrm{b}}(0.5, s)$ in Fig. 2.11b. As shown in the figure, $I_{\mathrm{b}}(0.5, s)$ is an average of $I_{\mathrm{b}}(0, s)$ and $I_{\mathrm{b}}(1, s)$. For distributions with unknown values of b, Eq. (2.11) is used to analyze the data using a numerical fit with b as a free fitting parameter. This method has been used recently to characterize the transition from regularity to wave-chaos in a 2D simulation, where the parameter b ranges from 0 to 0.85 as an increasing asymmetry is introduced into a 2D cavity's boundary [58]. Furthermore, the Brody distribution has also been used to characterize the experimental wave-chaos in both microwave [57] and optical cavities [52, 56].

In the next subsection, I introduce and characterize my experimental wave-chaotic cavity using the Brody CDF. Using a swept-frequency source, I measure and characterize the cavity's resonance spacings. In addition, I also examine the effects of wave chaos in the experimental cavity with regards to a sensing application.

2.2.1 Experimental Wave-Chaotic Cavity

The design of my experimental cavity is based on the well-known quarter-stadium wave-chaotic 2D structure [50, 57]. A photograph of the open cavity interior is shown in Fig. 2.12a. Constructed using 2 mm thick aluminum sheet metal, the cavity's length and width are approximately $L = 1.2$ m and $W = 0.6$ m, respectively. The height of the cavity is approximately $H = 8$ cm. Thus, for frequencies $f < c/(2H)$, which corresponds to approximately 2 GHz, the cavity can only support transverse magnetic (TM) modes [49]. This means that, for EM waves with frequencies less than 2 GHz, the cavity can be regarded as approximately a 2D structure. Based on the dimensions of the cavity, I estimate that the number of spatial

modes excited in the cavity is on the order of (at least) $50-100$. This is calculated by assuming a maximum frequency of 2 GHz (minimum wavelength of 15 cm) such that at least 4 modes are excited along the cavity's width and at least 8 modes are exited along the cavity's length. The additional asymmetric features of the cavity give the potential for additional spatial modes. Though a 2D system is not crucial for the operation of my imaging system (3D structures can show wave chaos [54]), using an approximately 2D system will allow me to later simplify the interactions between the scatterer and the internal EM radiation.

Inside the cavity is the scatterer: a small bottle filled with water with a 2D cross

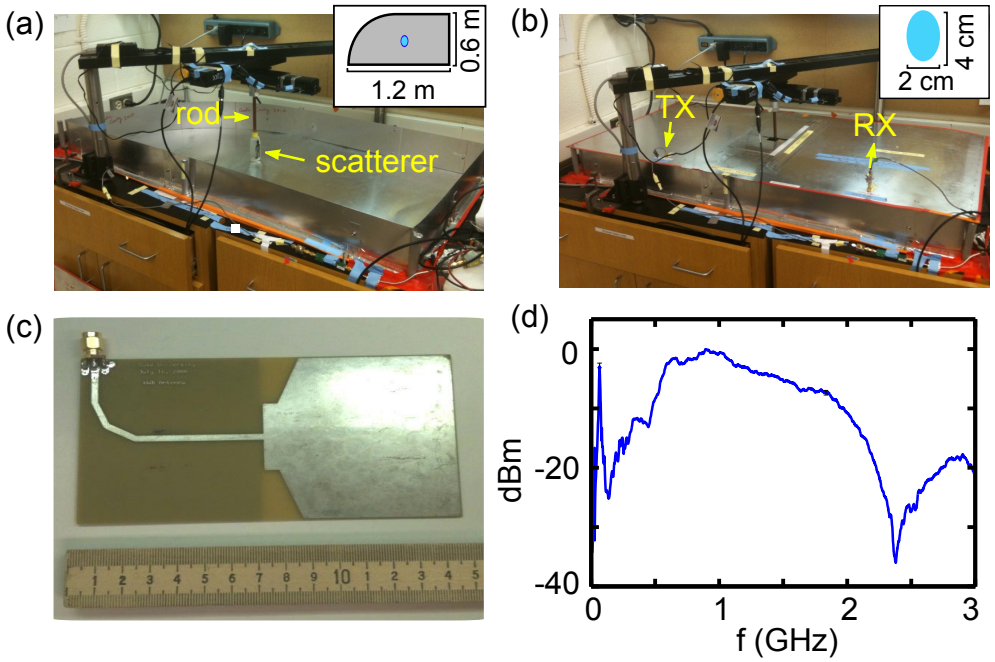

Figure 2.12: **Wave-chaotic cavity.** (a) Open interior of the cavity with the scatterer and rod labeled. The inset of the figure shows the cavity's 2D dimensions. (b) Closed exterior of the cavity with the TX and RX ports labeled. The inset of the figure shows the dimensions of the scatterer's cross-section. (c) Broadband copper antenna on a printed circuit board. (d) Near-field bandwidth of identical transmitting and receiving antennas, where errors indicate the accuracy of the spectrum analyzer (± 0.4 dBm).

sectional area of approximately 2 cm × 4 cm, as shown in the inset of Fig. 2.12b; the size of this water bottle is subwavelength when compared to the illuminating fields of the system. In the frequency range of $f \sim 100$ MHz -10 GHz, water has an index of refraction $n \sim 10$ [59], which means it will scatter the majority of any incident EM radiation. The absorption coefficient of water in this frequency range is $\alpha \sim 0.1 - 1$ cm^{-1} [59]. Thus, for example, any EM radiation at $f = 1$ GHz that transmits through the scatterer will be attenuated by a factor of ~ 0.75 in its intensity (based on the 2 cm × 4 cm cross section). As will be demonstrated later in this section, the addition of the scatterer in the cavity affects both the scattering paths and absorption of EM waves.

The top of the scatter is glued to a position-controlled rod (that resides outside of the cavity), and when the cavity is closed in Fig. 2.12b, the rod extends through a small square hole of dimensions 3 cm × 3 cm in the cavity's cover and is attached to translation stages for positioning the scatterer in 2D (the square hole confines the majority EM radiation for $f < 10$ GHz) The accuracy of the scatterer (water bottle) placement in the cavity is dependent on the position accuracy of the translation stages. In particular, the scatter placement at each 1D position (x) or 2D position (x, y) is assumed to be the exact programmed positions of the translation stages (the positions are programmed using LabVIEW, which requires a list of positions to be loaded from files with manually entered data). However, because the translation stages are not perfectly accurate, there is position error associated with each measurement in the system.

The position error of the translation stages is caused by the physical gears which turn to pull or push the mounting stages of the scatterer. Because these gears involve mechanical screws, there is a potential for backlash to occur when moving them back and forth; backlash is a history dependent error in positioning due to

approaching a position from different directions (for example, approaching from either the positive x direction or the negative x direction. In such systems, repetitive backlash can accumulate to create large errors. However, the translation stages used in this experiment have a backlash correction programmed into them. For each programmed position, the stages translate to the approximate location and then perform a small pivot about the position in order to correct for backlash. Thus, each position is always approached from the same direction (for example, positive x and positive y). With this backlash correction in both translation stages, it is assumed that the scatterer's position is accurate to within 5 μm (based on the manufacturers data sheets for components Zaber Technologies TLSR150B and Thorlabs LTS150).

All measurements in the system are made when it is covered, and the input and output ports of the cavity are also labeled as the TX and RX ports, respectively. At these input and output ports are identical transmitting and receiving antennas, respectively. These antennas are designed for a broadband frequency spectrum, similar to the power spectral density (PSD) of the temporal chaos in Fig. 4.17k. A photograph of one of these antennas is shown in Fig. 2.12b. A near-field measurement of the antenna's normalized transmitted bandwidth is given in Fig. 2.12c. This measurement, which is performed in the open laboratory, tracks the transmitted power between two identical versions of the antennas as a function of frequency. Fig. 2.12d shows that the relative transmitted power is broadband over $f = 0.8-2$ GHz (based on a -10 dB cutoff) and that a resonance exists in the room at around 50 MHz. Because the antennas are confined in the cavity, this resonance will not be present during the system's imaging mode-of-operation (for a characterization of the antenna far-field efficiency, see Appendix B).

Using these antennas to transmit and receive EM radiation, I measure the cavity's resonances to characterize its level of wave chaos with and without the scatterer.

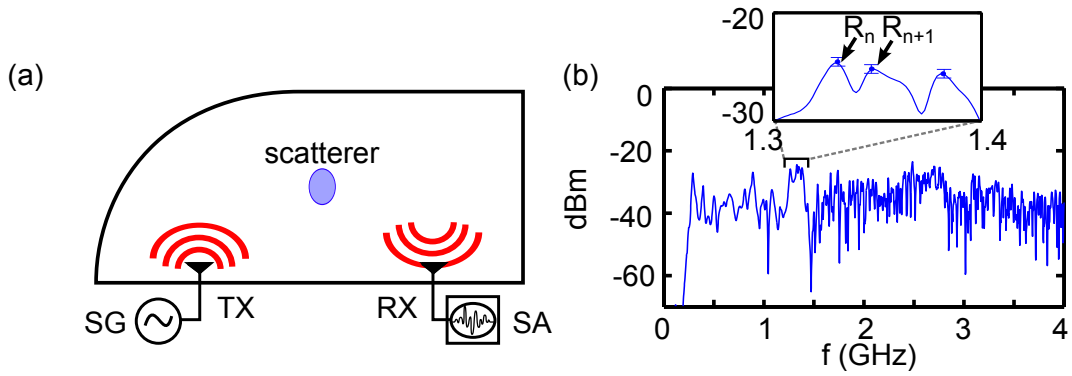

Figure 2.13: **Measuring the experimental resonances** of the cavity. (a) Experiment setup for measuring the resonances (with and without the scatterer) using a swept-frequency signal generator (SG) and a spectrum analyzer (SA). (b) The experimental resonances of the cavity with the scatterer as a function of frequency f. A zoom of the boxed region shows an example of two resonances R_n and R_{n+1}. Errors indicate the accuracy ±0.4 dBm of the SA. Resonances are located using MATLAB's *findpeaks* algorithm, which locates local maxima, where the parameters of the algorithm are specified such that consecutive local maxima must be spaced by at least 3 MHz (mean spacing between resonance peaks is 13.4 MHz) and must be greater than −70 dBm (mean resonance peak height is −44 dBm).

The setup for this measurement is shown in Fig. 2.13a, where a signal generator (SG) outputs a continuous wave signal with carrier frequency f to the cavity's TX antenna. The output of the cavity is measured at the RX antenna using a spectrum analyzer (SA). The cavity's resonances are measured by scanning f and measuring the output power at each frequency. The resulting spectrum with the scatterer is shown in Fig. 2.13b over a frequency sweep of $f = 0-4$ GHz (for a comparison of the resonances without the scatterer, see Fig. 2.15d). Based on the figure, the cavity's resonances are spaced irregularly with a decreasing spacing $s_n = R_{n+1} - R_n$ as f increases.

To fully characterize the cavity with and without the scatterer, these resonance spacings are measured over a large range of frequencies ($f = 0-10$ GHz) and stored in each configuration. Over this frequency range, the normalized histograms

of the s_n distribution are plotted in Figs. 2.14a-b along with the Poisson and Wigner distributions using Eqs. (2.9) and (2.8), respectively, for comparison (note: there is no fit to the data for these reference curves). In each case (without and with the scatterer), the level of wave chaos is quantified by fits to the experimental CDF $I(s)$, which yields the fitting parameters $b = 0.68 \pm 0.11$ without the scatterer and $b = 0.75 \pm 0.10$ with the scatterer. In Figs. 2.14c-d, the experimental CDFs are plotted along with their respective fits, and based on these results, the experimental cavity demonstrates a non-zero level of wave chaos with and without the scatterer.

As demonstrated in Ref. [55], the a percentage of the resonances in an experimental quarter-stadium billiard can overlap due to their finite width and hence be missing from the statistics to conjecture the presence of wave chaos. The authors of this work showed that, by cooling the cavity, its walls can become super-conducting and the resonances become sharper, leading to fewer missed values. From their work, they find that between 0.75 and 17.5 GHz, 162 out of 1060 resonances are lost when the measurements are made at room temperature, which equates to approximately 18.4% (162/898) [55]. Based on their work, I approximate that my experimental results for measuring cavity resonances may be missing up to ~ 132 modes (out of 869) for $f = 0-10$ GHz. This information is important to acknowledge when evaluating the statistics of the resonance spacings. In summary, the results of Fig. 2.14 are only approximations of the cavity's resonance statistics. Nevertheless, the well-know, wave-chaotic quarter-stadium shape gives rise to complex scattering, and, as shown in Ch. 3, the subwavelength sensing results of this dissertation are measured at room temperature.

For comparison, I also calculate the statistics for the wave chaos in the cavity over smaller frequency ranges. As shown in Tab. 2.1, the fitting parameter b for the CDFs (with and without the scatterer) are given for $f = 0-3$ GHz, $f = 0-6.5$

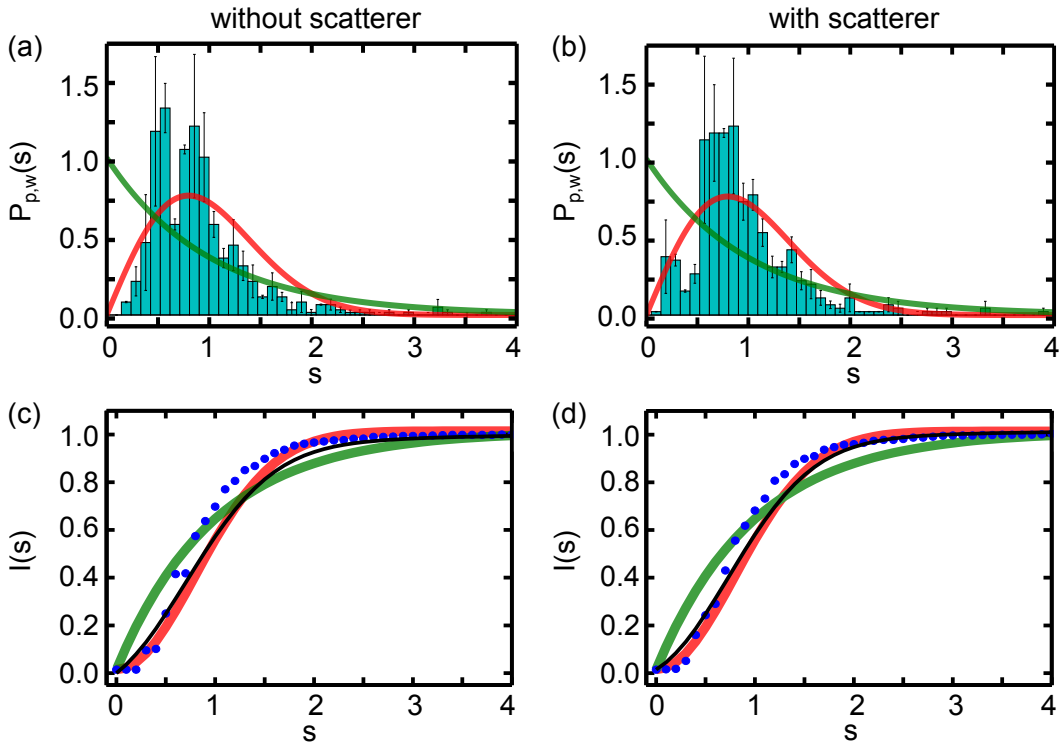

Figure 2.14: **Experimental distributions** of s_n (c) without and (d) with the scatterer. The bin size $\Delta s = 0.1$, and the errors in the histogram height represent changes to the histogram counts due to perturbations $\Delta s = 0.1 \pm (5 \times 10^{-3})$, where more than 80% of the spacings in s_n remain fixed for these perturbations. In (c) and (d), Poisson (green curve) and Wigner (red curve) distributions are plotted for reference. Cumulative distribution functions (e) without and (f) with the scatterer of s_n (blue dots) and fit (black curve) with the cumulative Poisson (green curve) and Wigner (red curve) distributions for reference.

GHz, and $f = 0 - 10$ GHz. In the table, b decreases for smaller frequency ranges, but it is consistently larger with the scatterer in the cavity in each case. Therefore, over these frequency ranges, the level of wave chaos in the cavity is increased by including a subwavelength scatterer.

An additional technique for characterizing the cavity uses a measurement known as the system's *pulse response* [54]. For this measurement, a short pulse of EM energy $r_{\text{in}}(t)$ of length $\delta t = 100$ ps is applied to the TX antenna, as shown in Figs. 2.15a-b. The cavity's output pulse response $r_{\text{out}}(t)$ is then measured on an oscil-

Table 2.1: Fitting parameters of the cumulative distribution functions used to characterize the wave-chaotic cavity.

frequency range (GHz)	b, without scatterer	b, with scatterer
$0-3$	0.28 ± 0.22	0.46 ± 0.19
$0-6.5$	0.59 ± 0.13	0.65 ± 0.12
$0-10$	0.68 ± 0.11	0.75 ± 0.10

loscope that is connected to the RX antenna. As shown in Fig. 2.15c, $r_{\text{out}}(t)$ is a complex oscillatory signal with an exponential decay in its amplitude. To accurately measure the complexity of $r_{\text{out}}(t)$ with a high SNR, this measurement (as well as all future measurements of $r_{\text{out}}(t)$) are created using 100 averaged waveforms. The baseline noise from our measurement oscilloscope is approximately ± 3 mV with a standard deviation of $\sigma_{\text{noise}} \sim 0.3$ mV. Using an averaged measure for $r_{\text{out}}(t)$, σ_{noise} is potentially reduced by a factor of 10. However, due to the discretization of the measured signal on the digital oscilloscope, oscillations below 50 μV cannot be resolved).

In addition, the time of arrival of oscillations in $r_{\text{out}}(t)$ (relative to the injection time of $r_{\text{in}}(t)$) indicates a minimum time $T_{\text{min}} \sim 4.5$ ns for EM energy to propagate through the cavity, which corresponds to a distance $d \sim cT_{\text{min}}$ that is approximately twice the cavity width (~ 1.2 m) and indicates a single reflection off of the cavity's boundary before exiting. Furthermore, the long term ringing of $r_{\text{out}}(t)$ demonstrates an energy storage time $T >> \delta t$. Lastly, Using the integrated power of the input pulse and output pulse responses,

$$P_{\text{in,out}} = \frac{R}{T} \int_0^T r_{\text{in,out}}(t')^2 \, \mathrm{d}t', \tag{2.12}$$

where $R = 50\ \Omega$, I can approximate the normalized power-loss as EM energy prop-

agates through the cavity: $P_{\text{out}}/P_{\text{in}} \sim 0.007$. Note that this power loss also includes the attenuating effects of the antennas. Thus, this pulse response provides additional information about the loss of the cavity system and demonstrates some of the complex effects of its wave chaos in the time domain.

Also shown in Fig. 2.15c, $r_{\text{out}}(t)$ illustrates the detectable changes in the output pulse response of the cavity when the scatterer is removed from the cavity. In the figure, there are small visible shifts in the pulse response ringing when compared to cavity with the scatter. Furthermore, the normalized power-loss of the cavity without the scatter is lower $P_{\text{out}}/P_{\text{in}} \sim 0.008$. These two changes show a clear indication that the scatterer not only changes the scattering paths of radiation but also absorbs a small amount of the EM energy.

In both cases, with and without the scatter, the Fourier transforms of the input pulse and output pulse responses $\tilde{r}_{\text{in}}$ and $\tilde{r}_{\text{out}}$, respectively, are used to approximate the transfer function of the cavity system

$$H_{\text{cavity}} \sim \frac{\tilde{r}_{\text{in}}}{\tilde{r}_{\text{out}}}, \tag{2.13}$$

where the magnitude of the transfer function $|H_{\text{cavity}}(f)|$ as a function of frequency f represents another measure of the cavity's resonances. In Fig. 2.15d, I plot the transfer function magnitudes $|H_{\text{cavity}}(f)|$ for the cases with and without the scatterer. In the figure, the spectra are similar but also demonstrate a detectable difference in the location of the resonances when the scatterer is introduced into the cavity.

In summary, my experimental cavity exhibits a non-zero level wave chaos with and without a subwavelength scatterer. Furthermore, I show that the addition of the subwavelength scatterer is detectable using the pulse response of the cavity. In the next subsection, I review briefly the recent published works on the applications

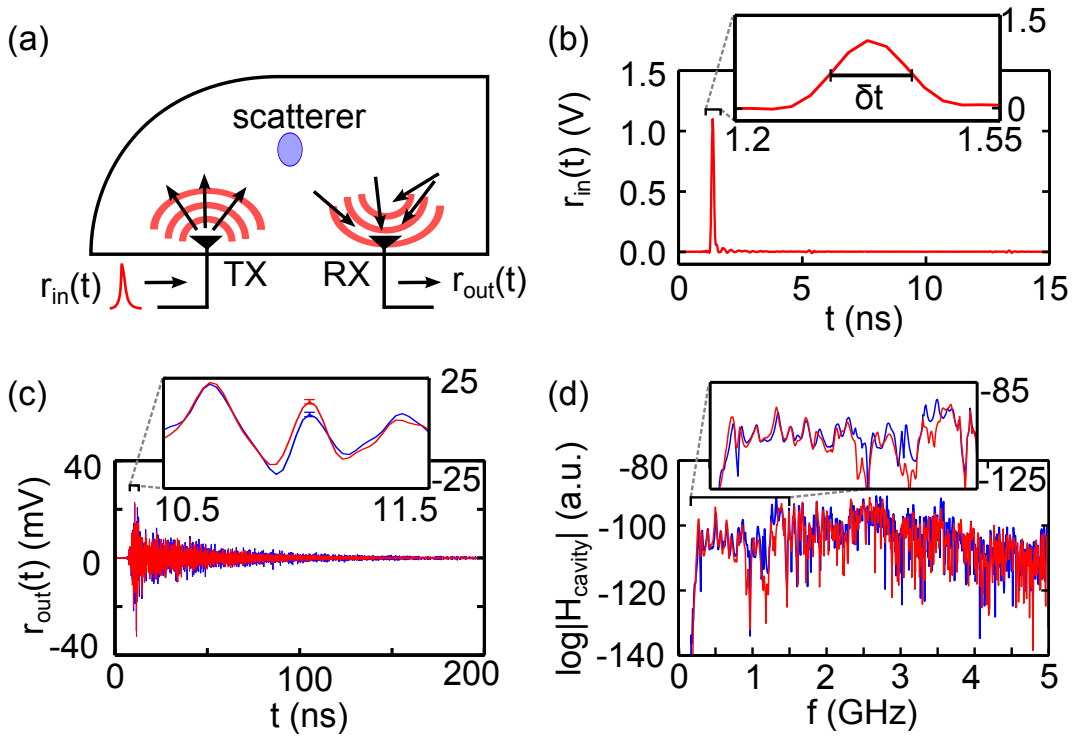

Figure 2.15: **Pulse response.** (a) Experimental measurement of the pulse response $r_{\text{out}}(t)$ of the cavity using a short EM pulse $r_{\text{in}}(t)$. (b) Input pulse $r_{\text{in}}(t)$ with full width at half maximum of $\sim$ 100 ps (generated using the error performance analyzer Agilent 70843). (c) Pulse responses $r_{\text{out}}(t)$ with (red curve) and without (blue curve) the scatterer. Error bars indicate the standard deviation of the noise floor ($\pm$1 mV) of the oscilloscope for each measurement. (d) Cavity spectra $|H_{\text{cavity}}(f)|$ with (red curve) and without (blue curve) the scatterer. In the zoom of (d), the horizontal axis is from 0.2 GHz to 1.5 GHz. In (c) and (d), zooms of the waveforms highlight some of the small quantitative changes in the system when the scatterer is added.

of wave-chaotic cavities for sensing that serve as the inspiration for my work.

2.2.2 Applications of Wave-Chaotic Cavities for Sensing and Imaging Scatterer Perturbations

Recently, researchers have shown that wave-chaotic cavities can be used for various sensor applications. For example, using short, acoustic pulses in an enclosed,

wave-chaotic stairwell, Taddesse *et al.* demonstrated that wave chaos can be used to detect the presence of an intruder, such as a person or a person-sized object [60]. Their sensing scheme is as follows. First, the empty cavity's pulse response is recorded as a reference. Then, if an intruding object enters the cavity, the pulse response is altered qualitatively and uniquely, depending on the size and location of the object, and this change is detected by calculating a cross correlation coefficient with the reference pulse response. This demonstrates that each unique perturbation to the cavity's interior gives rise to a unique pulse response (or set of resonances) that can be exploited for sensing. Furthermore, this intrusion detection scheme is incredibly useful because it exploits the complex scattering of a real-world, wave-chaotic cavity (the stairwell).

In addition, using a database of pre-recorded pulse responses for reference in a wave-chaotic cavity, Ing *et al.* have demonstrated that wave chaos can be used to localize a perturbation in 2D [61]. This wave-chaotic sensing technique relies on measuring changes to the pulse response and then using a correlation algorithm to match these perturbations to one of the many pre-recorded reference pulse-responses. This particular technique has a shown a sensitivity $\sim \lambda$, where λ is the mean wavelength of the injected pulse.

The work presented in this dissertation is inspired specifically by these scientific achievements. Next, using a similar pulse-response sensing technique, I will show, in a simple example, that my wave-chaotic cavity has a subwavelength sensitivity to the location of the subwavelength scatterer along a 1D path.

2.2.3 Subwavelength 1D Position Imaging of a Subwavelength Scatterer in a Wave-Chaotic Cavity

My 1D imaging scheme in a wave-chaotic cavity involves measuring the pulse

response of the cavity with the scatterer at various locations along a 1D path. The basic setup for this experiment is depicted in Fig. 2.16a. In the figure, the scatter translates in the x direction along a 12 mm path in 20 μm steps using a translation stage (the translation stage, Zaber Technologies (TLSR150B), has an error in its relative position of ± 5 μm). At each reference point x_n ($n \in [1, N]$) along the vertical 1D path, the position-dependent pulse response $r_{\text{out}}(x_n, t)$ of the cavity is measured and recorded. As an example of the changes to the pulse response of the cavity from scatterer translations, I plot both $r_{\text{out}}(x_1 = 0\,\text{mm}, t)$ and $r_{\text{out}}(x_N = 12\text{mm}, t)$ in Fig. 2.16b. Based on the figure, the difference between these two pulse responses is small but detectable.

How can we use the changes in r_{out} to deduce information about the scatterer location? To answer this question, I measure an additional pulse response of the system with the scatterer at a location x^* somewhere along the 1D path. I choose x^* such that $x_n < x^* < x_{n+1}$, where $r_{\text{out}}(x_n, t)$ and $r_{\text{out}}(x_{n+1}, t)$ are successive reference pulse responses that are separated by 20 μm. Thus, the pulse response at $r_{\text{out}}(x^*, t)$ should not match perfectly with any one of the reference acquisitions. The goal is then to use time series analysis and comparisons of $r_{\text{out}}(x^*, t)$ and $r_{\text{out}}(x_n, t)$ (over all n) to locate x^*.

Based on previous works [54], the cross-correlation coefficients C [38] and difference coefficients D defined respectively by

$$C(A(t), B(t)) = \frac{\int_0^T (A(t') - \bar{A}(t'))(B(t') - \bar{B}(t'))\,\mathrm{d}t'}{\sqrt{\int_0^T (A(t') - \bar{A}(t'))^2\,\mathrm{d}t'}\sqrt{\int_0^T (B(t') - \bar{B}(t'))^2\,\mathrm{d}t'}}, \tag{2.14}$$

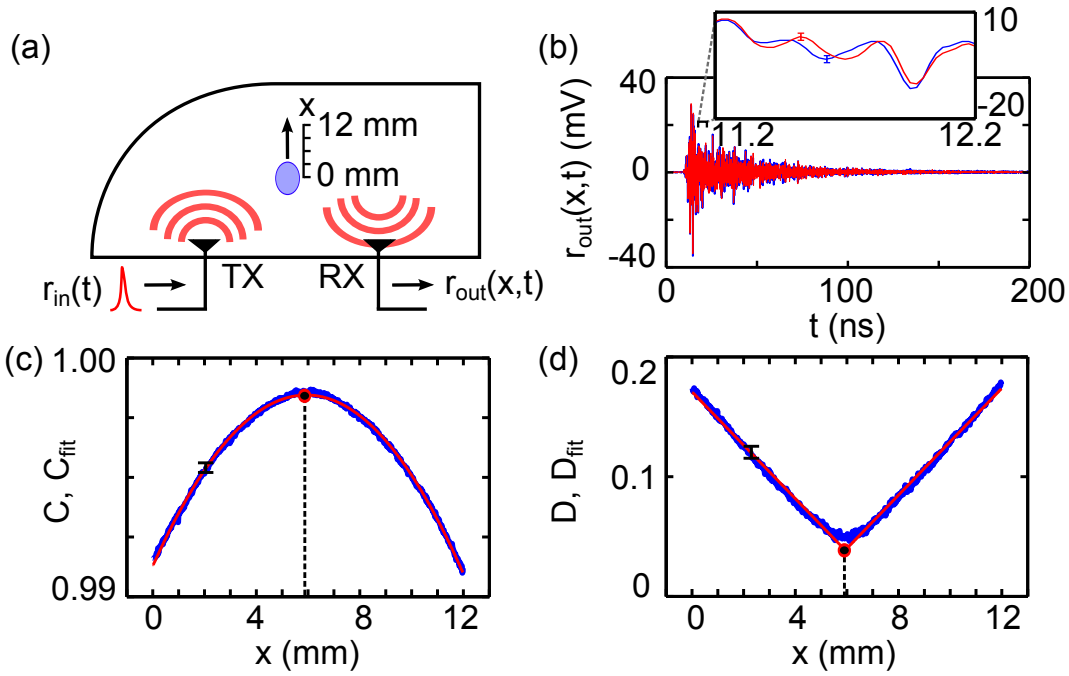

Figure 2.16: **1D sensing with wave chaos** (a) Setup for 1D sensing scheme. (b) Pulse response of the cavity with the scatterer at $x = 0$ cm (red) and at $x = 1.2$ cm (blue). Error bars indicate the standard deviation of the noise floor (± 1 mV) of the oscilloscope for each measurement. In each time series, the signal-to-noise ratio is $\mathrm{RMS_S}/\mathrm{RMS_N} \sim 11$, where $\mathrm{RMS_S}$ ($\mathrm{RMS_N}$) is the root-mean-square of the signal (noise). (c) Computed correlation coefficients C and (d) difference coefficients D in blue. Fitting functions in (c) and (d) are given by the red curves $C_{\mathrm{fit}}(x)$ and $D_{\mathrm{fit}}(x)$, respectively, where the extrema are labeled with black dots, indicating the fitted values of x^*_{fit}. The errors bars in (c) and (d) represent the standard deviations of C and D for 50 consecutive pulse responses for a fixed scatterer position. The position error in x is ± 5 μm given by the translation stage (Zaber Technologies TLSR150B).

where $\bar{A}$ is the mean value of A over the time of acquisition $t \in [0, T]$ and

$$D(A(t), B(t)) = \frac{\int_0^T |A(t') - B(t')|\,\mathrm{d}t'}{\int_0^T |A(t')|\,\mathrm{d}t'}. \tag{2.15}$$

The resulting $C(r_{\mathrm{out}}(x_n, t), r_{\mathrm{out}}(x^*, t))$ and $D(r_{\mathrm{out}}(x_n, t), r_{\mathrm{out}}(x^*, t))$ are plotted in Figs. 2.16c-d. In the figure, the values of C and D never reach 1 or 0 due to noise

and discretization errors in the waveforms. But, based on Eqs. (2.14)-(2.15), the maximum of $C(x_n, x^*)$ and the minimum of $D(x_n, x^*)$ correspond to the position x_n that is closest to x^*.

Using these experimental extrema automatically limits our resolution to $\Delta x = x_{n+1} - x_n = 20$ μm, and we know that x^* lies between reference points. Similar to the imaging methods discussed in Chapter 1, I use a numerical fitting of the experimental data to yield an enhanced resolution. Thus, I fit C and D using the continuous quadratic and piecewise-linear fitting functions

$$C_{\text{fit}}(x) = c_1 + c_2(x - x^*_{\text{fit}})^2, \tag{2.16}$$

and

$$D_{\text{fit}}(x) = d_1 + d_2|(x - x^*_{\text{fit}})|, \tag{2.17}$$

respectively (these fitting functions are chosen based on the visual form of the data and different functions may yield different results). The functions $C_{\text{fit}}(x)$ and $D_{\text{fit}}(x)$ are also plotted in Figs. 2.16c-d with values $c_1 = (9.98 \pm 0.01) \times 10^{-1}$, $c_2 = (2.2 \pm 0.01) \times 10^{-4}$ mm^{-2}, $d_1 = 0.04 \pm 0.01$, and $d_2 = 0.02 \pm 0.01$ mm^{-1} (errors represent the 90% confidence intervals of the parameters of the fits). Also, the root-mean-square (RMS) differences between the data and fits yields 1.2% and 2.4% errors for the total ranges of C and D, respectively. For both fits, $x^*_{\text{fit}} = 5.93 \pm 0.01$ mm, where $x^* = 6.01 \pm 0.05$ mm. Thus, this 1D sensing scheme can localize the scatterer to within ~ 0.1 mm which is approximately $\lambda/600$, where $\lambda = 6$ cm is the average wavelength of the injected EM pulse (calculated by assuming the average frequency of a 100 ps pulse is ~ 5 GHz). These 1D measurements serve as a benchmark for comparing the results of my feedback imaging system in the next chapter.

2.3 Summary

In summary, I examine both time-delayed nonlinear feedback systems and wave chaotic cavities in this chapter. The first section is devoted to the introduction of the dynamics in a time-delayed nonlinear feedback system. Using an experimental nonlinear circuit, I show the existence of steady-state, periodic, quasiperiodic, and chaotic dynamics of a single-loop, ultra-high-frequency system by tuning the net gain of the feedback loop. I also demonstrate qualitatively similar results using a simple numerical model for this time-delay system. Lastly, I give a few examples of how changes to these dynamical states, which arise due to perturbations in the feedback parameters, can be exploited for sensing applications.

In the second section, I provide a brief introduction to wave chaos and the some of the mathematical concepts used to characterize a wave-chaotic cavity. Using the resonances of an experimental cavity, I demonstrate the existence of wave chaos in this component of my experiment. Then, based on previous applications that use wave chaos for sensing, I demonstrate a 1D sensing technique for imaging the position of a subwavelength scatterer with subwavelength resolution ($\lambda/600$).

In the next chapter, I combine my nonlinear circuit and wave-chaotic cavity to form a new time-delayed nonlinear feedback system. This new cavity-feedback system can image the position of the scatterer with an improved 1D resolution ($\lambda/10,000$) and a 2D resolution ($\lambda/300$) using the system's various dynamical states. In addition, the cavity-feedback system does not require an external source, which reduces the cost for this type of subwavelength position sensor. As a comparison, the error performance analyzer that produces 100 ps pulses for $r_{\text{in}}(t)$ is $\sim$ \$60,000, whereas the cost of the additional components in the self-oscillating, cavity-feedback system are $<$ \$1,000. Furthermore, the bandwidth of the cavity-

feedback system is less than that of the pulse response, and therefore a lower temporal resolution for measurements (sampling rate) with less recorded data are used to produce vastly subwavelength position-sensing resolutions.

Chapter 3

Subwavelength Sensing Using Nonlinear Feedback in a Wave-Chaotic Cavity

This chapter presents the results of a new experiment for subwavelength sensing that combines a time-delayed nonlinear feedback system with a wave-chaotic cavity to resolve the position of a scatterer. Its content is divided into four sections. In the first two sections, I present the conceptual overview and the detailed experimental setup for the sensing system based on the results from the previous chapter. In the last two sections, I examine the various dynamical states of the system: periodicity, quasiperiodicity, and chaos. For each of these three dynamical states, I present methods for sensing both qualitative and quantitative changes of the dynamics with respect to the location of the scatterer. The goal of this chapter is to explore the potential of this new type of time-delayed nonlinear feedback system to image the position of the scatterer with subwavelength resolution.

The experimental system that is the focus of this chapter was constructed with the help of Hugo Cavalcante. The resulting analysis of the dynamics was analyzed with the help of Daniel Gauthier. Lastly, as mentioned in Ch. 1, I published the most significant results of this chapter, the 2D position-sensing modality, in Ref. [21].

3.1 Conceptual Overview

As shown in Ch. 2, a microwave wave-chaotic cavity allows for many different scattering paths for the injected EM energy. After a short input pulse $r_{\text{in}}(t)$ is applied to the cavity's TX antenna, the output of the cavity shows a complex waveform $r_{\text{out}}(t)$ at the RX antenna. Besides being the pulse response of the system, $r_{\text{out}}(t)$

can also be viewed as a set of propagation delays of times τ_i with gain coefficients g_i. In other words, each time τ_i at which the radiation arrives at the RX antenna is a measure of the path length of one of the multiple paths of the input signal through the cavity. As shown in Fig. 3.1a, the time axis of the pulse response plot is τ_i and its amplitude is g_i. The discrete index i indicates a discrete time (an approximation) corresponding to each data point in the pulse response (τ_i, g_i). Thus, the wave-chaotic cavity is a distribution of delays and gains, as depicted in Fig. 3.1b. In addition, in the previous chapter, the pulse response $r_{\text{out}}(t)$ is sensitive to the scatterer's presence and position in the wave-chaotic cavity. Consequently, the joint delay-gain distribution (τ_i, g_i) associated with the cavity depends on the location of the scatterer.

In Ch. 2, I also introduce the basic ingredients of a time-delayed nonlinear feedback system comprising a nonlinear element, gain, and delay, as shown in Fig. 3.1c. Specifically, I demonstrated an example of a time-delayed nonlinear feedback system where the output of a nonlinear circuit is amplified with gain G and delayed through a single time delay τ before being fed back to its input. This time delay is realized using coaxial cables that serve as waveguides for the propagating voltages $\text{v}(t)$. The feedback parameters τ and G govern the dynamical state of the system and small parameter variations can lead to measurable dynamical changes for sensing applications.

To realize my subwavelength sensing system, I substitute the single-valued time delay of the coaxial cables with the delay-gain distribution of the wave-chaotic cavity, as illustrated in Fig. 3.1d. The amplified output of the nonlinear circuit $\text{v}(t)$ is injected directly into the wave-chaotic cavity through the TX antenna. The delay-gain distribution of the cavity splits the injected EM energy in $\text{v}(t)$ among many different propagation paths. At the RX antenna, the delayed and attenuated EM energy

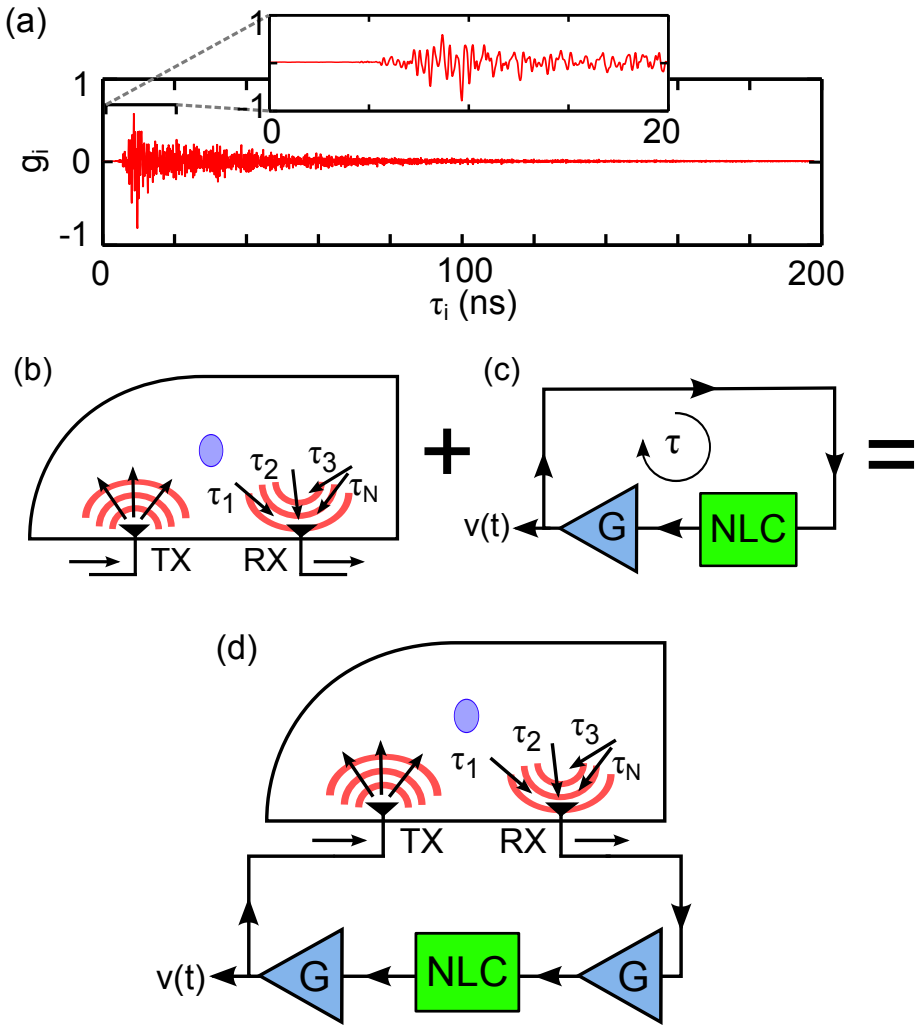

Figure 3.1: **Conceptual overview of the subwavelength sensing system** (a) Delay distribution of the wave-chaotic cavity with a zoom of the region between $\tau_i = 0$ and $\tau_i = 20$ ns. The data is collected using 100 averaged waveforms. The spacing between data points (τ_i, g_i) is $\Delta\tau = \tau_{i+1} - \tau_i = 0.025$ ns. (b) The delays τ_i labeled in a schematic representation of the wave-chaotic cavity. (c) A schematic representation of the basic ingredients for a time-delayed nonlinear feedback system. (d) Schematic representation of the combined wave-chaotic cavity and time-delayed nonlinear feedback system. The propagation delays τ_i of the delay distribution are now the time delays of the nonlinear feedback loop.

is collected and amplified before being injected back to the input of the nonlinear circuit. This forms a closed-loop, cavity-feedback system that circulates EM energy. The resulting system self oscillates with dynamics that depends on the delay-gain

distribution of the feedback, or in other words, the location of the scatterer.

In the next section, I give a detailed description of the experimental setup and components in this cavity-feedback system.

3.2 Experimental Setup

The experimental setup for the cavity-feedback system uses similar electronic components to the single-loop time-delayed nonlinear feedback system from Chapter 2. As shown in Fig. 3.2a, the output of the nonlinear circuit (NLC) v_{out} passes first through the amplifier A_1. Different from the single-loop setup, after A_1, v_{out} is directed through a low-pass filter (LPF) that cuts all frequencies above $f_{max} \sim 2$ GHz arising at the output of the NLC. As a result, this filter limits the minimum wavelength in the cavity to $\lambda_{min} \sim c/f_{max} \sim 15$ cm, which gives some control over the potential dynamical range of the illumination source and limits the EM radiation in the cavity to TM modes, forcing only 2D interactions with the scatterer. After the low-pass filter, a directional coupler (dir-c) directs a portion of the signal $v(t)$ to a broadband measurement oscilloscope.

Passing through the directional coupler, the voltage $v(t)$ is also coupled directly to the TX antenna of the wave-chaotic cavity where it radiates. The radiated EM energy scatters and reflects off of the water scatterer with position (x, y) and the boundary of the cavity before being partially collected by the RX antenna. After the RX antenna, the collected EM radiation is amplified as a voltage through amplifier A_2. The output voltage of this amplifier v_{in} passes through the bias-T that is associated with the nonlinear circuit, adding the constant voltage v_b. The sum ($v_{in} + v_b$) is then injected at the input of the NLC. As an added measure for minimizing the effects of external EM noise, the nonlinear circuit and bias-T are also placed in

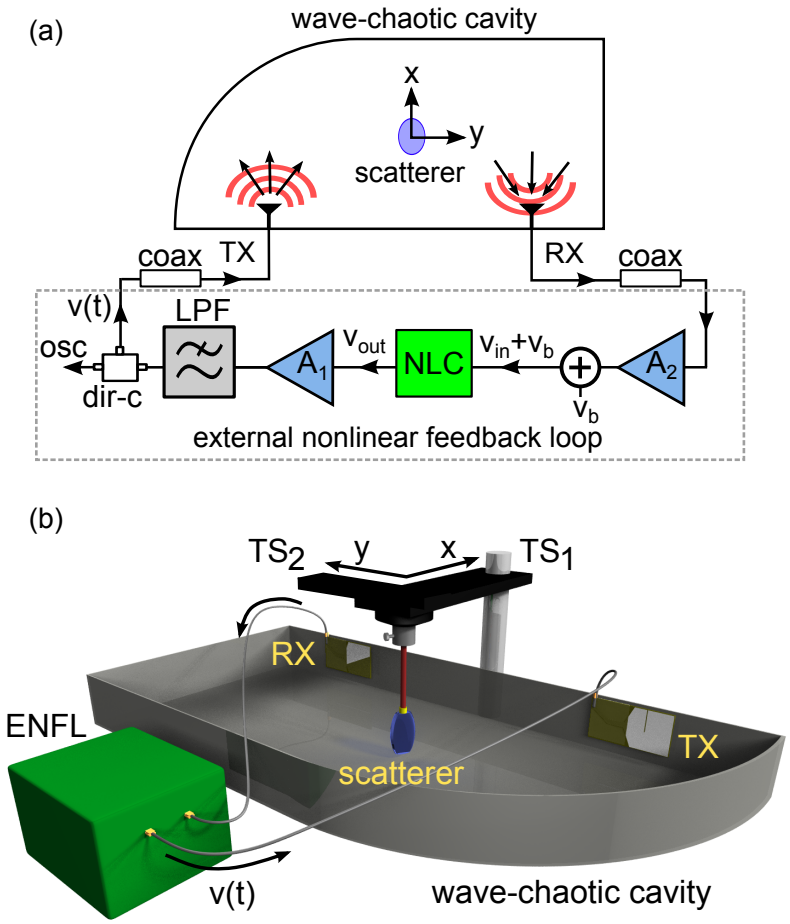

Figure 3.2: **Cavity-feedback system** comprised of a wave-chaotic cavity and an external nonlinear feedback loop (ENFL). (a) The nonlinear circuit (NLC) drives the amplifier A_1 (Mini-Circuits ZX60-3018G+), a low-pass filter (LPF, comprised of filters in series: Mini-Circuits ZBFV-925+ and Mini-Circuits ZBFV-925+), a directional coupler (dir-c, Mini-Circuits ZX30-9-4+), the TX and RX antennas, the amplifier A_2 (comprised of two amplifiers in series: Mini-Circuits ZX60-3018G+ and Picosecond Pulse Labs 5828-108), and a bias-T (Mini-Circuits ZFBT-6G+) with bias voltage v_b. Coaxial cables (coax) connect these components and act as additional propagation delays. The coupling port of the dir-c is measured with a 8-GHz-analog-bandwidth 40-GS/s oscilloscope (Agilent DSO80804B). (b) 3D rendering of the system. The output $v(t)$ of the ENFL interacts with the scatterer via TX and RX antennas. The scatterer's position is controlled by the translation stages TS_1 (Zaber Technologies TLSR150B) and TS_2 (Thorlabs LTS150) in the x and y directions, respectively.

a shielded aluminum box, but there is no active stabilization to control the thermal or vibrational effects of the experimental environment.

In addition to the components in the 2D schematic shown in Fig. 3.2a, the scatter position (x, y) is controlled using translation stages. To visualize the locations and roles of these translation stages, a simplified 3D rendering of the experimental system is shown in Fig. 3.2b. For the ease of the reader, all of the components of the external nonlinear feedback loop (NLC, A_1, A_2, LPF, dir-c, bias-T) are represented by a green box labeled as ENFL in the figure. Inside the cavity, the scatterer is positioned in the x and y directions by the computer controlled translation stages TS_1 and TS_2, respectively. Each of these two translation stages has a relative positioning resolution of ± 5 μm ($\sim \lambda_{\text{min}}/30,000$). Recall that this position error is does not accumulate due to backlash correction that is programmed into the translation stages.

When the system is switched on, it self oscillates and leads to the formation of a complex interference pattern inside of the wave-chaotic cavity. This interference pattern may undergo spatio-temporal variations depending on the frequency content and relative phases of the oscillatory dynamics. Furthermore, as the scatterer moves in the wave-chaotic cavity, the modes of the cavity shift, thus affecting the dynamical state of the system. As I will show throughout this chapter, the scalar voltage v(t) alone provides enough information about the changes in the cavity-feedback system to image the relative position of the scatterer with subwavelength resolution. As mentioned briefly in Ch. 1, this is a surprising result and is quite different from typical imaging systems that use array detectors with multiple measurements to resolve spatial features.

In the next section, I begin by characterizing the dynamical diversity of the system as a function of the scatterer's location.

3.3 Position-Dependent Dynamics

To demonstrate the qualitatively the sensing capabilities of the cavity-feedback system, I first consider a displacement of the scatterer along a 1D path from relative positions $x_{\text{rel}} = 0$ mm to $x_{\text{rel}} = 12$ mm in steps of 10 μm. At each position of the scatterer, I record a single time series of $\text{v}(t)$ to characterize the state of the system. To start, for the scatterer at $x_{\text{rel}} = 0$ mm, I switch the system on and tune v_b in the NLC such that $\text{v}(t)$ exhibits periodic oscillations, as shown in Fig. 3.3a, with a corresponding Hopf frequency $f_\text{H} \sim 1.33$ GHz shown in the PSD of Fig. 3.3b.

As the scatterer translates, I observe three bifurcations. The first is a torus bifurcation leading to the quasiperiodic oscillations, as shown in Fig. 3.3c, which demonstrate an amplitude modulation at a frequency $f_\text{T} \sim 34$ MHz. In addition, due to frequency mixing, the quasiperiodic PSD also shows frequencies $f_\text{H} - f_\text{T} \sim 1.30$ GHz and $f_\text{H} + f_\text{T} \sim 1.36$ GHz in Fig. 3.3d. The second bifurcation is from quasiperiodicity to a chaotic state called *chaotic breathers* [62]. Shown in Fig. 3.3e, the amplitude of oscillations takes on a complex form that periodically collapses to $\text{v}(t) \sim -0.25$ V as if the dynamics are inhaling and exhaling (breathing). The result of this complex amplitude modulation is a broadening of the PSD (see Fig. 3.3f). The third bifurcation leads to a broadband chaotic state (see Fig. 3.3g) with highly irregular oscillations that result in a relatively flat bandwidth from 20 MHz – 2 GHz (see Fig. 3.3h).

The locations of these bifurcations are marked on a bifurcation diagram shown in Fig. 3.4a. In the figure, I plot the density of local maxima v_max of $\text{v}(t)$ for each of the recorded time series along the 1D path as a function of the bifurcation parameter x. In the figure, I also label the regions of periodicity (P) from $x_{\text{rel}} = 0$ mm – 1.4 mm, quasiperiodicity (QP) from $x_{\text{rel}} = 1.4$ mm – 8 mm, and the two different

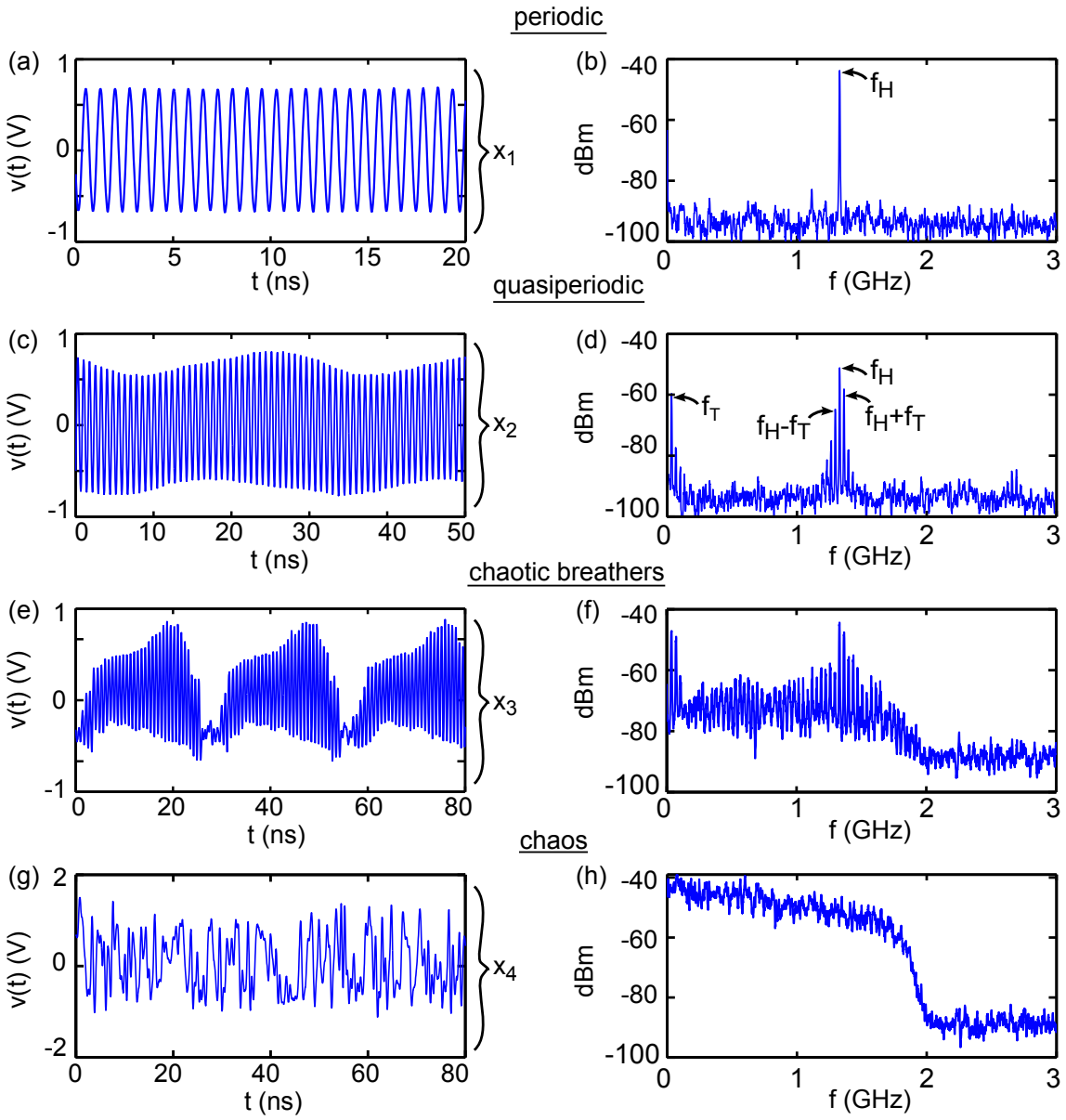

Figure 3.3: **Dynamics of the cavity-feedback system.** (a), (c), (e), (g) Time series v(t) and (b), (d), (f), (h) power spectral densities (PSDs) with the scatterer at the relative positions $x_1 = 1$ mm, $x_2 = 2$ mm, $x_3 = 9.5$ mm, and $x_4 = 11$ mm. The noise level in each time series is approximately $\sigma_N = 1.2$ mV, which is given by the standard of the noise floor of the oscilloscope during the time series acquisition.

time-evolving chaotic states (C1 and C2) from $x_{\text{rel}} = 8$ mm – 9.8 mm and $x_{\text{rel}} =$ 9.8 mm – 12 mm, respectively. In the periodic region, v_{max} is concentrated around

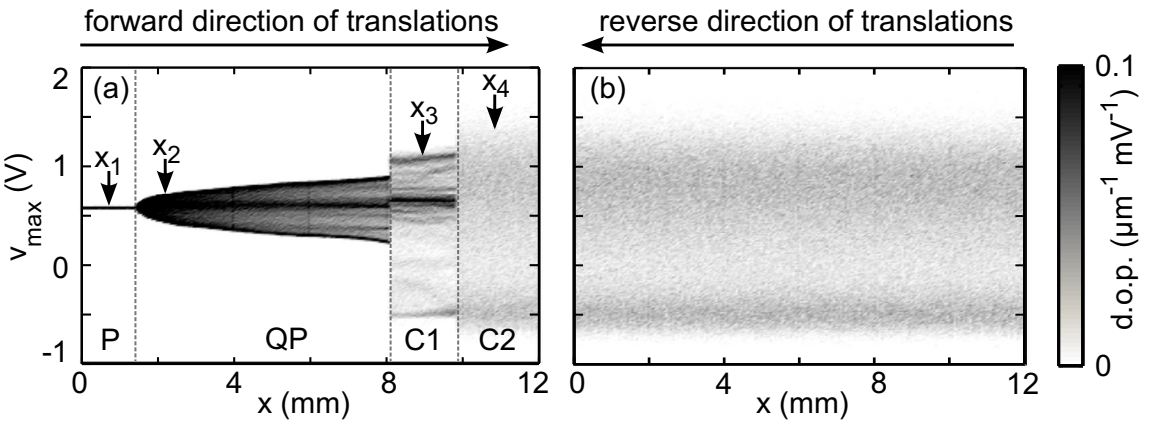

Figure 3.4: **Bifurcation diagrams.** Density of local maxima v_{max} plotted as a function of scatterer position x for the (a) forward direction from $x_{rel} = 0$ mm to $x_{rel} = 12$ mm and the (b) reverse direction from $x_{rel} = 12$ mm to $x_{rel} = 0$ mm. The color bar indicates the density of points (d.o.p) with a minimum value of 0 μm^{-1} mV^{-1} indicated in white and the saturation value of 0.1 μm^{-1} mV^{-1} indicated in black. The positions x_1, x_2, x_3, and x_4 are labeled to indicate the density of the v_{max} for the dynamics presented in Fig. 3.3.

$v_{max} \sim 0.6$ V, and the quasiperiodic region demonstrates a spreading in the density of v_{max} about this line. In the chaotic-breather region, the density is spread further with a concentrated region about $v_{max} \sim 0.7$ V. Lastly in the chaotic state, the density of local maxima is at its lowest, ranging between -0.5 V to 1.5 V.

This bifurcation diagram demonstrates qualitatively the changes in the cavity-feedback system from scatterer movements. For a direct comparison of the results, this is the same 12 mm path used in Chapter 2 to demonstrate 1D sensing using the wave-chaotic cavity's pulse response. But, when viewing these bifurcations over a 1D path, it is difficult to quantify a sensing resolution of the system. While in the periodic region (P in Fig. 3.4), the density of v_{max} does not change, whereas in the quasiperiodic region (QP), the spread in v_{max} grows as the scatterer translates. In addition, from a single 10 μm change in the scatterer's position ($\lambda_{min}/15,000$) at the boundaries of these behaviors, the dynamics can change drastically through

bifurcations. Although it is easy to detect changes in the dynamics from specific scatterer translations, the inverse problem of determining the scatterer's position from specific bifurcations does not have a well defined solution.

Furthermore, to analyze the history dependence of these dynamical changes, I scan the scatterer's location in the reverse direction from $x_{\text{rel}} = 12$ mm to $x_{\text{rel}} = 0$ mm. Starting with the system exhibiting the broadband chaos (C2), the time series of v(t) are recorded along the reverse 1D path in 10 μm increments. Interestingly, as shown in Fig. 3.4b, the system remains chaotic over the entire 12 mm path, demonstrating the existence of multi-stability: Different dynamical states are accessible with identical parameters (scatter positions). As a consequence, the dynamics may not depend on the absolute position of the scatterer in the cavity, but rather the paths through which the scatterer translates.

From a sensing point-of-view, the dynamical hysteresis from bifurcations can yield both advantages and disadvantages. If the cavity-feedback system is being used as an intrusion-detection device, then the multi-stability can be an advantage. To see this, consider the situation when a hypothetical intruder enters and leaves the scattering environment of the cavity; the dynamics of the system may change in an irreversible way, thus indicating an intrusion. However, from an imaging point-of-view, the hysteresis induced by multi-stability is a disadvantage. If the dynamics of the imaging system are not repeatable, then quantitative changes in the scatterer location cannot be resolved.

Thus, in next section, I tune the parameters of the system such that its dynamical states remain stable and avoid bifurcations/multi-stability in order to establish techniques for imaging the position of the scatterer with quantifiable resolutions.

3.4 Dynamical Sensing

In this section, I show that each of the system's dynamical states (periodic, quasiperiodic, and chaotic) can be used for imaging the scatterer's position with subwavelength resolution. In particular, I present the results of my experiments in chronological order to highlight the progression of my sensing techniques, beginning with chaos, then changing to periodicity, and then finally quasiperiodicity.

3.4.1 Sensing with Chaotic Dynamics

My initial hypothesis for sensing in the cavity-feedback system is as follows: Because temporal chaos is known for its sensitivity to small perturbations, the EM radiation from a chaotic dynamical state will give the best possible resolution for sensing scatterer movements. Thus, I use the chaotic signal shown in Figs. 3.3g-h, which is the most complex and hence broadband signal observed in the output of the system (chaotic breathers are not as broadband and are more difficult to find experimentally). When injected into the cavity, the broadband chaotic spectrum of $v(t)$ occupies the irregularly spaced resonances of the wave-chaotic cavity. As the scatterer moves, the resonances of the cavity shift (see Ch. 2), resulting in changes of the chaotic dynamics. The chaos is sensitive to the scatterer's location, however, detecting these changes can be a difficult problem.

To illustrate the limitations of using the chaotic dynamics for position sensing, I examine two different chaotic time series from the system when the scatterer is at the relative positions $x_{\text{rel}} = 0$ mm and $x_{\text{rel}} = 5$ mm. Shown in Figs. 3.5, the chaotic time series at these scatter positions are both complex with broadband PSD's. In addition, the 2D phase-space projection of each chaotic time series demonstrates that the chaotic attractors are qualitatively similar. Detecting all of the differences

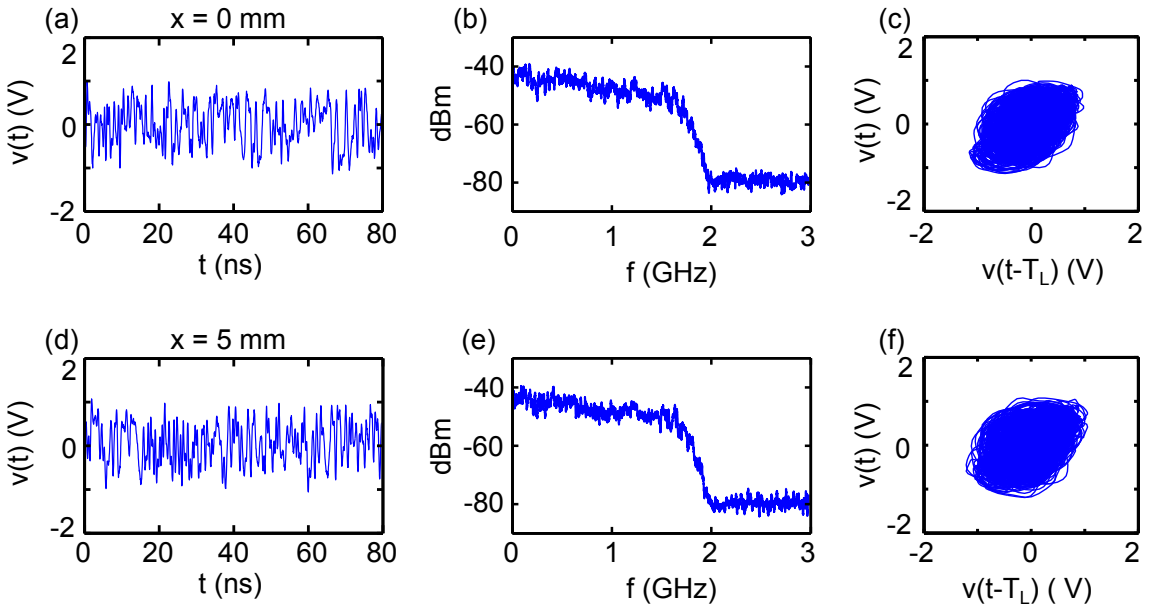

Figure 3.5: **Broadband chaos for two different scatterer positions.** (a) Chaotic time series, (b) power spectral density (PSD), and (c) phase space projection (PSP) when the scatterer is at position $x_{\text{rel}} = 0$ mm. (d) Chaotic time series (d) PSD, and (f) PSP when the scatterer is at position $x_{\text{rel}} = 5$ mm. In the PSPs, the time lag $T_L = 0.3$ ns.

between these chaotic time series, if there are any, does not have an easy solution. There are statistical measures for detecting changes in chaotic attractors, such as the rate of trajectory divergence known as the Lyapunov exponent [63], the dimension of the attractor [64], or even the use of a matched model to predict parameter variations [65]. But, these methods may not be sensitive to small changes or robust against experimental noise [43]. In addition most methods have only been proven to work for low-dimensional, well-known chaotic systems.

Instead of trying to detect all of the changes between the chaotic dynamics in Figs. 3.5a-c and in Figs. 3.5d-f, I instead focus on detecting a particular change to its dynamical trajectories. Similar to the detection of large amplitude rogue waves in laser systems with feedback [66], I locate the large-amplitude trajectories (LATs) that flow through the outer regions of the phase space projections. Because of the

band-pass filtered nature of the system, the density of the attractor is high near $v(t) = v(t - T_L) = 0$, but, in the outer regions away from the origin, the density of the trajectories along the chaotic attractor is much smaller. As I will show, these LATs are caused by large-amplitude spikes in the temporal evolution of $v(t)$, and thus, by their own nature, they stand out when compared to the other complex oscillations of the broadband chaos.

In the experimental system, I locate these LATs using the triggering feature of our digital oscilloscope. Shown in Fig. 3.6a, I reacquire the time series for the broadband chaos with the scatterer at position $x_{\text{rel}} = 0$ mm. In this case, however, the trigger voltage v_{trigger} has been moved from $v_{\text{trigger}} = 0$ V (approximately where it has been for all previous measurements) to approximately $v_{\text{trigger}} = 1.6$ V. When the trigger is at this level, each chaotic time series is acquired only when a large-amplitude spike crosses this threshold and triggers the oscilloscope acquisition. Once triggered, the oscilloscope records the time series surrounding the spike at time $t = 0$. To visualize the actual LAT, the phase-space projection (PSP) of this time series is plotted in Fig. 3.6b. Comparing this figure with PSPs in Figs. 3.5c,f, there is a visible trajectory that leaves the dense attractor and briefly visits the outer region of the phase space projection.

In order to understand how these LATs change with respect to scatterer movements, I first characterize the LATs for a fixed scatterer position. To do so, I use the averaging feature of the digital oscilloscope, which continuously averages the acquired waveforms with a moving average function

$$\bar{v}(t) = \frac{1}{100} \sum_{n=1}^{n=100} v_n(t), \tag{3.1}$$

where $v_n(t)$ is the n^{th} time series in the moving average. Using a trigger level at

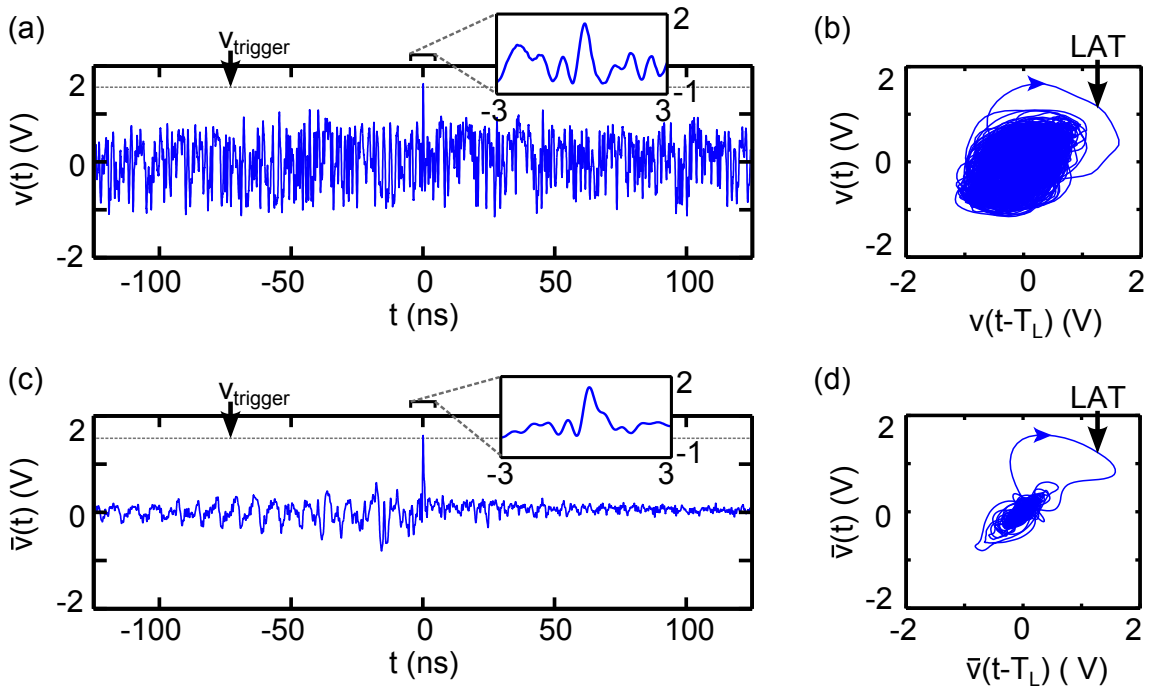

Figure 3.6: **Large-amplitude spike event and trajectory using a high level trigger.** (a) Chaotic time series v(t) acquired from the oscilloscope with $v_{trigger} \sim 1.6$ V. (b) Phase space projection (PSP) of the high-level triggered chaos. (c) Averaged time series and (d) PSP for $\bar{v}(t)$ with $v_{trigger} \sim 1.6$ V. In the PSPs of (b) and (d), the time lag $T_L = 0.3$ ns and the large amplitude trajectories (LATs) are labeled with arrows to indicate the direction of the flow.

approximately $v_{trigger} = 1.6$ V, the averaged chaotic waveform $\bar{v}(t)$ at $x_{rel} = 0$ mm is plotted in Fig. 3.6c. The figure, which shows the average of many different large-amplitude spikes for a fixed scatterer position, reveals a steady underlying structure that represents the correlated regions of the chaotic time series near the spikes [66]. In other words, on average, whenever there is a large-spike event, the temporal evolutions of v(t) preceding the spike and slightly after the spike are approximately repeated. Beyond this structure (approximately $t < -125$ ns and $t > 100$ ns), the signal collapses to $\bar{v}(t) \sim 0$ V because the trajectories are no longer correlated. In addition, the phase-space projection of the averaged $\bar{v}(t)$ is shown in Fig. 3.6d. Comparing this with the non-averaged case in Fig. 3.6b, the averaged LAT is now

larger with respect to the system's averaged attractor. The shape of the labeled LAT is also slightly different because it takes into account the averaged trajectories of the attractor during many large-spike events. Thus, the time series and phase-space projections in Figs. 3.6c-d present a simple characterization of the LATs for a fixed scatterer position.

Though a phase space projection is useful for visualizing the LATs, it is the underlying structures of $\bar{v}(t)$ near the averaged spike-events that change with respect to the scatterer's position. As a result, I focus on the time series for $\bar{v}(t)$ to demonstrate the system's chaos-based sensing. As an example of the changes to its underlying structures, I plot $\bar{v}(t)$ for the system with the scatterer at relative positions $x_{\text{rel}} = 0$ mm and $x_{\text{rel}} = 5$ mm in Fig. 3.7a. As shown by the inset, the difference between these two waveforms is small but detectable. The goal is to record these changes as a function of the scatterer position and see if they can be used for tracking its location.

Similar to the 1D sensing in Ch. 2, I acquire a set of reference time series $\bar{v}(x_n, t)$ (instead of pulse responses $r_{\text{out}}(x_n, t)$) along a 1D path in the x direction at positions x_n. In this case, the reference waveforms are taken from $x_{\text{rel}} = 0$ to $x_{\text{rel}} = 5$ mm in 200 μm increments ($\Delta x_n = x_{n+1} - x_n = 200$ μm). In addition to each $\bar{v}(x_n, t)$, I acquire the waveform $\bar{v}(x^*, t)$ at an arbitrary position x^*, where $x_n < x^* < x_{n+1}$. Using a similar analysis to the 1D sensing technique in Ch. 2, I calculate the cross-correlation coefficients $C(\bar{v}(x_n, t), \bar{v}(x^*, t))$ and difference coefficients $D(\bar{v}(x_n, t), \bar{v}(x^*, t))$ for all x_n using Eqs. (2.14) - (2.15). The results of these calculations are shown in Figs. 3.7b-c. The global extrema for the correlation and difference functions correspond to the $\bar{v}(x_n, t)$ that is most similar to $\bar{v}(x_n, t)$. Thus, the positions of these extrema give a prediction for x^* with a discretized resolution Δx_n.

Using Eqs. (2.16) - (2.17) from Ch. 2, the cross-correlation and difference fitting functions $C_{\text{fit}}(x)$ and $D_{\text{fit}}(x)$ can be used to achieve an enhanced resolution. These fits are chosen based on the analysis in Ch. 2 and allow for a direct comparison between the performance levels of the chaotic dynamics in the feedback system and the pulse responses of the cavity. These fitted functions, which are also plotted in Figs. 3.7b-c yield the coefficients $c_1 = 0.997 \pm (2 \times 10^{-3})$, $c_2 = 0.002 \pm (10^{-4})$, $d_1 = 0.073 \pm 0.025$, and $d_2 = 0.039 \pm 0.025$ (the errors represent the 90% confidence intervals of the parameters of the fits). Also, the root-mean-square (RMS) differences between the data and fits yields 8.7×10^{-4} and 1.12×10^{-2} for C and D, respectively, which represent ∼6% and ∼10% errors of the total the respective experimental ranges. The fitted values for x^* are $x^*_{\text{fit}} = 2.44 \pm (2 \times 10^{-3})$ mm for $C_{\text{fit}}(x)$ and $x^*_{\text{fit}} = 2.46 \pm 0.025$ mm for $D_{\text{fit}}(x)$. Averaging these values gives $\bar{x}^*_{\text{fit}} = 2.45$ mm which should be compared to $x^* = 2.50$ mm. Thus, this 1D chaos-based sensing technique can image the position of the scatterer with a resolution of approximately 50 μm, which corresponds to $\lambda_{\text{min}}/3,000$.

In conclusion, imaging the 1D position of a scatterer with broadband dynamical chaos yields an improved resolution when compared to the sole use of wave chaos with a resolution of $\lambda/600$. Using the oscilloscope's triggering and averaging features, I demonstrate that small changes to the chaotic attractor can be detected and quantified. Furthermore, this method creates its own illuminating field and does not require the assistance of an expensive pulse generator.

However, my chaos-based sensing technique exploits the underlying structures of $\bar{v}(t)$, which are small-amplitude signals when compared to the chaos that circulates through the feedback loop. In addition, in order to recover these structures and create a simple sensing procedure, a large amount of information in the chaos is discarded through averaging. Rather than try to develop statistical measures that

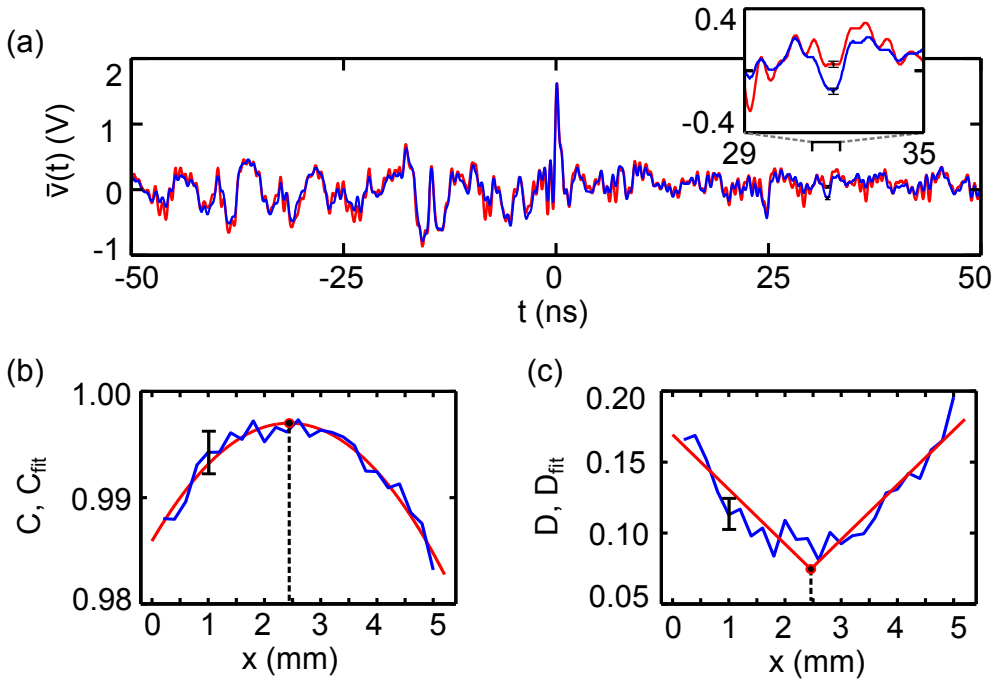

Figure 3.7: **1D sensing with chaos.** (a) Chaotic time series $\bar{v}(t)$ acquired from the oscilloscope with a high level trigger and the scatterer at $x_{\text{rel}} = 0$ mm (blue curve) and $x_{\text{rel}} = 5$ mm (red curve). The error bars represents the standard deviation of the waveform ±20 mV for 50 consecutive measurements at a fixed scatterer location. (b) Normalized cross-correlation coefficients $C(\bar{v}(x_n, t), \bar{v}(x^*, t))$ as a function of x (blue curve) with the curve $C_{\text{fit}}(x)$ indicating the position of the fitted maximum of the data (red curve). (c) Difference coefficients $D(\bar{v}(x_n, t), \bar{v}(x^*, t))$ as a function of x (blue curve) with the curve $D_{\text{fit}}(x)$ indicating the position of the fitted minimum of the data (red curve). The errors bars in (b) and (c) represent the standard deviations of C and D for 50 consecutive measurements at fixed scatterer position. The position error in x is ±5 μm given by the translation stage (Zaber Technologies TLSR150B).

use all of the changes to the entire chaotic waveform for imaging, I choose to use a simpler dynamical state with easily detectable changes. Thus, in the next subsection, I demonstrate my results for imaging the position of the scatterer in the cavity-feedback system using a periodic dynamical state.

3.4.2 Sensing with Periodic Dynamics

As mentioned in Ch. 2, the dynamical changes in a periodic signal from a nonlinear feedback system can be used for simple sensing applications. In the opto-electronic sensor system, small changes to the net time delay of its feedback loop cause shifts in the periodic frequency of oscillation. In the cavity-feedback system, under the proper conditions, both the periodic signal's amplitude and frequency can be sensitive to the scatterer position. To operate the imaging system with periodic oscillations, v_b of the NLC is tuned such its dynamics are periodic without being near a bifurcation point. As shown in Figs. 3.8a-b, the time series oscillates at $f_H \sim 1.35$ GHz with amplitude $A \sim 0.76$ V. Furthermore, in Fig. 3.8c the phase space projection of the periodic signal is a simple limit cycle. Using this dynamical state, I follow the small changes in A and f_H as a function of the scatterer position.

To observe small shifts in f_H with high precision, I use a particular measurement procedure. Typically, to observe a frequency with a resolution Δf using a digital oscilloscope, a time series must be acquired with a minimum time-length $\Delta t = (\Delta f)^{-1}$. This criterion is based on the Fourier transform when converting from the time domain to the frequency domain. However, this limit is only in place for resolving absolute frequencies. If the starting frequency f_H is known with high

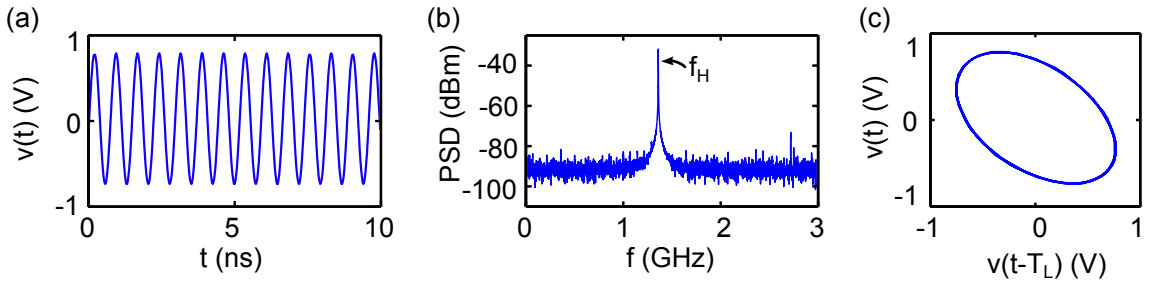

Figure 3.8: **Periodic dynamics used for sensing.** (a) Periodic time series, (b) power spectral density, and (c) phase space projection with lag time $T_L = 1$ ns.

resolution and I am only interesting in the relative shifts about this value, then the Fourier transform limit does not apply and a shift Δf can be resolved with much less data.

Here is how: Measuring a small frequency shift can be accomplished experimentally by changing the trigger timing of the waveform acquisition known as the *trigger skew*. The trigger skew is the amount of time that the oscilloscope waits between its initial triggering and the acquisition of a waveform (this principle is outlined in Fig. 3.9). For example, using a trigger skew time $t_s = 10\ \mu s$ means that after an input voltage v(t) crosses the trigger threshold at time $t = 0$, the oscilloscope waits 10 μs before acquiring the waveform with high sampling rate (40 Gs/s).

For a periodic waveform v(t), a large trigger skew t_s means that small frequency shifts Δf_{H} can be observed as apparent phase shifts $\Delta\phi = 2\pi\Delta f_{\mathrm{H}}(t - ts)$ across the oscilloscope's delayed acquisition window. In Fig. 3.9, a periodic waveform v(t) triggers the oscilloscope at time $t = 0$. The oscilloscope then waits a time t_s before sampling a time series which is displayed on its delayed acquisition window (see Fig. 3.9a). The observed waveform is a periodic signal of frequency f_H with a relative initial phase ϕ_o. In Fig. 3.9b, the signal v(t) again triggers the oscilloscope at time $t = 0$, but this time, the frequency of oscillations has shifted to $f_{\mathrm{H}} + \Delta f_{\mathrm{H}}$ with $\Delta f_{\mathrm{H}} << f_{\mathrm{H}}$. At time t_s, the oscilloscope acquisition window displays a waveform with shifted relative phase $\phi_o - \Delta\phi$. Therefore, by using the two data sets from both acquisitions, the frequency shift Δf_{H} can be approximated using the fitting function

$$\mathrm{v}(t) = A\sin[2\pi(f_{\mathrm{H}} + \Delta f_{\mathrm{H}})(t - t_s)], \tag{3.2}$$

where A and Δf_{H} are fitting parameters and f_{H} is known beforehand with high precision (f_{H} is measured prior to this procedure using a long time series). Using

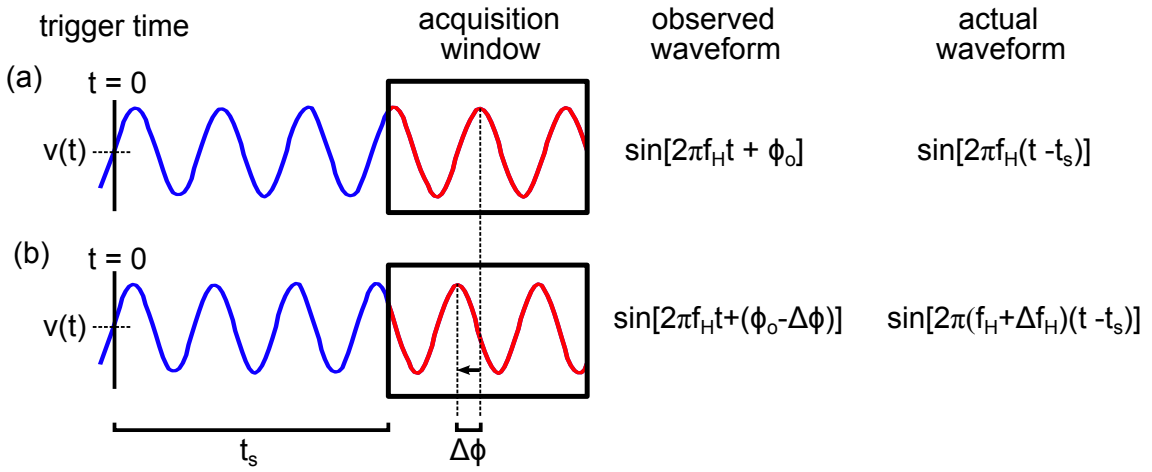

Figure 3.9: **Trigger skew technique for measuring small frequency shifts.** (a) The periodic sine wave v(t) with frequency f_{H} triggers the oscilloscope at the trigger time $t = 0$, which then displays the observed waveform after a trigger skew time t_s in red on the acquisition window. (b) After a small frequency shift Δf_H, the sine wave triggers the oscilloscope and, within the acquisition window, there appears an observed phase shift $\Delta\phi$ that can be used with t_s and f_H recover the value of the frequency shift Δf_H with high precision.

an acquisition window time of only $\Delta t = 50$ ns (which based on the Fourier limit yields $\Delta f = 1/\Delta t = 20$ MHz) and a trigger skew of $t_s = 2.5$ μs, this measurement technique, when combined with averaging multiple waveforms, has shown a potential frequency resolution of $\Delta f = \pm 3$ kHz (see Appendix C). The limiting factor of this frequency resolution is now set by the phase stability of the signal after many oscillations between $t = 0$ and $t = t_s$ rather than the length of the recorded time series.

Thus, the limit of these frequency shift measurements is actually set by the signal Δf_{H} relative to the jitter of the waveform. To further enhance this limit, multiple time series can be averaged together using Eq. (3.1) such that each acquisition of the oscilloscope produces a $\bar{\mathrm{v}}(t)$ with less jitter. The shift Δf_{H} is then determined in the same procedure using a fit of $\bar{\mathrm{v}}(t)$ with Eq. (3.2).

Applying this method with an averaged periodic $\bar{v}(t)$ in the cavity-feedback system, I can track the scatterer with subwavelength precision as it translates along a 1D path. The scatterer is moved from the relative position $x_{\text{rel}} = 0$ mm to $x_{\text{rel}} = 10$ mm in 10 μm steps such that the periodic dynamics remain stable and lead to detectable Δf_{H}. For each position of the scatterer, the amplitude A and frequency shift Δf_{H} are approximated using a fit to the data $\bar{v}(t)$ with Eq. 3.2, an oscilloscope trigger skew $t_s = 10$ μs, and an absolute frequency $f_{\text{H}} \sim 1.35$ GHz (at a frequency of 1.35 GHz, the cavity has a quality factor $Q \sim 130$).

Examples of the experimental shifts and the resulting fits are shown in Figs. 3.10a-b for the scatterer at positions $x_{\text{rel}} = 0$ mm and $x_{\text{rel}} = 1$ mm. In the figures, the time axes begin at time $t = t_s$ and a vertical line is used to mark the apparent phase shift $\Delta\phi$ of the waveform on the acquisition window as the scatterer moves. The parameters of fitted functions also indicate a relative frequency shift between these two scatterer positions of $\Delta f_{\text{H}} \sim -50$ kHz.

Using the fits, the amplitude A and frequency shift Δf_{H} of $\bar{v}(t)$ are calculated over the entire 10 mm range. In Fig. 3.10c, the amplitude A decreases on average with respect to x with a standard deviation $\sigma_A = 2.1$ mV. However, in Fig. 3.10d, the frequency shifts Δf_{H} are monotonic with respect to x, covering a total range of ~ 400 kHz, which demonstrates a fractional shift that is $\Delta f_{\text{H}}/f_{\text{H}} \sim 0.1\%$ of system's original frequency. The high sensitivity and stability of Δf_{H} with respect to x can be observed through successive zooms of the data in Figs. 3.10e-f. In these figures, the smooth characteristic of Δf_H is shown to be preserved between the data points down to a scale of ~ 20 μm. Also, note that though the scatterer's position contains experimental errors from the translation stage accuracy (see Section 2.2.1), these errors do not cause significant measurement errors for the frequency shifts. This conclusion is based on calibration measurements of the system's minimum observ-

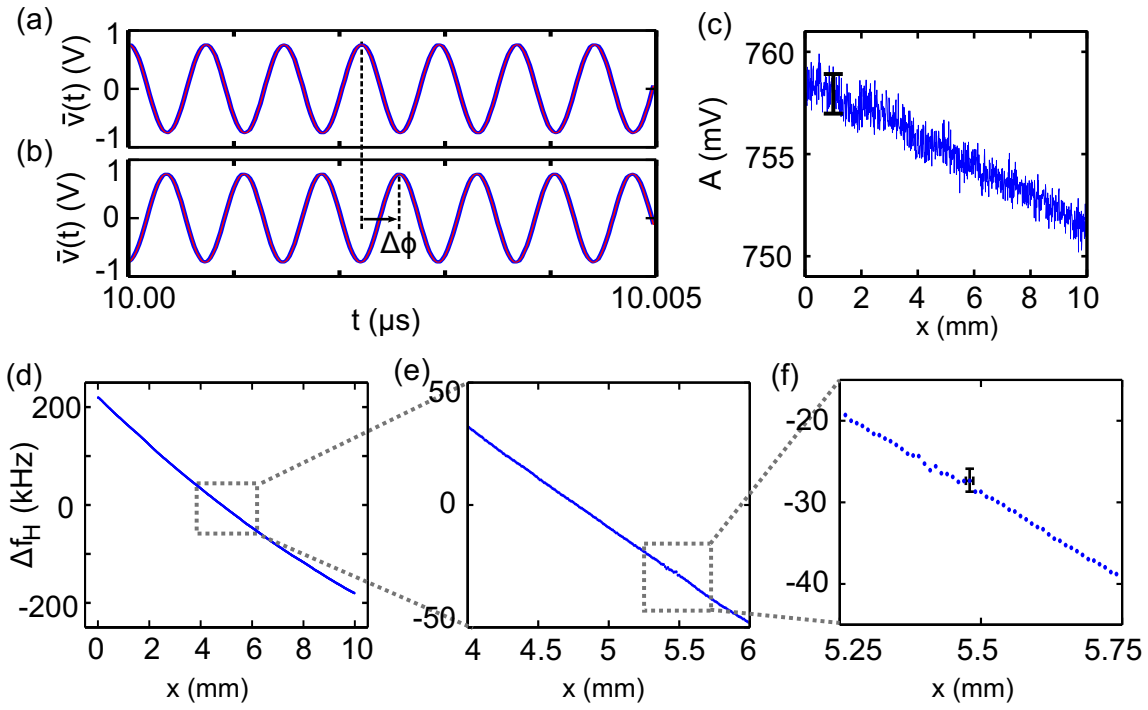

Figure 3.10: **1D sensing with periodic dynamics.** Time series $\bar{v}(t)$ (blue curve) with overlaid fitted function (red curve) at (a) $x_{\text{rel}} = 0$ mm and (b) $x_{\text{rel}} = 1$ mm. The apparent phase shift $\Delta\phi$ (from the large trigger skew $t_s = 10\ \mu$s) on of the time series is marked with dash lines. (c) Amplitude of the periodic signal as a function of x. The error bar indicates the standard deviation $\sigma = 2$ mV of the noise floor of the oscilloscope after 100 averages. (d)-(f) Successive zooms of the frequency shift Δf_H. The mean of the overall shift has been subtracted from (d) for easier relative comparisons. The erorr bars in (f) indicate the frequency measurement error of the fitting method (~ 3 kHz) and the translational stage position error ($\pm 5\ \mu$m).

able frequency shift ~ 3 KHz as well as the experimental drift (temperature and humidity changes) observed in the system (see Appendix B). Thus, the errors associated with experimental drift of the system's parameters over time contribute more significantly than the experimental error associated with the scatter's 2D position.

Though I am measuring two observables A and Δf_{H}, I am only trying to resolve a single piece of information, the position of the scatterer x. Thus, I only need one of my measured observables, and based on the SNR of the frequency shifts when compared to the amplitude shifts, I choose Δf_{H} to track the scatterer. To quantify

the system's resolution for 1D sensing with periodicity, I fit the frequency shifts with the quadratic function

$$\Delta f_{\mathrm{H}} = a_o + a_1 x + a_2 x^2, \tag{3.3}$$

where $a_o = 218.7 \pm 0.9$ kHz, $a_1 = -51.1 \pm 0.9$ kHz mm^{-1}, and $a_2 = 1.1 \pm 0.9$ kHz mm^{-2} (errors represent the 90% confidence intervals of the fits). The fitted function represents a mapping between the observed frequency shifts and the position of the scatterer. Therefore, inverting the map, which is just the solution to the quadratic equation, yields the predicted positions $\hat{x}$ based on the experimental data

$$\hat{x} = \frac{-a_1 - \sqrt{a_1^2 - 4a_2(a_o - \Delta f_{\mathrm{H}})}}{2a_2}, \tag{3.4}$$

where the root-mean-square difference between the actual x values and the predicted $\hat{x}$ is $x_{\mathrm{RMS}} = 10.6$ μm. With frequency $f_{\mathrm{H}} \sim 1.35$ GHz, the wavelength of the EM radiation in the cavity is $\lambda \sim 22.2$ cm; this means that the 1D resolution for imaging the position of the scatterer is $\sim \lambda/20,000$. To help illustrate the performance level of my method, I examine the predicted scatterer positions versus the actual scatterer positions. In Fig. 3.11a, the data is aligned on a near straight line with slope approximately equal to one and with errors that are smaller than the size of the data points (see Fig. 3.11b for a plot of $x - \hat{x}$).

Using periodic dynamics leads to a greater resolution for imaging a 1D position when compared to chaotic dynamics. In addition, the sensing mechanism is much simpler as it requires a single-valued observable (frequency shifts) that can be tracked by a fitting function. Furthermore, this technique utilizes the frequency shift of the entire waveform v(t), even though only a small portion of data is necessary to measure it. In other words, the majority of the information contained in v(t) is being used for imaging. The only discarded information is the changes in

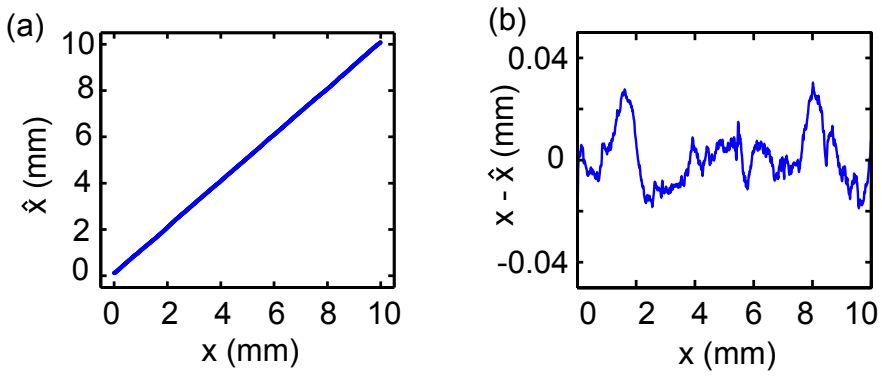

Figure 3.11: **1D predicted positions using periodicity.** (a) Predicted position $\hat{x}$ versus actual position x using the inverted map. (b) Errors $(x - \hat{x})$ of the mapping as a function of x.

the amplitude of oscillations. Based on Fig. 3.10b, the amplitude does shift with scatterer position, but the measured shifts are on the same order of magnitude as the noise floor of the oscilloscope ($\sim$ 2 mV), which (if used) limit the resolution of the system. As a consequence of using only the frequency shifts, the periodic data can only provide one useful observable, and therefore it is limited to 1D sensing.

In order to eventually resolve the scatterer's position in more than one dimension with vastly subwavelength resolution, additional independent observables must be extracted from v(t). Based on the success of using a single frequency shift for 1D sensing, in the next subsection, I consider a quasiperiodic signal, which contains two main frequency components (f_T, f_H), as a candidate to perform 2D subwavelength position sensing.

3.4.3 Sensing with Quasiperiodic Dynamics

To go beyond the 1D periodic sensing, I tune v_b so that v(t) is in a quasiperiodic dynamical state for a 2D area (5 mm $\times$ 5 mm) of scatterer positions. Example time series, frequency spectra, and phase space projections of the quasiperiodicity for a

fixed 2D object position (x, y) are shown in Figs. 3.12a-c, where the quasiperiodic signal is typical from a torus bifurcation; the fast oscillations in $\mathrm{v}(t)$ are modulated with a slow-varying, time-evolving amplitude (note that the SNR of this signal is a factor of 10 times greater than the SNR of $r_{\mathrm{out}}(t)$ in Ch. 2 used for 1D sensing). As shown by the PSD, for this particular set of parameters and initial relative placement of the scatterer ($x_{\mathrm{rel}} = 0$ mm, $y_{\mathrm{rel}} = 0$ mm), the frequencies from the Hopf and torus bifurcations are $f_{\mathrm{H}} \sim 1.57$ GHz and $f_{\mathrm{T}} \sim 0.21$ GHz, respectively. The mixed harmonics of these frequencies are $(f_{\mathrm{H}} - f_{\mathrm{T}}) \sim 1.36$ GHz and $(f_{\mathrm{H}} + f_{\mathrm{H}}) \sim 1.77$ GHz. At a frequency of 1.77 GHz (the highest frequency in the quasiperiodic oscillations), the cavity has a quality factor $Q \sim 170$. Furthermore, based on the time-scale separation of f_{H} and f_{T}, the torus shape of the attractor is conveniently visualized in the phase space projection $(\mathrm{v}(t), \mathrm{v}(t - T_L))$.

In this subsection, I will show that the incommensurate frequencies f_{H} and f_{T} can shift independently with respect to 2D scatterer translations. Imaging the scatterer's position entails measuring shifts $(\Delta f_{\mathrm{H}}, \Delta f_{\mathrm{T}})$ in these quasiperiodic frequency components. In this quasiperiodic mode-of-operation, I first demonstrate the capabilities of the system for 1D sensing, which can be compared to the previous results for periodic and chaos-based sensing. Then, moving beyond 1D position sensing, I use a new mapping technique to resolve the scatterer in 2D with subwavelength resolution.

Similar to the periodic sensing, to follow changes in the frequencies of $\mathrm{v}(t)$ with high precision, I use a large t_s for triggering the oscilloscope, and I also use its averaging feature to increase the SNR using multiple waveforms. In addition, in order to average over quasiperiodic waveforms, the trigger height $\mathrm{v}_{\mathrm{trigger}}$ must also be tuned to trigger only on the maxima of largest amplitudes. These maxima correspond to regions of the quasiperiodic signal where the independent, incommensurate fre-

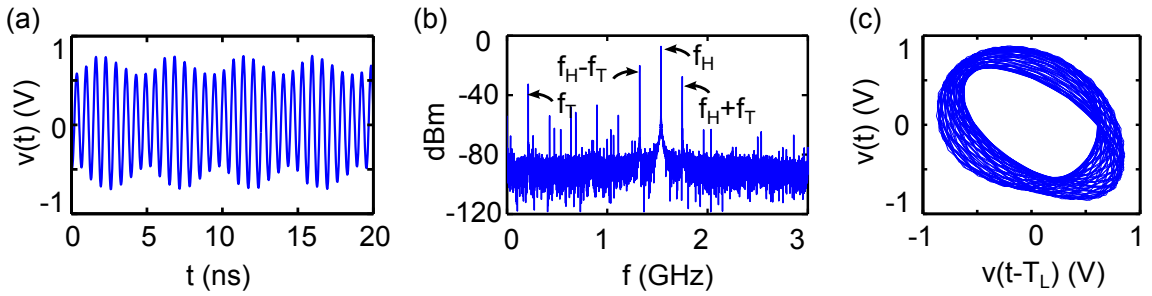

Figure 3.12: **Quasiperodic dynamics used for imaging.** (a) Temporal evolution v(t) of a typical quasiperiodic state used for position sensing. In the time series, the signal-to-noise ratio is $\mathrm{RMS_S/RMS_N} \sim 150$, where $\mathrm{RMS_S}$ ($\mathrm{RMS_N}$) is the root-mean-square of the signal (noise) (b) Power spectral density (PSD) of this signal with Hopf and torus frequencies labeled f_H and f_T, respectively, as well as the harmonics $f_H \pm f_T$ (c) Phase space projection with time lag $T_L = 1.55$ ns.

quencies add constructively and can be used as reference points for averaging multiple, successively triggered waveforms (in contrast, if $\mathrm{v_{trigger}} = 0$ V, the non-periodic nature of the quasiperiodic signal will cause the averaged waveforms to collapse to zero).

With the averaged data from the delayed acquisition window of the oscilloscope, I approximate the shifts to the system's frequencies using a nonlinear least-squares-regression to a model for a four-tone quasiperiodic signal [67]

$$\bar{\mathrm{v}}(t) = \sum_{i=1}^{i=4} A_i \sin[2\pi(f_i + \Delta f_i)(t - t_s)], \tag{3.5}$$

where $t_s = 2.5$ μs, $f_1 = f_\mathrm{T}$, $f_2 = (f_\mathrm{H} - f_\mathrm{T})$, $f_3 = f_\mathrm{H}$, and $f_4 = (f_\mathrm{H} + f_\mathrm{T})$, and where A_i and Δf_i are free fitting parameters. Two examples are shown in Figs. 3.13a-b, where $\bar{\mathrm{v}}(t)$ is acquired and fitted at relative scatterer positions $x_\mathrm{rel} = 0$ mm and $x_\mathrm{rel} = 2$ mm for a constant relative position in the y direction. In the figure, a phase shift $\Delta\phi$ marks the relative shift in the amplitude-modulation phase. In the experiment, the phase shift associated with the fast carrier frequency is difficult to see

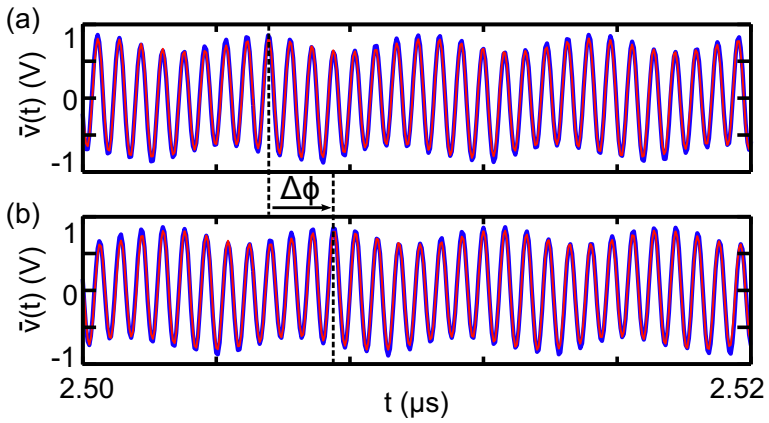

Figure 3.13: **Fitted quasiperodic dynamics** on the delayed acquisition window of the oscilloscope with trigger skew $t_s = 2.5$ μs. The averaged signals $\bar{v}(t)$ (blue curves) and fitted function (red curves) for scatterer positions (a) $x_{\text{rel}} = 0$ mm and (b) $x_{\text{rel}} = 2$ mm. The phase shift of the amplitude modulation is marked by $\Delta\phi$.

by eye but it is still captured with the fits. For a calibrated waveform with known frequency shifts, this technique yields a ±3 kHz frequency resolution, which is approximately 0.5% of the total observed experimental frequency shifts (see Appendix C).

1D Sensing

To demonstrate 1D position sensing, I translate the object along the path $x_{\text{rel}} = 0$ mm - 5 mm while $y_{\text{rel}} = 2.5$ mm. I then translate the object along an orthogonal path $y_{\text{rel}} = 0$ - 5 mm while $x_{\text{rel}} = 2.5$ mm. All translations are made in 0.5 mm steps. Shown in Figs. 3.14a-b, the measured frequency shifts Δf_{H}, Δf_{T}, $\Delta(f_{\text{H}} - f_{\text{T}})$, and $\Delta(f_{\text{H}} + f_{\text{T}})$ are plotted for the 1D paths along the orthogonal x and y directions, respectively. Similar to the periodic case, along each of the paths, the quasiperiodic frequencies shift monotonically. In addition, for the x and y directions, they shift by different amounts and at different rates. Recall that the position errors of the motor do not cause significant errors in the frequency shift measurements when compared

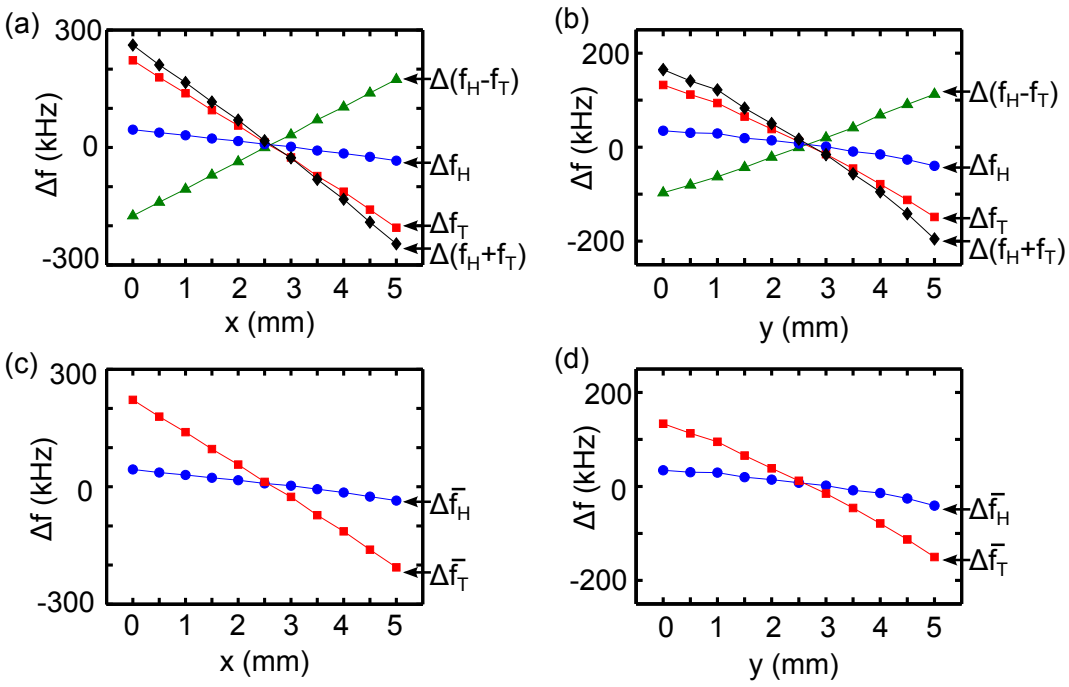

Figure 3.14: 1D sensing with quasiperiodicity. Frequency shifts $\Delta f_{\rm T}$ (red squares), $\Delta(f_{\rm H}-f_{\rm T})$ (green triangles), $\Delta f_{\rm H}$ (blue circles), and $\Delta(f_{\rm H}+f_{\rm T})$ (black diamonds) as a function of scatterer position in the (a) x and (b) y directions. The mean of each frequency shift is removed for easier comparison. Averaged frequency shifts $\Delta\bar{f}_{\rm T}$ (red squares) and $\Delta\bar{f}_{\rm H}$ (blue circles) as a function of (c) x direction, where the fit from Eq. (3.8) yields $a_1 = 2.8$ mm/kHz, $a_2 = -8.7$ mm/kHz, $c_0 = 27{,}113.0$ mm, $c_1 = -439.2$ and $c_2 = 1.5$ mm^{-1}, and (d) along the y direction, where the fit from Eq. (3.9) yields $b_1 = 0.8$ mm/kHz, $b_2 = -0.5$ mm/kHz, $d_0 = -73{,}452.0$ mm, $d_1 = 242.0$, and $d_2 = -2.0$ mm^{-1}. The error in the measurement of each frequency is ~ 3 kHz, which is smaller than the size of the data points.

to the experimental drift of the system.

Before using these dynamical changes to establish a 1D map, I first combine the frequency shift data from the harmonics $\Delta(f_{\rm T}\pm f_{\rm H})$ with the primary modes $\Delta f_{\rm H}$ and $\Delta f_{\rm T}$. These additional measures lead to new observables $\Delta\bar{f}_{\rm T}$ and $\Delta\bar{f}_{\rm H}$ with reduced statistical errors and increased SNR. The new observables are given respectively by

$$\Delta\bar{f}_{\rm T} = \frac{1}{3}[\Delta(f_{\rm H}-f_{\rm T}) - \Delta(f_{\rm H}+f_{\rm T}) + \Delta f_{\rm T}], \tag{3.6}$$

and

$$\Delta\bar{f}_{\mathrm{H}} = \frac{1}{3}[\Delta(f_{\mathrm{H}} - f_{\mathrm{T}}) + \Delta(f_{\mathrm{H}} + f_{\mathrm{T}}) + \Delta f_{\mathrm{H}}]. \tag{3.7}$$

The frequency shifts $\Delta\bar{f}_{\mathrm{T}}$ and $\Delta\bar{f}_{\mathrm{H}}$ are used in the quasiperiodic imaging mode-of-operation.

To create the mapping between these spectral shifts and 1D positions, I separately fit $\Delta\bar{f}_{\mathrm{T}}$ and $\Delta\bar{f}_{\mathrm{H}}$ in the x and y directions with second order polynomials

$$a_1\Delta\bar{f}_{\mathrm{T}}(x) + a_2\Delta\bar{f}_{\mathrm{H}}(x) = c_0 + c_1 x + c_2 x^2, \tag{3.8}$$

$$b_1\Delta\bar{f}_{\mathrm{T}}(y) + b_2\Delta\bar{f}_{\mathrm{H}}(y) = d_0 + d_1 y + d_2 y^2, \tag{3.9}$$

where $\Delta\bar{f}_{\mathrm{T}}(x)$ and $\Delta\bar{f}_{\mathrm{H}}(x)$ refer to the observed shifts in the x direction and $\Delta\bar{f}_{\mathrm{T}}(y)$ and $\Delta\bar{f}_{\mathrm{H}}(y)$ refer to the shifts in the y direction. I optimize the coefficients a_i and c_i (b_i and d_i) using a nonlinear least-squares-fit to a model for the scatterer position. As a result, the root-mean-square (RMS) errors for the frequency shift map is 1.45 kHz (0.86 kHz) along x (y) direction. By inverting these maps, I calculate the predicted object positions $\hat{x}$ and $\hat{y}$, and I plot the predicted versus actual positions in Figs. 3.15a,c with the errors in Figs. 3.15b,d. The resulting RMS error between the actual and predicted positions is 9.2 μm (23.7 μm) for x (y). This demonstrates resolutions of $\lambda/16,000$ and $\lambda/6,000$ for the orthogonal x and y directions, respectively ($\lambda_{\mathrm{min}} \sim 15$ cm for the maximum possible frequency in the system $f_{\mathrm{max}} =$ 2 GHz). Thus, the average 2D resolution is $\sim \lambda/10,000$.

Thus, similar to the periodic sensing technique, the quasiperiodic signal v(t) demonstrates a vastly subwavelength sensitivity to the scatterer's position. However, in this case, the 1D resolution for imaging the y position is slightly degraded. This could be a product of several different factors. For example, the experimental

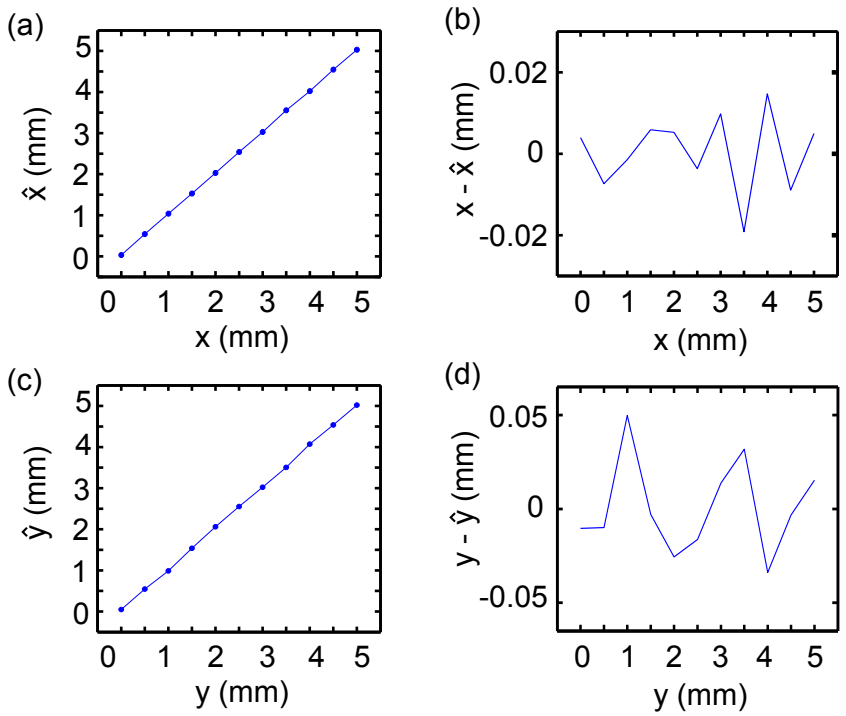

Figure 3.15: 1D predicted positions using quasiperiodicity. (a) Predicted position $\hat{x}$ versus actual position x using the inverted map. (b) Errors of the $\hat{x}$ mapping as a function of x. (c) Predicted position $\hat{y}$ versus actual position y using the inverted map. (d) Errors of the $\hat{y}$ mapping as a function of y.

parameters necessary for quasiperiodicity may not be as sensitive to changes in the y direction. Regardless of its slightly degraded y resolution, I am primarily interested in the quasiperiodic signal for its potential to sense position information in 2D. Using the same measurement techniques from the 1D case, I now consider the scatterer translations in both the x and y directions simultaneously.

2D Sensing

Imaging the scatterer's position in both the x and y directions simultaneously requires two independently changing observables. In the quasiperiodic case, these are f_{T} and f_{H}. In the cavity-feedback system, I measured the averaged frequency shifts

$\Delta\bar{f}_{\mathrm{T}}(x,y)$ and $\Delta\bar{f}_{\mathrm{H}}(x,y)$ which are now multivariate functions of $(x,\ y)$. I measure these frequency shifts along a 2D grid in the 5 mm $\times$ 5 mm sensing area. Recall that for each position of the scatterer along the 2D calibration grid, the translation stages use the backlash correction to minimize the positioning errors. This backlash correction is also present during the test path of the scatterer within the calibration grid. At each programmed position of the scatterer along the test path, the translations stages pivot before coming to a rest. Once at rest, the frequency shifts of the system are measured. The resulting data is shown in Fig. 3.15, where the frequency shifts are now represented as surfaces in 3D plots. To recover the scatterer position, it remains to determine if exists an invertible mapping for $(\Delta\bar{f}_{\mathrm{T}}(x,y),\ \Delta\bar{f}_{\mathrm{H}}(x,y))$.

Because the observed frequency shifts are small and near planar, I fit them in the 5 mm $\times$ 5 mm area with plane equations

$$\Delta\bar{f}_{\mathrm{T}}(x,y) = \alpha_1 x + \beta_1 y + \epsilon_1, \tag{3.10}$$

$$\Delta\bar{f}_{\mathrm{H}}(x,y) = \alpha_2 x + \beta_2 y + \epsilon_2. \tag{3.11}$$

To check for an invertible map, it suffices to show that the fitted $\Delta\bar{f}_{\mathrm{T}}(x,y)$ and $\Delta\bar{f}_{\mathrm{H}}(x,y)$ are linearly independent. Thus, using Cramer's rule, if the determinant $|\alpha_1\beta_2 - \alpha_2\beta_1| \neq 0$, then the planes are linearly independent in this area and can allow us to simultaneously measure x and y coordinates [68]. The planar fits from Eqs. (3.10) and (3.11) yield $\alpha_1 = -84.68$ kHz/mm, $\alpha_2 = -15.20$ kHz/mm, $\beta_1 = -56.74$ kHz/mm, $\beta_2 = -14.75$ kHz/mm, $\epsilon_1 = 11.72$ MHz and $\epsilon_2 = 2.43$ MHz. The measured determinant $|\alpha_1\beta_2 - \alpha_2\beta_1| = 386$ kHz^2/mm^2 with an error of 5.8 kHz^2/mm^2. Thus, the planar-like frequency shifts are approximately linearly independent.

It remains to create the mapping: $(\Delta\bar{f}_{\mathrm{T}}(x,y),\ \Delta\bar{f}_{\mathrm{H}}(x,y)) \longleftrightarrow (x,y)$. In the 1D

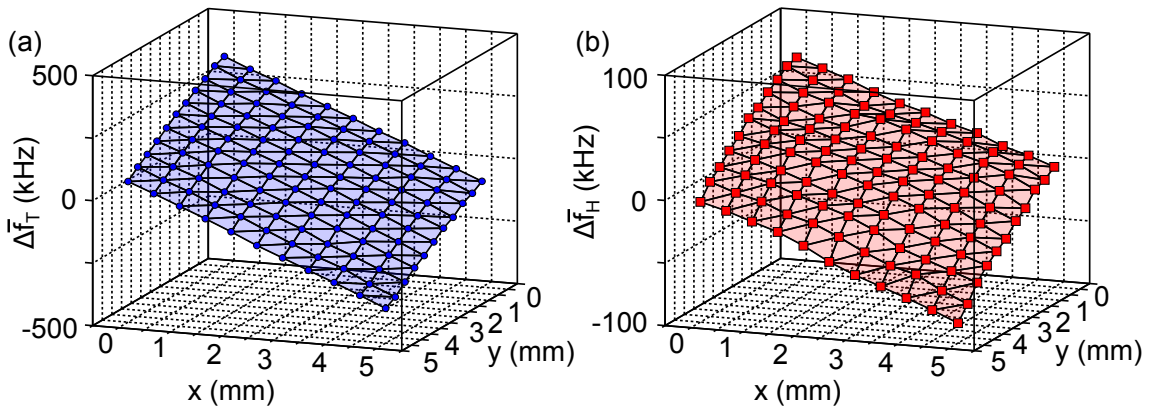

Figure 3.16: **2D sensing with quasiperiodicity.** Frequency shifts (a) $\Delta\bar{f}_T$ and (b) $\Delta\bar{f}_H$ as a function of scatterer locations (x, y) in a 5 mm × 5 mm grid of positions. The mean of each of the frequency shifts has been subtracted for easier comparison.

case, I have the freedom to optimize the fitting parameters in Eqs. (3.8) and (3.9) for x and y separately. In the 2-D case, all of the fitting parameters α_i, β_i, and ϵ_i in Eqs. (3.10) and (3.11) are present in the solutions for both x and y. Thus, I cannot optimize the fits in the x and y directions separately and instead I use these fitted planes as the initial 2D mapping for imaging the position of the scatterer. This constraint, combined with the system's fluctuations and approximation that these surfaces are planar, limits the 2D resolution. The planar fit of $\Delta\bar{f}_T(x, y)$ ($\Delta\bar{f}_H(x, y)$) gives a RMS frequency error of 4.17 kHz (7.26 kHz).

Using the inverted equations of the planes in Eqs. (3.10) - (3.11), the continuous mapping for an arbitrary position (x, y) is represented as

$$\hat{x} = \frac{(\Delta\bar{f}_T(x,y) - \epsilon_1)\beta_2 - (\Delta\bar{f}_H(x,y) - \epsilon_2)\beta_1}{\alpha_1\beta_2 - \alpha_2\beta_1}, \tag{3.12}$$

$$\hat{y} = \frac{(\Delta\bar{f}_H(x,y) - \epsilon_2)\alpha_1 - (\Delta\bar{f}_T(x,y) - \epsilon_1)\alpha_1}{\alpha_1\beta_2 - \alpha_2\beta_1}. \tag{3.13}$$

Using these equations, I first calculate the errors associated with the calibration grid.

As an example of the reconstructed calibration grid using the planar mapping, see Fig. 3.17a.

In the figure, the reconstructed calibration grid is distorted such that the recovered x and y positions do not necessarily lie on the grid. To quantify these distortions, I measure two different quantities. First, the reconstructed grid path shows RMS position error of 340 μm (620 μm) for x (y), yielding an average 2D resolution of $\sim \lambda/300$. As an additional figure of merit, the maximum errors $(x_{\max}, y_{\max})$ observed in the 2D calibration grid are $x_{\max} = 0.72$ mm and ($\sim \lambda/200$) $y_{\max} = 1.22$ mm ($\sim \lambda/120$)). Again, these errors in the reconstruction of the calibration grid are vastly subwavelength. However, because the calibration grid is distorted, all position sensing measurements will also suffer from similar distortions. Before moving on to such position sensing measurements, I first discuss and rule out the sources of the errors (distortions) in the calibration grid path.

Due to the micron precision of these measurements, it is important to verify that the experimental errors in the reconstructed calibration grid path are not due to inaccurate scatterer positioning (it was hypothesized that the glue that holds the scatterer to the translation stage may stretch and the scatterer may not be positioned correctly with respect to the translation stage to which it is attached). Thus, the correlation of the scatterer displacement with respect to the programmed translation stage position is quantified using an additional experiment described in Appendix B. In this appendix, the relative scatterer displacement is directly measured using a dial drop indicator that contacts the scatterer itself. Using several different measurements, I quantify that the errors associated with the scatterer position is approximately 10 μm. This is on the same order of magnitude as the errors associated with the translation stages and is orders of magnitude smaller than the observed RMS and maximum errors. Therefore, the scatterer positioning errors (and transla-

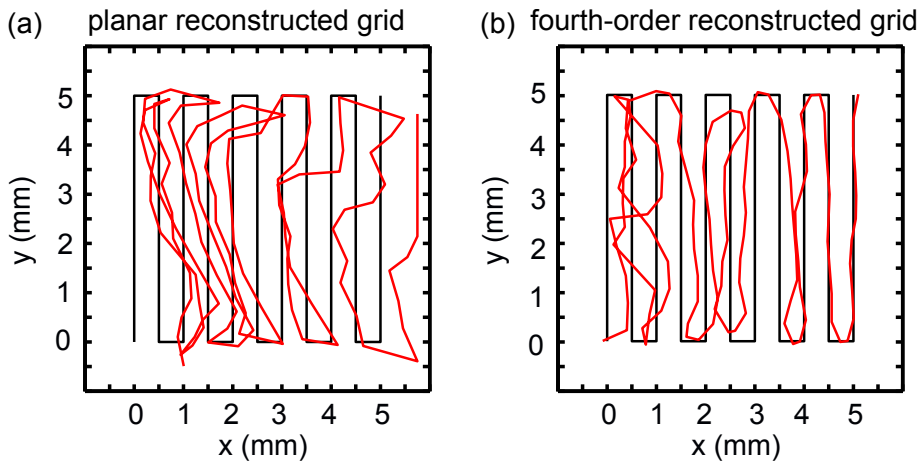

Figure 3.17: **Reconstructed calibration grids** (a) using a planar mapping and (b) a fourth-order mapping between frequency shifts $(\Delta\bar{f}_{\mathrm{T}}, \Delta\bar{f}_{\mathrm{H}})$ and the scatterer position (x, y). The reconstructed grids are shown in red and the actual path used for the calibration grid is shown in black.

tion stage errors) do not play a large role in the experimental distortions observed in the reconstructed grid path. Rather, the approximation that the frequency shifts are planar as well as the frequency fluctuations and drift (also, see Appendix B) are the main sources of error in the reconstruction of the calibration grid path for the cavity-feedback system.

Lastly, I quantify an average dynamic range for sensing within calibration grid to be ~ 10 (5 mm/ 0.5 mm). This dynamic range is a lower bound on the potential dynamic range of the system because the measurements are confined to a 2D area. However, because quasiperiodicity can exist for a larger range of object positions (without bifurcating to periodicity or chaos), the upper bound of the system's dynamic range has the potential to be larger. For example, in separate experiments, I have verified that quasiperiodicity can exist in over 1 cm distances in both the x and y directions. This shows that there is a potential for the dynamics range to be $20 \sim$ 10 mm / 0.5 mm assuming that the position errors remain the same over this larger

area. But, based on the bifurcation diagram, it is clear that, for certain parameter values, the system can bifurcate from quasiperiodicity to chaos in less than in 1 cm. In order to try to find the true upper bound of this experimental system, multiple bifurcation diagrams must be collected in both the x and y directions for different bias voltages of the nonlinear circuit input and different gain values for the feedback loop to determine the largest and most sensitive windows of quasiperiodicity. Thus, as a future direction of research (not explored here), it is of interest to determine the upper bound on the dynamics range for a given cavity (see Ch. 7).

To test the system's 2D sensing mode-of-operation, I use the frequency shifts in Figs. 3.16a-b as a calibration grid for the scatterer's shape and orientation at each position in the 5 mm × 5 mm area. In the next and last subsection, the scatterer is now moved through an arbitrary path in this 2D area, and I use the calibration grid to reconstruct its movements with subwavelength resolution.

Sensing the position of the object along an arbitrary path

In the 2D area, the scatterer is moved through the discrete positions (x_n, y_n) for $n = 1$ to $n = 32$, where only the starting position (x_1, y_1) lies on the calibration grid from the previous section and serves as a reference point for the relative frequency shifts. The path is plotted along with the calibration grid points in Fig. 3.18c. The goal of this test is to then measure the frequency shifts $(\Delta\bar{f}_{\mathrm{T}}(x_n, y_n), \Delta\bar{f}_{\mathrm{H}}(x_n, y_n))$ and use the 2D mapping of the calibration grid to reconstruct the successive scatterer positions. As shown in Figs. 3.18a-b, the observed frequency shifts along this arbitrary path are plotted as a function of the index n. In the figures, the frequency shifts $\Delta\bar{f}_{\mathrm{T}}(x_n, y_n)$ and $\Delta\bar{f}_{\mathrm{H}}(x_n, y_n)$ range over ±300 kHz and ±50 kHz, respectively, and neither data set shows monotonic changes with increasing n.

To recover the positions (x_n, y_n), I use two different procedures. The first uses

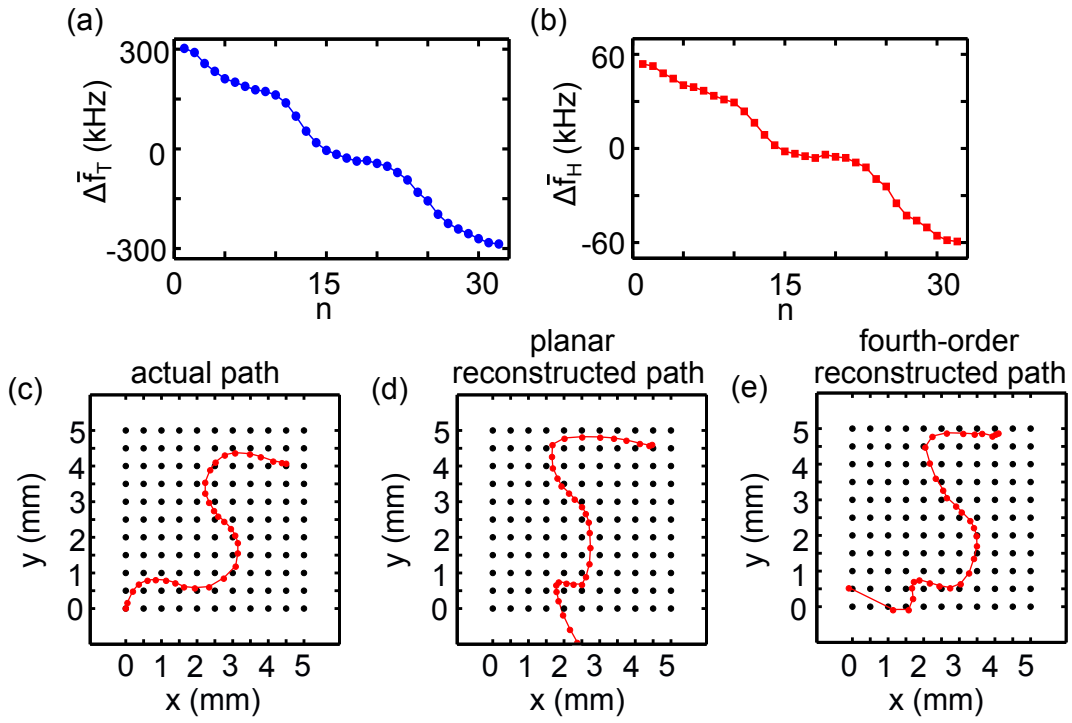

Figure 3.18: **2D predicted positions using quasiperiodicity.** Frequency shifts (a) $\Delta\bar{f}_T$ and (b) $\Delta\bar{f}_H$ as a function of n different scatterer positions along (c) the 2D arbitrary path (red curve) within the calibrated grid (black dots). Using the calibrated grid and the measured frequency shifts, the scatterer path is reconstructed using (d) a planar first-order map and (e) a fourth-order map (red curves).

the planar mapping of the calibration frequency-shift surfaces to interpolate the scatter locations. These inverted equations yield a predicted path of the scatterer $(\hat{x}_n, \hat{y}_n)$, as shown in Fig. 3.18d. The RMS errors between the predicted and actual x and y positions are 550 μm and 850 μm, respectively (on average, $\sim \lambda/300$). In addition, the maximum observed errors are $x_{\max} = 0.75$ mm and ($\sim \lambda/200$) $y_{\max} = 2.11$ mm ($\sim \lambda/70$). Thus, the resolution of reconstructing the scatter's position with the planar mapping is degraded when compared to the resolution of the calibration grid. This most likely means that errors in the planar map are compounded by the calibration and reconstruction procedure.

Furthermore, this implies that the resolution may be improved using higher or-

der mappings. As just one example, I fit the calibration data with fourth-order 2D frequency shift maps

$$\Delta\bar{f}_{\mathrm{T}}(x,y) = \sum_{i=1}^{i=4}\left(a_i x^i + b_i y^i\right) + \sum_{j=0}^{j=3}\sum_{k=0}^{k=3} A_{j,k} x^j y^k, \tag{3.14}$$

$$\Delta\bar{f}_{\mathrm{H}}(x,y) = \sum_{i=1}^{i=4}\left(c_i x^i + d_i y^i\right) + \sum_{j=0}^{j=3}\sum_{k=0}^{k=3} B_{j,k} x^j y^k, \tag{3.15}$$

where a_i, b_i, c_i, d_i, $A_{j,k}$, and $B_{j,k}$ are all free fitting parameters, and the values of the fitted coefficients are listed in Appendix B. Such an increase to the map's complexity means that the frequency to position mapping is no longer analytically invertible. Consequently, the predicted values $\hat{x}$ and $\hat{y}$ must be solved numerically.

The resulting fourth-order map yields RMS differences between the predicted and actual x and y values of 200 μm and 350 μm, respectively ($\sim \lambda/650$) along the 2D calibration grid. Using this mapping, the reconstructed calibration grid is plotted in Fig. 3.17b. In the figure, there is a visible improvement over the reconstruction of the calibration grid path shown in Fig. 3.17a. In addition, using the fourth-order mappings, the maximum observed errors $(x_{\max}, y_{\max})$ in the 2D calibration grid are $x_{\max} = 0.60$ mm and ($\sim \lambda/250$) $y_{\max} = 1.12$ mm ($\sim \lambda/130$). Thus, when using a high-order fitting function, $(\mathrm{RMS_x}, \mathrm{RMS_y}, x_{\max}, y_{\max})$ is imporved by $\sim (41\%, 51\%, 16\%, 8\%)$, respectively, where the percent improvement is defined as the ratio in the decrease of the resolution relative to the original resolution using the planar mapping. These percentages are representative of the amount of distortions that are caused by the approximating the frequency shifts as planes. The remaining errors are most likely caused by drift in the frequency shifts and noise in the electronics of the system.

In addition, the reconstruction of the scatterer's path shows improvement in

Fig. 3.18e with lower RMS errors of 600 μm and 410 μm for the x and y positions, respectively ($\sim \lambda/400$) and maximum observed errors $x_{\max} = 0.80$ mm and ($\sim \lambda/190$) $y_{\max} = 1.38$ mm ($\sim \lambda/110$). These represent $\sim (0\%, 51\%, 0\%, 35\%)$ improvements for $(\mathrm{RMS_x}, \mathrm{RMS_y}, x_{\max}, y_{\max})$, respectively. Interestingly, the errors do not decrease in the x direction. This is most likely due to the shifts in the y direction contain the most deviation from a planar surface. Thus, overall, my attempt to increase the system's resolution using a fourth-order mapping yields improved 2D resolving capabilities. I have verified that further increasing the complexity of the mapping does not significantly reduce the errors of the reconstructed path. And thus it must be drifts due to temperature/pressure of the enclose air and noise in the detection system that limits the resolution of my imaging system. This concludes the proof-of-concept tests using the cavity-feedback system for imaging the position of the subwavelength scatterer.

3.5 Summary

In summary, this chapter demonstrates a new position-sensing system that combines time-delayed nonlinear feedback and a wave-chaotic cavity. For different parameters of the cavity-feedback system, the observed EM oscillations can range from simple periodicity to broadband chaos. Specifically, the dynamics of the system depend on small changes to the time delays and attenuation in its feedback, which are manifested through scatterer translations in the cavity.

Through various experimental tests, I demonstrate techniques for exploiting these changes to image the position of the scatterer with subwavelength resolution. More specifically, chaos-based sensing shows a 1D resolution of $\lambda/3,000$, periodic-based sensing shows a 1D resolution of $\lambda/20,000$, and quasiperiodic-based sensing

shows an average 1D resolution of $\sim \lambda/10,000$ and an average 2D resolution of $\sim \lambda/300$. For comparison, a scanning near-field microwave microscope uses RF frequencies from a stable source to achieve subwavelength sensitivity ($\sim \lambda/750{,}000$) of near planar surfaces [69]. In contrast, my system uses nonlinear feedback to internally generate multiple independent frequencies and measures multiple degrees-of-freedom. Moreover, my method uses a stationary pair of antennas to extract 2D spatial information of a 3D scatterer, making it free of mechanically-moving parts.

Due to the cavity's height, there are no allowable TM modes in the cavity for frequencies less than 2 GHz. Based on the low-pass filtering at the output of the external nonlinear feedback loop, no EM radiation at frequencies above 2 GHz enter into the cavity. Thus, EM radiation propagates in the cavity transversely and only interacts with the scatterer from the x and y directions (as opposed to the vertical z direction). This is the configuration chosen in other quarter-stadium systems in order to evaluate the quasi-2D behavior of the scattering system [49]. Based on the height restriction of the cavity and low-pass filtering of the injected waves, the EM fields in the cavity are polarized such that only TE modes propagate. However, the experiments shown throughout this chapter to do not demonstrate that TE modes are necessary to observe subwavelength changes in the cavity. Because I have not fully characterized the polarization of my antennas, I can only conclude that, given the setup shown here, these experiments are sufficient for observing subwavelength changes. As discussed in Ch. 2, 3D structures can show wave chaos and include both TE and TM modes. Thus, as a future direction, one can explore the sensitivity of subwavelength changes depending on the polarization of the injected EM radiation (see Ch. 7).

This work also extends the Larsen effect, a phenomenon where positive audio-feedback between a microphone and audio amplifier results in periodic acoustic

oscillations [70]. The frequency of oscillation, known as the Larsen frequency, is highly dependent on the propagation paths of the acoustic wave. A perturbation to these propagation paths shifts the Larsen frequency [70]. Using a quasiperiodic analog of the Larsen effect, I combine a nonlinear feedback oscillator with multiple EM reflections in a scattering environment to exploit the inherent sensitivity of the system. To the best of my knowledge, this approach is the first to measure multiple spatial degrees of freedom on a subwavelength scale using a scalar signal. It also demonstrates the first application of a quasiperiodic signal for sensing purposes, adding an alternative to the short list of subwavelength imaging techniques.

To optimize the system, I see several options to improve the system's resolution. Currently, resolution limitations are based on the SNR of v(t). Increasing the number of frequency harmonics through nonlinear mixing gives additional measures of the independent modes and improves the system's SNR. Also, because the cavity Q is proportional to the number of interactions between the subwavelength object and the EM energy inside of the cavity, the resolution of this technique should also scale with Q.

This system could find applications beyond position sensing. For example, the scattering and absorption of a subwavelength object strongly depend on its geometry, and this approach, which is sensitive to the shape, orientation, and characteristics of the scatterer, can most likely quantitatively track these properties. Also, similar to [70], analyzing dynamical states can monitor changes in the EM properties of materials in the cavity.

Lastly, I also conjecture that this method can be implemented using EM waves in the optical domain. Semiconductor lasers with time-delayed optical feedback are known to display complex dynamical behaviors in which the output intensity varies in time, including quasiperiodicity [71–73]. Furthermore, optical wave-chaos has

been demonstrated using optical cavities [48, 74]. Therefore, I envision a completely optical version of this technique where a laser receives feedback from a wave-chaotic optical cavity. Such a system will be capable of imaging the position of a scatterer on a 2D nanometer scale. Preliminary tests of an optical system are presented in Ch. 7.

Based on the results of this chapter, there are many different topics for future investigations. For example, chaos-based or periodic-based sensing could be further developed and optimized using well-known extremely broadband [35] or extremely narrow-band [75] nonlinear opto-electronic oscillators in a wave-chaotic cavity, respectively. Moreover, other configurations of the cavity itself could be studied: Does the level of wave chaos, allowable bandwidth, or antenna placement affect the dynamics/resolution? All of these questions are all valid and worthy of investigation. However, due to the novelty of the quasiperiodic sensing technique, I choose to focus the remaining chapters of this dissertation on the quasiperiodic dynamics in the current configuration of the cavity-feedback system to further the development of a general theory for quasiperiodic sensing in band-pass filtered, time-delayed nonlinear feedback systems.

Chapter 4

Modeling the Cavity-Feedback System

In this chapter, I derive a mathematical model for the cavity-feedback system that reproduces qualitatively similar quasiperiodic dynamics in comparison to experimental observations. The quasiperiodic behavior is an essential component of the two-dimensional, subwavelength position-sensing modality. The modeling of the cavity-feedback system is divided into three main sections: (i) a detailed characterization and modeling of the nonlinear circuit (NLC), (ii) a representation of the wave-chaotic cavity in terms of a delay-gain distribution, and (iii) a full model that combines (i) and (ii) and generates the quasiperiodic dynamics. The goal of this chapter is to demonstrate that the cavity-feedback system, which uses both time-delayed nonlinear feedback and a wave-chaotic cavity, can be represented by a simple theoretical model. This model serves as a method of prediction for the observed experimental phenomena and provides further evidence for the interpretations of the cavity-feedback system in both past and future chapters.

The results for modeling the nonlinear circuit in this chapter are an extension of the model created by Zheng Gao, who designed the specific transistor-based circuit featured in this dissertation. Rather than model the NLC as an RLC circuit (Zheng Gao's model, see Appendix A), I take a different approach for modeling using a combination of a nonlinear function and ideal filters. These results are also a continuation of the simple model from Ch. 2 for the original circuit design from Ref. [22] (see Appendix A for the details of these differences). My model for the wave-chaotic cavity and the cavity-feedback system also benefited from discussions with Daniel Gauthier and Damien Rontani. The experimental procedure for acquiring the

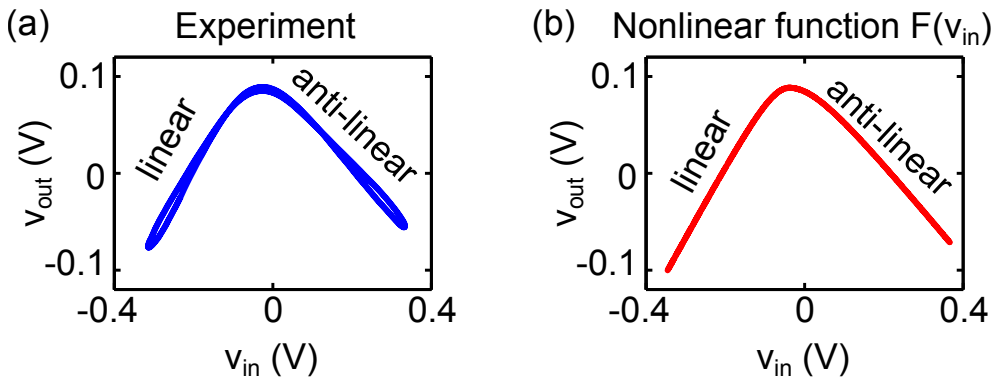

Figure 4.1: **Review of circuit operation.** (a) Input-output characteristics of the experimental circuit measured at a driving frequency $f = 270$ MHz with $v_b = 0.7$ V and with its linear and anti-linear regimes labeled accordingly. (b) Functional fit of the experimental data using the nonlinear function $F(v_{in}) = v_o - \sqrt{A^2(v_{in}+v_b-v_T)^2) - a_o^2}$, where $A = A_L$ (slope of the linear regime), if $(v_{in}+v_b) \leq v_T$, and $A = A_R$ (the slope of the anti-linear regime) if $(v_{in}+v_b) > v_T$.

pulse responses of the cavity was also designed with the help of Hugo Cavalcante.

4.1 Modeling the Nonlinear Circuit

The nonlinear circuit (NLC), which contains a transistor and other passive electronic components, is characterized briefly in Ch. 2, where I demonstrate that the input-output relationship of the circuit's voltages (v_{in} and v_{out}) can be approximated by a piecewise-linear function $F(v_{in})$. As a reminder, the experimental data, the numerical fit, and the general form of $F(v_{in})$ are provided in Fig. 4.1. In Fig. 4.1a, the input-output characteristics of the nonlinear circuit show a linear regime (a line with positive slope) and an anti-linear regime (a line with negative slope) when driven by a sinusoidal signal of frequency $f = 270$ MHz. As shown in Ch. 2, the fit in Fig. 4.1b provides a simple nonlinear function to approximate the operations of the NLC.

However, this characterization is not complete because at high-frequencies ($f >$

1 GHz), the simple tent-like shape of the nonlinear circuit's input-output relationship is distorted. These distortions cannot be modeled by a simple nonlinear function. Because the typical dynamics of the cavity-feedback system contain such high frequencies (see Ch. 3), it is important to investigate these effects in order to build a more realistic model for the cavity-feedback system. Therefore, in this section, I first detail the distortions of the NLC and then use various modeling techniques to reproduce approximately these behaviors.

It should be noted that the specific results from the characterization and modeling of the circuit are not used outside of this chapter. They are presented here to highlight the experimental non-idealities, but they are not essential to the mechanisms that produce quasiperiodic dynamics. For those not interested in the details of the circuit operation, I suggest advancing to Ch. 5, where a more general model of the cavity-feedback system (and its nonlinearity) is used to predict analytically the quasiperiodic frequencies. This general model is inspired by the characterization and modeling of the NLC but does not include the details that follow here.

4.1.1 High-Frequency Distortions and Low-Pass Filtering Effects

To characterize the nonlinear circuit's operation at high frequencies, I use several different input signals v_{in} with frequencies ranging from $f = 500$ MHz to $f = 1.9$ GHz. Similar to Fig. 4.1a, I monitor both v_{in} and v_{out} of the NLC on separate channels of a high-speed digital oscilloscope. As shown in Fig. 4.2, the nonlinear mode-of-operation for the circuit is frequency dependent with distortions resulting in an opening of the tent-like shape.

From this figure, there are several features of the distortions that can give a basic insight into their general causes. For example, the amplitudes of v_{out} decrease with

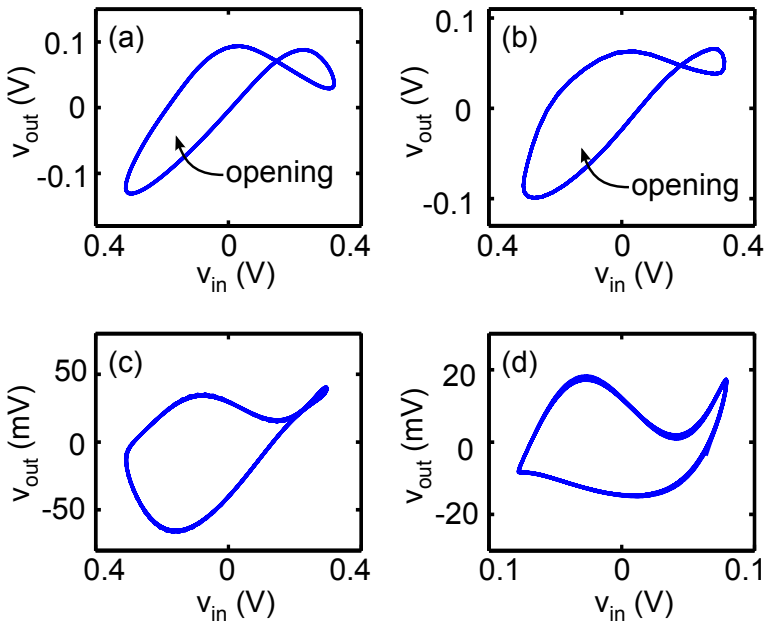

Figure 4.2: **Experimental high-frequency distortions.** Experimental distortions of v_{out} for sinusoidal driving signals v_{in} at frequencies(a) $f = 500$ MHz with $v_b = 0.65$ V, (b) $f = 1.1$ GHz with $v_b = 0.65$ V, (c) $f = 1.5$ GHz with $v_b = 0.7$ V, and (d) $f = 1.9$ GHz with $v_b = 0.74$ V. The frequencies used to create Fig. 4.2 are chosen to highlight the progression of these distortions for various bias voltages v_b In (a) and (b), the opening of the tent-like shape is labeled accordingly. For all measurements, the paths to the oscilloscope for v_{in} and v_{out} are approximately balanced with equal propagation times. The error of each voltage measurement is estimated as ±2 mV based on the standard deviation of the oscilloscope noise floor.

input driving frequency, which is typical with a low-pass filter. As shown in Fig. 4.3a, an example transfer function of a first-order low-pass filter with cutoff frequency $f_{LP} = 1$ GHz (based on a -3 dB power drop) demonstrates that signals with frequencies $f > f_{LP}$ are attenuated. The potential origins of this filtering (capacitive effects of the transistor) are discussed in more detail in Appendix C.

Furthermore, in Fig. 4.2, the opening of the tent-like shape becomes wider and more pronounced with increasing frequency, which can be attributed to an increase in the propagation delay τ_{pd} through the nonlinear circuit. To illustrate this idea conceptually, I use a numerical time series generated from the ideal nonlinear func-

tion F(v_{in}) with a sinusoidal input signal v_{in} shown in Fig. 4.4. For a propagation delay $\tau_{pd} = 0$ ns (Fig. 4.4a), the tent-like shape of the nonlinearity is preserved. However, as τ_{pd} increases, the tent-like shape between v_{in} and v_{out} begins to open (Figs. 4.4b-c), displaying similar features to those in Figs. 4.2a-b. Though Fig. 4.4 uses a constant input driving frequency, it demonstrates (artificially) that an increasing τ_{pd} through the circuit can result in open tent-like shapes.

Therefore, in the experiment, because the tent-like shape opens more for signals with higher frequencies, the propagation delay through the NLC is frequency dependent: $\tau_{pd}(f)$. This can also be understood as a frequency-dependent phase shift $\Delta\phi(f) \sim 2\pi\tau_{pf}(f)$ that changes with f. As shown by the phase characteristics of the transfer function in Fig. 4.3b, this type of phase shift can also be attributed to low-pass filter effects. These effects, which are non-ideal in the context of the NLC design, require further investigation to characterize their properties.

4.1.2 Modeling the Filtering Effects of the Nonlinear Circuit

Rather than modeling the currents and voltages in the NLC from first principles (see also Appendix C), my model for the filtering effects in the device uses two

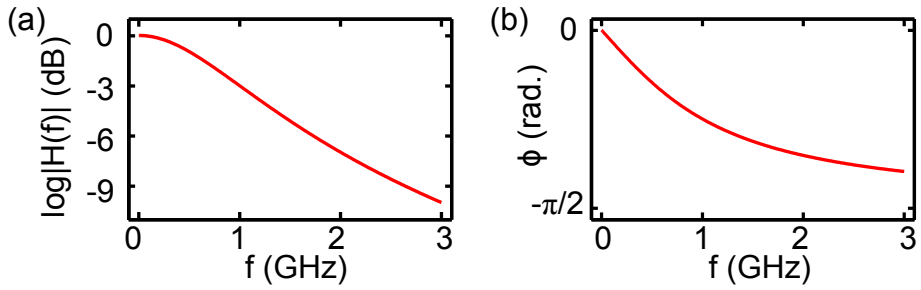

Figure 4.3: **First-order low-pass filter.** (a) Magnitude of the low-pass filter transfer function $H_{LP}(f) = \tilde{v}_{out}/\tilde{v}_{in}$ and (b) output phase ϕ of the filter with respect to input frequency f.

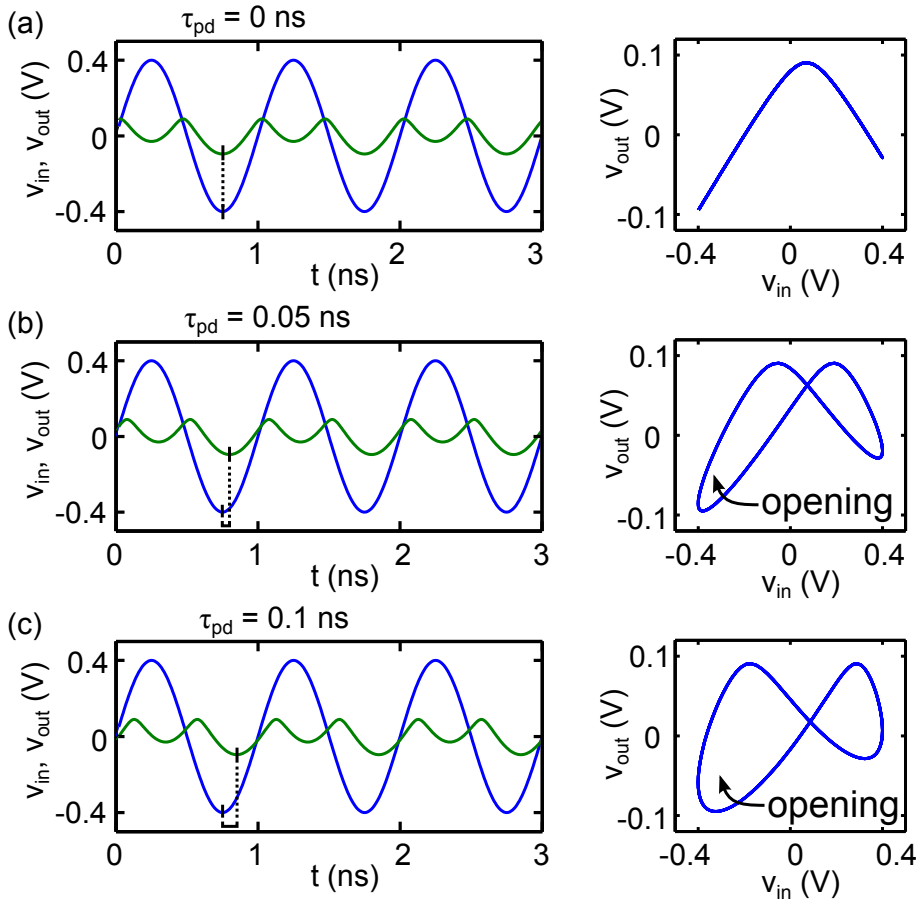

Figure 4.4: **Simulated effects of an increasing propagation delay.** A simulated input sinusoidal v_{in} at frequency $f = 1$ GHz drives nonlinear function $F(v)$ with bias voltage $v_b = 0.65$ V. The output v_{out} (green curve) plotted alongside v_{in} and plotted versus v_{in} for output propagation delays (a) $\tau_{pd} = 0$ ns, (b) $\tau_{pd} = 0.05$ ns, and (c) $\tau_{pd} = 0.1$ ns. Vertical lines with an arrow mark the increase in the propagation delays and the opening of the tent-like shapes are labeled in (a) and (b), accordingly.

mathematical filters at the output of the nonlinear function $F(v_{in})$. These additional filters represent a simple solution for reproducing the observed distorted behaviors that are reported in Fig. 4.2. In this section, I show that each of the two filters in my model characterizes separately the filtering effects for the NLC in its linear (L) and anti-linear (A) regimes.

First, the filtering effects of the NLC are measured in the linear and anti-linear

regimes using low-amplitude input signals v_{in} with a swept frequency f. To characterize the circuit in the linear regime, I use a v_b such that $v_b + v_{in} \leq v_T$, and, conversely, to characterize it in the anti-linear regime, I use v_b such that $v_b + v_{in} > v_T$. For each of these regimes, a spectrum analyzer measures $|H_{LP,(L,A)}| = |\tilde{v}_{out}/\tilde{v}_{in}|$, which represents the magnitude of a low-pass filter transfer function through the circuit in the linear (L) and anti-linear (A) regimes, respectively, where $\tilde{v}_{in}$ ($\tilde{v}_{out}$) is the Fourier transform of the input (output) voltage. The goal is to use these measurements, which are shown in Fig. 4.5, to approximate the output of the NLC as $F(v_{in})$ with the addition of low-pass filter models.

In the figure, it is clear that the magnitudes of the transfer functions in each regime are indeed low-pass filters, attenuating signals at high frequencies. However, it also apparent that the filtering effects have different frequency-dependent characteristics in the linear and anti-linear regimes. In other words, the intrinsic

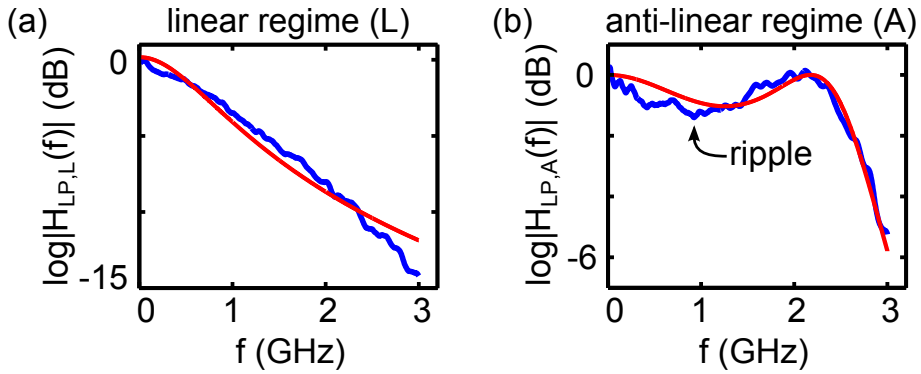

Figure 4.5: **Magnitudes of the transfer functions through the nonlinear circuit** in its (a) linear regime using $v_b = 0.65$ V and v_{in} with amplitude of 20 mV, and (b) in its anti-linear regime using $v_b = 0.85$ V and v_{in} with amplitude of 20 mV. The experimental data (blue curves) in (a) and (b) are fitted with the magnitudes of the transfer functions $H_{LP,L}(f)$ and $H_{LP,A}(f)$ (red curves), respectively. The largest discrepancies between the fits and the respective data occur at $f = 3.0$ GHz with a difference of 2.3 dB for $H_{LP,L}(f)$ and at $f = 0.42$ GHz with a difference of 0.8 dB for $H_{LP,A}(f)$, which present possible sources of error in the NLC model.

filtering effects of the NLC change when the transistor switches from inactive (in the linear regime) to active (in the anti-linear regime) and vice versa. Thus, when the cavity-feedback system is oscillating, the bandwidth of the transistor is switching rapidly between the frequency responses shown in Fig. 4.5a and Fig 4.5b. As I show at the end of this section, the model for the circuit must also switch its transfer function in the two regimes to reproduce the distortions of the NLC.

In the linear regime, I model the filtering effects with a first-order low-pass filter, whose transfer function magnitude reads

$$|H_{\mathrm{LP,\,L}}(f)| = \frac{1}{\sqrt{1+(f/f_{\mathrm{LP}})^2}}, \tag{4.1}$$

where $f_{\mathrm{LP,\,L}}$ is the low-pass cutoff frequency. Using a least-squares regression between Eq. (4.1) and the experimental data in Fig. 4.5a with $f_{\mathrm{LP,\,L}}$ as a free fitting parameter yields $f_{\mathrm{LP,\,L}} = 0.78 \pm 0.02$ GHz (the error represents the 90% confidence interval of the fitting parameter). The resulting fit, which is also plotted in Fig. 4.5a, gives the RMS difference with the data of 0.8 dB, which is a $\sim 6\%$ error of the overall experimental range. Increasing the degree of the low-pass filter improves the agreement of the fit, but, as I will show, this added complexity in the model is not necessary to reproduce the experimental distortions.

In the time domain, the effect of the low-pass filter in the linear regime can be modeled using an ordinary differential equation that reads

$$\dot{\mathrm{v}}_{\mathrm{LP,\,L}}(t) = 2\pi f_{\mathrm{LP,\,L}}[\mathrm{v}_F(t) - \mathrm{v}_{\mathrm{LP,\,L}}(t)], \tag{4.2}$$

where $\mathrm{v}_F = F(\mathrm{v}_{\mathrm{in}})$ is the output of the ideal nonlinear function that drives the filter. Thus, Eq. (4.2) represents a simple model for the NLC in its linear regime.

In the anti-linear regime, however, a more complicated model is necessary reproduce approximately the filtering effects shown in Fig. 4.5b. I use a fit of the transfer function magnitude of a third-order Chebyshev low-pass filter that reads

$$|H_{\mathrm{LP,\,A}}(f)| = \frac{1}{\sqrt{1+\epsilon^2[4(f/f_{\mathrm{LP,A}})^3 - 3(f/f_{\mathrm{LP,A}})^2]}}, \tag{4.3}$$

where $\epsilon = 0.51 \pm 0.01$ dB is known as the *ripple factor* that dictates the size of the ripple (labeled in Fig. 4.5b) in the magnitude of the transfer function and $f_{\mathrm{LP,\,A}} = 2.51 \pm 0.01$ GHz is the filter cutoff frequency [76, 77]. The fit of $|H_{\mathrm{LP,\,A}}(f)|$ is also plotted in Fig. 4.5b. In this case, the RMS difference between the fit and the data is 0.35 dB, which is a $\sim 7\%$ error of the overall experimental range, and thus the fit approximately captures the low-pass filtering in the anti-linear regime.

Written in the time domain, a third-order Chebyshev low-pass filter can be represented by a set of three first-order differential equations. These equations, which represent the model for the output of the NLC in the anti-linear regime are

$$\begin{bmatrix} \dot{x}_1(t) \\ \dot{x}_2(t) \\ \dot{x}_3(t) \end{bmatrix} = \begin{bmatrix} A_{1,1} & 0 & 0 \\ A_{2,1} & A_{2,2} & A_{2,3} \\ 0 & A_{3,2} & 0 \end{bmatrix} \begin{bmatrix} x_1(t) \\ x_2(t) \\ x_3(t) \end{bmatrix} + \begin{bmatrix} B_1 \mathrm{v}_F(t) \\ 0 \\ 0 \end{bmatrix}, \tag{4.4}$$

with the conversion for the output voltage

$$\mathrm{v}_{\mathrm{LP,\,A}}(t) = C_3 x_3(t), \tag{4.5}$$

where x_1, x_2, x_3 are auxiliary variables with units of volts (V), $\mathrm{v}_F = F(\mathrm{v}_{\mathrm{in}})$, $\mathrm{v}_{\mathrm{LP,\,A}}$ is the output of the Chebyshev low-pass filter, and $A_{1,1} = -9.78 \pm 0.03$ rad/ns, $A_{2,1} = 15.78 \pm 0.06$ rad/ns, $A_{2,2} = -9.79 \pm 0.03$ rad/ns, $A_{2,3} = -16.81 \pm 0.03$

rad/ns, $A_{3,2} = 16.81 \pm 0.03$ rad/ns, $B_1 = 15.78 \pm 0.06$ rad/ns, and $C_3 = 0.66 \pm 0.01$ (the errors represents the 90% confidence intervals of the fitting parameters). These variables are calculated using the parameters $f_{\mathrm{LP,\,A}}$ and ϵ. Thus, Eqs. (4.4) and (4.5) represent approximately the filtering effects of the NLC in the anti-linear regime.

It remains to combine the filtering effects of the linear and anti-linear regimes into a single model that can switch between the two different transfer functions. For this, I use an approximately piecewise-linear approach inspired by a result I recently published (see Ref. [78]). To model the approximately piecewise-linear switching, I first consider the system to be an ideal switch that depends on the threshold $\mathrm{v_T}$

$$\mathrm{v_s}(t) = \begin{cases} \mathrm{v_{LP,\,L}}(t), & \text{if } \mathrm{v_{in}} + \mathrm{v_b} \leq \mathrm{v_T} \\ \mathrm{v_{LP,\,A}}(t), & \text{if } \mathrm{v_{in}} + \mathrm{v_b} > \mathrm{v_T} \end{cases}. \tag{4.6}$$

The switching in Eq. (4.6) is infinitely fast and discontinuous and therefore non-physical. Thus, similar to Ref. [78], I choose to model the switching in the system's transfer function as

$$\mathrm{v_s}(t) = \left(\frac{1 - s(t)}{2}\right)\mathrm{v_{LP,\,L}}(t) + \left(\frac{1 + s(t)}{2}\right)\mathrm{v_{LP,\,A}}(t), \tag{4.7}$$

where $s(t)$ is a switching state modeled by

$$s(t) = \tanh(M[\mathrm{v_{in}}(t) + \mathrm{v_b} - \mathrm{v_T}]), \tag{4.8}$$

such that the hyperbolic tangent (tanh) serves as a continuous nonlinear switching function and M is a constant that describes the rate of the switching. In order to obtain an experimental value of M, I will use the data from Fig. 4.2 and perform a least-squares fit with the full model for the NLC.

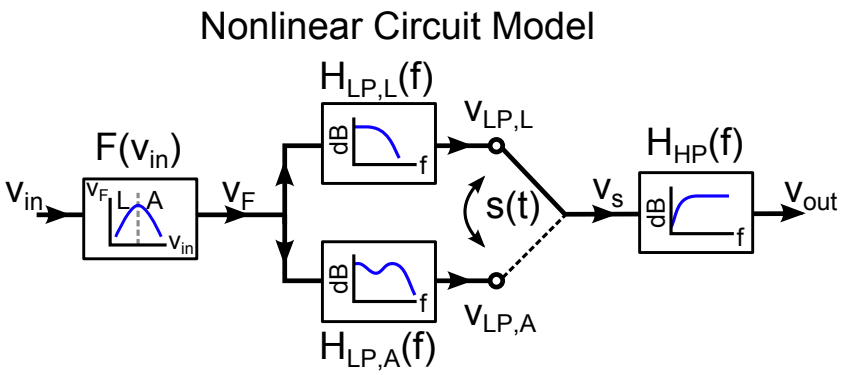

Figure 4.6: **Schematic representation of the NLC model.** The input voltage v_{in} drives the nonlinear function $F(v_{in}) = v_F$ and the low-pass filters $H_{LP,L}(f)$ and $H_{LP,A}(f)$ in parallel. The continuous switching function $s(t)$ switches v_s between the output voltages of these two filters ($v_{LP,L}$ and $v_{LP,A}$), which is then high-pass filtered (by transfer function $H_{HP}(f)$) to yield the output voltage v_{out} of the nonlinear circuit. The various blue curves represent the input-output tent-like shape of the nonlinear function $F(v_{in})$ (with linear (L) and anti-linear (A) regimes labeled) as well as the magnitudes of the different transfer functions as a function of frequency.

However, there is still one remaining component of the NLC model that is required to reproduce the ac-coupled effects of the circuit output (see Ch. 2: in the design of the NLC, there is an output capacitor C_2 that filters the direct-current component of output signals). To model the ac-coupled effects of the NLC, I use the filtering from a high-pass filter transfer function $H_{HP}(f)$ to model the output voltage v_{out}, which is represented in the time domain as

$$\dot{v}_{out}(t) = \dot{v}_s(t) - 2\pi f_{HP} v_{out}(t), \tag{4.9}$$

where $v_s(t)$ is calculated using Eqs. (4.7) - (4.8) and $f_{HP} = 10$ MHz is a conservative estimate of the high-pass filter cutoff frequency $1/(2\pi RC_2)$, where C_2 is the output capacitor of the NLC (see Ch. 2) and $R = 50\ \Omega$. This is conservative estimate ($f_H > 1/(2\pi RC_2)$) helps eliminate transient dynamics in the simulations of the circuit distortions.

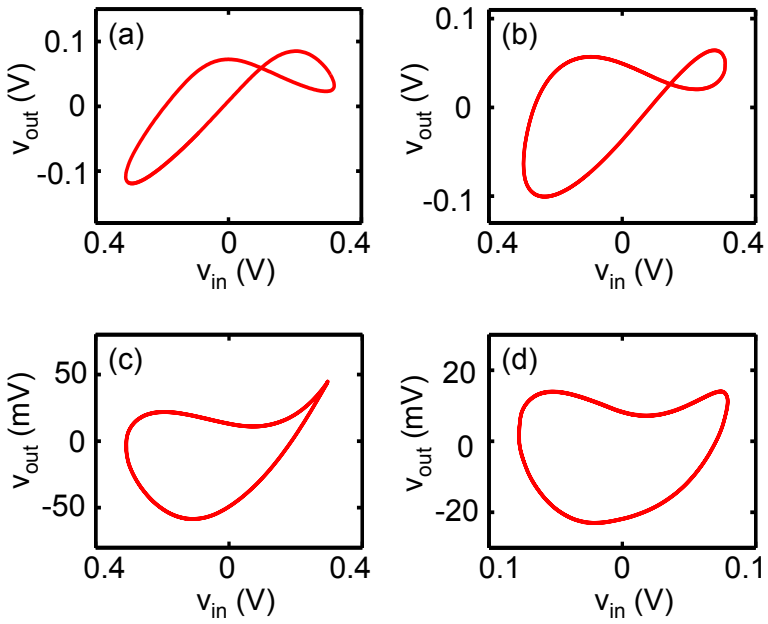

Figure 4.7: **Simulated high-frequency distortions.** Simulated v_{out} plotted as a function of v_{in} using the full model of the NLC and the experimental input sinusoidal signals v_{in} at frequencies and bias voltages of (a) $f = 500$ MHz with $v_b = 0.65$ V, (b) $f = 1.1$ GHz with $v_b = 0.65$ V, (c) $f = 1.5$ GHz with $v_b = 0.7$ V, and (d) $f = 1.9$ GHz with $v_b = 0.74$ V. The RMS errors between the data at f = (0.5, 0.7, 1.1, 1.5) GHz and the respective fits are (12.3 ,18.5 ,10.4, 6.8) mV, which represent $(6.0, 11.2, 6.3, 18.4)$% errors for the given experimental ranges.

Finally, the full NLC model is depicted with each of its separate components in Fig. 4.6. In the first component, the voltage v_{in} is processed by the nonlinear function $F(v_{in}) = v_F$, which is represented by a tent-like shape. In the second stage, v_F is processed by the flow-pass filter transfer functions $H_{LP,L}$ and $H_{LP,A}$ in parallel, and in the third stage, the continuous function $s(t)$ switches (depending on the value of v_{in}) between the two low-pass filter outputs ($v_{LP,L}$ or $v_{LP,A}$). Finally, in the last stage, the outputs from the filters $v_s(t)$, which follow a common path, are high-pass filtered to produce $v_{out}(t)$. All of these four stages represent Eqs. (4.7) - (4.9) as the full model for the nonlinear circuit.

Using Eqs. (4.7) - (4.9), I perform a least-squares fit to the four data sets in

Fig. 4.2 simultaneously with M as a free fitting parameter. The responses of the model for the NLC are plotted in Fig. 4.7 with the fitted value $M = 0.63 \pm 0.03$ V^{-1} (error represents the 90% confidence interval of the fitting parameter). The format of this figure is similar to that in Fig. 4.2 for easy comparison. The percent errors of the RMS differences between the data and the fits (see the caption of Fig. 4.7 for details) range from 6% to 18.4% for $f = 500$ MHz and $f = 1.9$ GHz, respectively. As illustrated by the simulated distortions, the model for the NLC reproduces qualitatively the observed experimental distortions and filtering effects at high-frequencies.

This concludes the section for modeling the nonlinear circuit. The results from this section will be used later in this chapter when I combine them with a representation of the wave-chaotic cavity to create a model for the cavity-feedback system. For now, I change topics and examine methods for modeling the wave-chaotic cavity.

4.2 Modeling the Wave-Chaotic Cavity

As mentioned briefly in the introduction of Ch. 3, the wave-chaotic cavity can be understood as a distribution of time delays and gain coefficients. This delay-gain distribution is measured using the cavity's pulse response, where a short pulse $r_{\text{in}}(t)$ ($\delta t = 0.1$ ns) is injected at the TX antenna (see Fig. 4.8a), and the output pulse response $r_{\text{out}}(t)$ is measured at the RX antenna using an oscilloscope (see Fig. 4.8b). The goal of this section is to examine how the delay-gain distribution (τ_i, g_i), which is acquired using $r_{\text{out}}(t)$, can be used to model the effects of the cavity on an arbitrary input signal.

To do so, I first examine the cavity in the frequency domain, where its transfer function can be applied to an arbitrary signal. Then, I switch to an equivalent

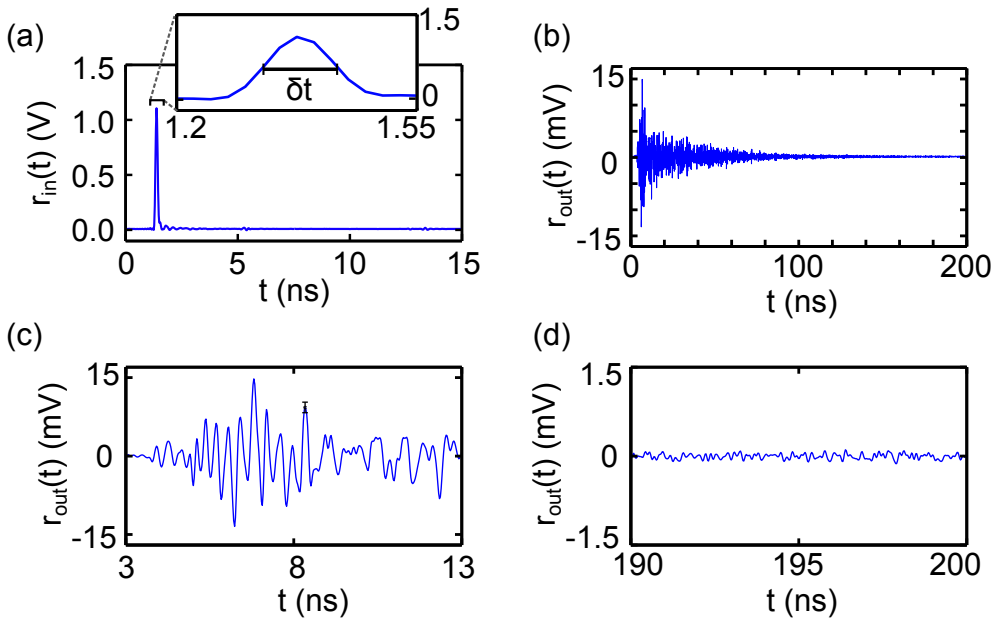

Figure 4.8: **Pulse response of the cavity.** (a) Injected pulse $r_{\text{in}}(t)$ of width $\delta t = 0.1$ ns and (b) impulse response of the cavity $r_{\text{out}}(t)$. Zooms of the impulse response for (c) 3 ns $< t <$ 13 ns and (d) 195 ns $< t <$ 200 ns. Note the vertical axis change in (d). The error bars in (c) represents the approximate standard deviation of the noise floor ± 1 mV of the waveform for these measurements. As shown in (d), the amplitude of r_{out} at $t = 200$ ns is within the noise level. Also, note the vertical axis change from (c) to (d).

time-domain representation of the cavity that is necessary because it will later be combined with the nonlinear circuit model, which contains an inherent nonlinear function and is also simulated in the time domain.

4.2.1 Frequency Domain Representation of the Cavity

In the frequency domain representation, the wave-chaotic cavity can be treated as a filter [79]: The cavity is a linear system with an input and an output that attenuates and blocks signals at certain frequencies and adds phase-delays. As with any linear system, the impulse response of the cavity fully characterizes its filtering effects [79]. Thus, using the pulse response, which is a finite-bandwidth representation

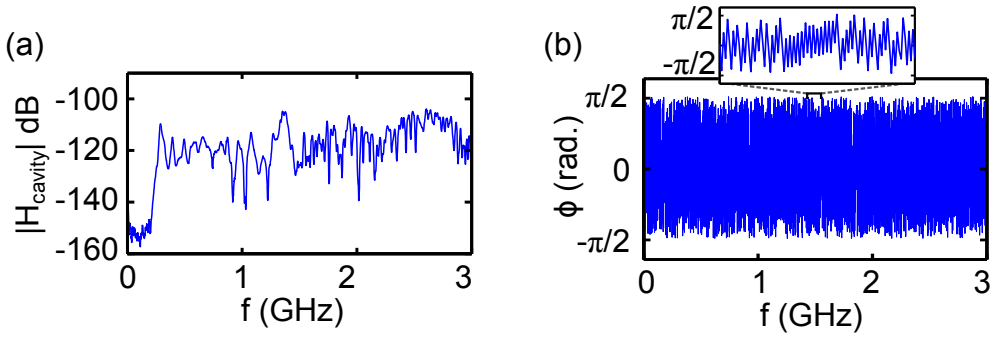

Figure 4.9: **Transfer function of the wave-chaotic cavity** calculated using the experimental data from $r_{\text{in}}(t)$ and $r_{\text{out}}(t)$. (a) Magnitude of the transfer function $H_{\text{cavity}}(f)$ and (b) output phase ϕ of the cavity with respect to input frequency f. The zoom shows ϕ for 1.5 GHz $< f <$ 1.6 GHz.

of its impulse response ($1/(\delta t) \sim 10$ GHz), I can reconstruct approximately the cavity's transfer function $H_{\text{cavity}}(f)$ (discussed briefly in Ch. 2) defined as

$$H_{\text{cavity}}(f) = \tilde{r}_{\text{out}}/\tilde{r}_{\text{in}}, \tag{4.10}$$

where $\tilde{r}_{\text{in}}$ and $\tilde{r}_{\text{in}}$ are the Fourier transforms of the input pulse and output pulse response, respectively. The magnitude and phase of $H_{\text{cavity}}(f)$ are plotted in Fig. 4.9, where the magnitude of $H_{\text{cavity}}(f)$ shows the resonances of the cavity and its phase shows the complexity of the frequency-dependent phase delays through cavity.

To demonstrate how $H_{\text{cavity}}(f)$ can be used to simulate the cavity's effects on an arbitrary input signal, I use the modulated pulse $m_{\text{in}}(t)$ shown in Fig. 4.10a, which is created experimentally using our signal generator. The modulation frequency $f = 1$ GHz is used to create a test signal of width ~ 15 ns with a frequency bandwidth that can be transmitted and received by the cavity's antennas (TX and RX). First, I apply $m_{\text{in}}(t)$ to the TX antenna and record the output $m_{\text{out}}(t)$ at the RX antenna using the oscilloscope. The experimental output of the cavity, which is plotted in Fig. 4.10b, shows a complex modulated response with a time duration $>>$ 15 ns.

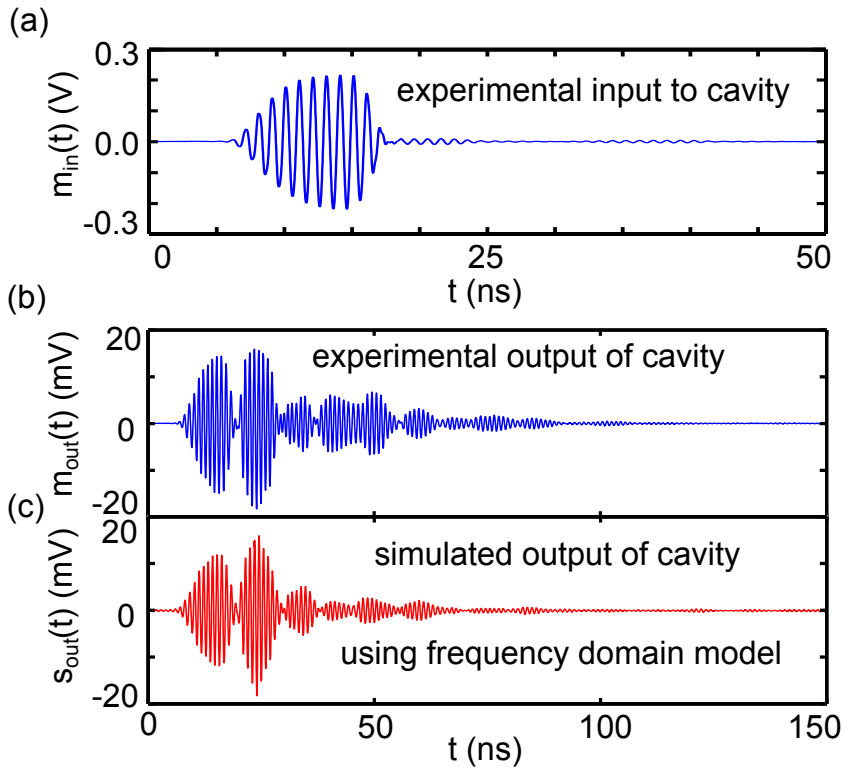

Figure 4.10: **Test signal to demonstrate the frequency domain model.** Temporal evolution of (a) the cavity input test signal $m_{\text{in}}(t)$ (created using the signal generator E8267D), (b) the experimental response of the cavity $m_{\text{out}}(t)$, and (c) the simulated cavity output s_{out}. In the figures, I have scaled the amplitudes of the waveforms by a constant factor to normalize the power in $m_{\text{in}}(t)$ to match that of $r_{\text{in}}(t)$. Also, note the change of the horizontal scales between (a) and (b)-(c).

To simulate the cavity's output, I apply the transfer function $H_{\text{cavity}}(f)$ to $\tilde{m}_{\text{in}}$, the Fourier transform of the input modulated signal $m_{\text{in}}(t)$, such that

$$\tilde{s}_{\text{out}} = H_{\text{cavity}}(f)\tilde{m}_{\text{in}}, \tag{4.11}$$

where $\tilde{s}_{\text{out}}$ is the Fourier transform of the simulated cavity output $s_{\text{out}}(t)$. The temporal evolution of $s_{\text{out}}(t)$ is then recovered using the inverse Fourier transform of $\tilde{s}_{\text{out}}$. To compare the experimental and simulated cavity outputs, I plot them together in Fig. 4.10b-c. As shown in the figures, the simulated and experimental waveforms

are quantitatively similar in frequency, phase, and overall envelope. The main differences are found in the amplitude near $t = 50$ ns. The RMS difference between the simulated cavity response and the data is $\sim$ 0.8 mV, which represents 2.2% of the experimental range. To further quantify these comparisons, I calculate the cross-correlation coefficient $C(m_{\text{out}}(t), s_{\text{out}}(t)) = 0.96$, which demonstrates that the experimental pulse response of the system (recorded by the oscilloscope) can be used to simulate the approximate effects of the wave-chaotic cavity.

The imperfect correlation value ($C < 1$) has several possible origins. For example, measurement noise can influence the pulse response calibration measurement r_{out}. Even with averaging, the amplitudes of r_{out} extend to the noise floor of the oscilloscope. In addition, the measurements of m_{in} and m_{out} also contain noise. The degraded correlation may also be caused by the finite length of the time series r_{out}. The Fourier transform is intended for infinitely long time series, and the pulse response is only measured until its amplitude decays to within the noise floor of the oscilloscope. These effects can distort the measured transfer function for the system.

Furthermore, before moving to the time-domain representation, I make one additional approximation of the transfer function: $H_{\text{cavity}}(f) \sim \tilde{r}_{\text{out}}$. Because the input pulse $r_{\text{in}}(t)$ is approximately a delta function $\delta(t)$, its Fourier transform $\tilde{r}_{\text{in}}$ is approximately a constant [79]. Therefore, dividing by $\tilde{r}_{\text{in}}$ in Eq. 4.10 is not necessary to recover the transfer function of the cavity. I therefore reduce this equation to $H_{\text{cavity}} = \tilde{r}_{\text{out}}$ and use it to calculate again $s_{\text{out}}(t)$ from $m_{\text{in}}(t)$. This second simulation, which need not be plotted due to its similarities to Fig. 4.10, yields $C(m_{\text{out}}(t), s_{\text{out}}(t)) = 0.95$. Thus, the simulation is approximately valid under the assumption $H_{\text{cavity}} \sim \tilde{r}_{\text{out}}$, which will now be used to simulate the cavity output in the time domain.

4.2.2 Time-Domain Representation of the Cavity

In the time domain, the simulation of the output of the cavity is represented using the convolution [79]

$$s_{\text{out}}(t) = \int_{-\infty}^{\infty} r_{\text{out}}(t')m_{\text{in}}(t-t')\,\mathrm{d}t'. \tag{4.12}$$

However, because the digital oscilloscope samples $r_{\text{out}}(t)$ with a discrete sampling time $\Delta t = 0.025$ ns, Eq. (4.12) is a actually a discrete sum and the variable t' is replaced with the discrete times τ_i

$$s_{\text{out}}(t) = \sum_{i=1}^{i=N} r_{\text{out}}(\tau_i)m_{\text{in}}(t-\tau_i), \tag{4.13}$$

where $m_{\text{in}}(t-\tau_i)$ is the value of $m_{\text{in}}(t)$ at a time $t-\tau_i$ in the past and N is the number of discretely sampled times in r_{out}. To help understand the operations performed

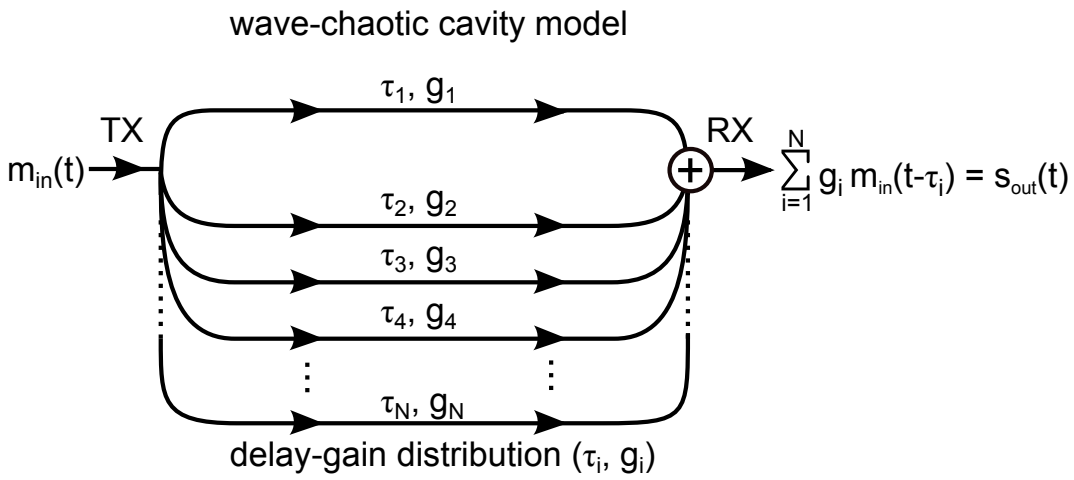

Figure 4.11: **Representation of the cavity model in the time domain**. The signal $m_{\text{in}}(t)$ is divided among the delay-gain distribution through paths with propagation delays τ_i and gain coefficients $g_i = r_{\text{out}}(\tau_i)$. The result is summed at the output of the cavity. The points representing the TX and RX antennas are labeled accordingly.

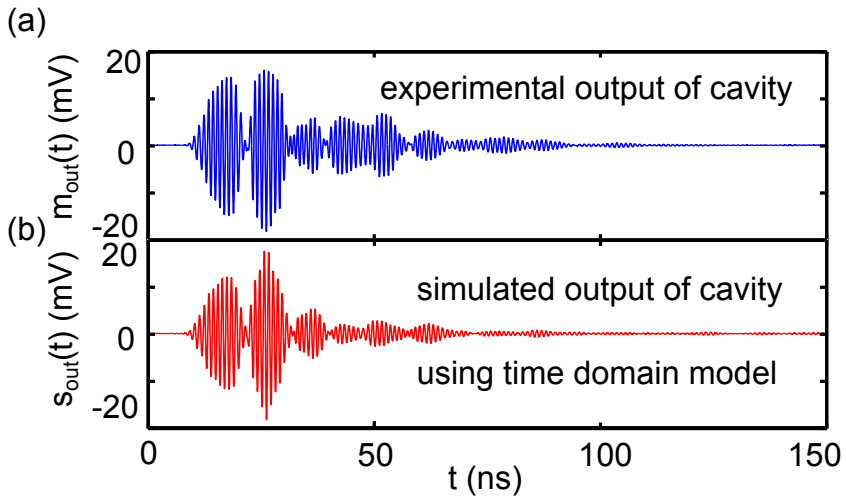

Figure 4.12: **Time domain simulations of the cavity**. (a) Experimental output $m_{\text{out}}(t)$ and (b) time-domain simulation of $s_{\text{out}}(t)$ using $\tau_{\text{max}} = 200$ ns.

by Eq. (4.13), a pictorial representation of the model is presented in Fig. 4.11. In the figure, $m_{\text{in}}(t)$ is injected at the input (the TX antenna in the experiment) of the delay-gain distribution, where it is divided among multiple paths with propagation delays τ_i and gain coefficients $g_i = r_{\text{out}}(\tau_i)$ before being summed at the output (the RX antenna in the experiment) to recover $s_{\text{out}}(t)$.

Using Eq. (4.13), I recalculate the simulated cavity output in the time domain using a time series for r_{out} with $N = 8000$ points, or equivalently $\tau_{\text{max}} = 200$ ns, where τ_{max} is the maximum value of τ_i such that $r_{\text{out}}(\tau_{\text{max}})$ from Fig. 4.8b is within the noise floor of the oscilloscope (note: the value of N can also be decreased while maintaining $\tau_{\text{max}} = 200$ ns if the waveform r_{out} is resampled at a lower sampling-rate that still satisfies the Nyquist sampling limit [76]). The resulting waveform $s_{\text{out}}(t)$ is shown in Fig. 4.12a and is plotted below the experimental cavity response $m_{\text{out}}(t)$ for comparison. Because the time and frequency representations are equivalent [79], the cross-correlation coefficient between experimental output $m_{\text{out}}(t)$ and the time-domain simulation s_{out} is $C(m_{\text{out}}(t), s_{\text{out}}(t)) = 0.95$. As I will show in

the next section, using the time domain representation of the cavity transfer function provides a model for the cavity-feedback system that is capable of reproducing qualitatively similar results when compared to experimental quasiperiodic dynamics.

4.3 Modeling the Cavity-Feedback System

As a reminder, a representation of the experimental system is depicted in Fig. 4.13a. In the figure, the wave-chaotic cavity is highlighted in red with the graphical representation of the cavity's model. The external nonlinear feedback loop of the system is comprised of amplifiers (A_1 and A_2), the nonlinear circuit (NLC), a low-pass filter (LPF), a directional coupler (dir-c), and an added variable attenuator (VA) to control the gain of the system. At this point in Ch. 4, I have only presented a model for the NLC, (highlighted in red in Fig. 4.13a with its graphical representation), and not the remaining components in feedback loop. Thus, to begin this section, I first propose a simple model for the remaining components A_1, A_2, LPF, dir-c, and VA. Because of their linearity, I model these as a single component (also known as a *lumped* element) with properties similar to each of the components in series, as shown in Fig. 4.13b.

Similar to the feedback loop in Ch. 2, due to the limited bandwidth of these lumped components, I choose to model them as a band-pass filter with gain. The schematic representation of this simplified model is depicted in Fig. 4.13c. Using a signal generator and spectrum analyzer, I measure the magnitude of the transfer function for these components together over a typical frequency range of the dynamics (10 MHz $< f <$ 2 GHz). As shown in Fig. 4.14, they attenuate low and high frequencies, thus behaving similar to a two-pole bandpass filter with transfer

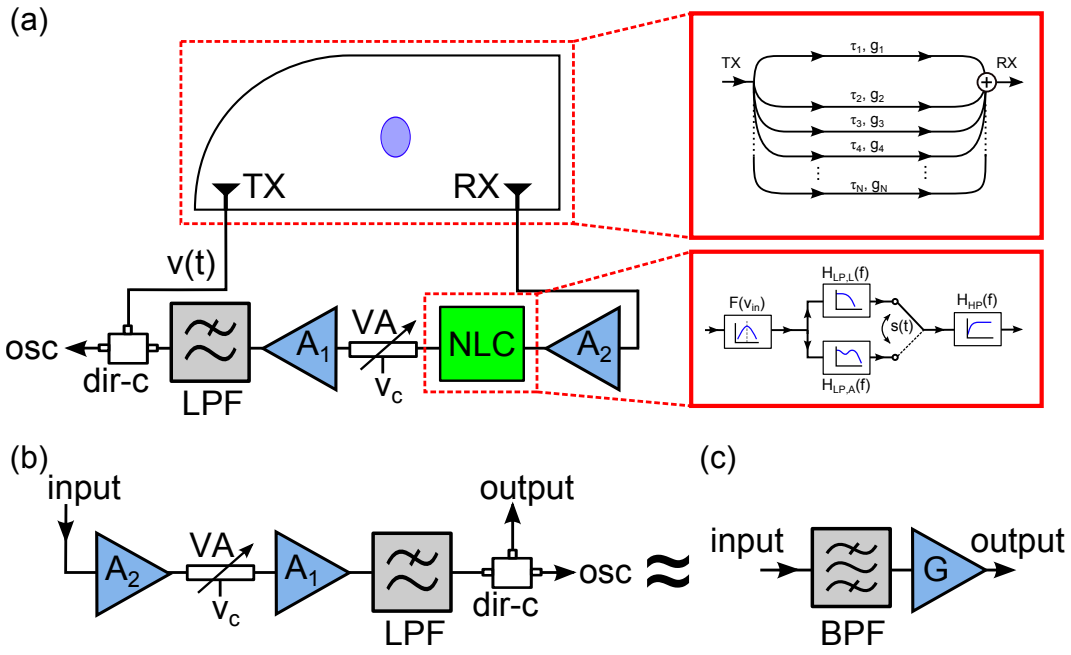

Figure 4.13: Review of cavity-feedback system. (a) Experimental setup for the cavity-feedback system with the cavity and nonlinear circuit (NLC) highlighted in red and their corresponding graphical representations. In addition, a variable attenuator (VA) is added to the external feedback loop to control the gain of the system for a fixed scatterer position. (b) All of the elements of the external feedback loop, except for the NLC, can be modeled as a single lumped element with properties similar to each of the components in series. (c) The lumped element in (b) can be modeled as a band-pass filter (BPF) with gain G.

function magnitude $|H_{\mathrm{BP}}(f)|$ (see Ch. 2). To determine the experimental values for the low and high cutoff frequencies of the band-pass filter transfer function ($f^{(-)}$ and $f^{(+)}$, respectively), I fit $|H_{\mathrm{BP}}(f)|$ to the experimental data with $f^{(+)}$ and $f^{(-)}$ as the free fitting parameters at the -3 dB attenuation points of the bandwidth. The fit yields $f^{(+)} = 1.57 \pm 0.01$ GHz and $f^{(-)} = 0.41 \pm 0.01$ GHz (the errors represents the 90% confidence intervals of the fitting parameters) with a central frequency $f_{\mathrm{o}} = \sqrt{f^{(+)} f^{(-)}} \sim 800$ MHz. The RMS difference between the fit and the data is 0.23 dB, which is approximately 7.7% of the experimental range. Thus, using these parameters, the external feedback loop can be modeled using a band-pass filter at

the output of the NLC model.

Furthermore, I determine the net gain G of the entire feedback loop, which includes the wave-chaotic cavity, as a function of the control voltage v_c applied to the VA. To measure G, I use the setup shown in Fig. 4.15a. I choose to measure G this way because it eliminates issues when scaling the gain coefficients of the cavity (discussed later). A signal generator with constant amplitude and frequency drives the components VA, A_1, LPF, dir-c, the wave-chaotic cavity, and then A_2, where its output is measured on an oscilloscope. While tuning v_c, the amplitude of the output waveform is measured and used to compute the feedback loop gain, as shown in Fig. 4.15b. Similar to Ch.2, the gain G is approximately linear (and monotonic) with with respect to v_c with a slope of $\sim 0.3 \pm 0.2$ (error indicates the 90% confidence interval of the fitted slope).

Because this model of the net gain G includes the attenuation from the wave-chaotic cavity, the model for the cavity must be normalized to account for this. In

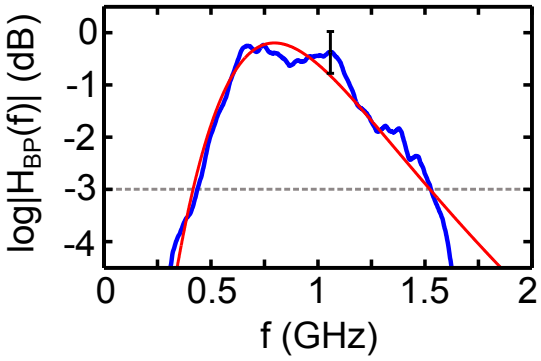

Figure 4.14: **Magnitude of the transfer function for the components in the external feedback loop** (blue curve) fitted with $|H_{\mathrm{BP}}(f)|$ (red curve). The horizontal dashed like indicates the -3 dB point of attenuation. The largest discrepancy between the fit and the data within the 3 dB interval occurs at $f = 1.07$ GHz with a difference of 4.8 dB, which is a possible source of error in the cavity-feedback model. The error bar in the figure represents the accuracy ± 0.4 dB of the spectrum analyzer (E4440A).

other words, to avoid additional attenuation in this model, r_{out} must be rescaled by a factor P such that the total integrated power loss through the cavity is unity

$$\frac{1}{P}\int_0^{\tau_{\max}} r_{\text{out}}(\tau)^2\,\mathrm{d}\tau = 1. \tag{4.14}$$

Using $r_{\text{out}} \to r_{\text{out}}/P$ simplifies the model for the gain coefficients $g_i = r_{\text{out}}(\tau_i)$ because they are now independent of the power from the injected pulse $r_{\text{in}}(t)$ and instead represent the relative gains of each delay τ_i.

Finally, using the models for the NLC, the wave-chaotic cavity, the external feedback loop, and the net gain G, I assemble the model for the cavity-feedback system, which is schematically represented in Fig. 4.16. In the figure, the input of the delay-gain distribution (with normalized g_i) is driven by the output voltage $Gv(t)$ of the NLC and BPF with gain and the output sum from the distribution drives the NLC, forming a closed feedback loop. Using the measured external loop time delay, $\tau_{\text{loop}} \sim 12.5$ ns, the minimum delay time through the entire cavity-feedback sys-

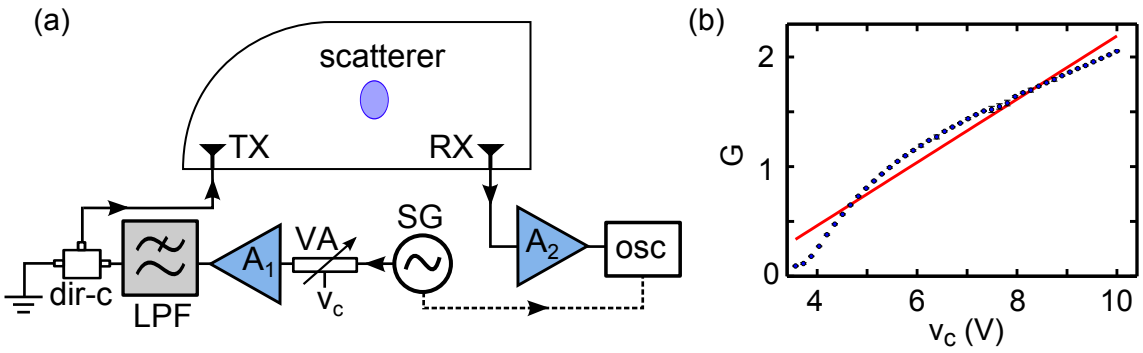

Figure 4.15: **Measurements of the net gain of the feedback loop.** (a) Experimental setup for measuring the gain of the entire feedback loop. (b) The net gain G as a function of v_c, which is measured using a sinusoidal waveform with frequency $f = 1.35$ GHz, the dominant frequency in the dynamics (see next subsection). The error bars for each measurement of G represent the fluctuations in the measured waveforms and the control voltage v_c is varied in steps of 160 ± 2 mV.

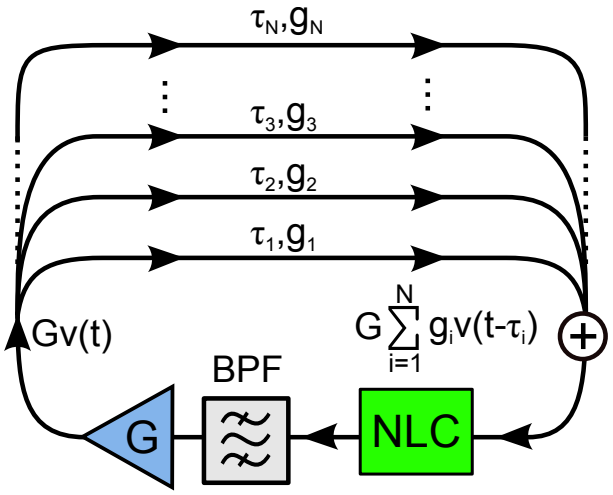

Figure 4.16: **Pictorial representation of the cavity-feedback system model.** The model for the nonlinear circuit (NLC) drives the band-pass filter (BPF) model of the external loop. The BPF output v(t) drives the delay-gain distribution (τ_i, g_i), which is summed at the input of the NLC.

tem model is approximately 17 ns ($[\tau_{\text{min}} \sim 4.5$ ns$] + [\tau_{\text{loop}} \sim 12.5$ ns$]$) and the maximum delay time through the entire feedback model is approximately 212.5 ns ($[\tau_{\text{max}} = 200$ ns$] + [\tau_{\text{loop}} \sim 12.5$ ns$]$), where τ_{min} and τ_{max} are approximately the minimum and maximum time-delays in the model of the wave-chaotic cavity, respectively.

The differential equations used to simulate the cavity-feedback system are listed below. Absent from these equations, I have omitted the high-pass filter at the output of the NLC because the band-pass filter in the external feedback loop accounts for the ac-coupled output of the system (as done in Ref. [22]). Thus, the model for the system is

$$\text{v}_{\text{in}}(t) = G \sum_{i=1}^{i=N} g_i \text{v}(t - \tau_i), \tag{4.15}$$

$$\text{v}_F(t) = F(\text{v}_{\text{in}}(t)) \tag{4.16}$$

$$\dot{\text{v}}_{\text{LP, L}}(t) = 2\pi f_{\text{LP, L}}[\text{v}_F(t) - \text{v}_{\text{LP, L}}(t)], \tag{4.17}$$

$$\begin{bmatrix} \dot{x}_1(t) \\ \dot{x}_2(t) \\ \dot{x}_3(t) \end{bmatrix} = \begin{bmatrix} A_{1,1} & 0 & 0 \\ A_{2,1} & A_{2,2} & A_{2,3} \\ 0 & A_{3,2} & 0 \end{bmatrix} \begin{bmatrix} x_1(t) \\ x_2(t) \\ x_3(t) \end{bmatrix} + \begin{bmatrix} B_1 \mathrm{v}_F(t) \\ 0 \\ 0 \end{bmatrix}, \tag{4.18}$$

$$\mathrm{v}_{\mathrm{LP,\,A}}(t) = C_3 x_3(t) \tag{4.19}$$

$$s(t) = \tanh(M[\mathrm{v}_{\mathrm{in}}(t) + \mathrm{v}_{\mathrm{b}} - \mathrm{v}_{\mathrm{T}}]), \tag{4.20}$$

$$\mathrm{v}_{\mathrm{s}}(t) = \left(\frac{1-s(t)}{2}\right)\mathrm{v}_{\mathrm{LP,\,L}}(t) + \left(\frac{1+s(t)}{2}\right)\mathrm{v}_{\mathrm{LP,\,A}}(t), \tag{4.21}$$

$$\frac{\dot{\mathrm{v}}(t)}{\Delta} + \mathrm{v}(t) + \frac{\omega_{\mathrm{o}}^2}{\Delta}\int_{-\infty}^{t} \mathrm{v}(t')\,\mathrm{d}t' = \mathrm{v}_{\mathrm{s}}(t), \tag{4.22}$$

where $\Delta = 2\pi(f^{(+)} - f^{(-)})$ and $\omega_o = 2\pi\sqrt{f^{(+)}f^{(-)}}$. Equations (4.15) - (4.22) represent the cumulative results of Ch. 4 thus far. It remains to examine the experimental system from which the parameters of these equations are determined and the subsequent dynamics and then compare the simulated results with the experimental data.

4.3.1 Cavity-Feedback System Dynamics

In this subsection, a comparison is made between the quasiperiodic dynamics of the experimental system and the model. The procedure for comparing the experiment to the simulation involves three main steps. First, the gain of the experimental feedback loop is tuned so that the dynamics of the system bifurcate from steady state to periodic and then to quasiperiodic. Using the gain, rather than the scatterer position, as the system's bifurcation parameter, gives control over the dynamics using a scalar quantity G (as opposed to a changing delay-gain distribution). In addition, because G is tuned slowly and in only one direction (increasing), the system does not experience multi-stability.

The second step involves switching the experimental system off and measuring the pulse response of the cavity without disturbing it. The goal is to acquire a waveform $r_{\text{out}}(t)$ that represents the exact delay-gain distribution that produced the quasiperiodic dynamics. Lastly, the third step involves simulating Eqs. (4.15) - (4.22) with the measured $r_{\text{out}}(t)$ using the gain G as its bifurcation parameter.

Experimental Dynamics

The experimental system exhibits steady-state dynamics $\text{v}(t) \sim 0$ V for approximately $G < 1$. When G is then tuned successively from $G \sim 0.9$ to $G \sim 2$, the system undergoes a Hopf and a torus bifurcation. As shown in Fig. 4.17, the temporal evolutions of $\text{v}(t)$ in the resulting periodic and quasiperiodic states are presented along with their corresponding power spectral densities (PSDs). In Figs. 4.17a-b, the periodic time series for $G \sim 1.5$ is sinusoidal at a Hopf frequency $f_{\text{H}} = 1.350 \pm 10^{-3}$ GHz (error represents the resolution of the frequency spacing for the Fourier transform magnitude). Interestingly, this frequency is far from the central frequency $f_{\text{o}} = 0.8$ GHz of the measured band-pass filter in the external feedback loop (in typical band-pass filtered systems with time-delayed nonlinear feedback, the Hopf frequency $f_H \sim f_{\text{o}}$ [29, 75, 78]). This means that the combination of the filtering effects in the nonlinear circuit and from the various time-delays in the cavity cause a large amount of frequency pulling, forcing the system to oscillate at a frequency f_H away from f_o.

Because the initial Hopf frequency is pulled away from the center of the band-pass filter, the torus frequencies are also shifted. As shown in Figs. 4.17c-d, the quasiperiodic dynamics and PSD are plotted for $G \sim 2$. The dynamics oscillate with an amplitude modulation frequency $f_{\text{T}} = 0.293 \pm 10^{-3}$ MHz and the PSD shows prominent peaks at f_{T}, f_{H} and the mixing frequencies $f_{\text{H}} - f_{\text{T}} = 1.055 \pm 10^{-3}$ GHz

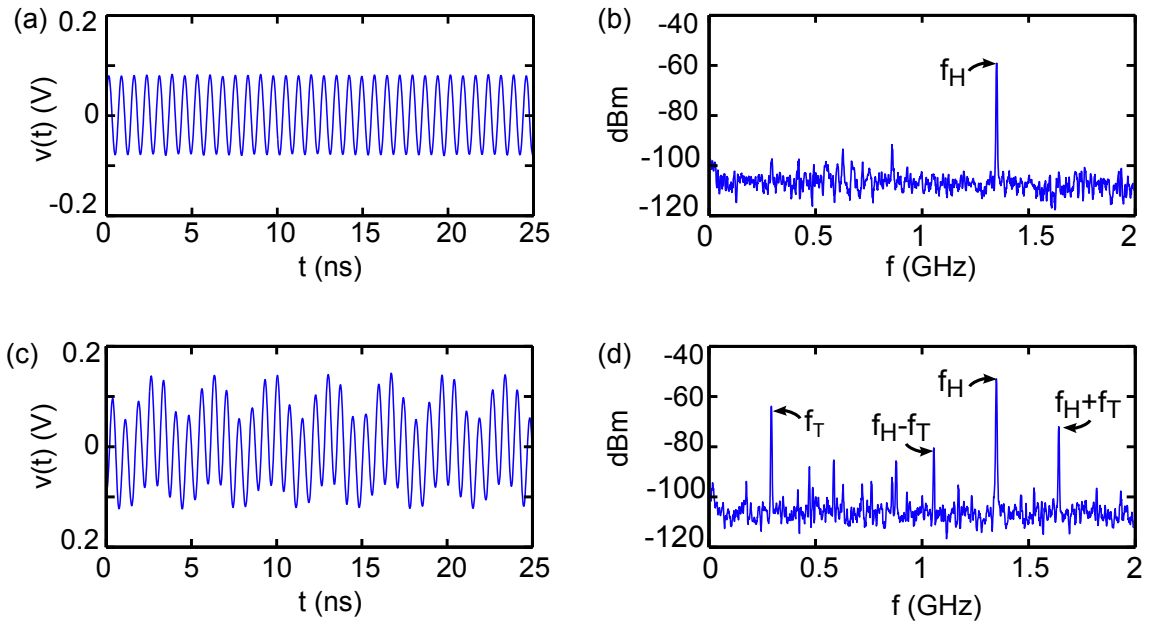

Figure 4.17: **Experimental cavity-feedback system dynamics.** (a) Periodic time series and (b) power spectral density (PSD) of v(t) for $G \sim 1.5$. (c) Quasiperiodic time series and (d) PSD for $G \sim 2$ In the experiment, the bias voltage in the nonlinear circuit is $v_b = 0.9$ V.

and $f_H + f_T = 1.642 \pm 10^{-3}$ GHz (errors represents the resolution of the frequency spacing for the Fourier transform magnitude). This distribution of quasiperiodic frequencies is qualitatively similar to the dynamics used for 2D position sensing in Ch. 3.

Delay-Gain Distribution

With the quasiperiodic dynamics measured, the system is switched off and the pulse response of the cavity is acquired for this configuration of the system (position of the scatterer, temperature of the room, humidity of the room, etc.). The plot of the measured $r_{out}(\tau_i) = g_i$ is shown in Fig. 4.18 for $\tau_1 = 0$ ns to $\tau_N = \tau_{max} = 200$ ns. Thus, it remains to simulate the cavity-feedback system with r_{out} as the delay-gain distribution of the model.

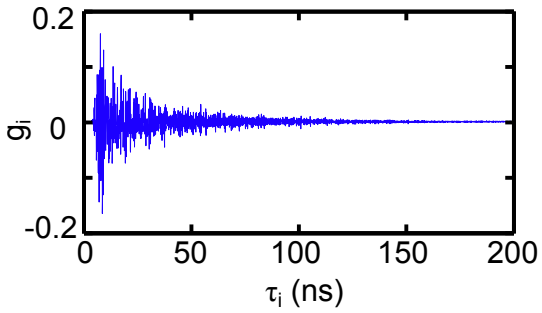

Figure 4.18: **Delay-gain distribution of the cavity-feedback system.** The pulse response $g_i = r_{\text{out}}(\tau_i)$ with $\tau_{\text{max}} = 200$ ns.

Simulated Dynamics

Beginning with $G = 0.9$ in Eqs. (4.15) - (4.21) of the model system, time series are generated (using an Adams-Bashforth numerical integrator algorithm) as G is increased to $G = 2$ such that the dynamics also exhibits Hopf and torus bifurcations. The temporal evolutions and PSDs of the periodic simulated dynamics are shown in Figs. 4.19a-b for $G = 1.5$. Similar to the experimental dynamics, the periodic state is nearly sinusoidal and the Hopf frequency is $f_{\text{H}} = 1.36$ GHz. The presence of such large frequency pulling in the model is a good indication that the individual models for the nonlinear circuit and delay-gain distribution correctly approximate the experimental system.

Furthermore, the quasiperiodic state and PSD from the simulation are plotted in Figs. 4.19c-d for $G = 2$. The temporal evolution of the dynamics is qualitatively similar to the experiment and the PSD shows a torus frequency at $f_{\text{T}} = 292$ MHz with frequency mixing at $f_{\text{H}} - f_{\text{T}} = 1.07$ GHz and $f_{\text{H}} + f_{\text{T}} = 1.65$ GHz. These frequencies represent the primary peaks of the simulated PSD (there are other peaks that correspond to linear combinations of f_{T} and f_{H}). Thus, this distribution of quasiperiodic frequencies is qualitatively similar to the experimental dynamics.

One possible reason for the differences between the simulated and experimen-

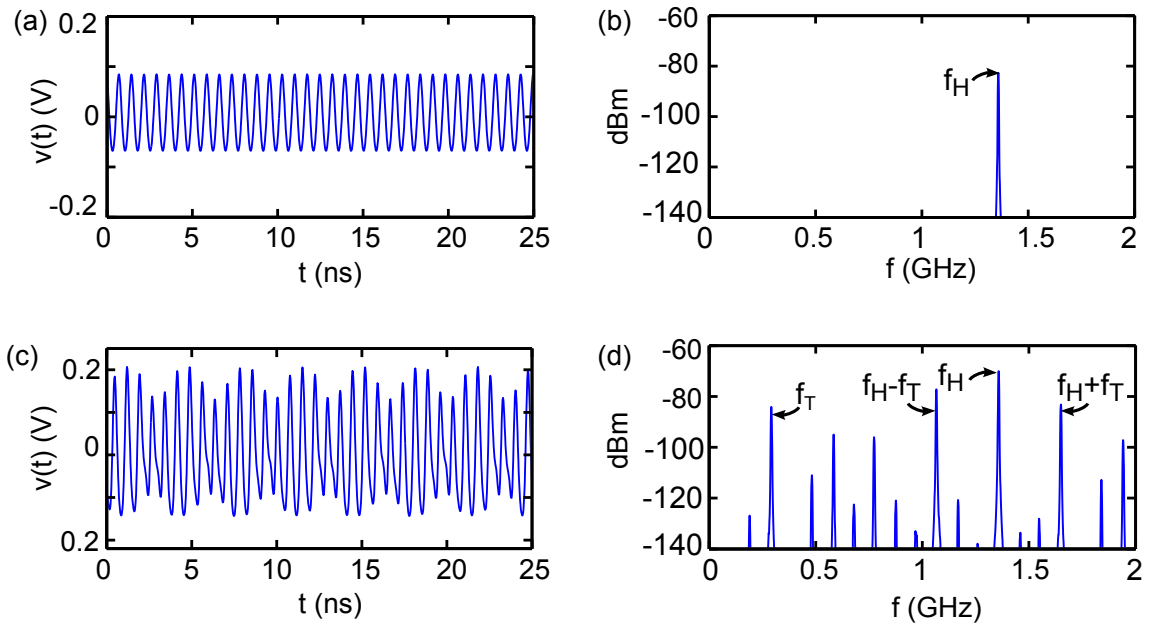

Figure 4.19: **Simulated cavity-feedback system dynamics.** (a) Periodic time series and (b) power spectral density (PSD) of v(t) for $G = 1.5$. (c) Quasiperiodic time series and (d) PSD for $G = 2$. The bias voltage in the model for the nonlinear circuit is $v_b = 0.9$ V.

tal quasiperiodic data can be attributed to the order of the filters in the model. As shown in the simulated quasiperiodic time series and PSD, there are harmonics (of f_H and f_T) that are not present in the experimental dynamics. Thus, the experimental system attenuates more frequencies than the simulation. Increasing the order of the first-order low-pass filter in the nonlinear circuit model as well as the order of the two-pole bandpass filter in the feedback loop is one option to try improving the model. However, higher-order filters add additional differential equations to the simulations and may not necessarily be enough of an improvement to yield more quantitative agreement. Rather than incease the model's complexity to obtain better agreement, I will show in the next chapter that a decrease in the model's complexity can provide a deeper insight into the origins of the system's quasiperiodic frequencies.

4.4 Summary

In conclusion, the cavity-feedback system can be simulated using separately developed models: (i) a nonlinear circuit model comprised of a nonlinear function that switches its output transfer function between two different low-pass filters, (ii) a wave-chaotic cavity model comprised of set of time-delays with relative gain coefficients, and (iii) an external feedback loop model comprised of a band-pass filter with gain. Each of these three models contains parameters that are obtained from experimental measurements. The main two components of the cavity-feedback system model, (i) and (ii), are summarized separately below.

Summary of Modeling the Nonlinear Circuit

In this chapter, I examine the nonlinear circuit's input-characteristics as a function of the input driving frequency. For high enough input amplitudes, the circuit creates a tent-like nonlinear function between its input and output voltages. But, as f increases (beyond $\sim$ 500 MHz), the amplitudes of the output signals decrease and the phase delay through the circuit increases. Both of these characteristics are typical of low-pass filtering effects at the output of the nonlinear circuit.

Then, in order to model these filtering effects, I measure separately the transfer functions of the nonlinear circuit in its linear and anti-linear regimes. Using the transfer function magnitudes of a first-order low-pass filter and a third-order Chebyshev filter, I fit these measurements and use the time-domain representations of the transfer functions to create an approximately piecewise-linear model. Lastly, using a model for a continuous switch and a high-pass filter to simulate the ac-coupled output of the circuit, I fit the model's output to the experimental high-frequency distortions.

Summary of Modeling the Wave-Chaotic Cavity

The wave-chaotic cavity can be modeled using a distribution of time-delays and gain coefficients that are obtained using the pulse response of the cavity $r_{\text{out}}(t)$. In the frequency domain, this representation of the model is a multiplication of the cavity's transfer function, and in the time domain, this is equivalent to a convolution with $r_{\text{out}}(t)$. Due to the discrete nature of the digital sampling oscilloscope, this convolution is actually a discrete sum.

Concluding Remarks

Overall, this chapter represents a methodology for deconstructing a complex experimental system into its essential components. The nonlinear circuit is the main component of the system and therefore its model uses the most detail. Although it is a transistor-based circuit, its main effects on the dynamics (including distortions) can be approximated with a nonlinear function and filtering. In addition, because the experimental system has a finite bandwidth associated with its electronics, the effects of the wave-chaotic cavity can be approximated with a finite pulse response as opposed to an infinitely sharp delta function. Lastly, each of the electronic components in the external feedback loop are all approximately linear and therefore can be treated as a lumped element in the model. The results of combining these models demonstrate that the quasiperiodic dynamics of the experiment can be numerically predicted (approximately) using a simulation. In the next chapter, rather than continue with numerical modeling, I focus on the mathematical representation of a simplified model for the cavity-feedback system to derive analytical expressions for estimating the quasiperiodic frequencies f_{H} and f_{T}.

Chapter 5

Predicting the Quasiperiodic Frequencies of the Cavity-Feedback System

The goal for this chapter is to gain insight into the mechanisms that lead to the quasiperiodic dynamics of cavity-feedback system. To do so, I develop a general theory for its quasiperiodicity using a simplified, though representative, model of the experimental setup. I simplify the full model of the cavity-feedback system from Ch. 5 by replacing the nonlinear circuit (NLC) with a cubic nonlinear function and by using a band-pass filter to describe the overall bandwidth of the system. Using this simplified model, I apply a linear-stability analysis and use the separation of the time scales to derive expressions for the frequencies at the onset of the Hopf and torus bifurcations.

In addition, I derive new methods for estimating these frequencies without having to access the quasiperiodic dynamics through simulations or experiments. These new methods are investigated to provide: (i) an intuitive approach for understanding the origins of the quasiperiodic frequencies and (ii) an approximation of the frequency distribution for determining the required bandwidth of measurement devices. As I will show in this chapter, my prediction methods can estimate the experimental quasiperiodic frequencies in the cavity-feedback system to within ±20 MHz, which is small in comparison to range of frequencies that are observed in Chs. 3-4 (0.2 GHz $< f <$ 1.8 GHz).

However, the resolution of the quasiperiodic frequency predictions cannot provide estimates of the frequency shifts $\Delta f_{\mathrm{T,H}}$ ($\sim$ kHz changes) as the scatterer translates (investigated in Ch. 6). Although my 2D position-sensing method uses $\Delta f_{\mathrm{T,H}}$

for imaging, the acquisition method for measuring these frequency shifts still requires the initial values of $f_{\mathrm{T,H}}$ as parameters of the numerical fit of the data (see Ch. 3 and Appendix B). Thus, the results from this chapter also provide estimates for the initial fitting parameters of the quasiperiodic data.

In order to help with the theory in this chapter, I switch my notation for the frequency f to the angular frequency $\omega = 2\pi f$ and change from quasiperiodicity frequencies f_{T} and f_{H} to the angular frequencies $\Omega_{\mathrm{T}} = 2\pi f_{\mathrm{T}}$ and $\Omega_{\mathrm{H}} = 2\pi f_{\mathrm{H}}$. This change accounts for the factors of 2π that arise throughout my derivations.

Lastly, several people contributed to the results that follow. Illing *et al.*'s work on band-pass filters with time-delayed nonlinear feedback [32] and Chembo *et al.*'s work on instabilities in OEOs [75] form the foundations for my linear stability analysis of the Hopf and torus bifurcations, respectively. Furthermore, communications with Thomas Erneux provided insight into the separation of time scales analysis, and Damien Rontani's numerical simulations allowed for well-resolved bifurcation diagrams to find the correct system parameters at the onset of quasiperiodicity and for a fast implementation of the frequency estimation methods. Finally, my experimental and theoretical results presented in this chapter are part of an investigation that is currently ongoing.

5.1 Simplified Model of the Cavity-Feedback System

In Ch. 4, I demonstrate that quasiperiodicity in the cavity-feedback system can be recovered using a model with three main components: (i) a nonlinear function with low-pass filters (with transfer functions $H_{\mathrm{LP,\,A,L}}(f)$) to represent the NLC, (ii) a joint delay-gain distribution (τ_i, g_i) where $i \in [1, N]$ for the wave-chaotic cavity, and (iii) a band-pass filter (with transfer function $H_{\mathrm{BP}}(f)$) and gain to represent the exter-

nal feedback loop. To simplify this model, I choose to combine the net effects of the low-pass filters from the NLC with the band-pass filter from the external feedback loop to create a unique band-pass-filter model that describes approximately the bandwidth of the entire cavity-feedback system, where the new bandpass-filter transfer function H'_{BP} reads

$$H'_{\mathrm{BP}}(\omega) \sim H_{\mathrm{LP,\,L,A}}(\omega) H_{\mathrm{BP}}(\omega). \tag{5.1}$$

This assumes that the overall bandwidth of the feedback loop is approximately a band-pass filter and that the changes in the NLC bandwidth from switching between $H_{\mathrm{LP,\,L}}(\omega)$ and $H_{\mathrm{LP,\,A}}(\omega)$ are not significant for predicting the quasiperiodic frequencies of the system (see Appendix C for more details of this approximation).

Furthermore, to simplify the analytics in this chapter, I also approximate the nonlinear function $F(\mathrm{v_{in}})$ with a third-order polynomial

$$F(\mathrm{v_{in}}) = \alpha_1(\mathrm{v_{in}} + \mathrm{v_b}) - [\alpha_2(\mathrm{v_{in}} + \mathrm{v_b})]^3, \tag{5.2}$$

where α_1, and α_2 are constant coefficients and where $\mathrm{v_b}$ is a constant used to tune the operating point of the nonlinearity (see Appendix C). Though these simplifications neglect aspects of the detailed model from Ch. 4, I show that the results from this simplified model can be used to approximate the frequencies Ω_{T} and Ω_{H} in the experimental system.

This simplified model is represented in Fig. 5.1a, where a band-pass filter outputs a time-evolving signal $\mathrm{v}(t)$ that is amplified by a gain G and split into N different paths, each of which has a propagation delay τ_i and gain coefficient g_i. All of the outputs from the feedback loops are then summed before driving the nonlinear

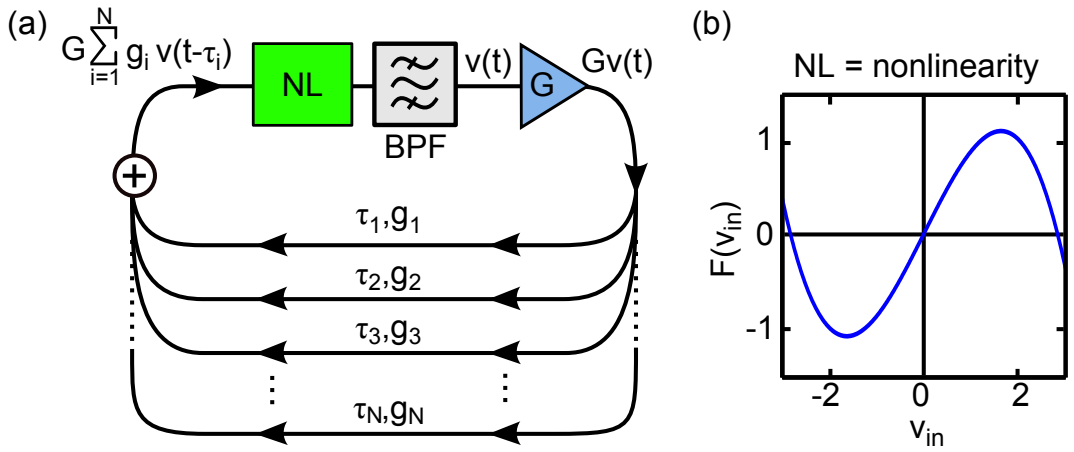

Figure 5.1: **Band-pass filter with nonlinear feedback.** (a) The output of a band–pass filter $\mathrm{v}(t)$ is split among N time-delays, each with propagation delay τ_i and gain coefficient g_i. The delayed outputs of each feedback loop are summed and amplified with linear gain G before passing through a nonlinearity (NL). The output of the NL drives the band-pass filter, forming a closed loop feedback system. (b) Cubic nonlinearity using the third-degree polynomial $F(\mathrm{v}_{\mathrm{in}})$ with $\alpha_1 = 1$, $\alpha_2 = 0.5$ and $\mathrm{v}_{\mathrm{b}} = 0$.

function, shown in Fig. 5.1b, to form the closed-loop feedback system.

The simplified model for the cavity-feedback system is described by the delay differential equation (DDE) for a band-pass filter with nonlinear feedback [80] and N time delays

$$\frac{\dot{\mathrm{v}}(t)}{\Delta} + \mathrm{v}(t) + \frac{\omega_{\mathrm{o}}^2}{\Delta}\int_{-\infty}^{t} \mathrm{v}(t')\,\mathrm{d}t' = F\left[G\sum_{i=1}^{N} g_i \mathrm{v}(t-\tau_i)\right], \tag{5.3}$$

where $\Delta = \omega^{(+)} - \omega^{(-)}$, $\omega_{\mathrm{o}} = \sqrt{\omega^{(+)}\omega^{(-)}}$, and $\omega^{(+)}$ ($\omega^{(-)}$) is the upper (lower) cutoff frequency of the new band-pass filter. The sum over all delayed terms $\mathrm{v}(t-\tau_i)$ with gain coefficients g_i allows for the interference of waves propagating through the feedback. Though the model for the cavity feedback is more complicated when compared to typical nonlinear feedback systems, it can easily be reduced to the systems shown in Refs. [22, 81, 82] for the $N = 1-3$ cases. Lastly, because each

g_i represents the loss of a path through the cavity, I limit the values of g_i to the physical case of $-1 < g_i < 1$ and $\sum_{i=1}^{N} |g_i| \leq 1$.

The typical approach to predict the dynamics of Eq. (5.3) involves measuring the experimental parameters ($\omega^{(+)}$, $\omega^{(-)}$, G, g_i, and τ_i) and then implementing a numeric model, similar to the methods in Ch. 4. Rather than repeating such a numerical analysis, I will instead use Eq. (5.3) as a starting point to predict analytically the frequencies Ω_{H} and Ω_{T} in the simplified model. Then, I will connect my theoretical analysis to a measurement based on a closed-loop transfer function derived from linear control theory [76] and demonstrate experimental methods for obtaining parameters needed to evaluate the predictions. As I will show, because this closed-loop transfer function is independent of the number of time delays in the feedback loop, this approach is applicable to the cavity-feedback system which, in reality, contains a continuum of time delays.

In the remainder of this chapter, I first discuss how I develop a method for predicting the Hopf bifurcation frequency Ω_{H} and test it with simulations of the simplified model with up to $N = 10$ time delays. There has already been extensive research on the Hopf bifurcation in band-pass filtered systems with a single time delay [32], and therefore a portion of this section reviews the literature on that subject. Then, I examine the frequency Ω_{T} of the torus bifurcation, which has only been studied for the cases of one [83], two [84], and three [75] time-delays in optoelectronic oscillators (OEOs). The analytical methods used in these references yield equations that must be solved numerically. Instead of following this approach, I provide new techniques for obtaining approximate predictions for Ω_{T} and test them with simulations of the simplified model with up to $N = 10$ time delays. Finally, I apply my methods experimentally in systems with $N = 1$ and $N = 2$ time delays as well as in the cavity-feedback system ($N >> 10$) to demonstrate the predictive

power of my approach on real systems.

5.2 Predicting the Frequency of the Hopf Bifurcation

5.2.1 Linear Stability Analysis

The initial Hopf bifurcation for a band-pass filter with nonlinear feedback results from an instability about its steady state, which gives rise to a limit cycle [32]. For the purposes of this analysis and without loss of generality, I set $\mathrm{v_b} = 0$ in the cubic nonlinearity. Typically, predicting the frequency Ω_H requires a linear stability analysis of Eq. (5.3) about its steady state $\mathrm{v}_s = 0$ [32]. The linearized equation that describes the evolution of a small perturbation $\delta\mathrm{v}$ about v_s reads

$$\frac{\delta\dot{\mathrm{v}}(t)}{\Delta} + \delta\mathrm{v}(t) + \frac{(\omega_o)^2}{\Delta}\int_{-\infty}^{t}\delta\mathrm{v}(t')\,\mathrm{d}t' = G\sum_{i=1}^{N} b_i\,\delta\mathrm{v}(t-\tau_i), \tag{5.4}$$

where $b_i = g_i\frac{\mathrm{d}F}{\mathrm{dv}}|_{\mathrm{v}_s} = F'(0)g_i$. In the next step, I assume a solution of the form $\delta\mathrm{v}(t) = Ae^{i\Omega_\mathrm{H}t}$, where A is a constant amplitude and Ω_H is the frequency of the Hopf bifurcation (for an illustration of this type of this type of Hopf bifurcation in a phase space representation, see Appendix C). This simplifies Eq. (5.4) to

$$\frac{i\Omega_\mathrm{H}}{\Delta} + 1 + \frac{\omega_\mathrm{o}^2}{i\Omega_\mathrm{H}\Delta} - G\sum_{i=1}^{N} b_i e^{-i\Omega_\mathrm{H}\tau_i} = 0. \tag{5.5}$$

To solve for Ω_H, references such as [32] and [35] separate the real and imaginary parts of Eq. (5.5) to yield coupled transcendental equations

$$G\sum_{i=1}^{N} b_i\cos(\Omega_\mathrm{H}\tau_i) = 1, \tag{5.6}$$

$$G\sum_{i=1}^{N} b_i \sin(\Omega_{\mathrm{H}}\tau_i) = \frac{\omega_{\mathrm{o}}^2 - \Omega_{\mathrm{H}}^2}{\Omega_{\mathrm{H}}\Delta}. \tag{5.7}$$

Because $\sum_{i=1}^{N} |g_i| \leq 1$, the condition $|GF'(0)| \geq 1$ must hold in order for Eq. (5.6) to be satisfied. This will be important for later discussions. Given (τ_i, g_i) as well as Δ and ω_{o}, Eqs. (5.6) and (5.7) can be solved numerically to predict the value of Ω_{H} at the initial Hopf bifurcation.

5.2.2 New Approach: Closed-Loop Transfer Function

Rather than taking this approach, which involves precise measurements of the system's parameters, I develop a new method to estimate Ω_{H} that can be used in the experimental system without having to measure (τ_i, g_i) and implementing a numerical computation. First, I focus on Eq. (5.5) and note that it is still valid if I take the magnitude of both sides

$$\left| \frac{i\Omega_{\mathrm{H}}}{\Delta} + 1 + \frac{\omega_{\mathrm{o}}^2}{i\Omega_{\mathrm{H}}\Delta} - G\sum_{i=1}^{N} b_i e^{-i\Omega_{\mathrm{H}}\tau_i} \right| = 0. \tag{5.8}$$

Instead of solving the condition for which the left-hand-side of Eq. (5.8) is zero, I am interested in solving when its inverse diverges

$$\frac{1}{|i\Omega_{\mathrm{H}}/\Delta + 1 + \omega_{\mathrm{o}}^2/(i\Omega_{\mathrm{H}}\Delta) - G\sum_{i=1}^{N} b_i e^{-i\Omega_{\mathrm{H}}\tau_i}|} \to \infty. \tag{5.9}$$

Interestingly, Eq. (5.9) is equivalent to the magnitude of a closed-loop transfer function that can be measured approximately in an experiment, where a closed-loop transfer function $H_{\mathrm{closed}}(\omega)$ describes the frequency response of a system that contains a closed feedback loop. In Fig. 5.2, I illustrate the differences between a device with an open-loop and a closed-loop transfer function, each containing

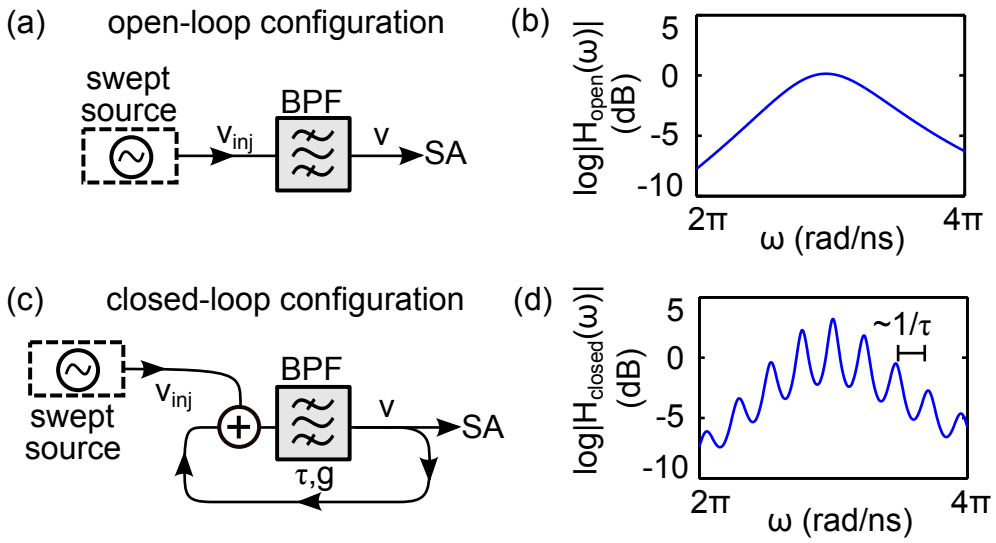

Figure 5.2: **Measuring open-loop and closed-loop transfer functions** of a band–pass filter using a swept source and spectrum analyzer (SA). (a) Open-loop configuration for measuring (b) $|H_{\text{open}}(\omega)|$ and (c) closed-loop configuration with time delay τ and gain coefficient $g = 0.3$ for measuring (d) $|H_{\text{closed}}(\omega)|$.

a band-pass filter. In Figs. 5.2a-b, the magnitude of the open-loop transfer function $|H_{\text{open}}(\omega)|$ is measured between its input and output using a sinusoidal signal generator with automatic frequency sweep (swept source) and a spectrum analyzer.

In Fig. 5.2c, the band-pass filter output is fed back to its input. The closed-loop transfer function of this system is only valid in the linear regime of the system where the dynamics do not self-oscillate. For this example, the gain coefficient $g = 0.3$ is chosen as the gain of the feedback loop (net loss is greater than net gain). The closed-loop transfer function magnitude $|H_{\text{closed}}(\omega)|$ in Fig. 5.2d now contains resonant peaks that are spaced by approximately $1/\tau$, where τ is the time delay of the closed loop. This type of closed-loop transfer function has been previously measured to predict the side-mode resonant peaks of an OEO with two time delays [81]. I will show that, in the cavity-feedback system, the resonances of the closed-loop transfer function can be used to predict approximately Ω_{H} and Ω_{T}.

Resonance Method for Predicting the Hopf Frequency

The general setup for the measurement of Eq. (5.9) is shown in Fig. 5.3a. Similar to Fig. 5.2b, it uses a swept source that drives the feedback loop and a spectrum analyzer to locate the closed-loop resonances. I refer to this prediction technique as the *resonance* (R) method in the rest of this dissertation. The amplitude of the injected signal $\mathrm{v}_{\mathrm{inj}}$ is small such that it probes the linear regime of $F(\mathrm{v}_{\mathrm{in}})$ near $F(0)$ with an approximate linear gain equal to $\sim F'(0)$. The ratio $H_{\mathrm{R}}(\omega) = \tilde{\mathrm{v}}/\tilde{\mathrm{v}}_{\mathrm{inj}}$ is equal to the closed-loop transfer function of the system, where $\tilde{\mathrm{v}}_{\mathrm{inj}}$ and $\tilde{\mathrm{v}}$ are the Fourier transforms of $\mathrm{v}_{\mathrm{inj}}$ and v, respectively. In a previously published work, I have verified that this technique can predict the multimode spectrum of a band-pass filtered nonlinear feedback system with a single time delay [85]. The magnitude of $H_{\mathrm{R}}(\omega)$ from Fig. 5.3a is given by

$$|H_{\mathrm{R}}(\omega)| = \left| \frac{\tilde{\mathrm{v}}}{\tilde{\mathrm{v}}_{inj}} \right| = \frac{1}{|i\omega/\Delta + 1 + \omega_{\mathrm{o}}^2/(i\omega\Delta) - G\sum_{i=1}^{N} b_i e^{-i\omega\tau_i}|}, \tag{5.10}$$

which is equivalent the left-hand-side of Eq. (5.9) for $\omega \to \Omega_{\mathrm{H}}$.

As mentioned earlier, this closed-loop transfer function is only valid where the dynamics do not self-oscillate. I previously noted that the condition $|GF'(0)| \geq 1$ is required in order for the system to exhibit a Hopf bifurcation. To suppress the limit cycle, I can always tune G to a value such that $|GF'(0)| < 1$. Thus, when measuring $|H_R(\omega)|$, the system never self-oscillates and always relaxes back to its stable fixed point at $\mathrm{v} = \mathrm{v}_s = 0$.

However, because this technique can only be applied when $|GF'(0)| < 1$, $\Omega_{\mathrm{H,R}}$ yields only an approximation for Ω_{H}. To illustrate this issue, I present a typical simulated bifurcation diagram of the dynamics with the Hopf and torus bifurcations

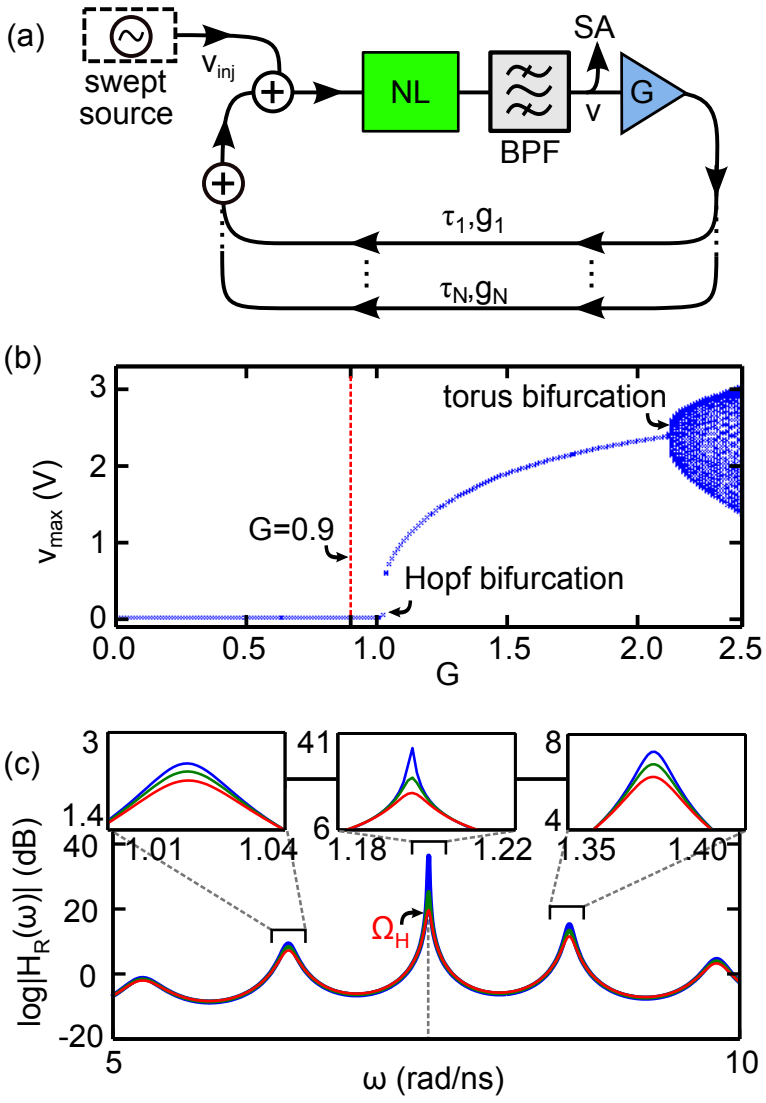

Figure 5.3: **Implementing the resonance method.** (a) General setup for measuring the magnitude of $H_R(\omega)$. (b) Bifurcation diagram illustrating the Hopf and torus bifurcation points with respect to the gain G. (c) $H_R(\omega)$ for $G = 0.9$ (red), $G = 0.95$ (green), and $G = 0.99$ (blue). In each of these three cases, the global maximum occurs at approximately the same frequency labeled by $\Omega_{H,R}$.

of the simplified model with $N = 1$ time delays in Fig. 5.3b (similar to Figs. 2.5 and 2.8). In this case $F'(0) = 1$ and the bifurcation tuning parameter is G. As shown in the figure, the Hopf bifurcation point occurs for $|G| > 1$. Beyond this point, the system self-oscillates. To implement the resonance method, the closed-loop transfer

function magnitude $|H_{\mathrm{R}}(\omega)|$ of the system is measured for $G = 0.9$ in Fig. 5.3c. The largest peak in $|H_{\mathrm{R}}(\omega)|$ is labeled as $\Omega_{\mathrm{H,\,R}}$, which is an estimation of the solution for Ω_{H} in Eq. (5.8). The assumption of this method is that this peak remains a global maximum as G is tuned up to and beyond the Hopf bifurcation point. To support this assumption, I also plot $|H_{\mathrm{R}}(\omega)|$ when the gain is tuned to $G = 0.95$ and $G = 0.99$ in Fig 5.3c. In both additional cases, the heights of the transfer function peaks scale together and the global maximum remains the same. As I will now show, this approximation can estimate Ω_{H} for most cases (there are a few cases where this assumption is not true and the global maximum changes when G is arbitrarily close to the bifurcation point and these cases are discussed in detail later).

To illustrate how this measurement can estimate Ω_{H}, I first examine two simple numerical examples. In Figs. 5.4a-b, I plot $|H_{\mathrm{R}}(\omega)|$ for a given (τ_i, g_i) in the $N = 1$ and $N = 2$ cases, respectively. In Figs. 5.4a-b, resonant peaks are spaced by approximately $1/\tau_{\mathrm{max}}$, where $\tau_{\mathrm{max}} = \max(\tau_i)$ for $i \in [1, N]$ (experimentally, I note that, as τ_{max} becomes large, the resolution of the resonance sweep is a limiting factor in this method). Typically, as the gain of the feedback is increased, the heights of these peaks grow, and, when the system bifurcates, the frequency resonance with the highest gain is equal to Ω_{H}. Subsequently, in each plot, the location of the largest peak is labeled as the estimate $\Omega_{\mathrm{H,R}}$.

To test the predictions made using $|H_{\mathrm{R}}(\omega)|$, I integrate numerically the solutions of Eq. (6.3) and increase G until the first Hopf bifurcation. In Figs. 5.4c-d, I plot the PSDs of the $N = 1$ and $N = 2$ cases after the Hopf bifurcation, respectively, labeling Ω_{H} as the largest peak in each spectrum. For the $N = 1$ ($N = 2$) the predicted $\Omega_{\mathrm{H,R}} = 8.872$ (8.891) rad/ns for $\Omega_{\mathrm{H}} = 8.870$ (8.884) rad/ns. Thus, the R method yields predictions with agreement to within $\pm 10^{-2}$ rad/ns in these two simple examples.

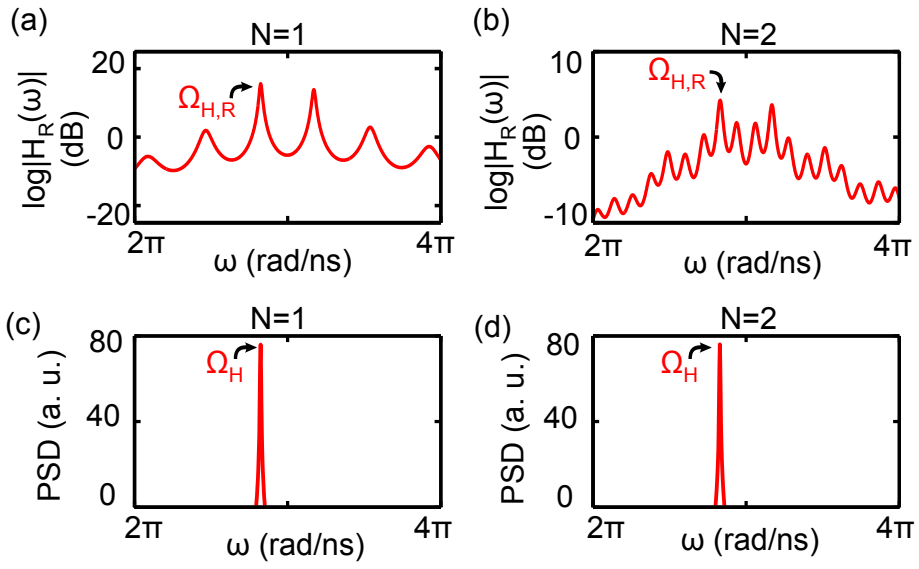

Figure 5.4: Predicting the first Hopf bifurcation frequency using the resonance method. (a) Simulated $|H_R(\omega)|$ for the simplest case of $N = 1$ with parameters $\omega^{(+)} = 10.7$ rad/ns, $\omega^{(-)} = 8.2$ rad/ns, $G = 0.9$, $g_1 = 1$, and $\tau_1 = 5$ ns. (b) Simulated $|H_R(\omega)|$ for the case of $N = 2$ with parameters $\omega^{(+)} = 10.7$ rad/ns, $\omega^{(-)} = 8.2$ rad/ns, $G = 0.9$, $g_1 = 0.2$, $g_2 = 0.3$, $\tau_1 = 5$ ns, and $\tau_2 = 12$ ns. Power spectral density (PSD) of the periodic solutions to Eq. (6.3) when the gain is tuned up to $G = 1.45$ for the (c) N=1 case and $G = 2.6$ for the (d) $N = 2$ case.

To test the R method in more complicated examples ($N > 2$), I perform systematic analyses for N ranging from 2 to 10. For each N, I simulate the system's bifurcation diagram 5 times, each with different (τ_i, g_i). For each case, I determine Ω_H and $\Omega_{H,R}$ (using $G = 0.95$), and in Fig. 5.5, I plot the mean $\mu(N)$ and standard deviation $\sigma(N)$ of the difference $(\Omega_H - \Omega_{H,R})$ as a function of N. Based on these simulations, I observe that $|\mu(N)| < 0.5$ rad/ns and $|\sigma(N)| < 1$ rad/ns for all N.

For the $N = 4$ cases, $\sigma(N = 4)$ and $\mu(N = 4)$ are larger in comparison to all other cases. This is because my calculations assume that the global maximum of $|\Omega_{H,R}|$ with $G = 0.95$ remains the global maximum as G is tuned beyond the Hopf bifurcation point. However, as detailed in Appendix C, this assumption can be false such that a nearby local maxima rises above my estimation when G is tuned slightly

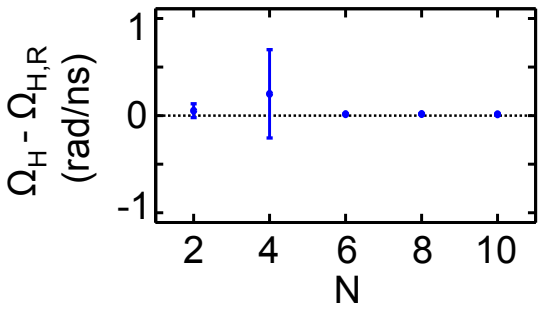

Figure 5.5: **Resonance sweep method for dynamical systems with multiple time-delays.** For each simulation with $N = 2$ to $N = 10$ feedback loops, τ_i and g_i are sampled from uniform distributions such that 5 ns $< \tau_i <$50 ns and $-1 < g_i < 1$. Once the gains are chosen, they are the renormalized using the condition $\sum_{i=1}^{N} |g_i| = 1$. The bandwidth parameters are chosen to be $\omega^{(+)} = 9.4$ and $\omega^{(-)} = 6.3$. When implementing the R method, $G = 0.95$. The predictions are tested by calculating the mean $\mu(N)$ (blue dots) and standard deviation $\sigma(N)$ (error bars) of $(\Omega_H - \Omega_{H,R})$ for each N.

above 0.95 while still below the Hopf bifurcation point. Thus, the limitations on the predictive power of this method are demonstrated by the $N = 4$ cases. However, even with this special case, Fig.5.5 demonstrates that the resonance method can be used to estimate Ω_H.

Lastly, I note that band-pass filtered systems with time-delayed nonlinear feedback can experience multi-stability and that this method is developed for predicting approximately Ω_H as G is increased monotonically. In the next section, I develop and use a similar technique for predicting the frequencies of the subsequent torus bifurcation.

5.3 Predicting the Frequency of the Torus Bifurcation

Recently, Chembo *et al.* [75] developed an analytical theory for predicting the instability of a microwave OEO in its periodic regime. Their results show that, for an

OEO with one time delay τ, a torus bifurcation occurs for large enough feedback gain G. The torus frequency Ω_{T} is mixed with the original Hopf frequency Ω_{H} so that the quasiperiodic frequencies present in the dynamics of $\mathrm{v}(t)$ are Ω_{H}, $\Omega_{\mathrm{H}}+\Omega_{\mathrm{T}}$, and $\Omega_{\mathrm{H}}-\Omega_{\mathrm{T}}$. Using their theory for an OEO with $N=1$, Ω_{T} is predicted to be $\sim \pi/\tau$. Their analytical theory serves as the primary motivation of my methods to predict Ω_{T} in a feedback system with N time delays and gains (τ_i, g_i).

In Ref. [75], an equation is derived to describe the slowly modulated amplitude of the periodic oscillations. This so-called *amplitude equation* governs the dynamics of the amplitude and can be used to perform an additional linear stability analysis to solve for the conditions of the torus bifurcation. In this section, I introduce a similar amplitude equation for my system with N time delays and analyze its steady-state properties. Then, with a linear stability analysis of that equation, I repeat the steps from the previous section for finding the conditions of the bifurcation and estimating the frequency Ω_{T}.

5.3.1 The Amplitude Equation

As shown in the previous section, after the initial Hopf bifurcation, the periodic dynamics of the system can be approximately modeled by $\mathrm{v}(t) = \frac{1}{2}A(e^{i\Omega_{\mathrm{H}}t} + e^{-i\Omega_{\mathrm{H}}t})$, where A is the amplitude of oscillations. As the gain of the feedback is increased, a second Hopf bifurcation occurs in the amplitude A, and the dynamical state of the system takes on the form $\mathrm{v}(t) \sim \frac{1}{2}A(t)(e^{i\Omega_{\mathrm{H}}t} + e^{-i\Omega_{\mathrm{H}}t})$, where $A(t)$ is the slowly varying amplitude. To simplify the analysis, I assume that $\Omega_{\mathrm{H}} \sim \omega_{\mathrm{o}}$, similar to Ref. [75]. Then, using a separation of time-scales between $A(t)$ and $e^{\pm i\omega_{\mathrm{o}}t}$ and assuming

$\omega_o > \Delta$, the dynamical equation for $A(t)$ can be approximated by

$$\dot{A}(t) = \frac{\Delta}{2}\left(F\left[G\sum_{i=1}^{N} g_i A(t-\tau_i)\right] - A(t)\right), \tag{5.11}$$

which is the system's amplitude equation (the details of its derivation and a simple example of the amplitude dynamics can be found in Appendix C). I note that Eq. (5.11) models a low-pass filter with time-delayed nonlinear feedback, similar to the well-known Ikeda system [36]. The low-pass cutoff frequency for the amplitude equation is $\Delta/2$, which is half of the bandwidth of the band-pass filter used in Eq. (5.3).

Using the amplitude equation, the torus bifurcation can be approximated as a second Hopf bifurcation of the amplitude A (see Appendix C). To analyze the Hopf bifurcation in the amplitude $A(t)$ (to quasiperiodicity in $v(t)$), I perform a linear stability analysis on the amplitude equation about its steady state A_s that satisfies

$$F(\bar{G}A_s) = A_s, \tag{5.12}$$

where $\bar{G} = G\sum_{i=1}^{N} g_i$. Given the simplified form of $F(v_{in})$ with $\alpha_1 = 1$, $\alpha_2 = 1/2$, and $v_b = 0$, the solution for the steady state amplitude as a function of $\bar{G}$ reduces to the analytical form

$$A_s = \pm\frac{\sqrt{\bar{G}-1}}{(\frac{1}{2}\bar{G})^{3/2}}, \tag{5.13}$$

which is consistent with the scaling of a supercritical Hopf bifurcation [23]. To help visualize the solution A_s, I plot in Fig. 5.6 the functions $y_1 = F(\bar{G}A)$ as well as $y_2 = A$, where $F(\bar{G}A)$ is plotted for two different values of $\bar{G}$. For $|\bar{G}| < 1$, the only solution is $A_s = 0$, however, for large enough $|\bar{G}|$, a new solution appears; it represents the steady state amplitude A_s of the limit cycle after the first Hopf bifurcation. The value

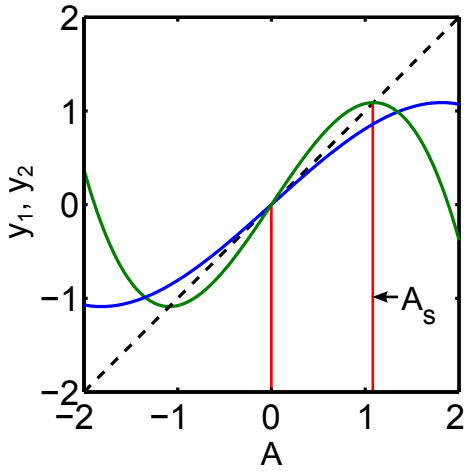

Figure 5.6: **Steady-state solutions of the amplitude equation.** (a) Intersections of the curve $y_1 = F(\bar{G}A)$ (blue for $\bar{G} = 0.9$ and green for $\bar{G} = 1.5$) and $y_2 = A$ (dotted line) give the steady state solution A_s for a stable limit cycle of the system.

of A_s with regards to the nonlinearity $F(\bar{G}A_s)$ is important for my methods and will be used in subsequent sections.

5.3.2 Linear Stability Analysis

The linearization of the amplitude equation about $A = A_s$ yields the dynamical equation for a perturbation δA

$$\delta\dot{A}(t) = \frac{\Delta}{2}\left[G\sum_{i=1}^{N} d_i \delta A(t-\tau_i) - \delta A(t)\right], \tag{5.14}$$

where $d_i = F'(\bar{G}A_s)g_i$ are constants (see Appendix C for the derivation of Eq. (5.14)). To investigate the stability of the amplitude equation and solve for Ω_T, I assume a solution of the form $\delta A(t) = Be^{i\Omega_T t}$ (for an illustration of this type of this type of torus bifurcation in a phase space representation, see Appendix C) and simplify Eq.

(5.14) to

$$\frac{2i\Omega_{\mathrm{T}}}{\Delta} + 1 + G\sum_{i=1}^{N} d_i e^{-i\Omega_{\mathrm{T}}\tau_i} = 0. \tag{5.15}$$

Similar to Eq. (5.5), this equation is solved by separating its real and imaginary parts to find the transcendental equations based on G, d_i, τ_i, and Δ

$$G\sum_{i=1}^{N} d_i \cos(\Omega_{\mathrm{T}}\tau_i) = 1, \tag{5.16}$$

$$G\sum_{i=1}^{N} d_i \sin(\Omega_{\mathrm{T}}\tau_i) = \frac{2\Omega_{\mathrm{T}}}{\Delta}. \tag{5.17}$$

In order for Eq. (5.16) to be satisfied, the condition $|GF'[\bar{G}A_s^*]| \geq 1$ is necessary, where A_s^* is the critical amplitude at the onset of the torus bifurcation. Typically, using such constraints, Ω_{T} is obtained by solving numerically Eqs. (5.16) and (5.17) given the system's parameters [32].

5.3.3 Closed-Loop Transfer Function

Instead, I repeat the procedure from Section 5.2 and construct a transfer function $H_{\mathrm{A}}(\omega)$ whose magnitude diverges at the solutions to Eq. (5.15)

$$|H_{\mathrm{A}}(\omega)| = \frac{1}{|2i\omega/\Delta + 1 - G\sum_{i=1}^{N} d_i e^{-i\omega\tau_i}|}. \tag{5.18}$$

Note that this transfer function is similar to Eq. (5.10), except that now the dependence on ω_o has been removed. This shifts the resonances of $|H_{\mathrm{A}}(\omega)|$ near the base-band frequencies of the system ($\omega \sim 0$). The value of Ω_T is estimated using the frequency of the global maxima of $|H_{\mathrm{A}}(\omega)|$. To test this method, I examine the two cases of a band-pass filter with time-delayed nonlinear feedback with $N = 1$

and $N = 2$ delays and gains discussed in the previous section, where I tune G such that the conditions $|GF'(0)| < 1$ and $|GF'(\bar{G}A_s^*)| < 1$ are satisfied and the system does not self oscillate.

Similar to $|H_R(\omega)|$, the global maxima of $|H_A(\omega)|$ represents an estimation for the Ω_T in Eq. (5.15). However, this estimation is different because the torus bifurcation point is located beyond the Hopf bifurcation point, as demonstrated in Fig. 5.3b. Therefore, $|H_A(\omega)|$ is always measured at a gain $G \sim 0.9$ that is far away from the torus bifurcation point (as opposed to the $|H_R(\omega)|$, which can be measured arbitrarily close to the Hopf bifurcation point). In addition, using $|H_A(\omega)|$ to estimate Ω_T assumes that its global maximum at $G \sim 0.9$ remains a global maximum for G tuned to the torus bifurcation. To support this assumption, I plot $|H_A(\omega)|$ as G is tuned to higher values in Fig. 5.7. The location of global maximum in the figure stays at approximately the same frequency (labeled $\Omega_{T,A}$) for $0.9 < G < 0.99$, and beyond this value I assume that continues to scale in a similar fashion (similar to the resonance method, this assumption can fail and is discussed in detail later).

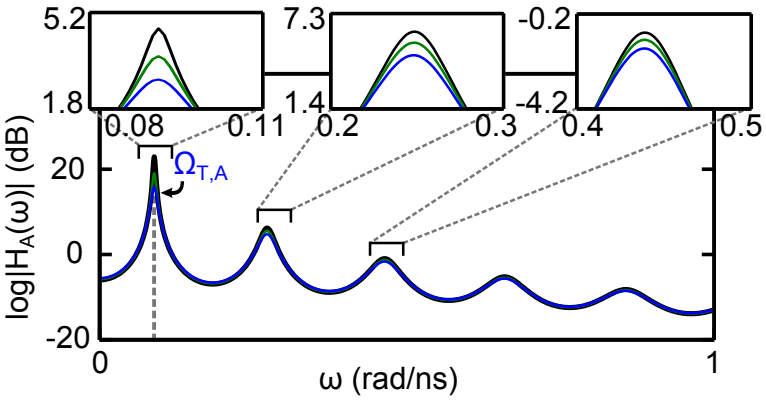

Figure 5.7: **Scaling of the closed-loop transfer function magnitude for the amplitude equation.** (a) $H_A(\omega)$ for $G = 0.9$ (blue), $G = 0.95$ (green), and $G = 0.99$ (black). In each of these three cases, the global maximum occurs at approximately the same frequency labeled by $\Omega_{T,A}$.

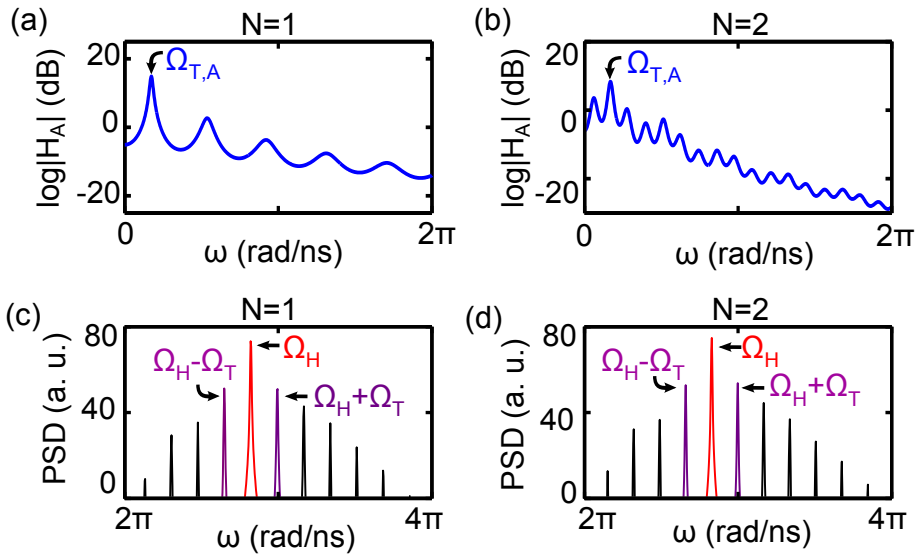

Figure 5.8: **Predicting the torus bifurcation frequencies using the closed-loop transfer function of the amplitude equation.** (a) Simulated $|H_A(\omega)|$ for the case of $N = 1$ with parameters $\omega^{(+)} = 10.7$ rad /ns, $\omega^{(-)} = 8.2$ rad/ns, $G = 0.9$, $g_1 = 1$, and $\tau_1 = 5$. (b) Simulated $|H_A(\omega)|$ for the case of $N = 2$ with parameters $\omega^{(+)} = 10.7$ rad/ns, $\omega^{(-)} = 8.2$ rad/ns, $G = 0.9$, $g_1 = 0.2$, $g_2 = 0.3$, and $\tau_1 = 5$, and $\tau_2 = 12$. PSD of the quasiperiodic solutions to Eq. (6.3) when the gain is tuned up to $G = 2.4$ for the (c) $N = 1$ case and $G = 4.8$ for the (d) $N = 2$ case.

To test this new closed-loop transfer function, I examine $|H_{\rm A}(\omega)|$ for the $N = 1$ and $N = 2$ cases. In Figs. 5.8a-b, I label the frequency at which $|H_{\rm A}(\omega)|$ is a maximum as $\Omega_{\rm T,A}$. In Figs. 5.8c-d, I also plot the PSDs of v(t) after the system has undergone a torus bifurcation and label the corresponding frequencies $\Omega_{\rm H}$ and $\Omega_{\rm H} \pm \Omega_{\rm T}$. In the $N = 1$ ($N = 2$) case, the predicted torus frequency is $\Omega_{\rm T,A} = 0.547$ (0.528) rad/ns and the observed torus frequency is $\Omega_{\rm T} = 0.542$ (0.534) rad/ns. Thus, in these cases, $|H_{\rm A}(\omega)|$ can be used to estimate $\Omega_{\rm T}$ to within ± 0.006 rad/ns.

However, from an experimental point-of-view, it is difficult to measure directly $|H_{\rm A}(\omega)|$ because it is the closed-loop transfer function for a low-pass filter that describes the spectrum of the amplitude equation; this low-pass filter does not actually exist in the experiment. However, I have developed two methods for recovering the

key parameters in $|H_{\mathrm{A}}(\omega)|$.

Method I: Amplitude Modulation

The first method for recovering $|H_{\mathrm{A}}(\omega)|$ is similar to that in Fig. 5.3a except that the swept source that produces $\mathrm{v}_{\mathrm{inj}}$ must be exchanged for an amplitude modulated waveform, as shown in Fig. 5.9a. The modulated waveform with carrier frequency Ω_{H} and modulation frequency ω reads

$$\mathrm{v}_{\mathrm{out}} = \frac{1}{2}(A_{\mathrm{o}} + m_{\mathrm{in}})(e^{i\Omega_{\mathrm{H}}t} + e^{-i\Omega_{\mathrm{H}}t}), \tag{5.19}$$

with

$$m_{\mathrm{inj}} = B_{\mathrm{in}}(e^{i\omega t} + e^{-i\omega t}). \tag{5.20}$$

Similar to Fig. 5.3a, the signal v_{in} drives the closed loop to produce an output signal

$$\mathrm{v} \sim \frac{1}{2}(A_{\mathrm{o}} + m_{\mathrm{out}})(e^{i\Omega_{\mathrm{H}}t} + e^{-i\Omega_{\mathrm{H}}t}), \tag{5.21}$$

with

$$m_{\mathrm{out}} = B_{\mathrm{out}}(e^{i\omega t} + e^{-i\omega t}). \tag{5.22}$$

Example plots of the amplitude modulations for $\mathrm{v}_{\mathrm{inj}}$ and v are shown in Fig. 5.9b. Based on the addition of the amplitude modulation source, I refer to this technique as the *amplitude modulation* (AM) method.

Similar to the R method, the AM method works only if the system does not self-oscillate, and therefore the constraints $|GF'(0)| < 1$ and $|F'(\bar{G}A_s^*)| < 1$ must be both satisfied. In addition, to access the part of $F(\mathrm{v}_{\mathrm{in}})$ that is associated with A_s^*, the condition $F'(\bar{G}A_s^*) < 0$ must also be satisfied. However, without precise

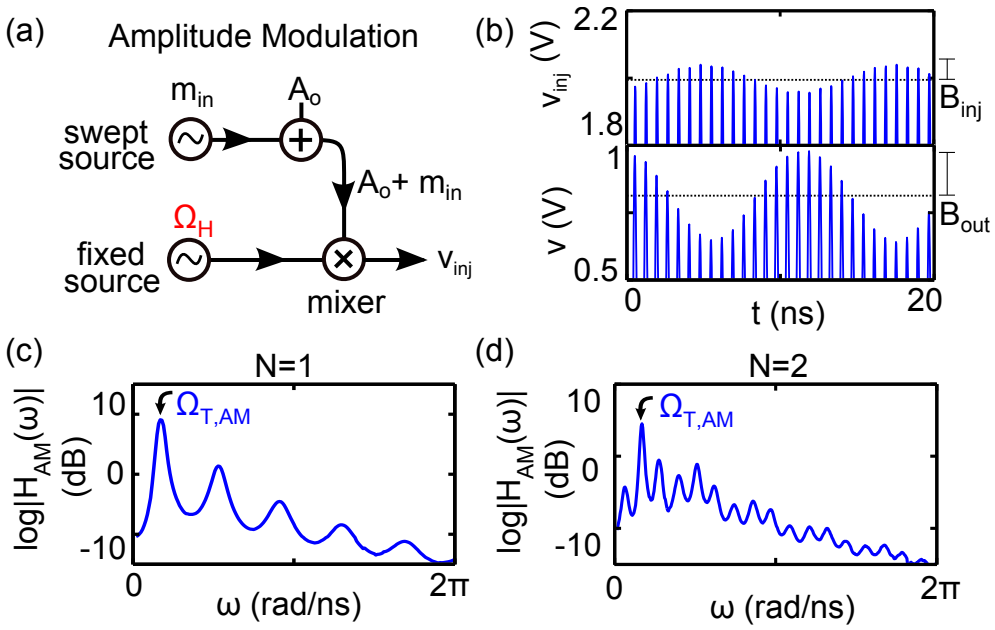

Figure 5.9: **Amplitude modulation method for predicting the torus frequencies.** (a) AM source produces an amplitude modulated waveform v_{inj} at carrier frequency Ω_H and tunable modulation frequency ω. (b) Typical modulation amplitudes in v_{inj} and v from the system with linearized feedback about A_o. The modulation amplitudes B_{inj} and B_{out} are labeled with vertical bars. Closed-loop transfer functions for the amplitude equation using $A_o = 2$, $B_{inj} = 0.05$, $G = 0.9$ for the previous (c) $N = 1$ and (d) $N = 2$ cases. Note that each point in these plots is the result of a separate simulation.
0.0

measurements of (τ_i, g_i), I can only estimate A_s^* using a constant A_o in its place. Thus, in order to probe the closed-loop transfer function of the amplitude equation, I choose $G = 0.9$ and $A_o = 2$ such that these constraints are satisfied.

Continuing with the derivation of the AM method, an approximation to $|H_A(\omega)|$ is given by

$$|H_{AM}(\omega)| = |B_{out}|/|B_{inj}|, \tag{5.23}$$

where B_{inj} and B_{out} are the injected and output modulation amplitudes, respectively. Plots of $|H_{AM}(\omega)|$ used in the simple examples for the $N = 1$ and $N = 2$ cases are

shown Figs. 5.9d-e. There are visible similarities between the plots of $|H_{\mathrm{AM}}(\omega)|$ and $|H_{\mathrm{A}}(\omega)|$ in 5.9d-e in Figs. 5.8a-b. The frequency at which $|H_{\mathrm{AM}}(\omega)|$ has a maximum is labeled as $\Omega_{\mathrm{T,\,AM}} = 0.534$ (0.534) rad/ns for the $N = 1$ ($N = 2$) case, which is within ±0.008 rad/ns of the observed value. For the application of this method in more complicated examples ($N > 2$), refer to the end of this section.

Method II: Shifted Resonances

The second method for approximating $|H_{\mathrm{A}}(\omega)|$ also uses a similar setup to the one shown in Fig. 5.3a except that $\mathrm{v_b}$ tuned to a value $\sim \bar{G}A_{\mathrm{o}}$. In this configuration, I measure the resonances of the feedback system when the nonlinearity is biased such that now the linear gain is now dictated by $F'(\bar{G}A_{\mathrm{o}})$ (as opposed to $F'(0)$). As a result, I substitute $b_i = F'(0)g_i$ for $c_i = F'(\bar{G}A_{\mathrm{o}})g_i$ in the transfer function $H_{\mathrm{R}}(\omega)$, which causes the resonances shift because b_i and c_i are of opposite sign. Therefore, I refer to this technique as the *shifted resonance* method (SR method).

The magnitude of the SR closed-loop transfer function is

$$|H_{\mathrm{SR}}(\omega)| \sim \frac{1}{|i\omega/\Delta + 1 + \omega_{\mathrm{o}}^2/(i\omega\Delta) - G\sum_{i=1}^{N} c_i e_i^{-i\omega\tau}|}. \tag{5.24}$$

The magnitude of $|H_{\mathrm{SR}}(\omega)|$ peaks at either $\omega = \Omega_{\mathrm{H}} - \Omega_{\mathrm{T}}$ or $\omega = \Omega_{\mathrm{H}} + \Omega_{\mathrm{T}}$. Similar to the AM method, given the value of Ω_{H} either from observation of the Hopf bifurcation or from a prior prediction, I can predict the approximate value of Ω_{T}.

To demonstrate simple examples, the shifted resonances of $|H_{\mathrm{SR}}(\omega)|$ are plotted in Figs. 5.10a-b for $N = 1$ and $N = 2$ cases, respectively. The frequency at which $|H_{\mathrm{SR}}(\omega)|$ has a maximum is labeled as either $\Omega_{\mathrm{H}} - \Omega_{\mathrm{T,SR}}$ or $\Omega_{\mathrm{H}} + \Omega_{\mathrm{T,SR}}$ depending on its location relative to Ω_{H}. To test these estimates, I plot the PSDs for $\mathrm{v}(t)$ after the torus bifurcation in Figs. 5.10c-d. As demonstrated by these two examples, the SR

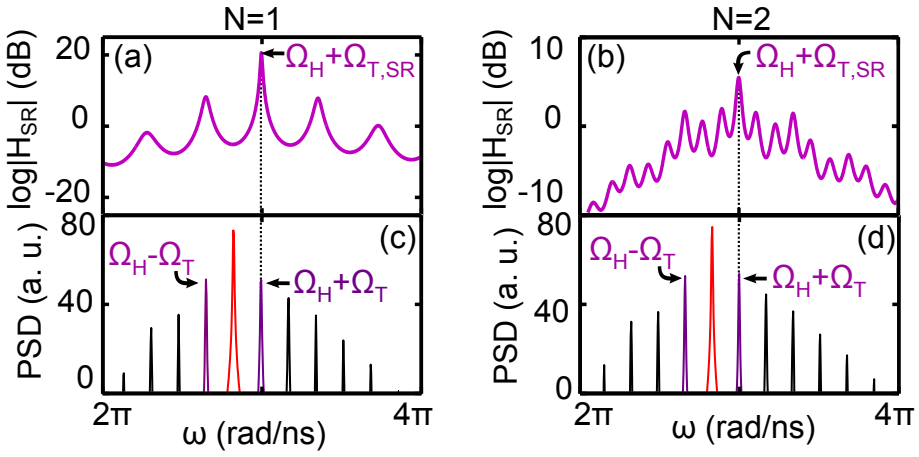

Figure 5.10: **Shifted resonance method for predicting the torus frequencies.** (a) Simulated $|H_{SR}(\omega)|$ for the case of $N = 1$ with parameters $\omega^{(+)} = 10.7$ rad/ns, $\omega^{(-)} = 8.2$ rad/ns, $G = 0.9$, $g_1 = 1$, and $\tau_1 = 5$. (b) Simulated $|H_{SR}(\omega)|$ for the case of $N = 2$ with parameters $\omega^{(+)} = 10.7$ rad/ns, $\omega^{(-)} = 8.2$ rad/ns, $G = 0.9$, $g_1 = 0.2$, $g_2 = 0.3$, $\tau_1 = 5$ ns, and $\tau_2 = 12$ ns. (c)-(d) Repeat of Figs. 5.8c-d.

method predicts $\Omega_{T,SR} = 0.542$ (0.533) rad/ns for $N = 1$ ($N = 2$) which is within ± 0.001 rad/ns of the observed value.

To understand the predictive power of the SR method, I examine

$$|H_{SR}(\omega \pm \Omega_H)| = \frac{1}{|i(\omega \pm \Omega_H)/\Delta + 1 + \omega_o^2/(i(\omega \pm \Omega_H)\Delta) - G\sum_{i=1}^{N} c_i e^{-i(\omega \pm \Omega_H)\tau_i}|}. \tag{5.25}$$

First, I note that $|H_R(\omega)|$ has a global maximum at $\omega = \Omega_H$, which is the frequency at which the denominator of Eq. (5.10) is minimum. Thus, I approximate $\Omega_H \tau_i \sim 2M_i\pi$, where M_i is an integer, and simplify $e^{-i(\omega \pm \Omega_H)\tau_i} \sim e^{-i\omega\tau_i}$. Next, I note that the transformation $\omega \to \omega \pm \Omega_H$ shifts all of the relevant peaks of $|H_{SR}(\omega \pm \Omega_H)|$ near the baseband of the amplitude equation ($\omega \sim 0$). Therefore, to simplify $|H_{SR}(\omega \pm \Omega_H)|$, I Taylor-series expand the term $\omega_o^2/(i(\omega \pm \Omega_H)\Delta)$ in the denominator of Eq. (5.25)

about $\omega = 0$, keeping only the first-order terms in ω

$$\frac{\omega_o^2}{i(\omega \pm \Omega_H)\Delta} \sim \frac{\omega_o^2}{i\Delta}\left(\frac{\pm 1}{\Omega_H} - \frac{\omega}{\Omega_H^2}\right). \tag{5.26}$$

I substitute this approximation into $|H_{SR}(\omega \pm \Omega_H)|$ along with the approximations that $\Omega_H \sim \omega_o$ and $c_i \sim d_i$ and simplify Eq. (5.25) to

$$|H_{SR}(\omega \pm \Omega_H)| \sim \frac{1}{|2i\omega/\Delta + 1 - G\sum_{i=1}^{N} d_i e^{-i\omega\tau_i}|}, \tag{5.27}$$

which is equal to the definition for $|H_A(\omega)|$. Therefore, due to the symmetry of $|H_A(\omega)|$ about $\omega = 0$, $|H_{SR}(\omega \pm \Omega_H)|$ has a global maxima at either $\omega = \Omega_T$ or $\omega = -\Omega_T$. Or, in other words, $|H_{SR}(\omega)|$ has a global maxima at $\omega = \Omega_H + \Omega_T$ or $\omega = \Omega_H - \Omega_T$.

AM and SR methods for $N > 2$

Similar to the previous section, I now test the AM and SR methods for more complicated examples ($N > 2$). I perform multiple simulations for a given N with randomly assigned τ_i and g_i. In Figs. 5.11, I show the results of the two methods for $N = 2$ to $N = 10$. For each N, I simulate the system's bifurcation diagram 5 times, each with different (τ_i, g_i). For each case, I calculate Ω_T, $\Omega_{T,AM}$, and $\Omega_{T,SR}$. In the figures, I plot the mean μ and standard deviation σ of the differences $(\Omega_T - \Omega_{T,AM})$ and $(\Omega_T - \Omega_{T,SR})$ as a function of N. Based on these simulations, I observe that $|\mu(N)| < 0.55$ rad/ns and $|\sigma(N)| < 1.1$ rad/ns for all N. Similar to the $N = 4$ case in Fig. 5.5, for the $N = 10$ case in Fig. 5.11, $\sigma(N = 10)$ and $\mu(N = 10)$ are larger in comparison to all other cases. Details of this case are provided in Appendix C. However, even with this special case, Fig.5.11 demonstrates that these two method

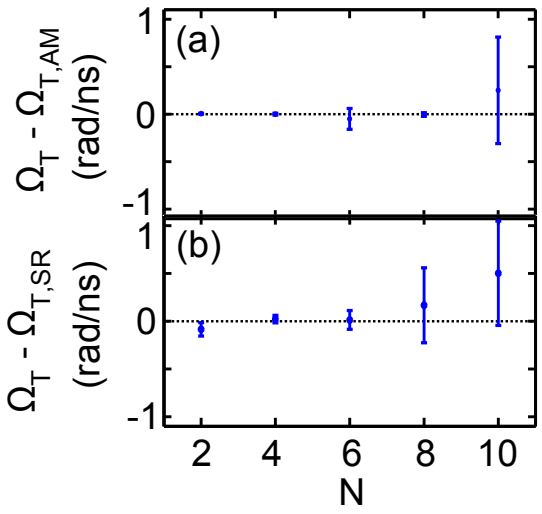

Figure 5.11: **Amplitude modulation and shifted resonance methods for determining the torus frequency in cases with multiple delays.** For each simulation with $N = 2$ to $N = 10$ feedback loops, τ_i and g_i are sampled from uniform distributions such that 5 ns $< \tau_i <$ 50 ns and $-1 < g_i < 1$. The chosen gains g_i are the renormalized using the condition $\sum_{i=1}^{N} |g_i| = 1$. The bandwidth parameters are chosen to be $\omega^{(+)} = 9.4$ rad/ns and $\omega^{(-)} = 6.3$ rad/ns. The predictions are tested by calculating the torus frequency Ω_T from the simulated dynamics. The results from the AM method are shown in (a) using $G = 0.95$, $A_o = 2$ and $B_{inj} = 0.05$, and the results from the SR method are shown in (b) using $G = 0.95$. The predictions are tested by calculating the mean $\mu(N)$ (blue dots) and standard deviation $\sigma(N)$ (error bars) of $(\Omega_T - \Omega_{T,AM})$ and $(\Omega_T - \Omega_{T,SR})$ for each N. Note that AM and SR methods use Ω_H in the predictions of $\Omega_{T,AM}$ and $\Omega_{T,SR}$. Using $\Omega_{H,R}$ increases the prediction errors.

can be used to estimate Ω_T.

In summary, I have shown that the frequencies associated with torus bifurcations can be estimated using the AM and SR methods, where the results demonstrate that the two methods have similar errors. From an experimental point-of-view, the SR method is easier to implement because it requires fewer signal sources. In addition, the AM method requires a signal that folds through the nonlinearity, which requires the signal sources produce a signal with a large enough amplitude A_o, whereas the SR can be implemented with relatively small amplitudes. However, regardless of the required equipment, both methods are valid for experimental testing.

5.4 Experimental Tests of the Prediction Methods

In this section, I test experimentally the R, AM, and SR methods for predicting the frequencies associated with the Hopf and torus bifurcations. First, I apply methods to band-pass filtered systems with time-delayed nonlinear feedback with $N = 1$ and $N = 2$ delays, and then I use a similar experimental setup from Ch. 4 to test these methods in the cavity-feedback system.

The setup for each experimental configuration is shown in Fig. 5.12, where a power splitter (PS) allows for the swept source (SS) to inject v_{inj} in the the feedback loops and the output v is measured on a spectrum analyzer via a directional coupler. In Fig. 5.12a, the experimental setup is similar to the feedback system presented in Ch. 2. In Fig. 5.12b, a new experimental setup is introduced that uses a additional powers splitters and amplifiers to split the output of the system between two distinct feedback loops before recombining them with a second power splitter.

The results of the R, SR, and AM predictions for the $N = 1$ and $N = 2$ cases are shown in Fig. 5.13a and Fig. 5.13b, respectively. For the $N = 1$ case in Fig. 5.13a, the R and SR methods predict that $\Omega_{H,R} = 5.001 \pm 0.025$ rad/ns and $\Omega_{T,SR} = 0.189 \pm 0.025$ rad/ns (errors for the H and SR methods represent the resolution of the experimental frequency sweeps), which is calculated using the predicted value $\Omega_{H,R}$. These two methods are plotted together to highlight the shifts in the resonances. In Fig. 5.13b, the AM method predicts that $\Omega_{T,AM} = 0.160 \pm 0.002$ rad/ns (errors for the AM method represents the resolution of the experimental frequency sweep). As shown in Fig. 5.13c, the $N = 1$ dynamics exhibit quasiperiodic frequencies at $\Omega_H = 5.006 \pm 0.003$ rad/ns and $\Omega_T = 0.198 \pm 0.003$ rad/ns (errors represent the frequency resolution of the Fourier transform of the quasiperiodic time series).

For the $N = 2$ case, the results of the R and SR closed-loop transfer predict

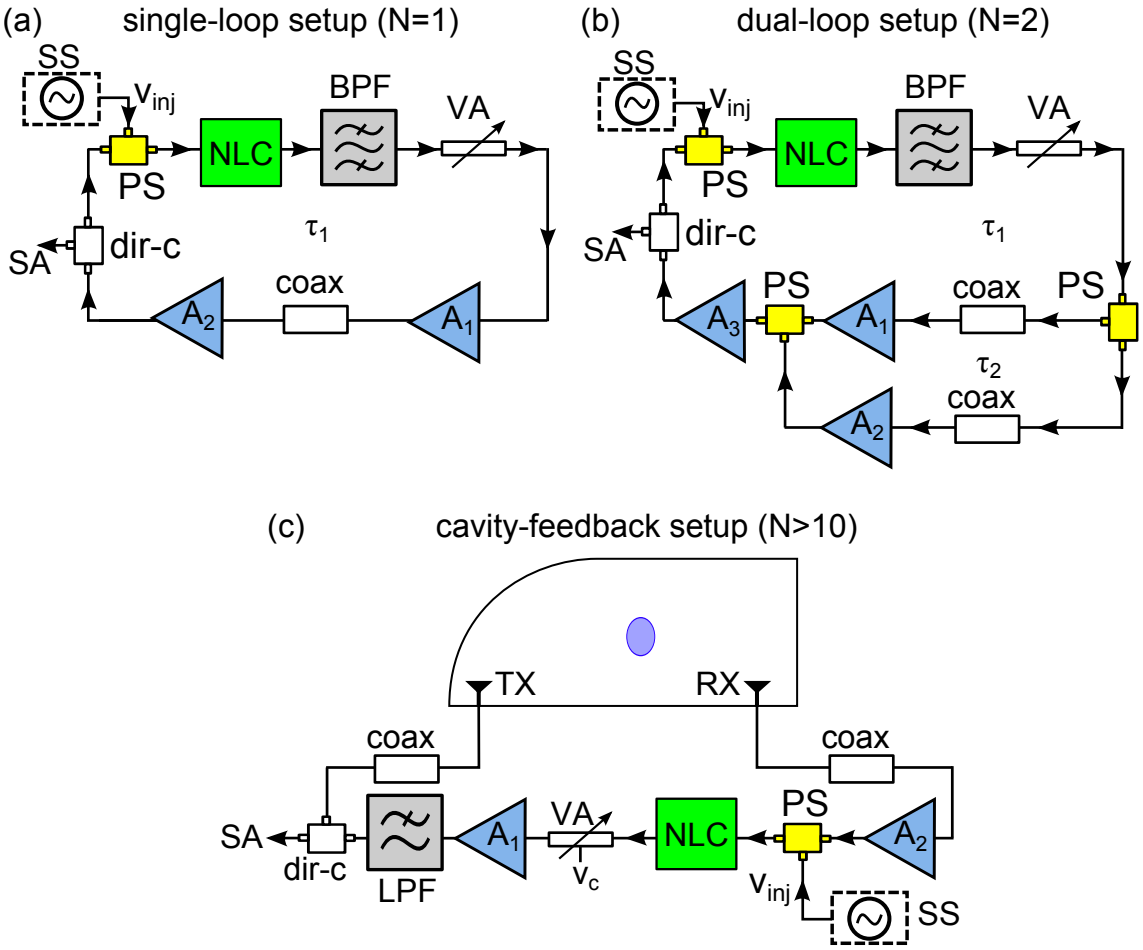

Figure 5.12: **Experimental setups for measuring the closed-loop transfer functions** in the (a) single-loop feedback system ($N = 1$), (b) dual loop feedback system ($N = 2$), and (c) cavity-feedback system ($N > 10$). In the setups, the following components are used: band-pass filter (BPF, Mini-Circuits ZBFV-925+), low-pass filter (LPF, Mini-Circuits ZBFV-925+ and Mini-Circuits ZBFV-925+), amplifier A_1 (Mini–Circuits ZX60-3016E+), amplifier A_2 (Mini-Circuits ZX60-3016E+), amplifier A_3 (Mini-Circuits ZX60-4018G+ and Picosecond Pulse Labs 5828-108), directional coupler (dir-c, Mini-Circuits ZX30-9-4+), power splitters PS_1 and PS_2 (PS, Picosecond Pulse Labs 5331-104), power splitter PS_2 (Mini-Circuits ZFRSC-42+), variable attenuator (VA, Mini-Circuits ZX73-2500+), swept source (SS, Agilent E8267D), and a spectrum analyzer (SA, Agilent E4440A). In the AM method, a second source (Tektronix AFG 3251) and a mixer (Mini-Circuits ADEX-10L) is used for the modulation.

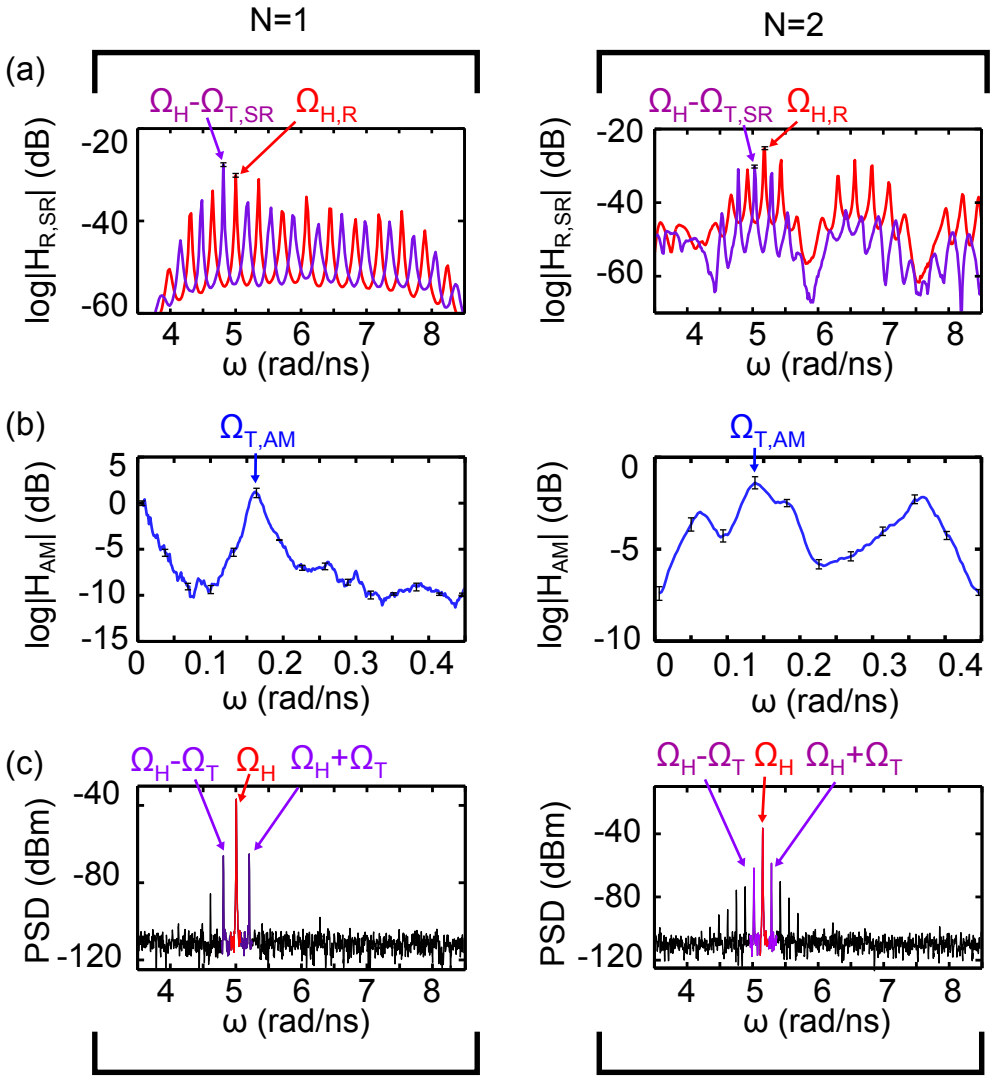

Figure 5.13: Experimental tests of the prediction methods in systems with one and two feedback loops. The $N = 1$ and $N = 2$ cases for (a) the resonance (R) and shifted resonance (SR) method, (b) the amplitude modulation (AM) method, and (c) the quasiperiodic frequency spectra of the experiments for the $N = 1$ and $N = 2$ cases after their respective Torus bifurcations. In all of the plots, the relevant Ω_H, Ω_T, and linear combinations are labeled. The frequency resolution in (a) is 0.025 rad/ns for N =1 and 0.016 rad/ns for N =2, in (b) is 0.002 rad/ns for N=1 and 0.003 rad/ns for N = 2, and in (c) is 0.003 rad/ns for N =1 and N=2. The error bars in (a) indicate the accuracy ±0.4 dBm of the spectrum analyzer and in (b) indicate the standard deviation in $|H_{AM}(\omega)|$ for a given ω.

that $\Omega_{H,R} = 5.186 \pm 0.016$ rad/ns and $\Omega_{T,SR} = 0.156 \pm 0.016$ rad/ns, and the AM method predicts that $\Omega_{T,AM} = 0.145 \pm 0.003$ rad/ns. To compare these results, the quasiperiodic frequency spectrum for the N=2 case shows that $\Omega_H = 5.155 \pm 0.003$ rad/ns and $\Omega_T = 0.133 \pm 0.003$ rad/ns. Therefore, in the N=1 and N=2 cases, the R, SR, and AM methods can predict Ω_H to within ~ 0.03 rad/ns and Ω_T to within ~ 0.04 rad/ns.

In the $N = 1$ and $N = 2$ experimental tests, the errors of the methods for estimating Ω_H and Ω_T are on the same orders of magnitude (~ 0.03 rad/ns). This is different from the simulated cases for $N = 1$ and $N = 2$, where the errors of the methods scale with the estimated frequencies (simulated Ω_H errors are $\sim 10^{-2}$ rad/ns and simulated are Ω_T errors $\sim 10^{-3}$ rad/ns for the N=1 and N=2 cases). Thus, experimental noise limits the predictive power of these methods in real systems such that the errors are $\sim 5\%$ of the mean Ω_H, and because $\Omega_T < \Omega_H$, the errors are $\sim 25\%$ of the mean Ω_T. Increasing the SNR of the system using more shielding and more resolved frequency sweeps may help to match the error scaling of the experiment with that of the simulation. In addition, Agilent Technologies recently introduced a nonlinear network analyzer (N5241A, cost $\sim \$80,000$), which can analyze the frequencies generated by a nonlinear circuit using a frequency sweep, and this analyzer may improve the accuracy of the AM method.

Lastly, I test the frequency prediction methods using the cavity-feedback system for a fixed scatterer position. As shown in Fig. 5.12c, an additional power splitter is placed in the external feedback loop to allow for v_{inj} from the swept source. Similar to the $N = 1$ and $N = 2$ cases, the output voltage v is measured on a spectrum analyzer using a directional coupler.

The results of the predictions and experimental quasiperiodic spectrum of the cavity-feedback system are shown in Fig. 5.14. In Fig. 5.14a, the R and SR methods

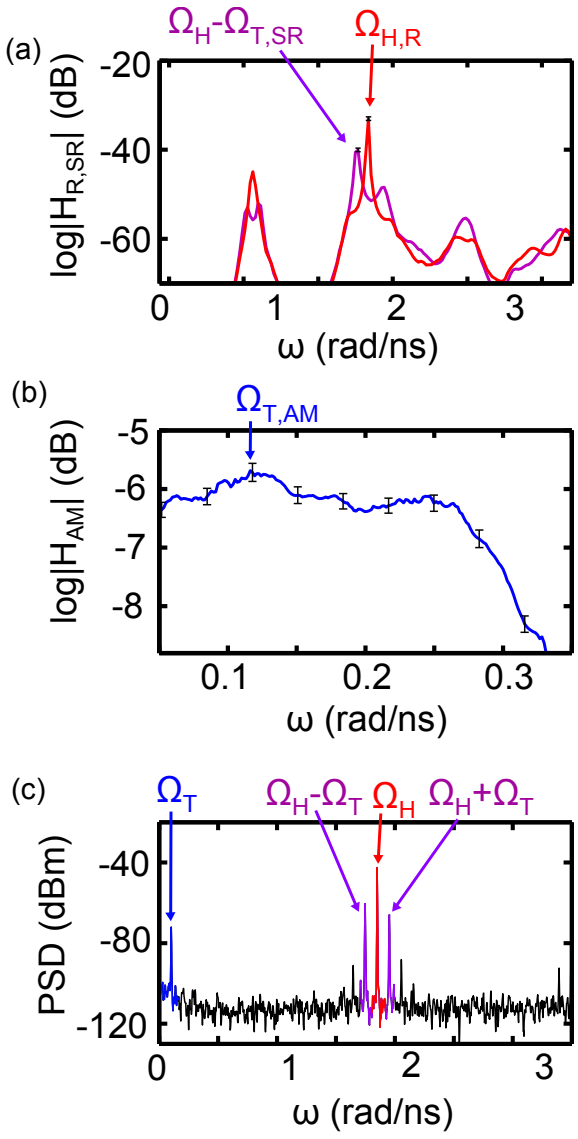

Figure 5.14: **Experimental tests of the prediction methods in the cavity-feedback system.** (a) The resonance (R) and shifted resonance (SR) methods, (b) the amplitude modulation (AM) method, and (c) the frequency spectrum of the experiment after the Torus bifurcation. In all of the plots, the relevant Ω_H, Ω_T, predictions, and linear combinations are labeled. The frequency resolution in (a) is 0.018 rad/ns, in (b) is 0.002 rad/ns, and in (c) is 0.002 rad/ns. The error bars in (a) indicate the accuracy ±0.4 dBm of the spectrum analyzer and in (b) indicate the standard deviation in $|H_{AM}(\omega)|$ for a given ω.

predict that $\Omega_{H,R} = 1.837 \pm 0.018$ rad/ns and $\Omega_{T,SR} = 0.070 \pm 0.018$ rad/ns, and in Fig. 5.14b, the AM method predicts that $\Omega_{T,AM} = 0.112 \pm 0.002$ rad/ns. As shown in Fig. 5.14c, the quasiperiodic dynamics show frequencies $\Omega_H = 1.850 \pm 0.002$ rad/ns and $\Omega_T = 0.103 \pm 0.002$ rad/ns. Therefore, for this scatterer position, the R, SR, and AM methods can predict the Hopf frequency to within ~ 0.013 rad/ns ($\sim 1\%$ of Ω_H) and the torus frequency to within ~ 0.033 rad/ns ($\sim 30\%$ of Ω_T, which is consistent with the $N = 1$ and $N = 2$ results for the experimental cases).

5.5 Summary

Throughout this chapter, I apply three frequency-estimation techniques: (i) the resonance (R) method, (ii) the amplitude modulation (AM) method, and (iii) the shifted resonance (SR) method in both simulations and experiments. Using simulations with up to $N = 10$ feedback loops, these methods estimate, on average, Ω_H to within ~ 0.05 rad/ns and Ω_T to within ~ 0.11 rad/ns, where the bandwidth of the simulated system is approximately 3 rad/ns. In addition, I apply these methods experimentally using single and dual-loop systems and the cavity-feedback system, demonstrating average predictions of Ω_H to within ± 0.02 rad/ns and Ω_T to within ~ 0.04 rad/ns, where the experimental bandwidths range between approximately 1 rad/ns and 6 rad/ns depending on the configuration. These experiments, which are only approximations to true band-pass filtered systems, highlight the flexibility of my prediction methods and confirm the validity of my original approximations. To the best of my knowledge, these are the first methods for estimating the frequencies of quasiperiodicity using closed-loop transfer functions. In principle, the derivations for these methods should be applicable to any number of feedback loops.

Furthermore, it is important to acknowledge that many experimental systems

can be classified as band-pass filters with nonlinear feedback, particularly OEOs [29]. Therefore, the results using my simplified model can be applied to OEOs with a similar nonlinearity. Because my methods are independent of most of the system parameters, I conjecture that they will help to improve the growing field of OEO applications, particularly in OEO systems with fiber Bragg gratings [86] or microresonators [87]. These results may also be useful for developing other applications that exploit quasiperiodic frequencies for sensing and imaging [21].

The results of this chapter show that, using certain experimental measures, it is possible to estimate the initial values of the frequencies Ω_{H} and Ω_{T}, which originate from the resonant peaks of the closed-loop transfer functions of the system. However, additional theory is necessary to understand the properties of the quasiperiodic dynamics with respect to changes in the scatterer's position. Thus, it remains to investigate in Ch. 6 the shifts of the frequencies $\Delta\Omega_{\mathrm{H}}$ and $\Delta\Omega_{\mathrm{T}}$ due to changes in the values of the system's delay-gain distribution.

Chapter 6

Quasiperiodic Frequency Shifts in a Two-Delay Feedback System

In this chapter, I examine the quasiperiodic dynamics of a time-delayed nonlinear feedback system with two time-delays. This two-delay feedback system is an example of a simplification of the cavity-feedback system. As shown in Fig. 6.1a, I approximate the cavity as a set of only two relevant propagation paths with time delays τ_1 and τ_2. These paths are chosen such that a small shift in the scatterer's position $(\Delta x, \Delta y)$ results in a small shift to the time delays $(\Delta\tau_1, \Delta\tau_2)$, respectively. The purpose of this simplification is to investigate a system with only two changing degrees-of-freedom in its feedback. Thus, this simplification can be represented schematically by the dual-feedback system shown in Fig. 6.1b. As I will show, the simplification still allows for 2D subwavelength sensing.

First, using the two-delay experimental system from Ch. 5, I demonstrate experimentally a simplified form of the quasiperiodic sensing technique by changing the feedback's delay distribution. Then, using the simplified model from Ch. 5 to represent the two-delay experimental system, I derive analytical expressions for the quasiperiodic frequency shifts and necessary conditions for the shifts to be independent with respect to changes in the values of the two time delays. I verify my theoretical results using a simulation and also compare them with the experimental data. As a result, I establish an understanding of the origins of a 2D quasiperiodic frequency-shift map, similar to the one used to reconstruct the subwavelength scatterer's 2D position (see Ch. 3). Finally, I examine the implications of this new theory for the full cavity-feedback system with many time delays.

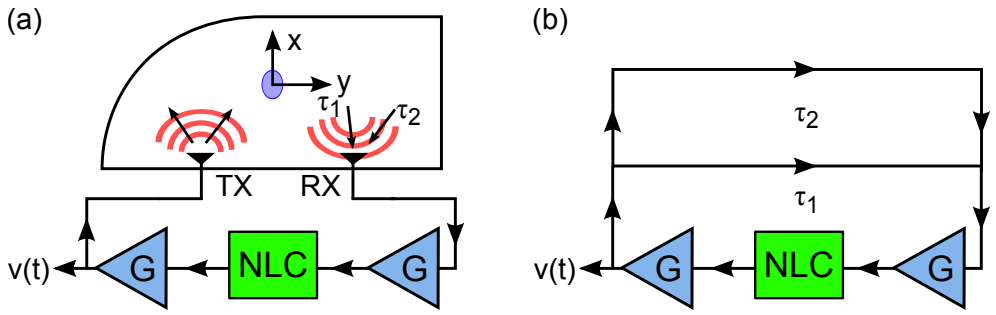

Figure 6.1: **Two-delay simplification of the cavity-feedback system.** (a) The cavity is approximated as having only two relevant propagation paths with time delays τ_1 and τ_2. In this case, consider that the scatterer's position in x and y determines τ_1 and τ_2, respectively. (b) Schematic representation of a two-delay cavity-feedback system with feedback delays τ_1 and τ_2.

Similar to Ch. 5., the results in this chapter benefit from the analyses of Ref. [32] and Ref. [75] for understanding Hopf and torus bifurcations in band-pass filtered systems, repsectively. The two-delay experimental system was constructed with the help of Andrés Aragoneses Aguado. Lastly, my experimental and theoretical results presented in this chapter are part of an investigation that is currently ongoing.

6.1 Experimental Two-Delay System

The experimental realization of the two-delay system is shown in Fig. 6.2. Similar to the cavity-feedback system, the two-delay system uses the nonlinear circuit (NLC) discussed in previous chapters. The output of the NLC drives a band-pass filter (BPF) and variable attenuator (VA), where it is then divided using a power splitter (PS) that splits the voltage evenly between two separate paths. Along each path, the signals passes through an amplifier (A_1 or A_2) and a variable delay line (VDL_1 or VDL_2). Both VDL_1 and VDL_2 are coaxial waveguides with a tunable lengths (Δx_1 and Δx_2, respectively) that are attached to computer-controlled translation stages to vary the net time-delays $\tau_1 \sim 19.3$ ns and $\tau_2 \sim 23.0$ ns, respectively. After

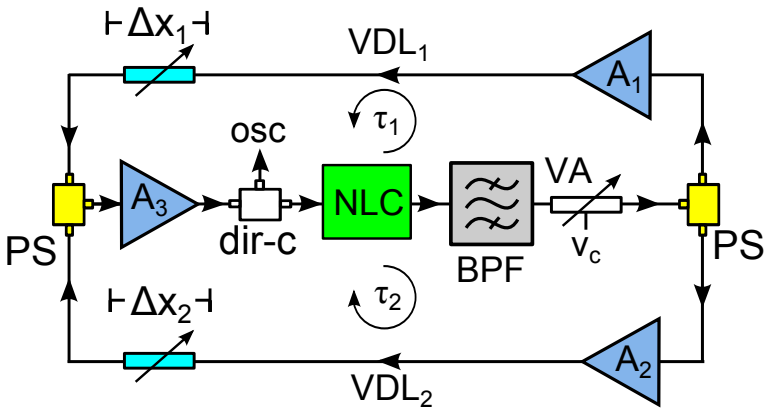

Figure 6.2: **Two-delay experimental feedback system.** The output of the nonlinear circuit (NLC) drives a band-pass filter (BPF, Mini-Circuits ZBFV-925+), a variable attenuator (VA, Mini-Circuits ZX73-2500+), a power splitter (PS, Picosecond Pulse Labs 5331-104), amplifiers A_1 and A_2 (both are Mini-Circuits ZX60-3016E+), variable delay-lines VDL_1 and VDL_2, a second PS, a third amplifier A_3 (Mini-Circuits ZX60-4018G+ and Picosecond Pulse Labs 5828-108), a directional coupler (dir-c, Mini-Circuits ZX30-9-4+), and the input of the NLC. The VDLs are comprised of coaxial waveguides known as line stretchers (Microlab/FXR SR-05B) that are attached to linear translation stages (each are Zaber Technologies TLSR150B) with relative length changes Δx_i. A portion of the signal in the feedback loop is measured as the voltage $v(t)$ on the oscilloscope (osc).

each VDL, the signals are combined using a second PS and a third amplifier (A_3), which drive a directional coupler (dir-c) and the input of the NLC, forming a closed feedback system.

Using the control voltage v_c of the variable attenuator, I tune the net gain of the total feedback such that the system's dynamics are in a quasiperiodic state (using a bias voltage $v_b = 0.85$ V). A typical quasiperiodic time series and its associated power spectral density (PSD) are plotted in Figs. 6.3a-b. In the figure, I label the main frequencies of the quasiperiodic state as $f_T = 22.2 \pm 0.2$ MHz, $f_H - f_T = 0.800 \pm (2 \times 10^{-4})$ GHz, $f_H = 0.822 \pm (2 \times 10^{-4})$ GHz, and $f_H + f_T = 0.844 \pm (2 \times 10^{-4})$ GHz, where f_H and f_T are the frequencies associated with the system's Hopf bifurcation and torus bifurcations, respectively.

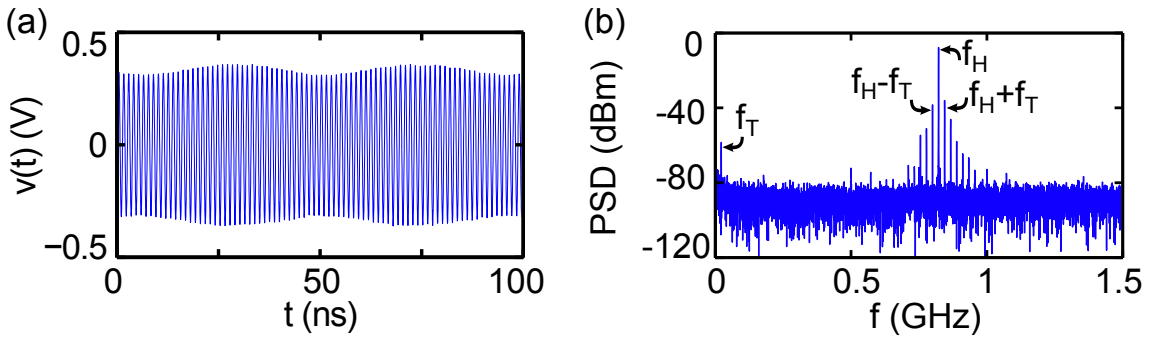

Figure 6.3: **Two-delay experimental quasiperiodic dynamics.** (a) Temporal evolution and (b) power spectral density (PSD) of typical quasiperiodic dynamics. In the time series, the signal-to-noise ratio is $\mathrm{RMS_S/RMS_N} \sim 80$, where $\mathrm{RMS_S}$ ($\mathrm{RMS_N}$) is the root-mean-square of the signal (noise). See Ch. 3 for a comparison of this value. In the PSD, the angular frequencies associated with the Hopf and Torus bifurcations and their linear combinations are labeled accordingly.

To understand how the frequencies (f_T, f_T) shift with changes in the values of (τ_1, τ_2), similar to the 2D grid of scatterer positions (x, y), I scan values of τ_1 and τ_2 in a grid of time-delays by translating $\mathrm{VDL_1}$ and $\mathrm{VDL_2}$ by Δx_1 and Δx_2, respectively. The grid of relative positions is defined by 0 mm$< \Delta x_1 <$ 2 mm and 0 mm $< \Delta x_2 <$ 2 mm (recall the relative error in the translation stage positioning is ± 5 μm with backlash correction). Using the approximate speed of an electromagnetic wave in a coaxial cable (1.974×10^8 m/s $\sim 2/3$c for 50 Ω impedance [88]), this is equivalent to shifting the relative values of the the time delays such that $0 < \Delta\tau_1 < 10$ ps and $0 < \Delta\tau_2 < 10$ ps. At each relative position $(\Delta x_1, \Delta x_2)$, I monitor the shifts to the quasiperiodic frequencies $\Delta\bar{f}_T$ and $\Delta\bar{f}_H$ (defined by Eqs. (3.6)-(3.7)). This leads to near-planar 2D calibration surfaces (see Figs. 6.4a-b).

To test the sensing from this calibration, I first fit the experimental data to create a map between $(\Delta\bar{f}_T, \Delta\bar{f}_H)$ and $(\Delta x_1, \Delta x_2)$. Based on the near planar surfaces in

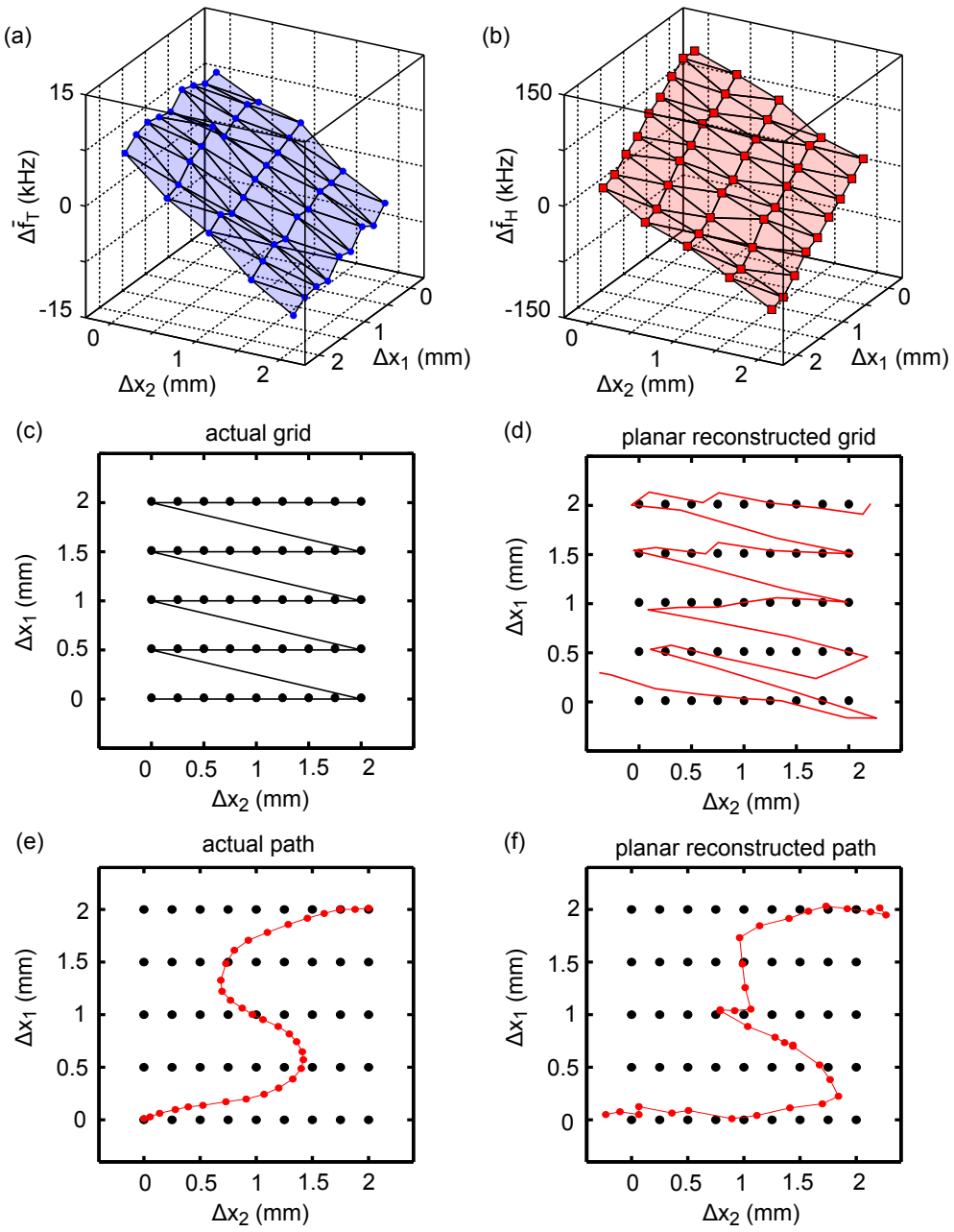

Figure 6.4: **Two-delay experimental quasiperiodic frequency shifts.** Frequency shifts (a) $\Delta\bar{f}_T$ and (b) $\Delta\bar{f}_{\mathrm{H}}$ as a function of $(\Delta x_1, \Delta x_2)$. (c) Calibration grid of $(\Delta x_1, \Delta x_2)$ and (d) reconstructed calibration grid (red curve). (e) Test path of $(\Delta x_1, \Delta x_2)$ (red curve) in the 2D grid of points (black dots). (f) Reconstructed path of $(\Delta x_1, \Delta x_2)$ (red curve) using the numerical map in the 2D grid of points (black dots).

Figs. 6.4a-b, I use the first-order multivariate functions

$$\Delta\bar{f}_{\mathrm{T}}(x_1, x_2) = c_1 + \alpha_1 \Delta x_1 + \beta_1 \Delta x_2, \tag{6.1}$$

$$\Delta\bar{f}_{\mathrm{H}}(x_1, x_2) = c_2 + \alpha_2 \Delta x_1 + \beta_2 \Delta x_2, \tag{6.2}$$

where $c_1 = -1.84 \pm 0.14$ kHz, $\alpha_1 = -8.00 \pm 0.12$ kHz mm^{-1}, and $\beta_1 = 10.17 \pm 0.20$ kHz mm^{-1}, and where $c_2 = -32.55 \pm 2.40$ kHz, $\alpha_2 = -60.40 \pm 2.20$ kHz mm^{-1}, and $\beta_2 = 104.31 \pm 3.61$ kHz mm^{-1} (errors represent the 90% confidence intervals of the fitting parameters). Similar to Ch. 3, these first-order functions are inverted to illustrate the errors associated with the planar mapping.

In Fig. 6.4c, the actual calibration grid path is shown and in Fig. 6.4d, the reconstructed grid is shown. The 2D reconstruction yields RMS errors of 0.48 mm ($\sim \lambda/500$) and 0.12 mm ($\sim \lambda/2,000$) for Δx_1 and Δx_2, respectively, for all positions in the 2D calibration grid. $\lambda \sim 23.7$ cm based on $f_{\mathrm{max}} \sim (f_{\mathrm{H}} + f_{\mathrm{T}})$. Higher harmonics are present in the dynamics but with less power. The average RMS errors between the predicted and actual shifts is $\Delta x_{\mathrm{RMS}} = 0.3$ mm, and the two-delay system can, on average, sense a 2D change to the lengths of a feedback loop to within $\sim \lambda/800$. This represents a lower bound on the average dynamic range of 2 mm / 0.3 mm ~ 7 (Similar to Ch. 3, this represents only a lower bound on the potential dynamic range of the system. To find the upper bound on the dynamic range, one would need to perform parameter sweeps for the bias voltage of the nonlinear circuit and gain of the feedback loop to find the configuration that yields the largest and most sensitive windows of quasiperiodicity). Interestingly, in this system, the calibration grid path is reconstructed with less distortion using a planar surface when compared to Fig. 3.17a. This is most likely due to the fact that the signals in the feedback loop are not propagating through a large cavity that is sen-

sitivity to humidity and temperature fluctuations. Lastly, the maximum observed errors of the shifts ($x_{1,\max}$, $x_{2,\max}$) give the lower bounds on the resolution in this particular experiment, where $x_{1,\max} = 0.73$ mm ($\sim \lambda/320$) and $x_{2,\max} = 0.28$ mm ($\sim \lambda/800$). Overall, this experiment demonstrates a 2D subwavelength sensitivity to subwavelength changes.

It should be noted that these errors are still an order of magnitude larger than the errors associated with the translation stage positioning that control the lengths of the coaxial waveguides. Thus, I approximate that the errors associated with the reconstruction of the calibration grid path are primarily due to drift in the system and the approximation that the surfaces in Figs. 6.4a-b are planar. Similar to Ch. 3, higher-order surfaces may reduce these errors, but for the purposes of this chapter, a first-order mapping will be useful for understanding how quasiperiodic frequencies shift in the theory to following section.

Before moving on to the theory, I test this 2D sensing resolution using an arbitrary path of time-delay shifts ($\Delta x_{1,n}, \Delta x_{2,n}$) within the calibration grid. As shown in Fig. 6.4e, none of the points along the actual path lie on the calibration grid except for the first and last point for reference. Using the frequency shifts ($\Delta f_{\mathrm{T},n}, \Delta f_{\mathrm{H},n}$) acquired at each of the $n = 33$ test points, I use the inverted maps from Eqs. (6.1) - (6.2) to reconstruct the time-delay shifts. The reconstructed path is shown in Fig. 6.4f, and the RMS errors between the actual and reconstructed delay shifts are 0.26 mm and 0.09 mm for x_1 and x_2 respectively, which, for this particular test, yields an improved average 2D length-sensing resolution of approximately $\lambda/1200$. In addition, the maximum observed errors are $x_{1,\max} = 0.52$ mm ($\sim \lambda/450$) and $x_{2,\max} = 0.17$ mm ($\sim \lambda/1,400$). These errors are on the same order of magnitude as those from the reconstruction of the calibration grid path and demonstrate less distortion in the shape of the path when compared to Fig. 3.18d. Again, this im-

provement is most likely due to less drift in the system because the cavity has been removed. Therefore, the two-delay feedback system is a simplified version of the cavity-feedback system, where there is no wave chaos (discussed in detail in Ch. 7) and the quasiperiodic sensing technique can be used to simultaneously detect time-delay shifts of (or changes in the lengths of) the feedback loops.

In the next section, I examine a simplified model of this dual-delay system that consists of a band-pass filter with two-delay nonlinear feedback. Using this simplified model and the results from Ch. 5, I derive an analytical expressions for the frequencies at the onset of the Hopf and torus bifurcations as a function of the system's time delays. For the purposes of this derivation, I use the notation of the angular frequencies $\omega = 2\pi f$, $\Omega_{\mathrm{T}} = 2\pi f_{\mathrm{T}}$, and $\Omega_{\mathrm{H}} = 2\pi f_{\mathrm{H}}$ due to the factors of 2π that arise throughout my calculations.

6.2 Model of the Two-Delay Feedback System

The simplified model for the two-delay feedback system is described by the delay differential equation (DDE) for a band-pass filter with nonlinear feedback [80] and $N = 2$ time delays

$$\frac{\dot{\mathrm{v}}(t)}{\Delta} + \mathrm{v}(t) + \frac{\omega_{\mathrm{o}}^2}{\Delta}\int_{-\infty}^{t} \mathrm{v}(t')\,\mathrm{d}t' = F\left(G\sum_{i=1}^{N=2} g_i \mathrm{v}(t-\tau_i)\right), \tag{6.3}$$

where g_i are the relative gain of the two feedback loops, G is the net gain of the overall feedback, $\Delta = \omega^{(+)} - \omega^{(-)}$ is the system's bandwidth, $\omega_o = \sqrt{\omega^{(+)}\omega^{(-)}}$ is the central frequency of the band-pass filter, and $\omega^{(+)}$ and $\omega^{(-)}$ are the upper and lower cutoff frequencies of the band-pass filter, respectively. Similar to Ch. 5, I

approximate the effect of the NLC by a cubic nonlinear function that reads

$$F(\mathrm{v_{in}}) = \alpha_1(\mathrm{v_{in}} + \mathrm{v_b}) - [\alpha_2(\mathrm{v_{in}} + \mathrm{v_b})]^3, \tag{6.4}$$

where $\mathrm{v_b}$ represents a bias voltage that tunes the operating point of the nonlinearity and $\alpha_1 = 1$ and $\alpha_2 = 0.5$ are positive constants for the purposes of this analysis. Without loss of generality, I also assume $\mathrm{v_b} = 0$.

Hopf Bifurcation in the Two-Delay Feedback System

The initial Hopf bifurcation result from an instability of the system about the steady state of $\mathrm{v}(t) = \mathrm{v}_s = 0$. Consider a small perturbation $\delta\mathrm{v}$ about the steady state; this leads to

$$\frac{\delta\dot{\mathrm{v}}(t)}{\Delta} + \delta\mathrm{v}(t) + \frac{\omega_o^2}{\Delta}\int_{-\infty}^{t} \delta\mathrm{v}(t')\,\mathrm{d}t' = G\sum_{i=1}^{N=2} b_i \delta\mathrm{v}(t-\tau_i), \tag{6.5}$$

where $b_i = g_i \frac{\mathrm{d}F}{\mathrm{dv}}|_{\mathrm{v}_s}$. To examine its stability, I assume solution of the form $\delta\mathrm{v}(t) = Ae^{\lambda t}$, where A is a real amplitude and λ is a complex eigenvalue.

The Hopf bifurcation arises when λ is a pure imaginary number. I denote $\lambda = i\Omega_\mathrm{H}$ with Ω_H a real frequency, and I solve for the conditions that this assumption holds. Substituting $\mathrm{v}(t) = Ae^{i\Omega_\mathrm{H} t}$ into the linearized Eq. 6.5 gives

$$\frac{i\Omega_\mathrm{H}}{\Delta} + 1 + \frac{\omega_o^2}{i\Omega_\mathrm{H}\Delta} - G\sum_{i=1}^{N=2} b_i e^{-i\Omega_\mathrm{H}\tau_i} = 0. \tag{6.6}$$

Separating Eq. (6.6) into its real and imaginary parts yields a pair of coupled transcendental equations

$$G\sum_{i=1}^{N=2} b_i \cos(\Omega_\mathrm{H}\tau_i) = 1, \tag{6.7}$$

$$G\sum_{i=1}^{N=2} b_i \sin(\Omega_{\mathrm{H}}\tau_i) = \frac{\omega_{\mathrm{o}}^2 - \Omega_{\mathrm{H}}^2}{\Omega_{\mathrm{H}}\Delta}. \tag{6.8}$$

To have a stable limit cycle at frequency Ω_{H}, these equations must be satisfied. Typically, these equations are solved numerically and for high enough G, the Hopf bifurcation emerges with $\Omega_{\mathrm{H}} \sim \omega_{\mathrm{o}}$ [81]. For now, I pause in this analysis and briefly analyze the conditions of the torus bifurcation in the two-delay feedback system.

Torus Bifurcation in the Two-Delay Feedback System

The analysis of the torus bifurcation is based on the amplitude equation (see Ch. 5) and serves as the motivation of the analysis of Ω_{T} in a system with a set of $N = 2$ time delays its the feedback. I examine the stability of the limit cycle's amplitude by assuming that the dynamics can be approximated as $\mathrm{v}(t) = \frac{1}{2}A(t)(e^{i\Omega_{\mathrm{H}}t} + e^{-i\Omega_{\mathrm{H}}t})$ once the system bifurcates to a torus, where $A(t)$ is slow varying amplitude. Then, using a separation of time-scales between $A(t)$ and $e^{\pm i\Omega_{\mathrm{H}}t}$, the dynamical equation for $A(t)$ can be approximated as

$$\dot{A}(t) = \frac{\Delta}{2}\left(F\left[G\sum_{i=1}^{N=2} g_i A(t-\tau_i)\right] - A(t)\right), \tag{6.9}$$

which is the amplitude equation from the Ch. 5 with $N = 2$ (see Appendix C for the full derivation). I consider a solution of the form $A(t) = A_s + \delta A$ and linearize the amplitude equation about A_s, the steady state that satisfies $F\left[\bar{G}A_s\right] = A_s$ with $\bar{G} \equiv G\sum_{j=1}^{j=2} g_j$. The result of the linearization is

$$\delta\dot{A}(t) = \frac{\Delta}{2}\left(G\sum_{i=1}^{N=2} d_i \delta A(t-\tau_i) - \delta A(t))\right), \tag{6.10}$$

with $d_i = g_i F'\left[\bar{G}A_s\right]$ (see also Appendix C for the derivation of Eq. (6.10) from the amplitude equation).

Because the torus bifurcation appears as a Hopf bifurcation in the amplitude equation [75], I propose the solution $\delta A(t) = Be^{i\Omega_T t}$ and substitute it into Eq. (6.10). This gives

$$\frac{2i\Omega_T}{\Delta} + 1 + G\sum_{i=1}^{N} d_i e^{-i\Omega_T \tau_i} = 0. \tag{6.11}$$

Similar to Eqs. (6.7) - (6.8), I separate Eq. (6.11) into its the real and imaginary parts as follows

$$G\sum_{i=1}^{N} d_i \cos(\Omega_T \tau_i) = 1, \tag{6.12}$$

$$G\sum_{i=1}^{N} d_i \sin(\Omega_T \tau_i) = \frac{2\Omega_T}{\Delta}. \tag{6.13}$$

To have a torus bifurcation with frequency Ω_T, these equations must be satisfied. In the next subsection, I use conditions from Eqs. (6.7) - (6.8) and Eqs. (6.12) - (6.13) to analyze the shifts on the values of Ω_H and Ω_T with respect to changes in the time delays τ_1 and τ_2.

6.2.1 Quasiperiodic Frequency Shifts

The goal of this subsection is to derive an equation to predict approximately how the frequencies (Ω_H, Ω_T) shift due to small perturbations in the time delays (τ_1, τ_2). To do so, I perturb the values of the individual time delays in Eqs. (6.7) and (6.12) and assume small shifts in $\Omega_{H,T}$. For simplicity, I also assume that the frequencies at the onset of the Hopf and torus bifurcations can be used to describe the shifts to $\Omega_{H,T}$ beyond these bifurcation points. Following these derivations, I use experimental data and numerical simulations to support these assumptions.

I begin by examining Ω_H and assume that τ_2 is fixed and there is a small perturbation to τ_1 such that $\tau_1 \rightarrow \tau_1 + p_1$ with $p_1 << \tau_1$. I assume this induces a small shift in Ω_H such that $\Omega_H \rightarrow \Omega_H + \epsilon_{H,1}$ with $\epsilon_{H,1} << \Omega_H$. I substitute these perturbed variables into Eq. (6.7) such that

$$b_1 \cos([\Omega_H + \epsilon_{H,1}][\tau_1 + p_1]) + b_2 \cos([\Omega_H + \epsilon_{H,1}]\tau_2) = \frac{1}{G'}, \tag{6.14}$$

where $G' = G + G_\epsilon$ and G_ϵ is the perturbation of the system's gain to reach the bifurcation point. Neglecting higher-order terms $\left(O(\epsilon_{H,1}^2), O(\epsilon_{H,1} p_1)\right)$, I approximate Eq. (6.14) as

$$b_1 \cos(\Omega_H \tau_1 + \Omega_H p_1 + \epsilon_{H,1}\tau_1) + b_2 \cos(\Omega_H \tau_2 + \epsilon_{H,1}\tau_2) = \frac{1}{G'}. \tag{6.15}$$

To simplify this expression, I rewrite it as

$$b_1 \cos(x + h) + b_2 \cos(y + q) = \frac{1}{G'}, \tag{6.16}$$

where $x = \Omega_H \tau_1$, $h = \Omega_H p_1 + \epsilon_{H,1}\tau_1$, $y = \Omega_H \tau_2$, and $q = \epsilon_{H,1}\tau_2$. I note that $h << x$ and $q << y$ and Taylor expand terms on the right-hand-side of Eq. (6.16) about x and y such that Eq. (6.15) becomes

$$\begin{aligned} b_1 \cos(\Omega_H \tau_1) - b_1 \sin(\Omega_H \tau_1)(\Omega_H p_1 + \epsilon_{H,1}\tau_1) \\ + b_2 \cos(\Omega_H \tau_2) - b_2 \epsilon_{H,1}\tau_2 \sin(\Omega_H \tau_2) = \frac{1}{G'}. \end{aligned} \tag{6.17}$$

I then approximate $G' \sim G$ such that Eq. (6.7) is still valid and Eq. (6.17) reduces to

$$-b_1 \sin(\Omega_H \tau_1)(\Omega_H p_1 + \epsilon_{H,1}\tau_1) \approx b_2 \epsilon_{H,1}\tau_2 \sin(\Omega_H \tau_2). \tag{6.18}$$

Solving for $\epsilon_{\mathrm{H},1}$ as a function of p_1 finally gives

$$\epsilon_{\mathrm{H},1}(p_1) = -\frac{p_1 \Omega_{\mathrm{H}} b_1 \sin(\Omega_{\mathrm{H}} \tau_1)}{\sum_{i=1}^{N=2} b_i \tau_i \sin(\Omega_{\mathrm{H}} \tau_i)}. \tag{6.19}$$

By an analog of reasoning for $\tau_2 \to \tau_2 + p_2$ with $p_2 << \tau_2$ and τ_1 fixed, I deduce that the Hopf frequency will shift $\Omega_{\mathrm{H}} \to \Omega_{\mathrm{H}} + \epsilon_{\mathrm{H},2}$ with $\epsilon_{\mathrm{H},2} << \Omega_{\mathrm{H}}$, such that

$$\epsilon_{\mathrm{H},2}(p_2) = -\frac{p_2 \Omega_{\mathrm{H}} b_2 \sin(\Omega_{\mathrm{H}} \tau_2)}{\sum_{i=1}^{N=2} b_i \tau_i \sin(\Omega_{\mathrm{H}} \tau_i)}. \tag{6.20}$$

Due to the linearized equations of the derivation, the total shift in $\epsilon_{\mathrm{H}} = \epsilon_{\mathrm{H},1} + \epsilon_{\mathrm{H},2}$ due to shifts p_1 and p_2 is

$$\epsilon_{\mathrm{H}}(p_1, p_2) = -\frac{\Omega_{\mathrm{H}} \sum_{i=1}^{N=2} p_i b_i \sin(\Omega_{\mathrm{H}} \tau_i)}{\sum_{i=1}^{N=2} b_i \tau_i \sin(\Omega_{\mathrm{H}} \tau_i)}. \tag{6.21}$$

As shown by this equation, ϵ_{H} depends on the initial value of Ω_{H}, both values of the time delays τ_1 and τ_2, and is proportional to the gain coefficient g_i along each feedback path ($b_i \propto g_i$). I also note that, although ω_{o} and Δ do not appear directly in Eq. (6.21), they are implicitly present in the value of Ω_{H} (see Eqs. (6.7) - (6.8)).

I now pause briefly to check the scaling of $\epsilon_{\mathrm{H}}(p_1, p_2)$ in a simple case. Consider $\epsilon_{\mathrm{H}}(p_1, p_2)$ for the $N = 1$ case of a single-delay system, where $\tau_1 = \tau_2$, $b_1 = b_2$, and $p_1 = p_2$ such that

$$\epsilon_{\mathrm{H}}(p_1) \to -\frac{\Omega_{\mathrm{H}} p_1}{\tau_1}. \tag{6.22}$$

This scaling is comparable to that of the Hopf bifurcation analysis from Ref. [32], where, for a single time-delay system with band-pass filtered nonlinear feedback,

the frequency of the initial Hopf bifurcation scales as

$$\Omega_{\mathrm{H}} \approx \frac{2\pi M}{\tau_1}, \tag{6.23}$$

where M is an integer or half-integer (depending on the sign of the gain). Ω_{H} is the M^{th} harmonic of the frequency $1/\tau_1$ [32]. By perturbing the value of the time delay $\tau_1 \to \tau_1 + p_1$ in Eq. (6.23) and Taylor expanding, I obtain

$$\Omega_{\mathrm{H}} + \epsilon_{\mathrm{H}} = \frac{2\pi M}{\tau_1 + p_1} \approx \frac{2\pi M}{\tau_1} - \frac{2\pi M p_1}{\tau_1^2} = \Omega_{\mathrm{H}} - \frac{\Omega_{\mathrm{H}} p_1}{\tau_1}. \tag{6.24}$$

Simplifying this expression yields

$$\epsilon_{\mathrm{H}} \approx -\frac{\Omega_{\mathrm{H}} p_1}{\tau_1}, \tag{6.25}$$

which is equivalent to Eq. (6.22). Thus, $\epsilon_{\mathrm{H}}(p_1, p_2)$ reduces to the correct scaling in the $N = 1$ case.

Next, I the examine the frequency shift of the torus frequency Ω_{T}. Using Eq. (6.12), I let $\tau_1 \to \tau_1 + p_1$ and $\tau_2 \to \tau_2 + p_2$ to induce a net frequency shift on the torus frequency $\Omega_{\mathrm{T}} \to \Omega_{\mathrm{T}} + \epsilon_{\mathrm{T}}$ with $\epsilon_{\mathrm{T}} << \Omega_{\mathrm{T}}$. Based on the analog between Eq. (6.7) and Eq. (6.12), it follows that

$$\epsilon_{\mathrm{T}}(p_1, p_2) = -\frac{\Omega_{\mathrm{T}} \sum_{i=1}^{N=2} p_i d_i \sin(\Omega_{\mathrm{T}} \tau_i)}{\sum_{i=1}^{N=2} d_i \tau_i \sin(\Omega_{\mathrm{T}} \tau_i)}. \tag{6.26}$$

Similar to ϵ_{H}, the value of ϵ_{T} depends directly on Ω_{T}, τ_i, p_i, and d_i. In addition, the dependence of ϵ_{T} on Δ is contained implicitly in the calculation of Ω_{T} (using Eqs. (6.12) - (6.13)).

Similar to the previous subsection, I check the scaling of ϵ_{T} for the $N = 1$ case

such that

$$\epsilon_{\mathrm{T}}(p_1) \to -\frac{\Omega_{\mathrm{T}} p_1}{\tau_1}. \tag{6.27}$$

This is consistent with the scaling found by Chembo *et al.* in Ref. [75] for a single-delay OEO, where

$$\Omega_{\mathrm{T}} \approx \frac{2\pi}{2\tau_1}, \tag{6.28}$$

such that, when Taylor expanding about a delay shift p_1, it reads

$$\Omega_{\mathrm{T}} + \epsilon_{\mathrm{T}} \approx \frac{2\pi}{2(\tau_1 + p_1)} \sim \frac{2\pi}{2\tau_1} - \frac{2\pi p_1}{2\tau_1^2} + \mathrm{O}(p_1^2), \tag{6.29}$$

and therefore

$$\epsilon_{\mathrm{T}} \approx -\frac{\Omega_{\mathrm{T}} p_1}{\tau_1}. \tag{6.30}$$

The derived expressions for linearized frequency shifts $\epsilon_{\mathrm{H}}(p_1, p_2)$ and $\epsilon_{\mathrm{T}}(p_1, p_2)$ represent planes in the (p_1, p_2) phase space. It remains to examine these planes together.

6.2.2 Linear Independence

In this subsection, I determine the conditions for which shifts in Ω_{H} and Ω_{T} are independent during changes in τ_1 and τ_2. Because I assume small and subsequently linear frequency shifts, it is sufficient to check if ϵ_{H} and ϵ_{T} are linearly independent. This represents the condition for which there exists a unique mapping between $(\epsilon_{\mathrm{H}}, \epsilon_{\mathrm{T}})$ and (p_1, p_2). To do so, I rewrite the expressions for ϵ_{H} and ϵ_{T} in Eqs. (6.21) and (6.26) as $\vec{\epsilon} = M\vec{p}$ using the matrix notation

$$\begin{bmatrix} \epsilon_{\mathrm{H}} \\ \epsilon_{\mathrm{T}} \end{bmatrix} = \begin{bmatrix} -b_1\Omega_{\mathrm{H}}\sin(\Omega_{\mathrm{H}}\tau_1)/B & -b_2\Omega_{\mathrm{H}}\sin(\Omega_{\mathrm{H}}\tau_2)/B \\ -d_1\Omega_{\mathrm{T}}\sin(\Omega_{\mathrm{T}}\tau_1)/D & -d_2\Omega_{\mathrm{T}}\sin(\Omega_{\mathrm{T}}\tau_2)/D \end{bmatrix} \begin{bmatrix} p_1 \\ p_2 \end{bmatrix}, \tag{6.31}$$

with $B \equiv \sum_{i=1}^{N=2} b_i \tau_i \sin(\Omega_H \tau_i)$ and $D \equiv \sum_{i=1}^{N=2} d_i \tau_i \sin(\Omega_T \tau_i)$. For ϵ_H and ϵ_T to be linearly independent, the determinant of X must be nonzero

$$\begin{vmatrix} -b_1 \Omega_H \sin(\Omega_H \tau_1)/B & -b_2 \Omega_H \sin(\Omega_H \tau_2)/B \\ -d_1 \Omega_T \sin(\Omega_T \tau_1)/D & -d_2 \Omega_T \sin(\Omega_T \tau_2)/D \end{vmatrix} \neq 0. \tag{6.32}$$

This is equivalent to

$$b_1 d_2 \sin(\Omega_H \tau_1)\sin(\Omega_T \tau_2) \neq b_2 d_1 \sin(\Omega_H \tau_2)\sin(\Omega_T \tau_1). \tag{6.33}$$

With $b_1 d_2 = b_2 d_1$, based on the definitions $b_i = g_i F'(0)$ and $d_i = g_i F'(\bar{G} A_s)$, Eq. (6.33) reduces to

$$\sin(\Omega_H \tau_1)\sin(\Omega_T \tau_2) \neq \sin(\Omega_H \tau_2)\sin(\Omega_T \tau_1). \tag{6.34}$$

Because it is not clear that all of the terms in Eq. (6.34) are nonzero, I cannot isolate the Ω_H and Ω_T terms on either side of the equation. Therefore, given the initial Hopf and torus frequencies Ω_H and Ω_T for an initial set of time delays τ_1 and τ_2, Eq. (6.34) represents the condition for linear independence between the frequency shifts given changes to values of the time delays. In general, for an arbitrary (Ω_T, Ω_H) and (τ_1, τ_2) in the dual-delay system, Eq. (6.34) must be verified numerically.

However, Eq. (6.34) does demonstrate that there is a particular constraint on the time-delays in order to form unique map: For $\tau_1 = \tau_2$, Eq. (6.34) is violated, regardless of the values for Ω_H and Ω_T (even with different gain coefficients $g_1 \neq g_2$). This illustrates that sensing with quasiperiodic frequency shifts requires an asymmetry in the delay-gain distribution.

6.3 Applications of the Quasiperiodic Frequency-Shift Theory

In this section, I test my derivations for the first-order map between the quasiperiodic frequency shifts and the values of the time delays, $(\epsilon_{\mathrm{H}}, \epsilon_{\mathrm{T}}) \longleftrightarrow (p_1, p_2)$ in two-delay feedback systems. First, I use numerical simulations of the simplified two-delay feedback model to show that Eq. (6.31) can describe approximately the frequency shifts in the system. Then, I compare the analytical shifts predicted by Eq. (6.31) with the experimental data in Figs. 6.4a-b.

6.3.1 Numerical Simulation

I integrate Eq. (6.3) with parameters $\omega^{(+)}/(2\pi) = 1.6$ GHz and $\omega^{(-)}/(2\pi) = 1.4$ GHz and time-delays $\tau_1 = 7$ ns and $\tau_2 = 12$ ns. Using gain coefficients $g_1 = g_2 = 0.5$, I tune the external gain of the model to $G = 3.5$ such that the system exhibits stable quasiperiodic dynamics with $\Omega_{\mathrm{H}}/(2\pi) = f_{\mathrm{H}} = 1.56$ GHz and $\Omega_{\mathrm{T}}/(2\pi) = f_{\mathrm{T}} = 0.052$ GHz, as shown in Figs. 6.5a-b. Then, using time delay shifts $p_1 = 0 - 15$ ps and $p_2 = 0 - 15$ ps in steps of 5 ps, I calculate the spectral shifts $(\Delta f_{\mathrm{H}}, \Delta f_{\mathrm{T}})$ for each set of time delays in the model. The results are shown in Fig. 6.5c, where the spectral shifts are approximately planar in the (p_1, p_2) parameter space (note: the observed frequency shifts are large in comparison to the experimental shifts in Fig. 6.4, and this will be discussed at the end of this chapter).

Using the system parameters $(f_{\mathrm{H}}, f_{\mathrm{T}})$ and (τ_1, τ_2), I compare these results to the analytical predictions for $(\epsilon_{\mathrm{H}}, \epsilon_{\mathrm{T}})$ from Eq. (6.31) over the values of (p_1, p_2). Shown in Fig. 6.5d, the analytically-predicted planar shifts show agreement with the simulated shifts, where the average RMS differences between the simulated shifts Δf_{T} and Δf_{H} and the analytically-predicted frequency shifts ϵ_{T} and ϵ_{H} are 258 kHz and 82 kHz, which represents 11.5% and 15.0% of the overall simulated shifts in f_{H}

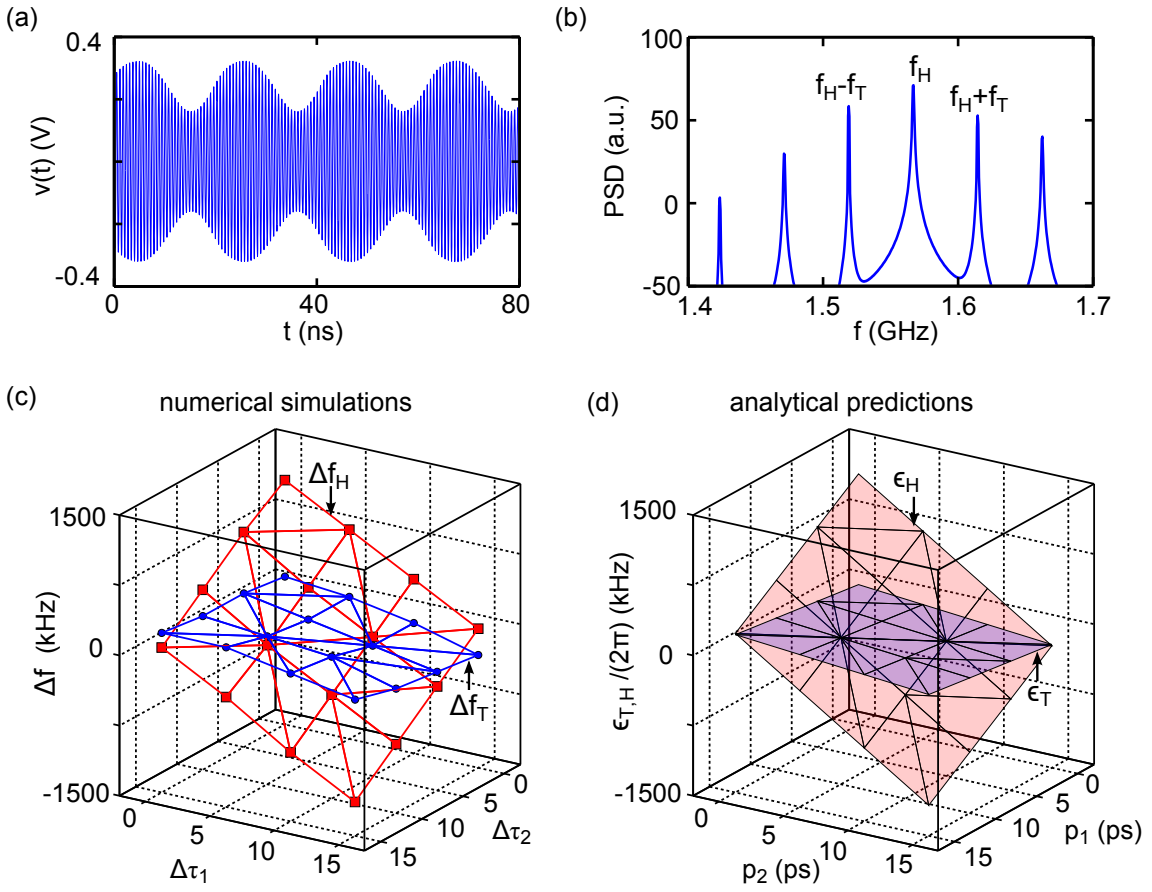

Figure 6.5: **Simulated and predicted spectral shifts in a two-delay system.** (a) Typical quasiperiodic time series for $v(t)$ from integrating the simplified model. (b) Power spectral density of the simulated $v(t)$ with f_H and $f_H \pm f_T$ labeled accordingly. (c) Simulated spectral shifts Δf_T (blue dots) and Δf_H (red squares) for the delay shifts $(\Delta\tau_1, \Delta\tau_2)$ associated with the delays $\tau_1 = 7$ ns and $\tau_2 = 12$ ns. (d) Analytically-predicted values of the planar spectral shifts $\epsilon_H/(2\pi)$ (blue) and $\epsilon_T/(2\pi)$ (red) calculated using Eq. (6.31) for the delay shifts (p_1, p_2).

and f_T, respectively. I have verified using higher-order expansions of Eqs. (6.14) and (6.17) that these discrepancies between the analytics and the simulations are not caused from neglecting the higher-order terms $\left(O(\epsilon_{H,1}^2), O(\epsilon_{H,1} p_1)\right)$. This is discussed more at the end of this subsection.

These analytical maps are invertible because Eq. (6.34) is satisfied, where the value of the determinant from Eq. (6.32) is nonzero (approximately 0.1 rad^2 ns^{-4}).

Therefore, the frequency shifts are linearly independent and can be used to reconstruct the values of the time-delay shifts. Considering the inverse of the planar mapping, the average RMS errors between the simulated and predicted time-delay shifts are 4.5 ps and 8.5 ps for $\Delta\tau_1$ and $\Delta\tau_2$, respectively. Therefore, assuming that $f_{\max} = f_{\mathrm{T}} + f_{\mathrm{H}}$ and that the feedback loops use coaxial cables (signal propagation speed is 1.974×10^8 m/s $\sim (2/3)$c), then the average dual-delay sensing resolution of the model system is approximately 1.3 mm $\sim \lambda/100$, where $\lambda = 12.4$ cm. Note that this resolution represents the accuracy of the analytical predictions; there is no fit to the data. This is different from all previous cases that use fitted functions to perform the 2D mapping.

The discrepancies between the numerical simulations and the analytical predictions demonstrate that the approximations made while deriving Eq. (6.31) limit the predictive power of the theory. In particular, the theory is derived only for the frequencies at the onset of the Hopf and torus bifurcations, but the quasiperiodic frequency shifts are measured for dynamics beyond the torus bifurcation point. To approximate the magnitude of this effect, I perform separate simulations with the same parameters except with the G tuned higher and hence farther away from the torus bifurcation point ($G \sim 3.48$). For $G = 3.7$, the RMS differences between the analytically predicted frequency shifts and the simulated frequencies shifts increase to 268 kHz and 154 kHz for f_{H} and f_{T}, respectively, which are 11.9% and 17.1% errors of the observed ranges. Furthermore, for $G = 3.9$, the RMS differences increase to 288 kHz and 483 kHz for f_{H} and f_{H}, respectively, which are 12.6% and 21.0% errors of the observed ranges. Thus tuning the gain farther away from the bifurcation point causes a larger discrepancy between the simulations and theory.

In addition to this effect, there are also several other factors that limit the predictive power of the theory. For example, the amplitude equation is derived on several

assumptions (see Appendix C) such as $\Omega_{\mathrm{H}} = \omega_o$. Also, ϵ_{T} and ϵ_{H} are derived using small shifts in order simplify the model to a set of linearized equations. Because these assumptions are not fully satisfied in the simulation, the analytical derivations can only predict approximately the frequency shifts of the quasiperiodic spectrum.

6.3.2 Experimental Data

Similar to the simulated data, I now compare the analytical predictions of the quasiperiodic frequency shifts from Eq. (6.31) to the observed experimental data in Figs. 6.4a-b. For convenience, the experimental shifts are replotted in Fig. 6.6a. Using Eq. (6.31), I calculate $(\epsilon_{\mathrm{T}}, \epsilon_{\mathrm{H}})$ for a set of time delay shifts (p_1, p_2), where $p_i = [1.974 \times 10^8]^{-1} \Delta x_i$. For a total translation of $\Delta x_i = 2$ mm, the time-delays shift by $p_i = 10$ ps. The analytically-predicted values for $(\epsilon_{\mathrm{T}}/(2\pi), \epsilon_{\mathrm{H}}/(2\pi))$ as a function of $(\Delta x_1, \Delta x_2)$ are shown in Fig. 6.6b.

The predictions approximately match the experimental frequency shifts, where the orders of magnitude and relative shifts for both Δf_{H} and Δf_{T} are predicted approximately by the analytical derivations for ϵ_{T} and ϵ_{H}, respectively. The average RMS differences between the experimental shifts $\Delta \bar{f}_{\mathrm{T}}$ and $\Delta \bar{f}_{\mathrm{H}}$ and the analytically-predicted frequency shifts ϵ_{T} and ϵ_{H} are 2.4 kHz and 46.2 kHz, which represent approximately 12.3% and 22.0% of the overall observed shifts in $\bar{f}_{\mathrm{T}}$ and $\bar{f}_{\mathrm{H}}$, respectively.

Note that this comparison assumes that an electromagnetic wave propagates through a coaxial cable (with 50 Ω impedance) with a speed equal to 2/3 the speed of light c (1.974×10^8 m/s). Because I have not directly measured the change to the propagation delay of a signal through the coaxial wave-guide with respect to small changes in the tunable feedback loop lengths, this approximation can lead

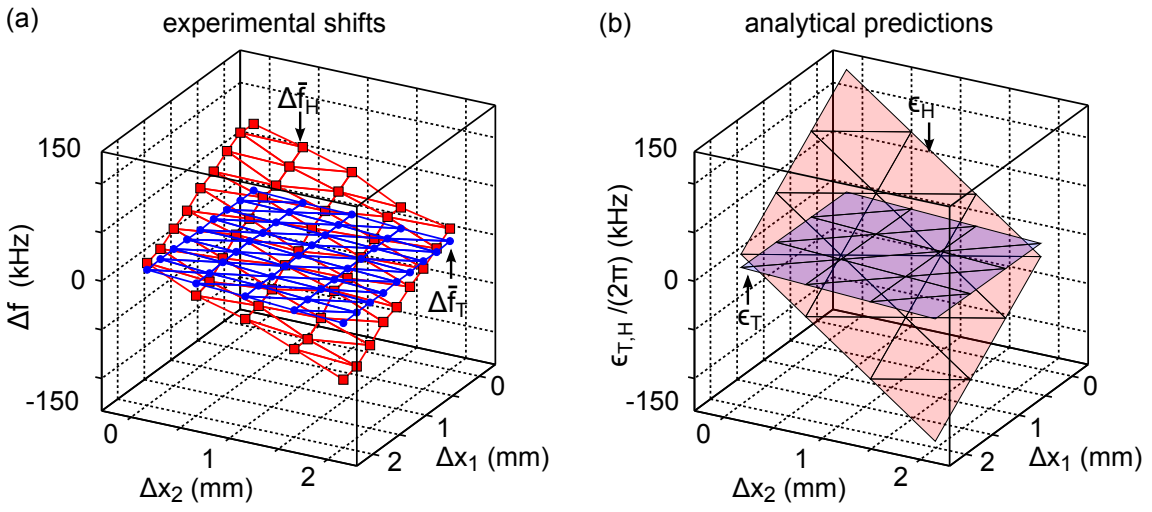

Figure 6.6: **Experimental and predicted spectral shifts in a two-delay system.** (a) Experimental spectral shifts Δf_{T} (blue dots) and Δf_{H} (red squares) for the feedback loop translations $(\Delta x_1, \Delta x_2)$ associated with the delays $\tau_1 = 19.3$ ns and $\tau_2 = 23.0$ ns and frequencies $f_{\mathrm{T}} \sim 0.02$ GHz and $f_{\mathrm{H}} \sim 0.82$ GHz. (b) Analytically-predicted values of the planar spectral shifts $\epsilon_{\mathrm{H}}/(2\pi)$ (blue) and $\epsilon_{\mathrm{T}}/(2\pi)$ (red) calculated using Eq. (6.31) with $\Delta x_i = [(2/3)\mathrm{c}]p_i$.

to an overall skew factor in the results of Fig. 6.6b. This represents a source of error in the differences between the analytically predicted and the experimentally observed frequency shifts. For example, a small adjustment to the theoretical speed of an electromagnetic wave in the coaxial waveguide (rather than 1.974×10^8 m/s, the speed is adjusted to $(1.974 + 0.1) \times 10^8$ m/s, which is a 5% correction in the wave speed) could account for approximately 2% of the observed differences (with this adjustment, the RMS differences between the experimental shifts $\Delta\bar{f}_{\mathrm{T}}$ and $\Delta\bar{f}_{\mathrm{H}}$ and the analytically-predicted frequency shifts ϵ_{T} and ϵ_{H} are 2.3 kHz and 42.8 kHz, which now represent approximately 12.7% and 20.3% of the experimentally observed ranges of frequency shifts).

In addition, using the analytically predicted shifts to describe a mapping, Eq. (6.34) is satisfied (the determinant of Eq. (6.32) is approximately $(-3 \pm 2.2) \times 10^{-4}$

rad^2 ns^{-4}) such that ϵ_T and ϵ_H are linearly independent. Thus, using the analytical derivation as the 2D map, the RMS error between the experimental and predicted translations is 6.8 mm and 7.7 mm for Δx_1 and Δx_2, respectively. Therefore, the average 2D sensing resolution of the experiment with the analytical map is approximately 7.2 mm $\sim \lambda/30$, where $\lambda = 23.4$ cm. Again, note that this resolution represents the quantitative agreement of the analytical predictions without an optimal fit to the data. Even though the resolution is worse when compared to the fit at the beginning of this chapter, this demonstrates that the analytically predicted frequency shifts scale correctly to match approximately those in the experiment and still ensure a subwavelength 2D resolution.

This quantitative agreement is interesting because the analytical derivations, which are approximations of the already-simplified model, do not take into account any of the experimental imperfections or any details of the nonlinear circuit's operation. Similar to Ch. 5, which showed that the simplified model of Eq. (6.3) can predict the approximate origins of f_H and f_T, this demonstrates that it also contains ingredients for mapping the approximate shifts of the experimental quasiperiodic frequencies. Although Eq. (6.31) is derived with many assumptions, it can still give insight into the physical phenomenon of complex nonlinear feedback experiments.

Furthermore, this analysis also shows that the quasiperiodic frequency shifts in this system are inherently sensitive to subwavelength changes. Even with all of my approximations, the simplified model shows a unique mapping for quasiperiodic frequency shifts with respect to time-delay changes. However, this analysis also shows that the vastly subwavelength resolutions observed at the beginning of this chapter and in Ch. 3 are achieved only by the numerical fits of the experimental data. Thus, the resolutions of this system (and the cavity-feedback system) depend on the ability to achieve good numerical fits, which rely on the experimental signal-

to-noise ratio (see Ch. 1 for details).

Using the results of this subsection as motivation, in the next section, I generalize the derivation of Eq. (6.31) in the context of the cavity-feedback system.

6.4 Extensions to the Cavity-Feedback System

In this final section, I generalize the derivations for Eq. (6.31) to a band-pass filtered nonlinear feedback system with $N >> 1$ time-delayed feedback loops. The main objective is to examine the implications of my previous derivations with regards to the cavity-feedback system and results of Ch. 3. To begin, I rewrite the Eqs (5.6) and (5.16) from Ch. 5 that read

$$G\sum_{i=1}^{N} b_i \cos(\Omega_{\mathrm{H}}\tau_i) = 1, \tag{6.35}$$

$$G\sum_{i=1}^{N} d_i \cos(\Omega_{\mathrm{T}}\tau_i) = 1. \tag{6.36}$$

Again, I can perform a perturbation analysis where $\Omega_{\mathrm{T,H}} \rightarrow \Omega_{\mathrm{T,H}} + \epsilon_{\mathrm{T,H}}$ with $\epsilon_{\mathrm{T,H}} << \Omega_{\mathrm{T,H}}$, due to shifts in the time delays $\tau_i \rightarrow \tau_i + p_i$ such that the total linearized frequency shifts are now described by

$$\epsilon_{\mathrm{H}}(p_1, p_2, ..., p_N) = -\frac{\Omega_H \sum_{i=1}^{N} p_i b_i \sin(\Omega_{\mathrm{H}}\tau_i)}{\sum_{i=1}^{N} b_i \sin(\Omega_{\mathrm{H}}\tau_i)\tau_i}, \tag{6.37}$$

$$\epsilon_{\mathrm{T}}(p_1, p_2, ..., p_N) = -\frac{\Omega_T \sum_{i=1}^{N} p_i d_i \sin(\Omega_{\mathrm{T}}\tau_i)}{\sum_{i=1}^{N} d_i \sin(\Omega_{\mathrm{T}}\tau_i)\tau_i}. \tag{6.38}$$

Equations (6.37) and (6.38) can be expressed together in the matrix notation $\vec{\epsilon} =$

$M\vec{p}$ as

$$\begin{bmatrix} \epsilon_{\mathrm{H}} \\ \epsilon_{\mathrm{T}} \end{bmatrix} = \begin{bmatrix} -b_1\Omega_{\mathrm{H}}\sin(\Omega_{\mathrm{H}}\tau_1)/B_N & \dots & -b_N\Omega_{\mathrm{H}}\sin(\Omega_{\mathrm{H}}\tau_N)/B_N \\ -d_1\Omega_{\mathrm{T}}\sin(\Omega_{\mathrm{T}}\tau_1)/D_N & \dots & -d_N\Omega_{\mathrm{T}}\sin(\Omega_{\mathrm{T}}\tau_N)/D_N \end{bmatrix} \begin{bmatrix} p_1 \\ \vdots \\ p_N \end{bmatrix}, \tag{6.39}$$

where M is now a matrix of size $(2 \times N)$, $\vec{p}$ is a column vector of size $(N \times 1)$, $B_N \equiv \sum_{i=1}^{N} b_i\tau_i\sin(\Omega_{\mathrm{H}}\tau_i)$, and $D_N \equiv \sum_{i=1}^{N} d_i\tau_i\sin(\Omega_{\mathrm{T}}\tau_i)$. From here, not much else can be deduced for the general case of N feedback loops without more information regarding $\vec{p}$. Since there are N possible time delay shifts and only two observed frequency changes, a unique mapping between $(\epsilon_H, \epsilon_T) \longleftrightarrow (p_1, .., p_N)$ is not possible in general.

However, Eq. (6.39) can help in providing further insight into the results of Ch. 3. In the cavity-feedback system, the scatterer's position is moved inside of a 2D area, which induces a change of the N time delays of the cavity feedback. The 2D displacements of the scatterer in the x and y directions led to a unique mapping between the frequency shifts $\vec{\epsilon} = (\epsilon_{\mathrm{H}}, \epsilon_{\mathrm{T}})$ and (x, y), where x and y represent relative changes to the scatterer's position, such that

$$\vec{\epsilon} = \begin{bmatrix} \epsilon_{\mathrm{H}} \\ \epsilon_{\mathrm{T}} \end{bmatrix} = \begin{bmatrix} \alpha_1 & \beta_1 \\ \alpha_2 & \beta_2 \end{bmatrix} \begin{bmatrix} x \\ y \end{bmatrix}, \tag{6.40}$$

where α_i and β_i are constants and the determinant $|\alpha_1\beta_2 - \alpha_2\beta_1| \neq 0$. This experimental mapping served as the initial calibration for the subwavelength position sensing system.

Now, suppose as the scatterer moves in the x and y directions, it perturbs the time delays by $\vec{p}_x$ and $\vec{p}_y$, respectively, where $\vec{p}_x$ and $\vec{p}_y$ are vectors of size $(N \times 1)$

such that

$$\vec{p}_x = \begin{bmatrix} xq_{x_1} \\ \vdots \\ xq_{x_N} \end{bmatrix}, \ \vec{p}_y = \begin{bmatrix} yq_{y_1} \\ \vdots \\ yq_{y_N} \end{bmatrix}, \tag{6.41}$$

where q_{x_i} and q_{y_i} are fixed delay shifts per unit of displacement, and where the total delay shift vector as $\vec{p} = \vec{p}_x + \vec{p}_y$, such that

$$\vec{p} = \begin{bmatrix} xq_{x_1} + yq_{y_1} \\ \vdots \\ xq_{x_N} + yq_{y_N} \end{bmatrix}. \tag{6.42}$$

Thus for $x = 0$, $\vec{p} \to \vec{p}_y$ and for $y = 0$, $\vec{p} \to \vec{p}_x$. I acknowledge that Eq. (6.42) approximates each delay shift as a linear function with respect to x and y. However, for small enough displacements, I can always Taylor expand any nonlinear delay shifts as a function of x and y so that this approximation is valid.

By substituting Eq. (6.42) into Eq. (6.39) and using the equality of $\vec{\epsilon}$ to Eq. (6.40), I obtain the following

$$\begin{aligned} \epsilon_{\mathrm{H}} = \alpha_1 x + \beta_1 y = (xq_{x_1} + yq_{y_1})(\frac{-b_1\Omega_{\mathrm{H}}}{B_N}\sin(\Omega_{\mathrm{H}}\tau_1)) \\ + (xq_{x_2} + yq_{y_2})(\frac{-b_2\Omega_{\mathrm{H}}}{B_N}\sin(\Omega_{\mathrm{H}}\tau_2)) \\ + \ldots + (xq_{x_N} + yq_{y_N})(-\frac{b_N\Omega_{\mathrm{H}}}{B_N}\sin(\Omega_{\mathrm{H}}\tau_N)), \end{aligned} \tag{6.43}$$

$$\epsilon_{\mathrm{T}} = \alpha_2 x + \beta_2 y = (x q_{x_1} + y q_{y_1})(\frac{-d_1 \Omega_{\mathrm{T}}}{D_N} \sin(\Omega_{\mathrm{T}} \tau_1)) + (x q_{x_2} + y q_{y_2})(\frac{-d_2 \Omega_{\mathrm{T}}}{D_N} \sin(\Omega_{\mathrm{T}} \tau_2)) + \ldots + (x q_{x_N} + y q_{y_N})(\frac{-d_N \Omega_{\mathrm{T}}}{D_N} \sin(\Omega_{\mathrm{T}} \tau_N)), \quad (6.44)$$

By equating the coefficients of x and y on the left and right-hand-sides of Eqs. (6.43) and (6.44), I solve for α_i and β_i as

$$\alpha_1 = -\frac{\Omega_{\mathrm{H}}}{B_N} \sum_{i=1}^{N} q_{x_i} b_i \sin(\Omega_{\mathrm{H}} \tau_i), \quad (6.45)$$

$$\alpha_2 = -\frac{\Omega_{\mathrm{T}}}{D_N} \sum_{i=1}^{N} q_{x_i} d_i \sin(\Omega_{\mathrm{T}} \tau_i), \quad (6.46)$$

$$\beta_1 = -\frac{\Omega_{\mathrm{H}}}{B_N} \sum_{i=1}^{N} q_{y_i} b_i \sin(\Omega_{\mathrm{H}} \tau_i), \quad (6.47)$$

$$\beta_2 = -\frac{\Omega_{\mathrm{T}}}{D_N} \sum_{i=1}^{N} q_{y_i} d_i \sin(\Omega_{\mathrm{T}} \tau_i). \quad (6.48)$$

Under these assumptions, I can also rewrite the determinant $|\alpha_1 \beta_2 - \alpha_2 \beta_1| \neq 0$ as

$$\sum_{i=1}^{N} q_{x_i} b_i \sin(\Omega_{\mathrm{H}} \tau_i) \sum_{j=1}^{N} q_{y_j} d_j \sin(\Omega_{\mathrm{T}} \tau_j) - \sum_{k=1}^{N} q_{x_k} d_k \sin(\Omega_{\mathrm{H}} \tau_k) \sum_{m=1}^{N} q_{y_m} b_m \sin(\Omega_{\mathrm{T}} \tau_m) \neq 0. \quad (6.49)$$

Equations (6.45) - (6.49) are an analytical interpretation of the fitting parameters α_i and β_i for the original experimental 2D mapping in Ch. 3. These parameters, which represent the planar frequency shifts of the cavity-feedback system, depend on the quasiperiodic frequencies Ω_{H} and Ω_{T}, the relative gains g_i along each of the feedback

paths of time-delay τ_i, and the linearized delay shifts per unit of translation x_i and y_i. Without more knowledge about the time-delay changes in the cavity-feedback system, an analytical approach to predicting the frequency shifts is not feasible, and even with knowledge of such time-delay changes, it is not practical for improving the system's resolution beyond that of the numerical fit.

6.5 Summary

In this chapter, I present the foundation for realizing a dual-delay sensing system using a band-pass filter with time-delayed nonlinear feedback. This two-delay system represents a simplification of the cavity-feedback system. Using an experimental system with two feedback loops, I demonstrate that the quasiperiodic dynamics form a map between the frequency shifts and the changes to the values of the time-delays of (or the translations of) the feedback loops. Furthermore, using a simplified model for the two-delay system and linear stability analysis, I derive the necessary conditions for the quasiperiodic frequency shifts to be linearly independent with respect to time-delay changes. I also demonstrate numerically that this analysis is approximately valid beyond the Hopf and torus bifurcation points and that the analytical theories can approximate the simulated frequency shifts. Furthermore, I show that the analytically-predicted frequencies can also approximate the experimental frequency shifts. Lastly, by extending the two-delay theories to a system with N feedback loops, I connect the frequency-shift derivations to the subwavelength position-sensing results of Ch. 3.

Earlier in the chapter, I also noted that the order of magnitudes for the experimental and analytically-predicted frequency shifts Δf_{H} in Fig. 6.6 is different than those in Figs. 6.5c-d, even though the delay shifts are approximately the same order

of magnitude $\Delta\tau_i \sim 10$ ps. This demonstrates the sensitivity of the quasiperiodic frequency shifts to the values of τ_1, τ_2, f_T, and f_H. For each set of parameters in the nonlinear feedback system, the quasiperiodic frequency-shift map can vary by orders of magnitude. Further study of this phenomenon may help to optimize a frequency-shift map for a given system.

Although my analysis was originally motivated by a specific electronic experiment, this methodology could be extended to other nonlinear feedback systems that exhibit quasiperiodicity, such as OEOs with a nearly identical set of dynamical equations. Using the frequency stability of such devices in the quasiperiodic regime may lead to exciting applications in areas of multi-parametric sensing, where independent measures can give more information about a system. Another example is the semiconductor laser with dual time-delayed feedback, which has been shown numerically to exhibit quasiperiodic dynamics [89]. Using an asymmetric feedback configuration, an all-optical feedback system has the potential for multi-parametric sensing on an optical wavelength scale. This future direction of research will be highlighted in Ch. 7.

Chapter 7

Conclusions and Future Directions

Throughout this thesis, I first presented my experimental methods for constructing a new type of system that uses nonlinear feedback in a wave-chaotic cavity. As shown in Ch. 3, this novel setup exhibits the potential for subwavelength position sensing of a subwavelength scatterer using various dynamical states. Using quasiperiodic frequencies shifts to map out position changes of the scatterer, I demonstrate a 2D subwavelength sensing resolution of $\lambda/300$. This mechanism relies on the ability to measure the quasiperiodic frequencies and for the frequency shifts to be independent. This particular phenomenon has never before been investigated. Thus, in Ch. 4, I show that that a numerical model can reproduce the frequencies, in Ch. 5, I provide analytical techniques for predicting the frequencies locations, and in Ch. 6, I investigate a simple system with similar behaviors to gain insight into the independence of the quasiperiodic frequency shifts. Overall, these chapters demonstrate a new understanding of quasiperiodicity frequencies in the context of sensing perturbation. In this final chapter, I summarize my main scientific contributions and discuss future directions.

7.1 Summary of the Main Scientific Results

The major contributions of this dissertation are (1) the first implementation of a wave-chaotic system with time-delayed nonlinear feedback for subwavelength sensing and (2) the development of a new 2D sensing technique that uses only scalar measurements of time-varying scattered fields. In particular, these scalar measurements map the frequencies of the quasiperiodic dynamics in the nonlinear feedback

system to the scatterer's relative location, which can be measured without the need for costly, high-resolution detectors. In addition, both of these contributions utilize an inexpensive electronic device and concepts from wave chaos, nonlinear dynamics, and subwavelength imaging.

In the previous chapters, using various experiments, models, and simulations, I narrow down the essential ingredients of this subwavelength sensing technique (a summary of each of the main reslults from Ch. 2 - Ch. 6 are presented at the end of Ch. 1). These ingredients include:

- a single-input, single-output nonlinear element (NLE) to create complex oscillations
- EM radiation (with average wavelength λ)
- feedback with a delay-gain distribution (τ_i, g_i) that varies with scatterer position
- dynamics with independent observables

These four ingredients give rise to a dynamically sensitive illuminating field that can localize an object in a complex scattering environment, such as a wave-chaotic cavity. The simplicity of these ingredients also offers many opportunities for future investigations.

Lastly, before moving on future directions, it is important to acknowledge that acoustic waves could also be used in a similar configuration. Such a system would broadcast acoustic waves from a speaker into a complex scattering medium and couple a portion of the scattered waves into a feedback loop using a microphone. This type of acoustic feedback system has been previously reported by Weaver *et al.* in Ref. [67] using periodic waves to sense qualitative changes in drying concrete.

Weaver *et al.* use the saturation of an amplifier as the system's nonlinearity, the concrete as the gain-delay distribution, and a periodic frequency shift to detect changes in the system. As mentioned briefly in Ch. 3, their work is an example of qualitative sensing technique that capitalizes on the Larsen effect, whereas my work creates a quantitative sensing method that uses a so-called quasiperiodic Larsen effect.

7.2 Future Directions

I acknowledge that, in the previous section, my list of ingredients to observe the quasiperiodic sensing mechanism does not explicitly include wave chaos. This is because wave chaos is not a necessary ingredient for multi-parametric sensing with quasiperiodicity (measuring multiple independent parameters simultaneously). Recall that the two-delay feedback system uses the simplest delay-gain distribution to demonstrate the 2D sensing. Therefore, although the original experiment to discover this sensing mechanism used a wave-chaotic cavity, it can be observed without the wave chaos.

Thus, as an interesting future direction of research, subwavelength sensing in a regular cavity (as opposed to a wave-chaotic cavity) can be investigated. Based on my list of ingredients, the quasiperiodic sensing mechanism should still be able to be observed in a regular cavity. However, it is unknown if wave chaos is essential for coupling the perturbations of the cavity's delay-gain distribution to the position of a subwavelength scatterer. I conjecture that the wave chaos enhances the system's sensitivity with regards to a subwavelength perturbation, but further investigation is necessary to confirm this. More specifically, one could quantify the resolution of the subwavelength sensing based on the level of wave chaos in the cavity, where the level of wave chaos is varied based on the degree of asymmetry in the cavity's

boundary.

However, one complication of this experimental investigation is that it is not clear how one would create a regular cavity with a scatterer; regular cavity's typically require a high degree of symmetry. In addition, the level of wave chaos may change with the scatterer's position, which could complicate making comparisons of the system's resolution in different configurations. Nonetheless, further investigation to understand the necessary (or sufficient) roles that wave chaos plays in subwavelength position sensing of a single scatterer is one of future interest. There has already been extensive research into different geometries for 2D wave-chaotic systems [48, 49, 51, 90], and applying nonlinear feedback to each of these systems with RX and TX antennas can give insight into their effects on the position-sensing resolution of a cavity-feedback system. Expanding the scattering and feedback to a 3D wave-chaotic cavity [54] may also affect the system's resolution.

Implementing 3D wave-chaotic cavities also opens up an additional future direction of research: 3D position sensing. However, in order to study 3D position sensing, an additional independent observable must also be introduced into the dynamics of the cavity-feedback system to resolve three degrees-of-freedom (x, y, z). My results suggest that one can resolve 3D positions using a quasiperiodic state with three independent frequencies. Complex quasiperiodic dynamical states are possible in time-delayed nonlinear feedback systems [22], but further study is required to create a three-tone quasiperiodic state that is stable in a cavity-feedback system for a 3D volume of interest. In addition, as mentioned in Ch. 3, altering the dimensions of the cavity can change the allowable polarization of the EM fields which as a result could alter the potential resolution of the system.

Interestingly, it has been proven in the literature that the existence of a system that exhibits dynamics with period three implies that dynamical chaos is also

possible in such a system. More specifically, in Ref. [91], it has been shown that controlled perturbations of a three-frequency torus can always give rise to chaos. This could present a potential problem for 3D position sensing: if a three-frequency quasiperiodic state always collapses to chaos, how can it be used to sense small perturbations such as changes to a scatterer's location? Because I have not explored three-frequency quasiperiodicity in my systems, I can only conjecture that such a problem would not allow for 3D position sensing.

However, I can instead propose a method for creating an artificial three-frequency quasiperiodic signal using band-limited channels that do not allow for cross talk. In this configuration, each frequency of the quasiperiodic signal is generated using a separate channel of the feedback loop. The nonlinearity of the feedback loops is just the saturation of amplifiers (similar to Ref. [67]). Thus, in each band-limited channel, only a periodic signal is created, and periodic signals from three different channels can be summed to create a pseudo-quasiperiodic signal with three independent frequencies. The advantage of this system is that it would not collapse to chaos. Lastly, although dynamical chaos was originally disregarded due to its complexity, the broadband nature and sensitivity of chaotic dynamics may have the potential for 3D sensing, given a more detailed, statistical analysis of the chaotic attractor and its changes with respect to a 3D scatterer position.

With additional independent observables in the feedback dynamics, there is also the potential for future research on sensing the position of multiple scatterers simultaneously. For additional scatterers, more degrees of freedom must be monitored simultaneously in order to resolve their positions. Investigating multiple scatterers also allows for studying the effects of shadowing. If each scatterer is illuminated from nearly all sides, there should be no shadows or blind spots while position sensing. Proving that the positions of multiple scatterers can be imaged simultaneously

represents another step towards realizing a practical imaging system.

As mentioned in Ch. 3 and 6, another future direction for this type of work is to map out regions of quasiperiodicity with respect to the system's parameters (delay offsets, bias voltage of the nonlinear circuit, gain of the feedback loop, bandwidth of the electronics, etc.). A better understanding of the windows of quasiperiodicity and the sensitivity for each of these windows will help to understand and maximize the potential dynamic range of the system.

As additional examples of future directions, wave chaos and nonlinear dynamics have recently been combined by another research group to explore their potential for secure communications applications [92]. This research group, which developed many of the original wave-chaos sensing-techniques that inspired my research, demonstrates the first study of adding a nonlinear device to the interior of a wave-chaotic cavity as the system's scatterer. In their paper, they credit my work as an "exciting new direction of research" for "adding objects with complex nonlinear dynamics to linear wave-chaotic systems" [92]. A future direction of Ref. [92] includes sensing the position of a nonlinear scatterer (as opposed to linear dielectric scatterer) with linear delayed feedback.

Furthermore, as mentioned briefly in Ch. 3, a natural extension of this work is wave chaos and nonlinear dynamics in the optical domain. This particular direction of research was recently highlighted in Ref. [93], a review article that discusses the future applications of sensing using the dynamics of nonlinear feedback systems. In the article, the authors acknowledge that the "combination of nonlinear-delayed feedback systems and wave-chaotic cavities gives rise to high sensitivity and sub-wavelength accuracy, overcoming even the diffraction limit" and "so far, the effect was demonstrated with radio-frequency waves, with a clear potential to be extended into the photonics domain" [93]. Therefore, as one of the immediate future direc-

tions of my work, I outline below the concept for an experimental setup for studying a new type of the cavity-feedback system using optical wave chaos and a semiconductor laser with time-delayed nonlinear feedback. Then, as a proof-of concept, I also demonstrate experimentally that the quasiperiodicity in a two-delay optical feedback system can already be used to yield subwavelength sensing results using my technique.

7.3 All-Optical Subwavelength Position Sensing Using Nonlinear Feedback in a Wave-Chaotic Cavity

In this section, I outline the main steps to create an all-optical version of the radio-frequency cavity-feedback system in order to image the position of a scatterer on a nanometer scale. In particular, I review the semiconductor laser feedback system with an external optical cavity. As shown in Tab. 7.1, the laser is the component that replaces the nonlinear circuit, now the central wavelength of the EM field is $\lambda \sim 1550$ nm, which is orders of magnitude smaller than the radio-frequency wavelengths (~ 15 cm). I also discuss some of the recent developments of wave chaos in 2D optical cavities that are several hundred micrometers in length and width. These optical microcavities represent the optical version of the microwave wave-chaotic cavity. Similar to the RF domain, the independent observables of the optical system are the quasiperiodic frequency shifts of the dynamics. Lastly, using a similar conceptual overview to that presented in Ch. 3, I give an example design of an all-optical subwavelength position-sensing system using the dynamics of the nonlinear laser system and the wave chaos of the optical microcavity.

For several decades, time-delayed nonlinear feedback has been studied in semiconductor laser systems [94]. A typical setup consists of a laser diode with optical

Table 7.1: Radio-frequency analogs of the proposed all-optical system for subwavelength position sensing using nonlinear feedback in a wave-chaotic cavity.

Ingredient	RF	Optical
λ	15 cm	1550 nm
NLE	transistor-based NLC	semiconductor laser-diode
(τ_i, g_i)	wave-chaotic cavity	chaotic optical microcavity
independent observables	quasiperiodic frequency shifts	quasiperiodic frequency shifts

feedback so that the light emitted by the laser is reflected off of a mirror and then coupled back into the laser cavity, as shown in Fig. 7.1a. The overall propagation of the optical signal leads to a feedback delay time of τ with an associated gain coefficient g. Due to the nonlinear interactions of photons inside of the laser cavity, this type of optical feedback can induce oscillations in the amplitude of the laser light [94]. In Fig. 7.1a, the intensity of the laser is monitored using a photo-detector, which converts the time-varying intensity of the optical signal into a voltage v(t) to be recorded on an oscilloscope. Depending on the values of the parameters of the feedback, for example (τ, g), the voltage v(t) can show steady-state, periodic, quasiperiodic, and chaotic dynamics [94]. The observed quasiperiodicity typically contains frequencies at several gigahertz [94]. Thus, similar to the electronic time-delayed nonlinear feedback system, a laser with optical feedback represents one of the main component of the imaging device.

The second component is an optical microcavity, which is comprises of a dielectric material in a certain geometry that can trap photons for extended periods of time [95]. Wave chaos has been observed in chaotic optical microcavities built using silicon structures [96] and in the cavities of vertical cavity emitting lasers (VCSELS) [52], where the resonances of the optical microcavities are used to characterize the

level wave chaos. In order to measure the resonances, light can be coupled into an optical microcavity through the evanescent field of a fiber-coupled laser diode that can sweep its frequency or wavelength, as shown in Fig. 7.1b. For a certain wavelength λ, the spatial modes of an optical cavity can be densely distributed in the cavity [52] and sensitive to the perturbations of subwavelength scatterers, such as that caused by the tip of a tapered optical fiber [17]. These perturbations can be detected as resonance shifts on a detector that records the net output power of the laser and the optical microcavity as a function of input wavelength [17]. In this type of open-loop system, nanometer-sized perturbations can be detected [17, 97–99].

Using a cavity-feedback configuration, the sensitivity offered by an optical microcavity can be combined with the dynamical sensitivity of a nonlinear feedback system. Hence, as shown in Fig. 7.1c, an all-optical version of the cavity-feedback system can be realized using a laser dioide with time-delayed optical feedback that is coupled into and out of a chaotic optical microcavity. In the time domain, this type of cavity can be characterized as a delay-gain distribution (τ_i, g_i), similar to pulse response in the microwave wave-chaotic cavity. Thus, the output of the laser is split along many paths through the cavity and the light that is coupled back into the laser cavity is delayed by time-delays τ_i with gain coefficients g_i. Due to the feedback, the laser intensity oscillates in time and the parameters of the system are adjusted such that v(t) is quasiperiodic. As a tapered optical fiber perturbs the evanescent field of the optical microcavity, the delay-gain distribution (τ_i, g_i) is perturbed and the frequencies of the quasiperiodicity shift. Using a calibration grid, these frequency shifts can be mapped out with respect to the fiber's position (x, y). Scaling the 2D position-sensing resolution of the radio-frequency cavity-feedback system ($\lambda/300$) to the optical domain, a laser diode that outputs a wavelength $\lambda \sim 1550$ nm is expected to image the position of the subwavelength fiber to within approximately 5

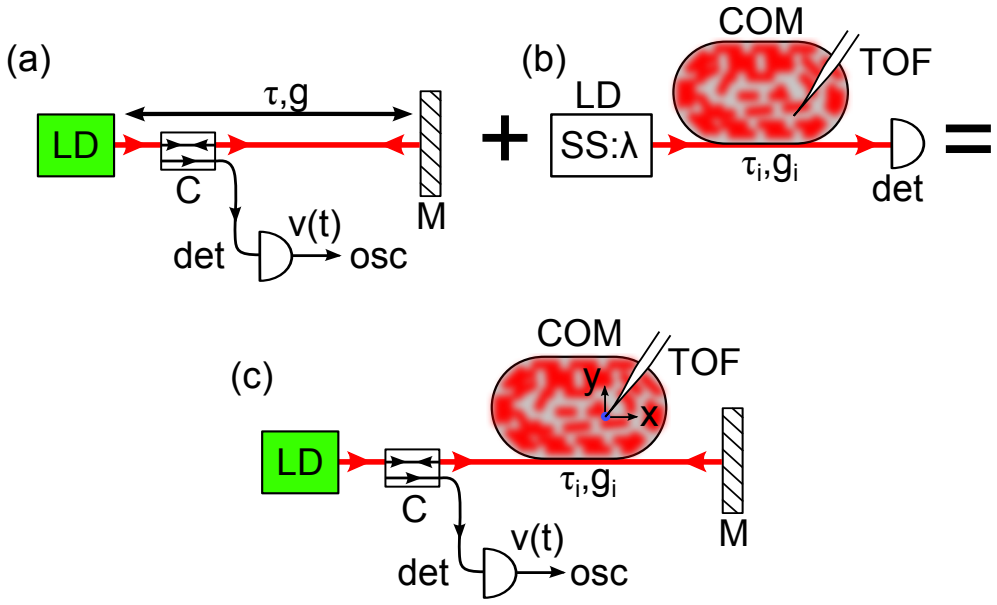

Figure 7.1: **Conceptual overview of the all-optical cavity-feedback system.** (a) Time-delayed nonlinear feedback in a semiconductor laser diode (LD). The output of LD is reflected by a mirror (M) and fed back to the laser cavity. A portion of the output power drives a coupler (C) for detection (det), which is then recorded as the voltage v(t) on an oscilloscope (osc). (b) The output of LD is coupled to a chaotic optical microcavity (COM). The wavelength of the laser λ is varied using a swept source (SS) while the output power is detected and recorded. The resonances of the cavity can be used to detect the presence of a tapered optical fiber (TOF). (c) The emitted light of LD is coupled into COM, reflected by a mirror and fed back to itself. The LD output also passes through a coupler (C) to a detector and oscilloscope, where it is recorded as a time-varying voltage v(t). The quasiperiodic frequency content of v(t) is used to reconstruct the position (x, y) of TOF.

nm. The proposed all-optical device would extend the main results of this thesis to create a new imaging system with nanometer precision.

In the next subsection, I use a two-delay setup to demonstrate an experimental proof-of-concept for nanometer position-sensing in an all-optical feedback system.

7.3.1 Proof-of-Concept: Two-Delay Sensing Using Quasiperiodicity in an All-Optical System

Though the work presented in this section shows a new experimental result, it

is still preliminary with regards to subwavelength sensing. Overall, the goal of this section is to demonstrate an experiment with quasiperiodic frequency shifts in an all optical feedback system that can sense multiple spatial degrees-of-freedom simultaneously. However, in order to claim the my subwavelength sensing system can be scaled to optical wavelengths, a full experimental system with a chaotic optical microcavity must be investigated. Thus, the two-delay optical feedback system illustrates a preliminary proof-of-concept for 2D subwavelength position sensing of a subwavelength scatterer.

Similar to the dual-loop configuration discussed in Ch. 6, this proof-of-concept system uses two independent variable time delays to map the frequency shifts in the quasiperiodic dynamics of an all-optical feedback system. The results presented here are preliminary and confirm that the frequency shifts of a nonlinear optical system can be used to sense simultaneous position changes on a nanometer scale. Thus, the two-delay optical feedback system represents a first step towards realizing the all-optical cavity-feedback system described in Fig. 7.1c. For each of the experimental measurements, Andrés Aragoneses Aguado aided in the experimental setup, data collection, and analysis. Lastly, these results are part of an investigation that is currently ongoing.

The experimental setup for the two-delay device is shown in Fig. 7.2 using a laser diode with $\lambda \sim 1550$ nm. The emitted light is attenuated and collimated using a lens. In free space, a beam splitter (BS) separates the optical field along two different paths with mirrors (M_1 and M_2) that reflect light back to the lens and into the laser cavity. The propagation distances along each path result in two different time-delays, $\tau_1 \sim 55.5$ ns and $\tau_2 \sim 55.6$ ns, with feedback strengths (gains g_1 and g_2) approximately equal. The relative values of the time-delays are controlled using piezoelectric transducers (PZT_1 and PZT_2) that move the positions of the mirrors

on a nanometer scale (see Appendix D for the calibration of the PZTs). Lastly, the output of the laser diode is also coupled to a detector and an oscilloscope (using a 90/10 coupler (C), where 90% of the optical power is transmitted to free space and 10% of the optical power is directed to the detector).

By adjusting the optical feedback strength, I tune the dynamics of the experimental system such that v(t) is quasiperiodic. As shown in Fig. 7.3a, the temporal evolution of v(t) shows a fast oscillatory signal with a modulated amplitude, and in Fig. 7.3b, the power spectral density (PSD) shows clusters of frequency peaks that range from 1 GHz to 7 GHz. Of the peaks in these four clusters, I quantify changes to the frequencies $f_1 = 1.1$ GHz, $f_2 = 2.1$ GHz, $f_3 = 5.4$ GHz, and $f_4 = 6.5$ GHz. The origins of the these frequencies are currently being investigated by our collaborators Andrés Aragoneses Aguado and Cristina Masoller at the Polytechnic

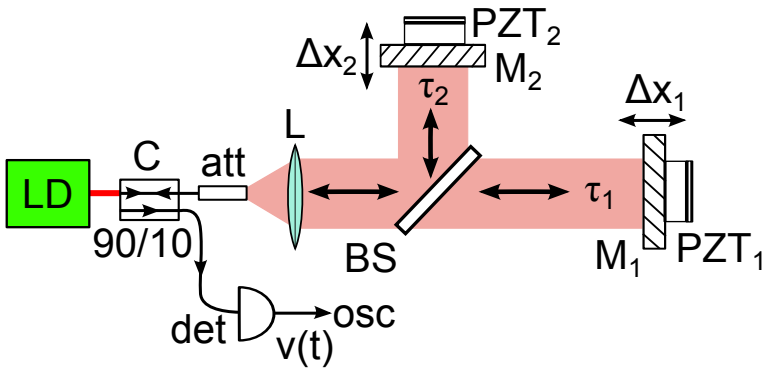

Figure 7.2: **Two-delay all-optical feedback system for subwavelength sensing.** The output of a laser diode (LD, Sumitomo SLT4416-DP) passes through a collimating lens (L) in free space, separates using a beam splitter (BS), is time-delayed along two separate paths with propagation delays τ_1 and τ_2, and feeds back to itself. Mirrors M_1 and M_2 at the end of these paths are attached to piezoelectric transducers (PZT_1 and PZT_2, Burleigh PZO-015) to make small adjustments to τ_1 and τ_2, respectively. Using an attenuator (att) and a 90/10 coupler (C), the feedback gain is controlled and the feedback signal is routed to a photodetector (det, New Focus 1544-B) and a high-speed oscilloscope (osc, DSO90804A).

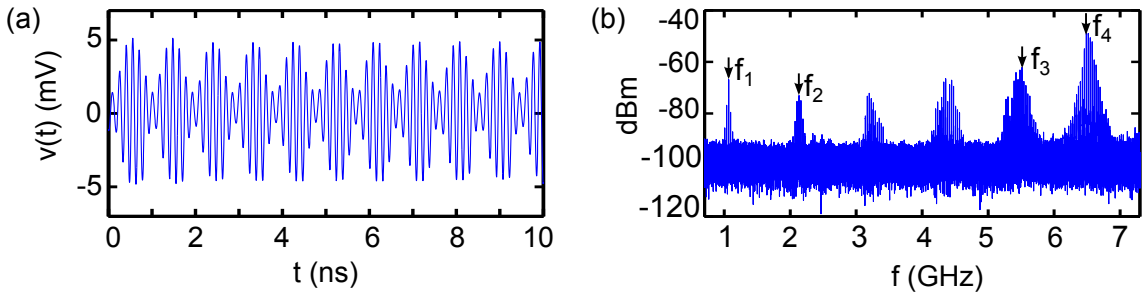

Figure 7.3: **Quasiperiodic dynamics of the two-delay optical feedback system.** (a) Temporal evolution of v(t), which represents the laser intensity oscillations: v(t) $\propto I(t) = |E(t)|^2$, where $I(t)$ is the intensity of the electric field with amplitude $E(t)$. (b) Power spectral density (PSD) of the oscillations.

University of Catalonia in Spain.

In the experimental system, I track the frequencies of the quasiperiodicity as τ_1 and τ_2 are adjusted simultaneously. To perform these adjustments, the positions of M_1 and M_2 are changed using computer-controlled, high-voltage power supplies to translate the PZTs. PZT_1 and PZT_2 are translated through a two-dimensional grid ($\sim$ 100 nm $\times$ 100 nm) of relative position changes $(\Delta x_1, \Delta x_2)$, respectively, so that $\Delta x_1 = 2\Delta\tau_1$ and $\Delta x_2 = 2\Delta\tau_2$ (the factors of 2 result from the optical signal propagating in both directions along the feedback paths). At each location of the PZTs, the quasiperiodic frequency shifts $(\Delta f_1, \Delta f_2, \Delta f_3, \Delta f_4)$ are measured using the large trigger-skew method on the digital oscilloscope (see Ch.3).

As an example of two of the quasiperiodic frequency shifts, I plot Δf_2 and Δf_4 as a function of $(\Delta x_1, \Delta x_2)$ in Figs. 7.4a-b. Unlike the near-planar frequency shifts observed in the radio-frequency system, the two-delay optical system produces quasiperiodic frequency shifts that take the form of surfaces with curvature (I hypothesize that smaller time delay changes in the optical system would also result in near planar surfaces). Using second-degree multivariate functions, I create

a map of these surfaces with respect to Δx_1 and Δx_2

$$\Delta f_2(\Delta x_1, \Delta x_2) = \sum_{i=1}^{i=2} \left(a_i \Delta x_1^i + b_i \Delta x_2^i \right) + \sum_{j=0}^{j=1} A_j \Delta x_1^j \Delta x_2^j, \tag{7.1}$$

$$\Delta f_4(\Delta x_1, \Delta x_2) = \sum_{i=1}^{i=2} \left(c_i \Delta x_1^i + d_i \Delta x_2^i \right) + \sum_{j=0}^{j=1} B_j \Delta x_1^j \Delta x_2^j, \tag{7.2}$$

where the fitted coefficients a_i, b_i, c_i, d_i, $A_{i,j}$, and $B_{i,j}$ are listed in Appendix D. Using these maps, I numerically solve for the predicted values $\Delta\hat{x}_1$ and $\Delta\hat{x}_2$.

The resulting predictions are first used to reconstruct the calibration grid path of the delay shifts. Figure 7.4c shows the actual calibration grid path and Fig. 7.4d shows the second-order grid reconstruction. In Fig. 7.4d, the reconstructed calibration grid shows distortions and hence errors in the predicted positions (Δx_1, Δx_2). The reconstructed grid yields RMS differences between the predicted and actual Δx_1 and Δx_2 values of 12.3 nm and 6.8 nm, respectively, which is an average resolution of $\sim \lambda/160$. Lastly, the maximum observed errors are $x_{1,\max} = 27.5$ nm ($\sim \lambda/60$) and $x_{2,\max} = 22.7$ nm ($\sim \lambda/70$), which sets a bound on the resolution, but nevertheless demonstrates subwavelength sensitivity over a 2D area.

Based on the results from Ch. 3, there are several potential sources of error that cause these distortions. The first source of error is from the approximation that the frequency shifts are second-order multivariate surfaces. Small fluctuations in the actual frequency shifts about the fitted surfaces can project to large fluctuations in the predicted positions. Similar to Ch. 3, to determine the contribution of this effect, higher-order fittings can be performed along with measurements of the system's drift and frequency fluctuations. Due to the sensitivity of the system, I conjecture that temperature fluctuations in the room are the main source of errors in the frequency measurements. Further investigation in temperature controlled

environments can help to eliminate this source of error.

In addition, changes to the mirror positions M_1 and M_2 that control the distances (Δx_1, Δx_2), are assumed to be linear with respect to the applied voltages and without hysteresis (see Appendix D). This approximation can contribute to the system's distortions if there are errors in the programmed grid positions. Based on the results from Appendix D, this is most likely not the case, but further investigation into this all-optical system with more precise nano-controlled stages will answer this question more definitively. Nevertheless, the reconstructed calibration grid projects approximately onto the original grid with subwavelength dimensions ($\sim$ 100 nm $\times$ 60 nm).

Finally, using Eqs. (7.1) - (7.2) for Δf_2 and Δf_4 as a calibration mapping, I test the dual position-sensing capabilities of the optical-feedback system using an arbitrary set of successive relative positions $\Delta x_{1,n}$ and $\Delta x_{2,n}$ within the calibration grid, where n is the index of test locations (see Ch. 3 and Ch. 6 for similar experimental tests). The test path of (Δx_1, Δx_2) in plotted in Fig. 7.4e, where only the first and last points of the path lie on the calibration grid for reference. For each point along the test path ($n = 33$ total points), the frequency shifts ($\Delta f_2, \Delta f_4$) are measured, and when using the functional form of the calibrated maps, the predicted path ($\Delta \hat{x}_{1,n}, \Delta \hat{x}_{2,n}$) is reconstructed numerically and shown in Fig. 7.4f.

Similar to the reconstructed calibration grid path, this reconstructed path is distorted. The overall shape of the path is qualitatively similar (preserving the "S" shape), but because the calibration grid is distorted in certain areas, the part of the path that lies in this area is distorted such that it extends beyond the grid. Quantitative comparisons reveal that the RMS differences between the predicted and actual $\Delta \hat{x}_{1,n}$ and $\Delta \hat{x}_{2,n}$ is 12.1 nm and 9.3 nm, respectively, yielding an average 2D resolution of $\sim \lambda/150$. The maximum observed errors are $x_{1,\max} = 28.7$ nm ($\sim \lambda/50$)

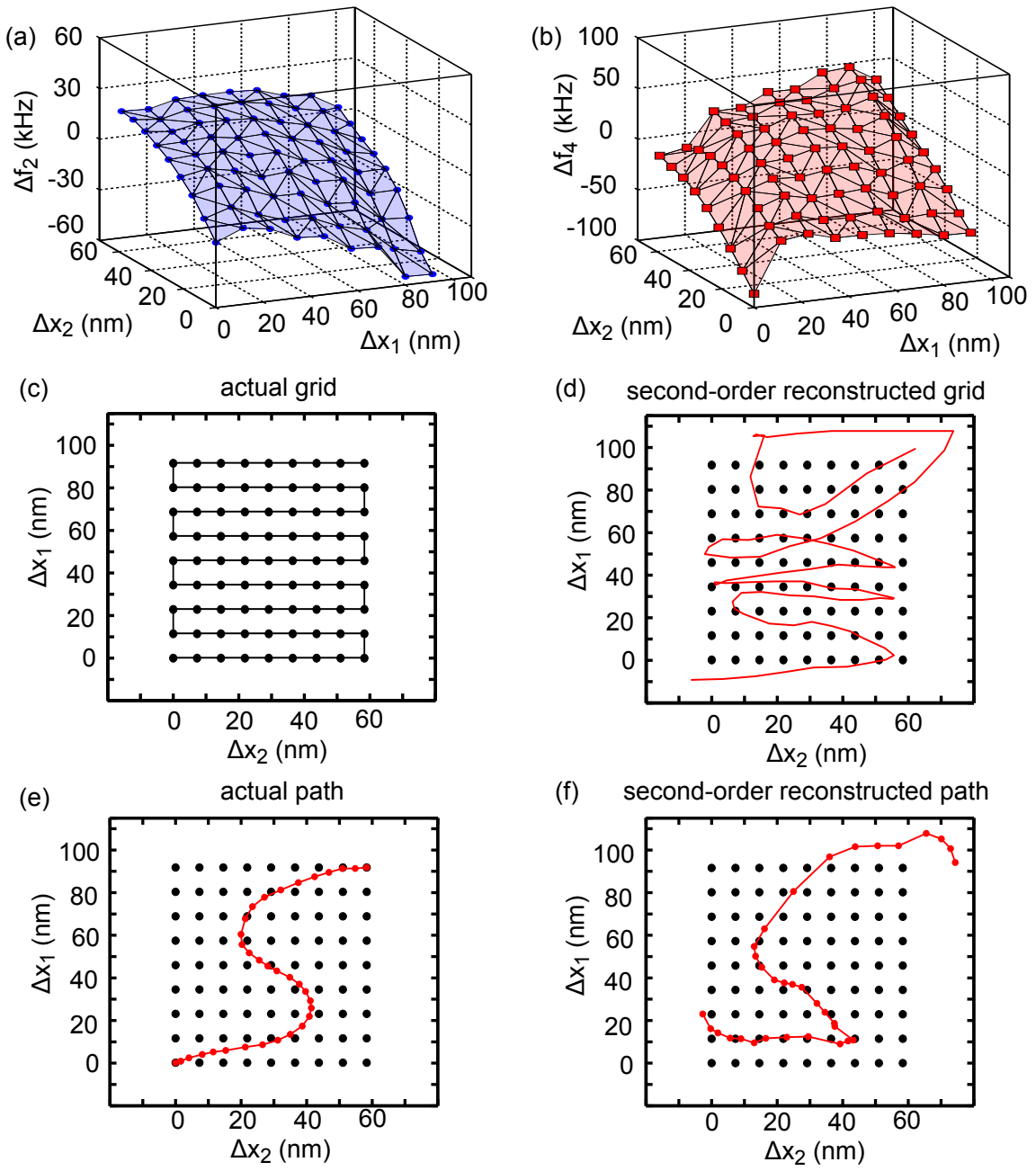

Figure 7.4: **Quasiperiodic frequency shifts used for subwavelength sensing.** Observed frequency shifts (a) Δf_2 and (b) Δf_4 as a function of the relative positions Δx_1 and Δx_2. (c) Calibration grid path (black curve) and (d) reconstructed grid path (red curve). (e) Actual path (red curve) of ($\Delta x_{1,n}$,$\Delta x_{2,n}$) positions to test the 2D grid (black dots) of the frequency shifts. (f) Reconstructed path (red curve) of the relative length shifts using the 2D grid (black dots).

and $x_{2,\max} = 19.5$ nm ($\sim \lambda/80$). Potential sources of these errors come from the approximation that the calibration grid is a second-order surface, errors mirror positions, and the potential for thermal fluctuations to cause frequency drift in the system. Further investigation of this optical system can help to understand and eliminate these sources of error. However, similar to the 2D sensing results from Ch. 3, even with these distortions in the reconstructed path, the average resolution given by the RMS errors and the maximum observed errors are still vastly subwavelength. Overall, these results demonstrate that independent position observables can indeed be reconstructed on a subwavelength scale using only a scalar optical signal and quasiperiodic frequency shifts.

Similar to Chs. 3 and 6, a lower bound on the system's average dynamics range is ~ 10 (100 nm / 10 nm). This is again only a lower bound and further investigation is required to measure the upper bound on the dynamic range. Based on the results from Ref. [89], quasiperiodicity in a two-delay optical feedback system can persist for external cavity length changes of up to 5 mm. Thus, based on this work, I estimate a potential upper bound for this system's 2D dynamic range as 10^5 (5 mm /8 nm). Of course, this range assumes that the PZTs also can move with nanometer precision over a 5 mm range and that noise and fluctuations in the system do not cause bifurcations. Thus, this all optical system shows great potential for new directions of exploration with regards to both sensing and dynamical systems. This concludes the proof-of-concept experimental test for 2D subwavelength position-sensing in an all-optical feedback system.

7.3.2 Concluding Remarks

The results of this two-delay optical feedback system combined with the results of the radio-frequency cavity-feedback system demonstrate a well-defined research

path for realizing a new device with nanometer imaging resolutions. Because lasers with optical feedback have been studied for decades, they present a solid foundation for creating a new dynamical system that is coupled to an optical microcavity. Based on the interest in these results thus far, other research group are beginning to explore the properties of nonlinear dynamics and wave chaos [92].

In conclusion, this dissertation demonstrates a new sensing modality using nonlinear dynamics. Using a wave-chaotic cavity as a complex scattering environment, I show that this modality can sense a subwavelength scatterer's position with vastly subwavelength resolution. I also implement this method in two different experiments with average wavelengths that differ by orders of magnitude and show that it can sense multiple degrees-of-freedom simultaneously.

In the future, because this technique is relatively inexpensive and simple, I hope that there are further investigations into the imaging capabilities of chaotic cavities with nonlinear feedback. To summarize, I believe that this new type of system can provide a simple method for tracking nano-sized scatterers. Ultimately, I would like to see the dynamics of a cavity-feedback system used to sense the position of nano-particle tags in biological systems to reconstruct images of cellular structures.

Appendix A

Nonlinear Circuit: Background and Discussion

This appendix serves as an added description of the nonlinear circuit (NLC) used in the various time-delayed feedback systems that are presented in this dissertation. In the first section, I present a brief explanation of the type of transistor used in the NLC, its operating characteristics, and a potential origin of the circuit's low-pass filtering effects at high frequencies. In the second section, I present a similar, lower-bandwidth nonlinear circuit described in Ref. [22] to compare to the high-frequency capabilities of my NLC. Lastly, using a simple model for the transistor in the NLC, I present equations for modeling the nonlinear circuit from first principles.

A.1 Bipolar Junction Transistors and Low-pass Filtering Effects

The transistor used in my experiments is an NPN Silicon Germanium RF transistor (Infinium Technologies BFP620), where the NPN junction classifies the device as a bipolar-junction-transistor (BJT) [100]. The bipolar junction refers to the connections between two types of semiconductors in a BJT, as shown by the NPN configuration in Fig. A.1, where one of the semiconductors is N-type with an excess of free electrons, and the other is a P-type semiconductor with a deficit of electrons. In the figure, the two junctions are the points of contact between the N and P semiconductors. On the surfaces of these semiconductors are metal contacts, labeled as the collector (C), the base (B) and the emitter (E), that allow for voltages to be applied to the N and P semiconductors, creating electric fields across the emitter-

base junction and the collector-base junction. Based on the values of the applied voltages v_C, v_B, and v_E (applied to the collector, base, and emitter, respectively), these electric fields can either block or allow currents to flow through the device. The circuit representation for the transistor (T) with these three voltages is shown in Fig. A.1b.

As an example, a simple circuit with a BJT transistor is depicted in Fig. A.1c. In the figure, a constant voltage v_{in} is applied to the base of the device. The collector is connected to a positive voltage V_{CC} with some resistance and to the output of the system v_{out}. Lastly, the emitter is connected to the ground. In this configuration, for $v_{in} = 0$ V, the voltage v_{out} is constant. However, for large enough v_{in}, current flows from the collector to the emitter and a proportional voltage drop is induced at v_{out}. This device is one of the building blocks of the NLC in Fig. A.1d.

To realize the tent-like shape for the input and output voltages of the NLC, the transistor T_1 is configured such that the supply voltage V_{cc} is connected directly to the collector, v_{in} drives the base, and the emitter is connected to the ground. For v_{in} below the threshold of the device, the current does not flow between the collector and emitter, but v_{in} can bypass the BJT through R_{NL} to the output, thus giving a linear relationship between input and output voltages. For v_{in} above the transistor threshold, there is a voltage drop on v_{out} that is proportional to v_{in}, thus yielding an anti-linear behavior. Together, the linear and anti-linear regimes produce the tent-like shape of the NLC.

There are various models for a BJT, each with a different level of complexity [100]. The choice of the model's complexity depends on the characteristics of the transistor that need to be reproduced in a simulation. For example, one of the simpler models for a BJT is known as the Ebers-Moll model, which is primarily used to model the output of the transistor for constant input voltages [100]. In the

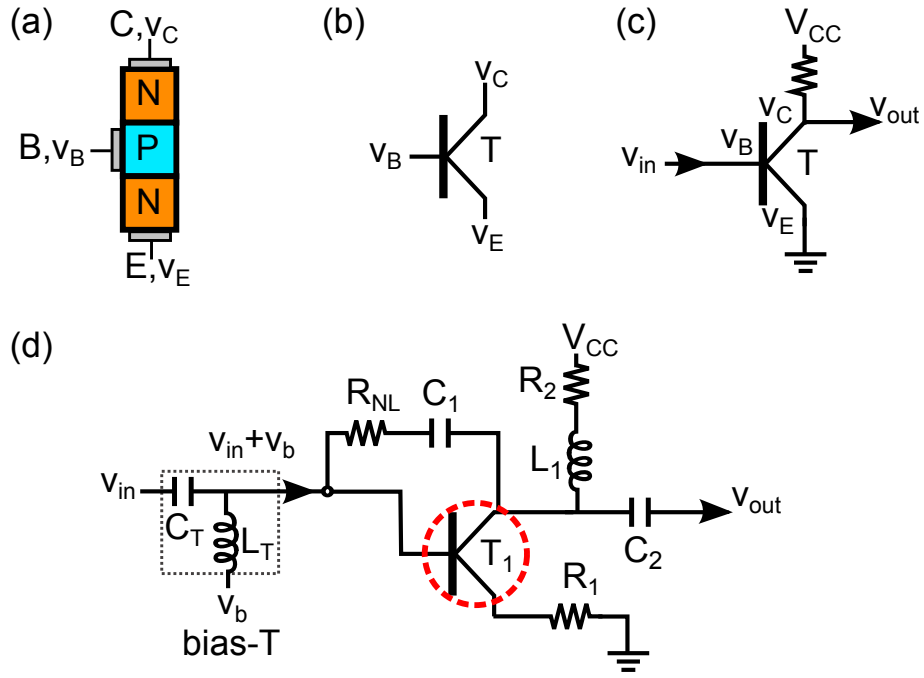

Figure A.1: **Bipolar junction transistor in the nonlinear circuit.** (a) Bipolar junction transistor with NPN junctions. The base (B), emitter (E), and collector (C) plates each have applied voltages v_B, v_E, and v_C, respectively. (b) The circuit symbol for a transistor (T) with the corresponding voltages labeled. (c) Transistor circuit illustrating how the output voltage v_{out} can change as a function of the input voltage v_{in}. (d) Circuit schematic for the NLC with the transistor T_1 highlighted by the red dotted circle (see Ch. 2 for details). The capacitor C_T and inductor L_T represent the bias-T (grey dotted box) that adds the voltages v_{in} and v_b

Ebers-Moll model, the transistor is treated as two different PN junctions such that the current across each junction can be calculated separately and then summed to give the currents at the collector, base, and emitter [100].

However, in reality, a transistor can be a dynamic device with time-evolving voltages. One of the issues with the non-static behavior of a transistor is the charge storage that can occur in the layers between the PN junctions [100]. As one example of a dynamical model that captures this effect, charge storage depletion can be included in the transistor model as a capacitive effect. As shown in Fig. A.2, the schematic of the transistor now includes intrinsic capacitances C_{BE}, between

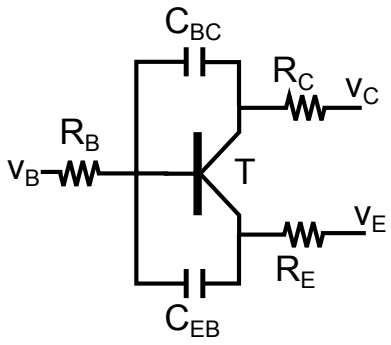

Figure A.2: **Schematic of a transistor with capacitive and resistive effects to simulate charge storage in the junctions.**

the base and emitter, and C_{BC}, between the collector and the base. In addition, the schematic also includes the intrinsic resistances that are associated with the collector, base, and emitter (R_{C}, R_{B}, and R_{E}, respectively). These cause frequency filtering of the voltages across the junctions. More complicated models can also include voltage-dependent capacitances that can change depending on the voltages across the junctions [100]. Thus, as the transistor switches from non-conducting to conducting (or vice versa), the filtering effects in the device change.

These types of intrinsic, voltage-dependent capacitances contribute to the low-pass filtering effects in the NLC. The particular BJT used in the NLC is chosen for the approximate values $C_{\mathrm{BE}} = 98.4$ fF and $C_{\mathrm{BC}} = 55.9$ fF, which are provided by manufacturers on the transistor's data sheet. These values should be compared to the values $C_{\mathrm{BE}} = 1$ pF and $C_{\mathrm{BC}} = 0.6$ pF in the original transistor-based circuit of Ref. [22] (NPN transistor: BFG520). With smaller intrinsic capacitances in the updated design, the filtering effects occur at higher frequencies in the NLC. To highlight this change, in the next section, I revisit the original circuit from Ref. [22] and show that its filtering effects, which are qualitatively similar to those in the NLC, occur at a lower range of frequencies (50 MHz $< f <$ 800 MHz).

A.2 Previous Circuit Design

Because the original circuit from Ref. [22] was first created in our lab, I am able to characterize the nonlinear aspects of the device myself. This particular nonlinear circuit is a modified test board (ERA-SM) from Mini-Circuits, shown in Fig. A.3a, where the original intent of these boards is for testing linear amplifiers. The main modification to the board is the replacement the Mini-Circuit's ERA-amplifier with the NPN wideband transistor BFG520 [22]. The circuit diagram for these modifications is reproduced in Fig. A.3b. Based on the schematic, for input voltages below the transistor threshold $v_T \sim 0.7$ V, the output current of the device is given by the voltage drop across R_N. For input voltages above v_T, the output current is the difference between the voltage drop across R_N and the collector current flowing through the transistor to ground.

To demonstrate the relationship between the circuit's input and output voltages, I reproduce a figure from Ref. [22] that characterizes the output voltages v_{out} of the circuit with respect to a sinusoidal driving signal v_{in}. Prior to the input of the circuit, a bias voltage of v_b is added to v_{in} to access the circuit's nonlinear regime. Using a

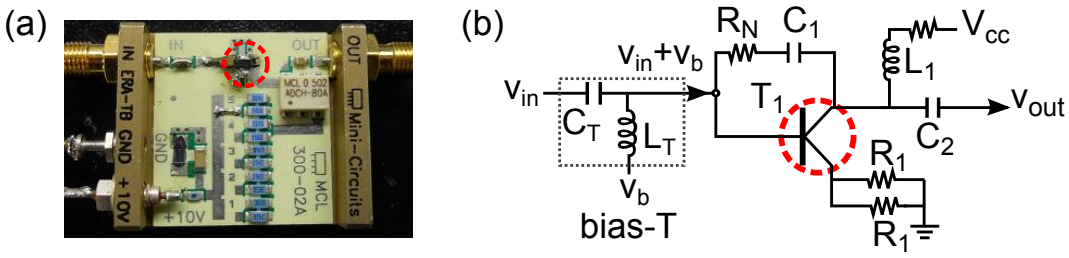

Figure A.3: **Illing *et al.* nonlinear circuit.** (a) Photograph of the previous circuit (from Ref. [22]), where the transistor is highlighted in the red dotted circle. (b) Circuit diagram of the original nonlinear circuit with transistor T_1, where $R_N = 68$ Ω, $R_1 = 4.75$ Ω, $R_2 = 47$ Ω, $C1 = 47$ nF, $C2 = 0.39$ μF, and L_1 is a radio-frequency choke (MCL Model AdcH-80A). The capacitor C_T and inductor L_T represent the bias-T (grey dotted box) that adds the voltages v_{in} and v_b.

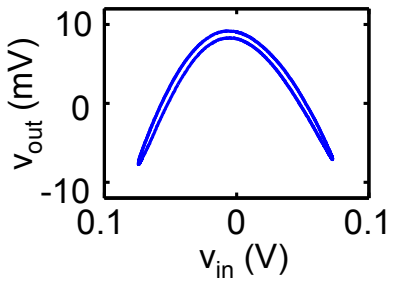

Figure A.4: **Illing *et al.* circuit characterization.** Characterization of v_{out} for a given v_{in} at 13 MHz with $v_b = 0.7$ V. In addition to the tent-like properties of v_{out}, the output voltage of the previous circuit is ac-coupled and therefore centered around $v_{out} = 0$ V.

driving signal at frequency $f = 13$ MHz and $v_b = 0.7$ V, I plot the waveform v_{in} versus v_{out} in Fig. A.4. For voltages below v_T, the transistor remains non-conducting and the circuit produces an approximately linear input-output relation (with positive slope). For voltages above v_T, the transistor allows current to flow through R_1 to ground, inducing an anti-linear input-output relation (with negative slope). Thus, based on the results for a 13 MHz input waveform, the original circuit performs a similar input-output, tent-like nonlinear function.

However, for higher frequency inputs, the circuit exhibits distortions similar to those observed in the NLC in Ch. 4. These distortions are demonstrated with a sinusoidal v_{in} at frequencies ranging from 50 MHz - 1 GHz in Fig. A.5. It is clear that the distortions become increasingly complex at higher frequencies and Illing *et al.* hypothesize in Ref. [22] that this is due to low-pass filtering in the circuit. However, this non-ideal behavior did not play a role in the work of Ref. [22] because the circuit operated in a lower range of frequencies (≤ 500 MHz).

In their original work, Illing *et al.* studied the dynamical behaviors of the NLC in a time-delayed feedback system. The basic setup for their feedback experiment is that in Ch. 2, where coaxial cables form the system's time delay τ. Similar to this

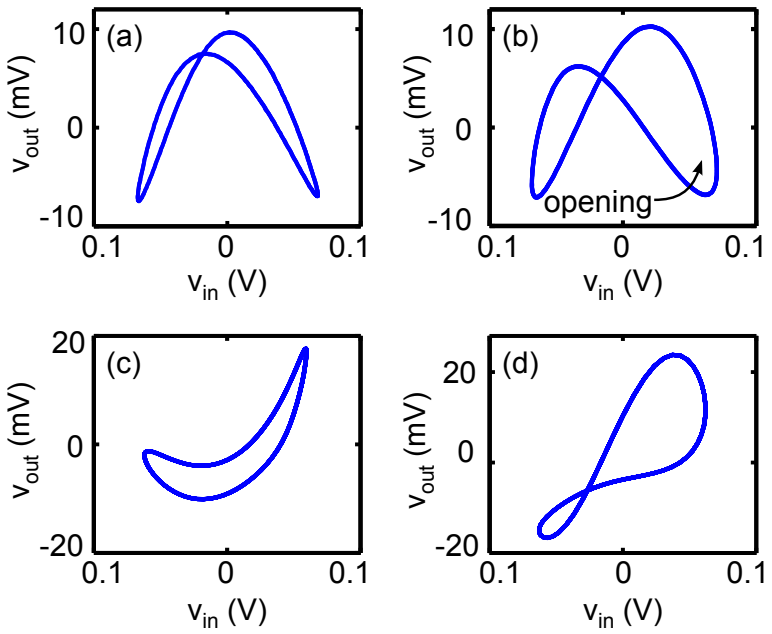

Figure A.5: **Distortions from the Illing *et al.* circuit.** Input voltages v_{in} versus output voltages v_{out} in the circuit from Ref. [22] for sinusoidal driving waveforms at frequencies (a) $f = 50$ MHz, (b) $f = 100$ MHz, (c) $f = 500$ MHz, and (d) $f = 800$ MHz. The opening of the tent-like function is highlighted in (b).

design, the net filtering of feedback components can be approximated as a band-pass filter with parameters $f^{(-)} = 110$ MHz and $f^{(+)} = 502$ MHz. Using the gain G of the feedback loop as a bifurcation tuning parameter, Illing *et al.* demonstrated that, for high enough gain, the system experiences a Hopf bifurcation to periodic oscillations. Further increasing G, they showed that the nonlinear feedback device can also exhibit both quasiperiodic dynamics and chaos. The observed dynamics contained frequencies up to approximately 500 MHz, which classifies the circuit as an ultra-high-frequency device [22].

The NLC in the cavity-feedback system also demonstrates tent-like input-output characteristics that are qualitatively similar to the Illing *et al.* circuit. The previous (BFG520) and updated (BFP620) transistors show significant distortions in the output of the nonlinear circuits for $f > 500$ MHz and for $f > 1$ GHz, respectively. As

mentioned earlier, a potential cause of these filtering effects is the resulting capacitive effects from charge storage depletion between the semiconductor junctions of the transistors. In order to demonstrate how these capacitances can play a role in the distortions of the output voltages from the circuits, I present a model for the NLC design that includes capacitive effects in the next section.

A.3 Nonlinear Circuit Model with Capacitive Effects

Here, I present a model that uses resistors (R), inductors (L), and capacitances (C) to represent the NLC. The model also includes capacitances to represent the charge storage of the BJT transistor [101]. For the simplicity of this demonstration, I assign constant capacitances that do not depend on the voltages through the transistor. In addition to these RLC equations, I model the currents in the transistor with a simple piecewise-linear function following Ref. [102]. The schematic of the RLC model is depicted in Fig. A.6 with the corresponding voltages (v), currents (I), capacitances (C), resistances (R), and inductances (L) labeled. As shown in the figure, there are added depletion capacitances C_{BE} and C_{BC} between the base and the emitter and the base and the collector of the transistor T_1, respectively. The purpose of this model is to demonstrate that the values of these capacitances across the transistor junctions can increase or decrease the level of distortions in the output voltages (away from the ideal tent-like shape) for a given input frequency range.

The RLC model is derived using the values of the changing voltages and currents in the circuit. First, I briefly derive these equations to give insight to their origins. In this model, the voltages $\mathrm{v_{BE}}$ and $\mathrm{v_{BC}}$ are defined as

$$\mathrm{v_{BE}} = \mathrm{v_B} - \mathrm{v_E}, \tag{A.1}$$

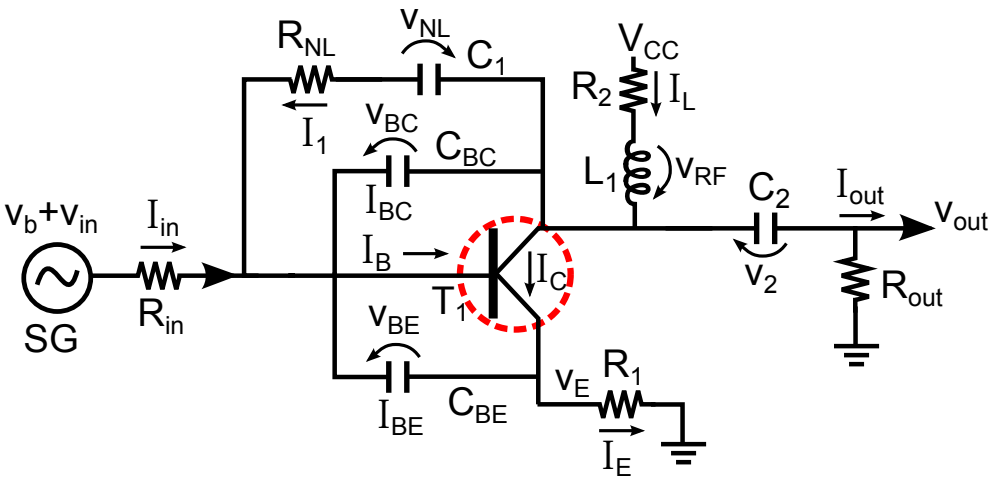

Figure A.6: **Circuit schematic of an RLC model for the NLC with depletion capacitances.** For simplicity, rather than including the bias-T components from Fig. A.1d, the bias voltage v_b is added directly to v_{in}. Arrows indicate the directions of positive voltage changes and positive current flows. An input resistance R_{in} and output resistance R_{out} model the impendances of the experimental signal generator (SG) and oscilloscope (osc). The transistor T_1 is highlighted by the red dotted circle.

$$v_{BC} = v_B - v_C, \tag{A.2}$$

where v_B, v_C, and v_E are the voltages applied to the transistor's base, collector, and emitter, respectively. The equations that describe the rate of change of voltages and currents across the system's capacitors and inductors are

$$C_1 \dot{v}_{NL} = I_1, \tag{A.3}$$

$$C_2 \dot{v}_2 = I_{out}, \tag{A.4}$$

$$L_1 \dot{I}_L = -v_{RF}, \tag{A.5}$$

$$C_{BE} \dot{v}_{BE} = I_{BE}, \tag{A.6}$$

$$C_{BC} \dot{v}_{BC} = I_{BC}. \tag{A.7}$$

Therefore, the state variables of this model are v_{NL}, v_2, I_L, v_{BE}, and v_{BC}. Summing the currents at the points of intersection in Fig. A.6 leads to

$$I_L = I_1 + I_{out} + I_C - I_{BC}, \tag{A.8}$$

$$I_{in} = I_B - I_1 + I_{BC} + I_{BE}, \tag{A.9}$$

$$I_{BE} + I_B + I_C = v_E/R_1, \tag{A.10}$$

and following the various paths of voltages in the circuit leads to

$$v_{in} - R_{in}I_{in} - v_{BE} - v_E = 0, \tag{A.11}$$

$$V_{CC} - R_2 I_L + v_{RF} - v_2 - I_{out}R_L = 0, \tag{A.12}$$

$$I_{out}R_L + v_2 + v_{BC} - v_E = 0, \tag{A.13}$$

$$-v_{NL} + I_1 R_{NL} - v_{BC} = 0. \tag{A.14}$$

It remains to express Eqs. (A.3) - (A.7) in terms of the state variables of the system. After extensive algebra, these equations can be rewritten as

$$\dot{v}_{NL} = \frac{-(v_{BC} + v_{NL})}{C_1 R_{NL}}, \tag{A.15}$$

$$\dot{v}_2 = G_1/(C_2 G_2), \tag{A.16}$$

$$\dot{I}_L = \frac{-(R_L G_1/G_2 + I_L R_2 + v_2 - V_{CC})}{L_1}, \tag{A.17}$$

$$\dot{v}_{BE} = \frac{-I_B G_2 - I_C G_2 + I_L R_{in} R_L + R_{in}(v_2 + v_{BC} + v_{BE}) + R_L(v_{in} - v_{BE})}{C_{BE} G_2}, \tag{A.18}$$

$$\dot{v}_{BC} = [I_C + G_1/G_2 - I_L - (v_{BC} + v_{NL})/R_N]/C_{BC}, \tag{A.19}$$

where

$$G_1 = I_{\mathrm{L}} R_1 R_{\mathrm{in}} - R_1(\mathrm{v}_2 + \mathrm{v}_{\mathrm{BC}} - \mathrm{v}_{\mathrm{in}}) - R_{\mathrm{in}}(\mathrm{v}_2 + \mathrm{v}_{\mathrm{BC}} - \mathrm{v}_{\mathrm{BE}}), \tag{A.20}$$

and

$$G_2 = R_1(R_{\mathrm{in}} + R_{\mathrm{L}}) + R_{\mathrm{in}} R_{\mathrm{L}}, \tag{A.21}$$

are commonly occurring terms in Eqs. (A.15) - (A.19). Lastly, I model the currents I_{B} and I_{C} through the transistor T_1 as a piecewise-linear model [102] that reads

$$I_{\mathrm{B}} = \begin{cases} 0, & \text{if } \mathrm{v}_{\mathrm{BE}} \leq \mathrm{v}_{\mathrm{T}} \\ (\mathrm{v}_{\mathrm{BE}} - \mathrm{v}_{\mathrm{T}})/R_{\mathrm{on}}, & \text{if } \mathrm{v}_{\mathrm{BE}} > \mathrm{v}_{\mathrm{T}} \end{cases}, \tag{A.22}$$

where R_{on} is the intrinsic resistance when the transistor is conducting and $I_{\mathrm{C}} = \beta I_{\mathrm{B}}$, where β is a constant [102]. Lastly, the output voltage of the model is

$$\mathrm{v}_{\mathrm{out}} = I_{\mathrm{out}} R_{\mathrm{out}} = C_2 \dot{\mathrm{v}}_2 R_{\mathrm{out}}. \tag{A.23}$$

Therefore, Eqs. A.15 - A.23 represent a model for the transistor-based nonlinear circuit with constant depletion capacitances.

To test this model, I first verify that it produces a tent-like nonlinear behavior between input and output voltages for low-frequency input voltages v_{in}. As shown in Fig. A.7, for a given set of circuit parameters and an input sinusoidal signal at frequency $f = 270$ MHz, the model produces a qualitatively similar tent-like nonlinear operation. The parameters chosen for this simulation are obtained from typical experimental values in the NLC and the values $C_{\mathrm{BE}} = 500$ fF and $C_{\mathrm{BC}} = 500$ fF are chosen such that the tent-like shape is preserved at $f = 270$ MHz.

Next, I demonstrate that this model can show distortions when driven by sinusoidal waveforms at higher frequencies. In Fig. A.8, the model parameters are kept

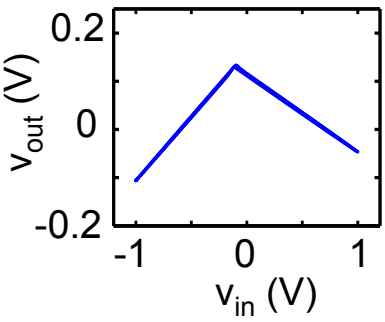

Figure A.7: **Input versus output voltages of the RLC model.** The output voltage v_{out} plotted as a function of v_{in} for a input driving frequency of $f = 270$ MHz with $v_b = 0.65$ V, $v_T = 0.72$ V and $V_{CC} = 1.3$ V. The parameters of the model are $R_{in} = 50$ Ω, $R_{NL} = 30$ Ω, $R_1 = 5.1$ Ω, $R_2 = 68$ Ω, $R_L = 50$ Ω, $R_{on} = 500$ Ω, $C_1 = 47$ nF, $C_2 = 100$ nF, $L_1 = 4$ nH, and $\beta = 60$ with the depletion capacitances $C_{BE} = 500$ fF and $C_{BC} = 500$ fF.

the same and the input of the model is now driven with sinusoidal signals at frequencies ranging from $f = 500$ MHz to $f = 1.9$ GHz. Similar to the experimental NLC, for higher input driving frequencies, the tent-like shape shows an opening, as highlighted in Fig. A.8d. This opening is due to a frequency-dependent phase-shift through the NLC model.

Lastly, I demonstrate that the capaciatances C_{BE} and C_{BC} play significant roles in determining the frequency range over which these types of distortions occur. To compare with the distortions in Fig. A.8, I increase the values of the depletion capicitances to $C_{BE} = 5$ pF and $C_{BC} = 5$ pF and simulate the RLC model for input driving signals over a frequency range $f = 100$ MHz to $f = 700$ MHz. The resulting input-output voltage relations are plotted in Fig. A.9, where the tent-like nonlinearity shows increased distortions at lower frequencies. For example, the opening of the tent-like nonlinear operation is more pronounced in Fig. A.9b for $f = 500$ MHz (with $C_{BE} = C_{BC} = 0.5$ pF) than in Fig. A.8b for $f = 1.9$ GHz (with $C_{BE} = C_{BC} = 500$ fF).

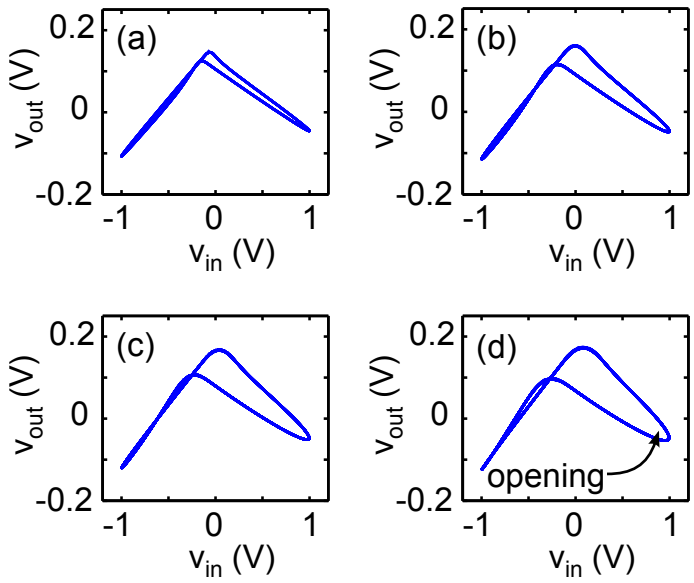

Figure A.8: **Distortions in the RLC model for low depletion capacitances.** Input voltages v_{in} versus output voltages v_{out} in the RLC circuit model for sinusoidal driving signals at frequencies (a) $f = 500$ MHz, (b) $f = 1.1$ GHz, (c) $f = 1.5$ GHz, and (d) $f = 1.9$ GHz with the depletion capacitances $C_{BE} = 500$ fF and $C_{BC} = 500$ fF.

Therefore, using a simple RLC model for the NLC, I have shown that the distortions in the output voltages of the nonlinear circuit can be reproduced qualitatively using depletion capacitances to model charge storage in the BJT transistor. Furthermore, using two different sets of constant capacitances for C_{BE} and C_{BC}, the model demonstrates that the distortions depend on the amount of charge storage between the junctions of the transistor. These two sets of capacitances represent qualitatively the change from the transistor BFG520 in Ref. [22] (with relatively high depletion capacitances) to the transistor BFP620 in the NLC of the cavity-feedback system (with relatively low depletion capacitances). The result of the change causes the distortions in the output of the NLC to occur for a higher range of frequencies.

Though the RLC model can demonstrate this behavior qualitatively, it is not used in the model for the cavity-feedback system for two primary reasons. First, the RLC model does not capture quantitatively the subtle distortions in the output of

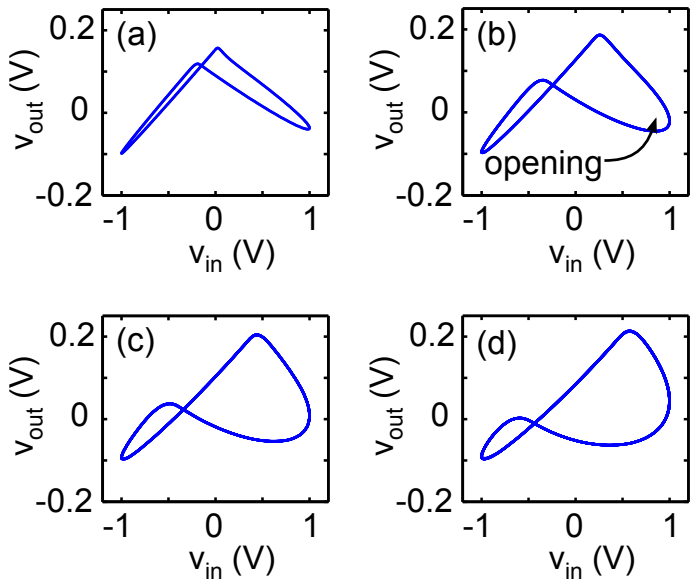

Figure A.9: **Distortions in the RLC model with high depletion capacitances.** Input voltages v_{in} versus output voltages v_{out} in the RLC circuit model for sinusoidal driving signals at frequencies (a) $f = 100$ MHz, (b) $f = 300$ MHz, (c) $f = 500$ MHz, and (d) $f = 700$ MHz with the depletion capacitances $C_{BE} = 5$ pF and $C_{BC} = 5$ pF.

experimental circuit. In order to build an RLC model that does capture these effects, additional features must be introduced such as nonlinear capacitances and a more accurate description of the transistor's currents. Each of these added complexities must then be matched to the experimental parameters. Rather than try to measure and model the nonlinear capacitances of the transistor, I use a "black box" approach, where the input and output of the unknown system or "black box" are measured and the simplest model is used to reproduce the observed effects. In the experimental nonlinear circuit, this approach leads to the model presented in Ch. 4.

The second reason for not using the RLC model for the NLC is to be consistent with the rest of the model for the cavity-feedback system. For example, the external feedback loop of the cavity-feedback system is modeled as a lumped-element band-pass filter. In principle, each element in the external feedback loop could be modeled from first principles based on its components. However, because the band-pass filter

is simpler and it captures the desired effects, there is no need to pursue a more complicated model. Thus, using a filter approach for modeling the NLC matches conceptually with the modeling approach for the rest of the cavity-feedback system.

A.4 Summary

In summary, the operating characteristics of the NLC are explained based on the properties of a BJT transistor. In addition, the frequency-dependent distortions can be attributed to charge storage in the BJT device. Using the original NLC from Ref. [22], I demonstrate that the previous circuit's input-output tent-like function and distortions are qualitatively similar to the circuit in the cavity-feedback system. Lastly, using RLC equations to model the device, I show that changing the values of the transistor's intrinsic capacitances can alter the frequency range for which these distortions arise, thus qualitatively representing the change from the Illing *et al.* circuit design to the NLC of the cavity-feedback system.

Appendix B

Calibration of Frequency Tracking

This appendix provides additional details of how I measure experimentally the frequency shifts of the periodic and quasiperiodic dynamics discussed in Ch. 3. In particular, I present the experimental calibration method for tracking frequencies and their drift. I also provide the antenna far-field efficiency and the coefficients of the fitted multivariate functions used for mapping the 2D position of the scatterer.

B.1 Frequency-Shift Measurements and Calibration

For each set of frequency measurements, a time series containing the relevant frequency information is acquired from a digital oscilloscope and transferred to a computer for analysis. I use an experimental technique with minimal data that is designed to measure small frequency shifts of a periodic or quasiperiodic signal with a known finite number of prominent frequency peaks.

Prior to measuring the frequency shifts, a 12.5 μs time series is saved as a reference. For a quasiperiodic signal, I calculate the Fourier Transform of the waveform and measure its four most prominent frequency peaks, where the waveform is long enough to guarantee sufficient resolution to distinguish these peaks from one another. A typical quasiperiodic time series and frequency spectrum is shown in Figs. B.1a-b. The locations of these peaks are recorded for later use as the seed parame-

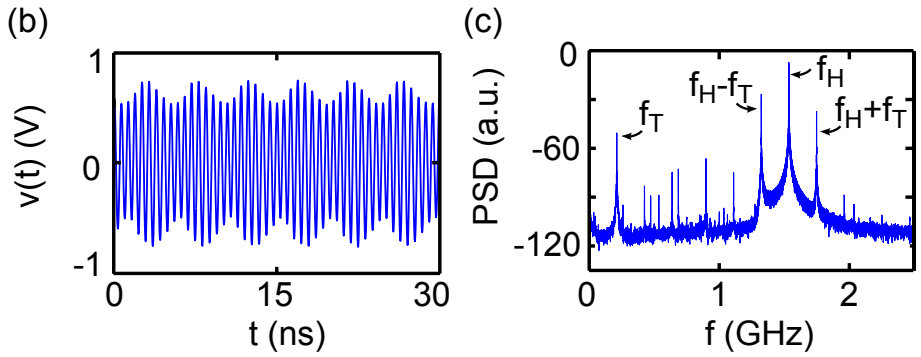

Figure B.1: **Typical quasiperiodicity in the experimental system.** (a) Temporal evolution of v(t) and (b) its power spectral density (PSD) with the prominent frequency peaks labeled f_T, f_H, $f_H - f_T$, and $f_H + f_T$.

ters of the fitting function

$$\bar{\mathrm{v}}(t) = \sum_{i=1}^{i=4} A_i \sin[2\pi(f_i + \Delta f_i)(t - t_s)], \tag{B.1}$$

with the trigger skew time $t_s = 2.5\ \mu$s, $f_1 = f_{\mathrm{T}}$, $f_2 = (f_{\mathrm{H}} - f_{\mathrm{T}})$, $f_3 = f_{\mathrm{H}}$, and $f_4 = (f_{\mathrm{H}} + f_{\mathrm{T}})$, and where A_i and Δf_i are free fitting parameters determined through a least-square regression. For each subsequent fit, the seed frequencies of the regression algorithm are taken to be equal to the prior set of fit frequencies. In doing so, I am assuming the relative shifts in the frequencies are small between consecutive fits, as described next.

The value of the trigger skew time t_s must be large to maximize the observable shift of the waveform in the acquisition window (see Chapter 3 for details). However, if the relative phase of the waveform changes by more than $\sim \pi/4$ from one object position to the next, the fitted values of the frequencies can jump by a large amount, which is not representative of the actual frequency shifts. Once the data has been analyzed over a region of the scatterer positions, each frequency shift Δf_i is then centered about zero by subtracting its average.

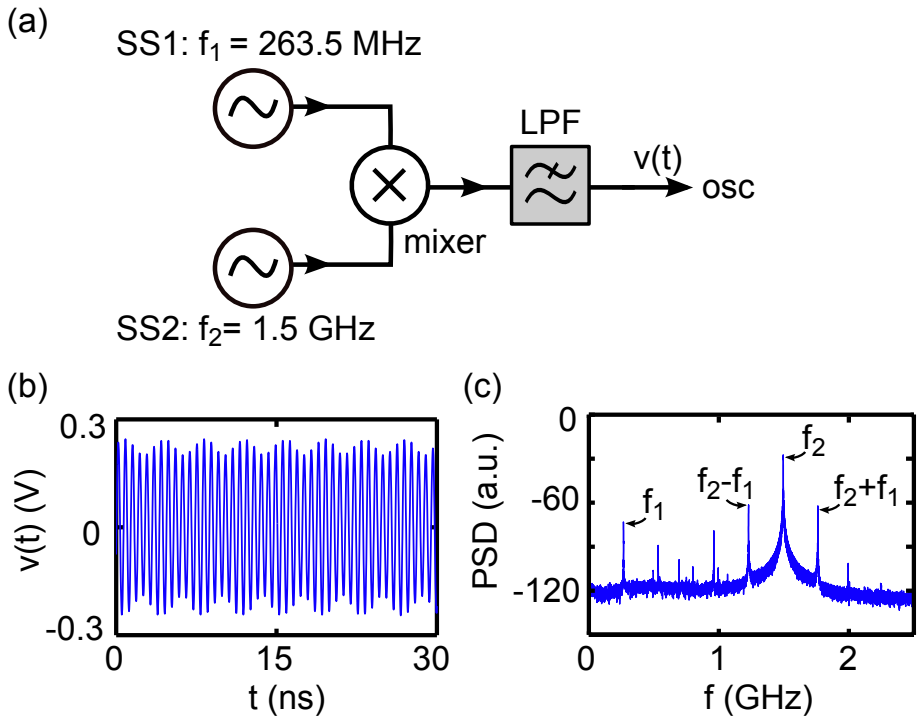

Figure B.2: **Calibration setup and signal generated for quantifying the measurement errors of frequency shifts.** (a) The frequency f_1 is generated by signal source 1 (SS1), a Hewlett Packard network analyzer (8753E), and the frequency f_2 is generated by signal source 2 (SS2), an Agilent Technologies signal generator (E8267D). I use the same low-pass filter (cascaded Mini-Circuits LFCN-1400, LFCN-2000) at the output of a mixer (Mini-Circuits ZFM-2000) that cuts all frequencies above 2 GHz and appears in the feedback loop of the cavity-feedback system. The resulting output voltage is (b) an artificially-generated quasiperiodic signal and with (b) power spectral density (PSD) that contains four prominent frequencies f_1, f_2, $f_2 - f_1$, and $f_2 + f_1$.

To quantify the error associated with this type of measurement method, I measure the frequency shifts of an engineered two-tone quasiperiodic signal generated with known frequencies. To create this signal, I mix the outputs of two independent signal sources with controllable frequencies f_1 and f_2, as shown in Fig. B.2a. The resulting waveforms and their corresponding frequency spectra are qualitatively similar to those observed in the nonlinear feedback loop, as shown in Figs. B.2b-c.

Using $t_s = 2.5\ \mu s$, I reproduce the experimental data acquisition for two differ-

ent calibration measurements. First, I fix the values of f_1 and f_2 and collect a set of 200 different times series from the output. Using the initial seed frequencies obtained from the programmed values of f_1 and f_2 and their linear combinations, I fit individually each time series using Eq. (B.1); consecutive fits are seeded with the previous set of fitted frequencies. I compare the values of the programmed values of f_1 and f_2 and their linear combinations with the 200 different fitted-frequency measures. Examples of the measured data for $\Delta\bar{f}_1$ and $\Delta\bar{f}_2$ are plotted in Figs. B.3a-b, where the averaged frequencies

$$\Delta\bar{f}_1 = [\Delta(f_2 - f_1) + \Delta f_1 - \Delta(f_2 + f_1)]/3, \tag{B.2}$$

$$\Delta\bar{f}_2 = [-\Delta(f_2 - f_1) + \Delta f_2 + \Delta(f_2 + f_1)]/3. \tag{B.3}$$

are similar to $\Delta\bar{f}_{\mathrm{T}}$ and $\Delta\bar{f}_{\mathrm{H}}$ (see Ch. 3). The root mean square (RMS) frequency differences between the measured values of $\Delta\bar{f}_1$ and $\Delta\bar{f}_2$ and the actual shifts are 3.3 kHz and 0.2 kHz, respectively. These values should be compared to the 1 Hz frequency resolution of the Hewlet Packard (8753E) signal source and the 1 mHz frequency resolution of the Agilent Technologies (E8267D) signal source.

In addition, I test the measurement technique with a calibrated frequency shift Δf_2. I collect 100 artificially-generated quasiperiodic time series where f_2 is increased by 10 kHz between each consecutive acquisition (+1 MHz total), and then collect 100 quasiperiodic time series where f_2 is decreased by 10 kHz between each consecutive acquisition (-1 MHz total). Using the initial values of f_1 and f_2 and their linear combinations as the initial seed frequencies, I fit the time series using Eq. (B.1). I compare the values of the known curves $\Delta\bar{f}_1$ and $\Delta\bar{f}_2$ with the fitted measures. Examples of the measured shifts for $\Delta\bar{f}_1$ and $\Delta\bar{f}_2$ are plotted in Figs. B.3c-d. The RMS frequency difference between the actual and measured $\Delta\bar{f}_1$ is 2.5

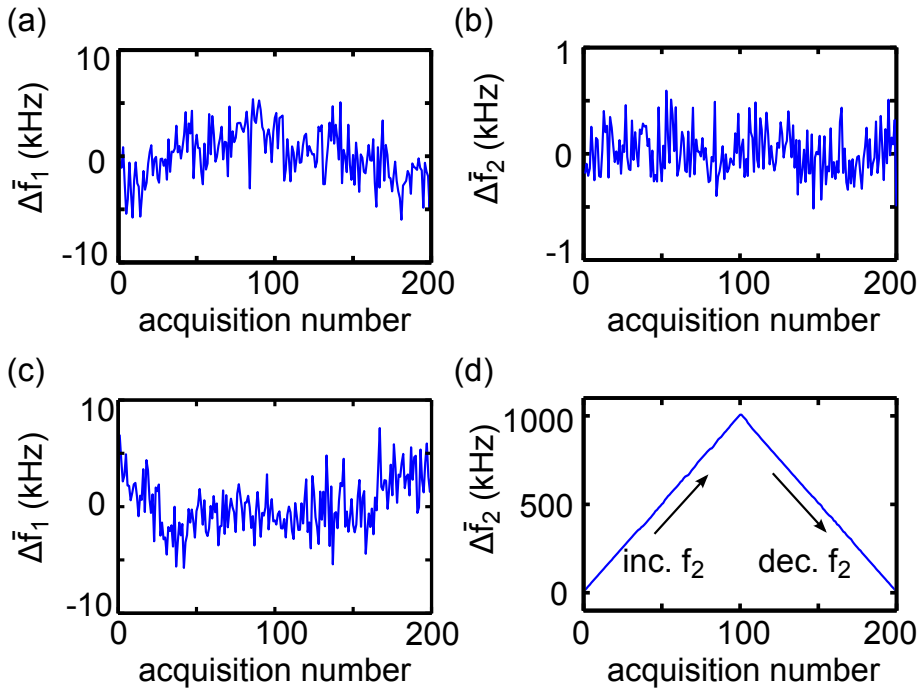

Figure B.3: **Calibration of the frequency shift-measurement technique using the artificially-generated quasiperiodic signal.** In the first test, both frequencies f_1 and f_2 are held constant such that (a) Δf_1 and (b) Δf_2 are approximately zero. In the second test, (a) f_1 is held constant such that $\Delta \bar{f}_1$ is approximately zero and (b) f_2 is increased such that $\Delta \bar{f}_2$ shifts.

kHz, and the average RMS frequency difference between $\Delta \bar{f}_2$ is 3.5 kHz. I compare the frequency differences from our calibration tests to the maximum observed frequency shift in the quasiperiodic signal of the nonlinear feedback loop ($\sim$ 500 kHz). Thus, the errors represent approximately 0.7% of the observed changes.

In summary, this measurement technique detects small shifts in the primary frequency components of a periodic or quasiperiodic signal with kilohertz resolution. In the next section, I show how parameter drift in the cavity-feedback system can lead to frequency drift in the dynamics.

B.2 Frequency Drift in the Cavity-Feedback System

As an example of the frequency drift in the experimental cavity-feedback system, I collect 500 measurements of $\Delta\bar{f}_{\mathrm{T}}$ and $\Delta\bar{f}_{\mathrm{H}}$ (see Chapter 3, Eqs. (3.6) - (3.7)) for fixed parameters of the feedback. The purpose of this measurement is to demonstrate that temperature and humidity fluctuations change the density of air in the wave-chaotic cavity and can affect the frequencies of oscillation. As shown in Figs. B.4a-b, the values of $\Delta\bar{f}_{\mathrm{T}}$ and $\Delta\bar{f}_{\mathrm{H}}$, which should be constant over time, can drift due to parameter fluctuations of the cavity-feedback system. Based on this experimental test, $\Delta\bar{f}_{\mathrm{T}}$ can drift with a standard deviation of $\sigma_{\mathrm{T}} = 3.3$ kHz and $\Delta\bar{f}_{\mathrm{H}}$ can drift with a standard deviation of $\sigma_{\mathrm{H}} = 7.5$ kHz over 500 waveform acquisitions. These drifts are within the same orders of magnitude as those observed during the calibration measurements of the frequency shifts using commercial signal sources in the previous section. Also, it should be noted that the correlation between the observed drifts $\Delta\bar{f}_{\mathrm{T}}$ and $\Delta\bar{f}_{\mathrm{H}}$ is approximately 60%, which means that, on average, the fluctuations in the system affect each frequency measure in a similar manner.

For the data of the 2D subwavelength position sensing in Chapter 3, there are 121 waveform acquisitions in the calibration grid and 32 waveform acquisitions in

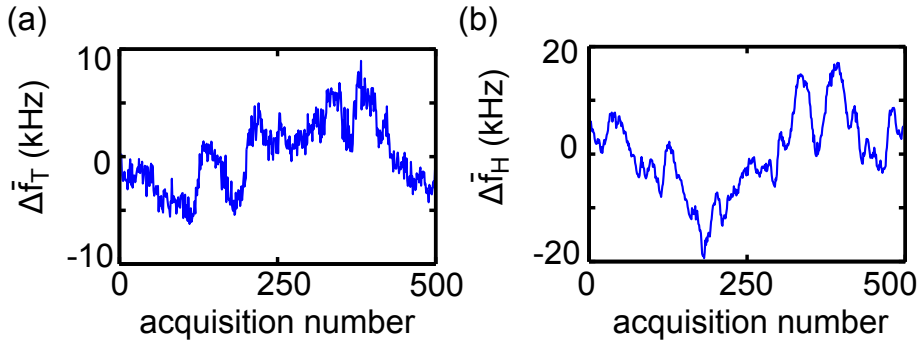

Figure B.4: **Frequency drift in the cavity-feedback system** for (a) $\Delta\bar{f}_{\mathrm{T}}$ and (b) $\Delta\bar{f}_{\mathrm{H}}$ where all parameters are held constant over 200 waveform acquisitions.

the test path. Across these measurements, the average frequency shifts for $\Delta\bar{f}_{\mathrm{T}}$ and $\Delta\bar{f}_{\mathrm{H}}$ between acquisitions is 41.5 kHz and 7.7 kHz, respectively. Therefore, it is possible for the drift to affect measurements of the frequency shifts, thus degrading the subwavelength resolution performance. To keep the influences of drift from becoming detrimental to the sensing mechanism, the cavity-feedback system is always switched on and given 30 minutes to stabilize its temperature before collecting data. In addition, data is collected at a time when the temperature is most stable in the laboratory (at night) and test data sets are acquired in succession to estimate the relative level of drift present in the system at that time.

B.3 Antenna Far-Field Efficiency

In order to further characterize my broadband antennas, I brought my TX antenna to a commercial facility (The Wireless Research Center of North Carolina). In this facility, they measure the far-field patterns and power efficiency of antennas using an anechoic chamber to remove reflections from the room. Using a sinusoidal driving signal with a swept frequency, they measured the power efficiency $P_{\mathrm{out}}/P_{\mathrm{in}}$ of the antenna, where P_{in} is the injected power to the antenna and P_{out} is the total power of the emitted radiation. The experimental efficiency of the antenna's far-field pattern in shown in Fig. B.5. Based on these results, the antenna shows an average efficiency of $\sim 75\%$ for 0.6 GHz $< f <$ 2 GHz.

B.4 Scatterer Displacement Measurements

As mentioned in Ch. 3, the relative position of the scatterer with respect to the programmed translation stage position must be measured in order to quantify the correlation between these positions. The reason for quantifying this correlation is

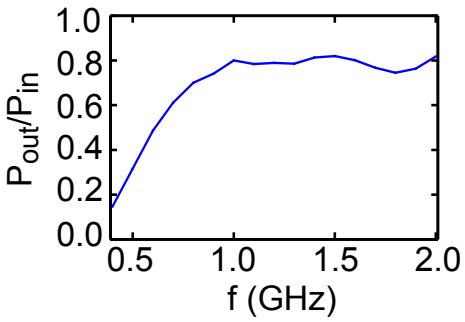

Figure B.5: **Antenna far-field efficiency** calculated by measuring $P_{\text{out}}/P_{\text{in}}$.

to determine the role of scatterer positioning errors in the distortions of the reconstructed calibration grid path in the 2D quasiperiodic sensing of the cavity-feedback system. The procedure for directly measuring the scatterer position follows (as mentioned in Ch. 3, it was hypothesized that the glue that holds the scatterer to the translation stage may stretch and the scatterer may not be positioned correctly).

The scatterers position is measured using a device known as a dial drop indicator. A picture of this device is shown in Fig. B.6a, where a dial indicator gives the relative position change of a contact stem. The contact stem makes contact with the scatterer as it is displaced in 1D using the translation stages. Each tick mark in the dial indicator is representative of a 25 μm displacement. In order to help remove ambiguities from reading the indicator in these measurements, the programmed displacements of the scatterer are all larger than 25 μm. All measurements are consecutive and repeated multiple times to avoid errors from thermal expansion of the materials are the temperature in the room fluctuates. In addition, a position of the scatterer was fixed and monitored for over 1 hour, showing no observable change from such fluctuations.

It should be noted that these measurements include the errors associated with the translation stage positioning. Based on the manufacturer's calibration of the

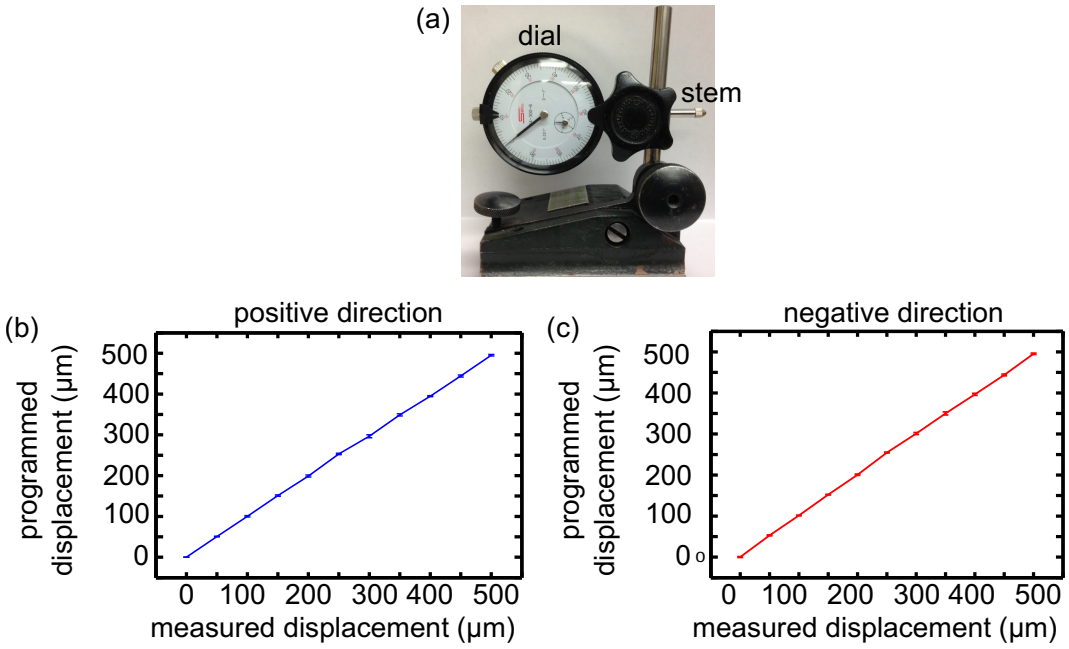

Figure B.6: **Scatterer displacement measurements.** (a) Dial drop indicator. (b) Measurmenets of the scatterer displacements in the positive direction and (c) the negative direction as a function of the programmed positions of the translation stage.

translation stages, they have relative positioning errors of approximately 5 μm. As mentioned in Ch. 3, these errors can be caused by backlash in the mechanical screws of the stages, and an automated backlash correction is in place in order to minimize such errors. During all measurements of the scatterer displacement using the dial indicator, there is backlash correction and the translation stage error should be $\sim \pm 5$ μm.

Based on the calibration grid spacing of 0.5 mm (see Fig. 3.17), I choose to measure the position of the scatterer with the dial indicator over a 1D displacement of 0.5 mm at 50 μm steps. The measurements for the scatterer displacements in the positive x (or y) direction are shown in Fig. B.6b and in the negative x (or y) direction are shown in Fig. B.6c. In each figure, the measured scatterer displacement

is plotted versus the programmed translation stage position. In the positive (negative) direction, the RMS error of the scatterer position is 5.5 ± 2.5 μm (5.7 ± 2.0 μm) and the maximum observed error is $\sim 12.0 \pm 2.5$ μm ($\sim 11.0 \pm 2.0$ μm). Error bars represent the standard deviation of measurements, and visually the two curve look nearly identical because these error bars are small in comparison to the 500 μm scale. Note that the maximum errors are approximately one half of a tick mark on the dial's indicator. As mentioned above, these errors are on the same order of magnitude as the relative positioning errors of the translation stage itself. Therefore, based on these results, I estimate that the positioning error due to the glue that holds the scatterer is on the order of 5 μm. Because this positioning error is orders of magnitude smaller than the 2D position errors in the reconstruction of the calibration grid path, they are not the main source of the distortions of Figs. 3.17a-b or Figs. 3.18c-d. This concludes the direct measurements of the scatterer displacement.

B.5 Coefficients of the Frequency-Shift Fits: 2D Postition Sensing

In Ch. 3, I fit the calibration grid data of the frequency shifts $(\Delta\bar{f}_{\mathrm{T}}, \Delta\bar{f}_{\mathrm{H}})$ with respect to the scatterer position (x, y) using the fourth-order multivariate functions

$$\Delta\bar{f}_{\mathrm{T}}(x,y) = \sum_{i=1}^{i=4}\left(a_i x^i + b_i y^i\right) + \sum_{j=0}^{j=3}\sum_{k=0}^{k=3} A_{j,k} x^j y^k, \tag{B.4}$$

$$\Delta\bar{f}_{\mathrm{H}}(x,y) = \sum_{i=1}^{i=4}\left(c_i x^i + d_i y^i\right) + \sum_{j=0}^{j=3}\sum_{k=0}^{k=3} B_{j,k} x^j y^k, \tag{B.5}$$

where the fitted parameters for $\Delta\bar{f}_{\mathrm{T,H}}(x, y)$ are listed in Table B.1 (errors in the parameters represent the standard deviations of the regression coefficients).

Table B.1: Coefficients of the 2D position-sensing frequency-shift fits

Coefficient	Fitted Value
a_1	$(-4.22 \pm 3.99) \times 10^5$ kHz mm^{-1}
a_2	$(3.68 \pm 6.15) \times 10^3$ kHz mm^{-2}
a_3	-16.0 ± 43.2 kHz mm^{-3}
a_4	0.0304 ± 0.11 kHz mm^{-4}
b_1	$(-5.73 \pm 2.54) \times 10^5$ kHz mm^{-1}
b_2	$(6.49 \pm 4.14) \times 10^3$ kHz mm^{-2}
b_3	-34.1 ± 34.8 kHz mm^{-3}
b_4	0.071 ± 0.12 kHz mm^{-4}
$A_{0,0}$	$(1.96 \pm 1.11) \times 10^7$ kHz
$A_{1,1}$	$(8.74 \pm 3.67) \times 10^3$ kHz mm^{-2}
$A_{1,2}$	-63.0 ± 26.6 kHz mm^{-3}
$A_{2,1}$	-46.6 ± 29.3 kHz mm^{-3}
$A_{2,2}$	0.16 ± 0.092 kHz mm^{-4}
$A_{1,3}$	0.16 ± 0.10 kHz mm^{-4}
$A_{3,1}$	0.086 ± 0.096 kHz mm^{-4}
c_1	$(-3.47 \pm 1.24) \times 10^5$ kHz mm^{-1}
c_2	$(3.70 \pm 1.89) \times 10^3$ kHz mm^{-2}
c_3	-17.3 ± 13.4 kHz mm^{-3}
c_4	0.03 ± 0.04 kHz mm^{-4}
d_1	$(-7.89 \pm 7.85) \times 10^4$ kHz mm^{-1}
d_2	$(-1.68 \pm 1.28) \times 10^3$ kHz mm^{-2}
d_3	26.3 ± 10.8 kHz mm^{-3}
d_4	-0.11 ± 0.04 kHz mm^{-4}
$B_{0,0}$	$(9.25 \pm 3.43) \times 10^6$ kHz
$B_{1,1}$	$(5.25 \pm 1.14) \times 10^3$ kHz mm^{-2}
$B_{1,2}$	-24.9 ± 8.2 kHz mm^{-3}
$B_{2,1}$	-38.2 ± 9.1 kHz mm^{-3}
$B_{2,2}$	0.09 ± 0.03 kHz mm^{-4}
$B_{1,3}$	0.04 ± 0.03 kHz mm^{-4}
$B_{3,1}$	0.09 ± 0.03 kHz mm^{-4}

Appendix C

Details of the Simplified Model, Bifurcations, Amplitude Equation, and Prediction Methods

In this appendix, I first detail the approximations that lead to the simplified model from Chs. 5-6. Second, I provide illustrations for the Hopf and the torus bifurcations in phase-space representations. Third, I derive the amplitude equation and its linearization for a band-pass filter with nonlinear feedback (Eq. 5.11 and Eq. 5.14) used in Chs. 5-6. Then, in order to demonstrate the properties of these derivations, I provide a simple numerical example of the amplitude equation in an open-loop configuration. Lastly, I show special cases of the closed-loop transfer functions from Ch. 5, which are derived from the amplitude equation and used to predict the quasiperiodic frequencies. The presented results are atypical (from a small subset of my data) and highlight the potential limitations in the predictive power of my new methods for estimating Ω_{H} and Ω_{T}.

C.1 Simplified Model Details

C.1.1 Bandwidth of the Simplified Model

The simplified model, which is first introduced in Ch. 5, uses a band-pass filter to approximate the net filtering effects of the nonlinear circuit (NLC) and the external feedback loop. This approximation is stated in Eq. 5.1 as the product of the transfer functions

$$H'_{\mathrm{BP}}(f) \sim H_{\mathrm{LP,\,L,A}}(\omega) H_{\mathrm{BP}}(f), \tag{C.1}$$

where $H_{\mathrm{LP,\,L,A}}$ is the transfer function that models the low-pass filtering effects of the NLC, H_{BP} is a transfer function that models the external feedback loop filtering, and H'_{BP} is new transfer function that approximates the net filtering as a band-pass filter (also note that the change in notation from the angular frequency ω to the frequency f does not change this approximation).

In this section, I first demonstrate that the product $H_{\mathrm{LP,\,L,A}}H_{\mathrm{BP}}$ behaves similarly to a band-pass filter using the experimental parameters of the transfer functions that are given in Ch. 4. As a reminder to the reader, in the linear regime, the transfer function $H_{\mathrm{LP,\,L}}(f)$ contains the single fitting parameter $f_{\mathrm{LP,\,L}} = 0.78{\pm}0.02$ GHz. Using this parameter, the theoretical magnitude $|H_{\mathrm{LP,\,A}}|$ is shown in Fig. C.1a. In the anti-linear regime, the transfer function $H_{\mathrm{LP,\,A}}(f)$ contains the fitting parameters $\epsilon = 0.51 \pm 0.01$ dB and $f_{\mathrm{LP,\,A}} = 2.51 \pm 0.01$ GHz, and the resulting theoretical $|H_{\mathrm{LP,\,A}}(f)|$ is also shown in Fig. C.1a. Finally, $H_{\mathrm{BP}}(f)$ contains the fitting parameters for the upper and lower frequency cutoffs, $f^{(+)} = 1.57 \pm 0.01$ GHz and $f^{(-)} = 0.41 \pm 0.01$ GHz, and its theoretical magnitude is shown in Fig. C.1a.

Using the analytical expressions for the transfer functions $H_{\mathrm{LP,\,L}}$, $H_{\mathrm{LP,\,A}}$, and H_{BP}, I compute $|H_{\mathrm{LP,\,L}}H_{\mathrm{BP}}|$ and $|H_{\mathrm{LP,\,A}}H_{\mathrm{BP}}|$, which are shown in Fig. C.1b. The resulting net magnitudes both resemble that of a band-pass filter. As a quantitative comparison of the differences between the two magnitudes, their RMS difference for $f = 0{-}2$ GHz is 1.7 dB (3.4% of the observed range). As a comparison to the transfer function for a true band-pass filter, I fit $|H_{\mathrm{LP,\,L}}H_{\mathrm{BP}}|$ and $|H_{\mathrm{LP,\,A}}H_{\mathrm{BP}}|$ simultaneously using $|H'_{\mathrm{BP}}(f)|$ for $f = 0 - 2$ GHz. The resulting fit is shown in Fig. C.1d, and the (new) band-pass filter fitting parameters are $f'^{(+)} = 1.2 \pm 0.01$ GHz and $f'^{(-)} = 0.34 \pm 0.004$ (errors represent the 90% confidence intervals of the fitting parameters). The RMS errors between the fitted $|H'_{\mathrm{BP}}|$ and $|H_{\mathrm{LP,\,L}}H_{\mathrm{BP}}|$ ($|H_{\mathrm{LP,\,A}}H_{\mathrm{BP}}|$) is 1.7 dB (1.5 dB) in the 2 GHz window, which represents 3.4% (3.0%) of the observed range. However,

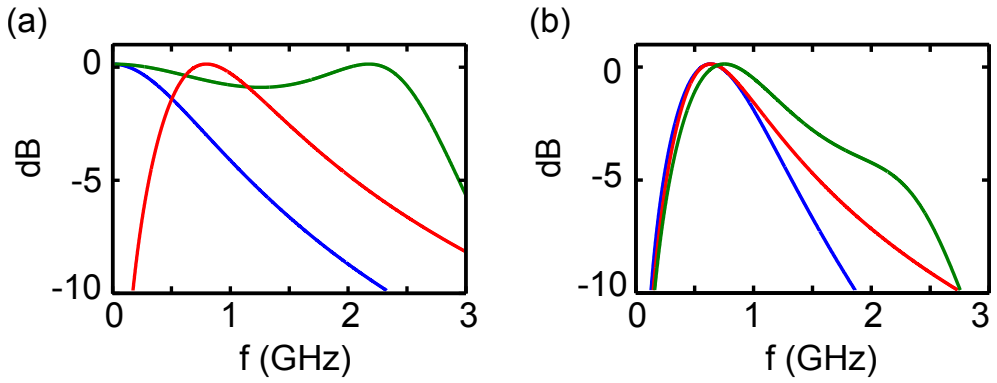

Figure C.1: **Transfer function magnitudes** (a) $\log|H_{\mathrm{LP,\,L}}(f)|$ (blue), $\log|H_{\mathrm{LP,\,A}}(f)|$ (green), and $\log|H_{\mathrm{BP}}(f)|$ (red). (d) Net transfer function magnitudes $\log|H_{\mathrm{LP,\,L}}(f)H_{\mathrm{BP}}(f)|$ (blue), $\log|H_{\mathrm{LP,\,A}}(f)H_{\mathrm{BP}}(f)|$ (green), and fitted transfer function magnitude $\log|H'_{\mathrm{BP}}(f)|$ (red).

the experimental feedback systems displays a wide range of frequencies, and any discrepancies with the simplified model's transfer function and that of the experimental systems can lead to be sources of error for estimating f_{T} and f_{H} in Ch. 5 and Δf_{T} and Δf_{H} in Ch. 6.

C.1.2 Nonlinearity of the Simplified Model

Furthermore, to simplify the analytics in Ch. 5, I also approximate the nonlinear function $F(\mathrm{v_{in}})$ with a third-order polynomial

$$F(\mathrm{v_{in}}) = \alpha_1(\mathrm{v_{in}} + \mathrm{v_b}) - [\alpha_2(\mathrm{v_{in}} + \mathrm{v_b})]^3, \tag{C.2}$$

where α_1, and α_2 are constant coefficients and where $\mathrm{v_b}$ is a constant used to tune the operating point of the nonlinearity. To demonstrate that this function can approximate the nonlinear operation associated with the NLC, I fit Eq. (C.2) to the experimental data from Fig. 4.1, and the resulting fit is shown in Fig. C.2. The parameters of the fit are $\alpha_1 = -0.43 \pm 0.01$, $\alpha_2 = -1.3 \pm 0.01$ V^{-2}, and where

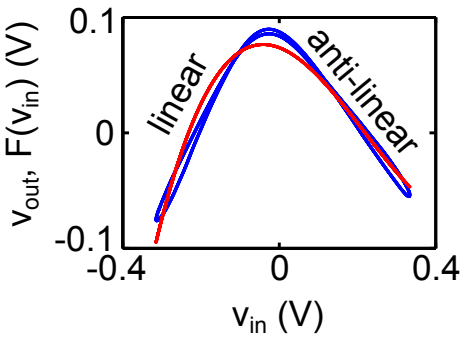

Figure C.2: **Simplified model of the system's nonlinearity.** Experimental data from the NLC (blue) where v_{in} is a sinusoidal driving signal at frequency $f = 260$ MHz with the numerical fit (red) of Eq. (C.2).

$v_b = -1.0 \pm 0.01$ V, and the RMS error of the fit is 0.11 V, which is 6.34% the experimental range. Though this fit can approximate the nonlinearity, the fitting parameters are not used in the derivations. Thus, without loss of generality, the coefficients can be arbitrary as long as the overall shape of the nonlinearity is preserved, particularly that $F(v_{in})$ is approximately piecewise-linear and that $F'(v_{in})$ changes signs as v_{in} crosses a threshold (from the linear regime to the anti-linear regime).

C.2 Phase-Space Representations of Bifurcations

In this section, I provide illustrations of the Hopf and torus bifurcations using a phase-space representation. The purpose of these illustrations is to provide additional insight into my reasoning during the derivations of the two bifurcation points in Ch. 5. For example, for the Hopf bifurcation, the dynamical state transitions abruptly from a steady-state voltage $v(t) = v_s = 0$ to an oscillatory state $v(t) \sim Ae^{i\Omega_H t}$. In phase space, this transition is represented as a fixed point that bifurcates to a limit cycle with radius A that revolves at an angular frequency Ω_H,

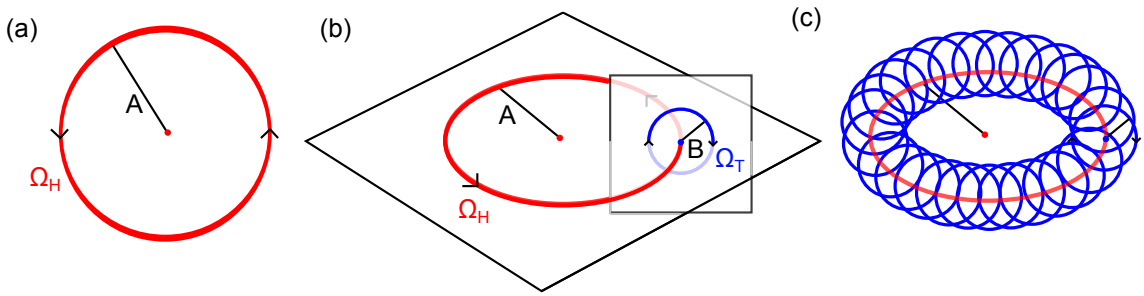

Figure C.3: Phase-space illustrations of Hopf and torus bifurcations. (a) Representation of a super-critical Hopf bifurcation to a limit cycle with Hopf frequency Ω_H and amplitude A. (b) Representation of a torus bifurcation with torus freqency Ω_T and amplitude B with (c) the resulting torus.

as shown in Fig. C.3a.

For the torus bifurcation, the amplitude A of the periodic dynamics begins to oscillate slowly such that $A(t) \sim Be^{i\Omega_T t}$. In phase space, this transition is represented as a second limit cycle with radius B that appears along the exterior the Hopf limit cycle and revolves at an angular frequency Ω_T, as shown in Fig. C.3b. This second limit cycle travels around the Hopf limit cycle and thus the resulting trajectories follow the torus Fig. C.3c. However, I note that this representation of the torus is misleading because, in all torus bifurcations shown in this dissertation, $\Omega_T << \Omega_H$. Thus, the Hopf limit cycle repeats many times before torus limit cycle makes one revolution (this is difficult to illustrate). Regardless, for all Hopf and torus bifurcations shown in this dissertation, Figs. C.3a-b illustrate the approximate phase-space representations.

C.3 Deriving the Amplitude Equation

The amplitude equation is a dynamical model that approximates the describes evolution of slowly-evolving dynamics in the amplitude (or envelope) of Eq. (6.3). This

derivation is based on the work from Ref. [75], where Chembo *et al.* derive the amplitude equation for a specific nonlinearity for $N = 1$ time delays in the feedback loop. Here, I generalize their derivation to a system with N time delays. For my derivation, I reprint Eq. (6.3) here

$$\frac{\dot{\mathrm{v}}(t)}{\Delta} + \mathrm{v}(t) + \frac{\omega_\mathrm{o}^2}{\Delta}\int_{-\infty}^{t} \mathrm{v}(t')\,\mathrm{d}t' = y(t), \tag{C.3}$$

where $y(t) = F\left[G\sum_{i=1}^{N} g_i \mathrm{v}(t-\tau_i)\right]$ is the input to the band-pass filter. In addition, for the purposes of this analysis, I temporarily simplify Eq. (C.3) by taking the derivative with respect to time on both sides

$$\frac{\ddot{\mathrm{v}}(t)}{\Delta} + \dot{\mathrm{v}}(t) + \frac{\omega_\mathrm{o}^2}{\Delta}\mathrm{v}(t) = \dot{y}(t). \tag{C.4}$$

Following Eq. (C.4), there are two main assumptions that go into the derivation of the amplitude equation. The first assumption is that, after the initial Hopf bifurcation, the solution of Eq. (C.3) takes on the form

$$\mathrm{v}(t) \sim \frac{1}{2}A(t)(e^{i\omega_\mathrm{o}t} + e^{-i\omega_\mathrm{o}t}), \tag{C.5}$$

where $A(t)$ is a slowly evolving amplitude. Based on my previous analysis, I know that $\Omega_\mathrm{T} << \Omega_\mathrm{H}$, where Ω_T is torus frequency that appears as an oscillation in $A(t)$. In addition, I know that Ω_H tends to be near the center of the (net) band-pass filter, and therefore $\Omega_\mathrm{H} \sim \omega_\mathrm{o}$ in this approximation.

The second assumption is that bandwidth of the band-pass filter Δ is small relative to the frequency of oscillation, which in this case is the band-pass filter ω_o. In the experiment, the combined bandwidth of the external feedback loop, the nonlinear circuit, and the wave-chaotic cavity is $\Delta \sim 5.4$ rad/ns, while the frequency

of oscillation $\omega_o \sim 4.0$ rad/ns (see previous section). In this case, $\Delta/\omega_o \sim 1.35$ rad/ns. However, the experimental system (with the antennas and cavity) tends to oscillate at frequencies $\Omega_H > 2\pi$ rad/ns, and thus $\Delta/\omega_o < 1$ (assuming $\Omega_H \sim \omega_o$).

With these two assumptions, I rewrite Eq. (C.4) in terms of the small parameter $\varepsilon \equiv \Delta/\omega_o$

$$\ddot{v}(t) + \varepsilon\omega_o\dot{v}(t) + \omega_o^2 v(t) = \varepsilon\omega_o\dot{y}(t). \tag{C.6}$$

I now perform a separation of timescales analysis on Eq. (C.6). Using the two different times scales in the carrier and modulation frequencies in $v(t)$, I approximate it as

$$v(t) \sim v_o(T_o, T_1) + \varepsilon v_1(T_o, T_1) + O(\varepsilon^2), \tag{C.7}$$

where $T_o = t$ is a fast time and $T_1 = \varepsilon t$ is a slow time. In addition, since $y(t)$ is a function of $v(t)$, I also approximate it as

$$y(t) \sim y_o(T_o, T_1) + \varepsilon y_1(T_o, T_1) + O(\varepsilon^2). \tag{C.8}$$

The separation of timescales must also be applied to any derivatives in t such that

$$\frac{d}{dt} \sim D_o + \varepsilon D_1 + O(\varepsilon^2), \tag{C.9}$$

where $D_j = \frac{\partial}{\partial T_j}$ are partial derivatives. It follows that

$$\frac{d^2}{dt^2} \sim (D_o + \varepsilon D_1)^2 \sim D_o^2 + 2\varepsilon D_o D_1 + O(\varepsilon^2). \tag{C.10}$$

It now remains to substitute Eqs. (C.8) - (C.10) into Eq. (C.6) and examine separately the terms of $O(\varepsilon^0)$ and $O(\varepsilon^1)$. Collecting the terms of $O(\varepsilon^0)$ yields to

dynamical equation

$$D_{\mathrm{o}}^2 \mathrm{v}_{\mathrm{o}} + \omega^2 \mathrm{v}_{\mathrm{o}} = 0, \tag{C.11}$$

which is the equation for a simple harmonic oscillator with resonance at ω_{o}. The solution

$$\mathrm{v}_{\mathrm{o}}(T_{\mathrm{o}}, T_1) = \frac{1}{2} A(T_1)(e^{i\omega_{\mathrm{o}} T_{\mathrm{o}}} + e^{-i\omega_{\mathrm{o}} T_{\mathrm{o}}}), \tag{C.12}$$

is consistent with my previous assumptions. Factorizing the terms of $\mathrm{O}(\varepsilon^1)$ yields a second dynamical equation

$$D_{\mathrm{o}}^2 \mathrm{v}_1 + \omega^2 \mathrm{v}_1 = -2D_{\mathrm{o}} D_1 \mathrm{v}_{\mathrm{o}} - \omega_{\mathrm{o}} D_{\mathrm{o}} \mathrm{v}_{\mathrm{o}} + \omega_{\mathrm{o}} D_{\mathrm{o}} y_{\mathrm{o}}. \tag{C.13}$$

Note that all of the terms on the right-hand-side of Eq. (C.13) oscillate with frequency ω_{o}. Therefore, if I consider v_1 as the dynamical variable of the left-hand-side, then Eq. (C.13) is a driven harmonic oscillator with resonance at ω_{o} that is driven on resonance. This will cause the solution of v_{o} to diverge unless all of the resonant terms in ω_{o} on the right-hand-side cancel [75]. In other words,

$$2D_{\mathrm{o}} D_1 \mathrm{v}_{\mathrm{o}} = -\omega_{\mathrm{o}} D_{\mathrm{o}} \mathrm{v}_{\mathrm{o}} + \omega_{\mathrm{o}} D_{\mathrm{o}} y_{\mathrm{o}}. \tag{C.14}$$

Because all of the terms in Eq. (C.14) contain the partial derivative D_{o}, I can integrate it with respect to T_{o} on both sides, which yields

$$2D_1 \mathrm{v}_{\mathrm{o}} = -\omega_{\mathrm{o}} \mathrm{v}_{\mathrm{o}} + \omega_{\mathrm{o}} y_{\mathrm{o}}. \tag{C.15}$$

I substitute in the solution for v_{o} in Eq. (C.15) and get

$$2D_1 \frac{A(T_1)}{2}(e^{i\omega_{\mathrm{o}} T_{\mathrm{o}}} + e^{-i\omega_{\mathrm{o}} T_{\mathrm{o}}}) = -\omega_{\mathrm{o}} \frac{A(T_1)}{2}(e^{i\omega_{\mathrm{o}} T_{\mathrm{o}}} + e^{-i\omega_{\mathrm{o}} T_{\mathrm{o}}}) + \omega_{\mathrm{o}} y_{\mathrm{o}}, \tag{C.16}$$

with

$$y_o = F\left[G\sum_{i=1}^{N} g_i A(T_1 - \varepsilon\tau_i)\left(\frac{e^{i\omega_o(T_o-\tau_i)} + e^{-i\omega_o(T_o-\tau_i)}}{2}\right)\right]. \tag{C.17}$$

I approximate the expression in Eq. (C.17) by assuming that the solution is periodic in time with an integer or half-integer number of wavelengths in the system's net feedback loop, corresponding to the phase condition $e^{\pm i\omega_o\tau_i} \sim 1$. This results in

$$\sum_{i=1}^{N} g_i A(T_1 - \varepsilon\tau_i)e^{\pm i\omega_o(T_o-\tau_i)} \sim \sum_{i=1}^{N} g_i A(T_1 - \varepsilon\tau_i)e^{\pm i\omega_o T_o}. \tag{C.18}$$

Therefore, using this approximation, I rewrite y_o as

$$y_o \sim F\left[G\sum_{i=1}^{N} g_i A(T_1 - \varepsilon\tau_i)\left(\frac{e^{i\omega_o T_o} + e^{-i\omega_o T_o}}{2}\right)\right]. \tag{C.19}$$

Before substituting this approximation for y_o into Eq. (C.16), I make one last approximation that

$$y_o \sim F\left[G\sum_{i=1}^{N} g_i A(T_1 - \varepsilon\tau_i)\right]\left(\frac{e^{i\omega_o T_o} + e^{-i\omega_o T_o}}{2}\right). \tag{C.20}$$

Typically, for a general nonlinearity, this approximation is not valid. However, for nonlinearities of the form $F(v) = v - \alpha v^3$, I can show that this approximation is valid in band-pass filtered systems. Consider the following general case:

$$F\left[\beta\left(\frac{e^{i\omega_o t} + e^{-i\omega_o t}}{2}\right)\right] = \beta\left(\frac{e^{i\omega_o t} + e^{-i\omega_o t}}{2}\right) - \alpha\beta^3\left(\frac{e^{i\omega_o t} + e^{-i\omega_o t}}{2}\right)^3. \tag{C.21}$$

Expanding the third order term gives

$$\alpha\beta^3\left(\frac{e^{i\omega_o t} + e^{-i\omega_o t}}{2}\right)^3 = \alpha\frac{\beta^3}{8}[3(e^{i\omega_o t} + e^{-i\omega_o t}) + (e^{3i\omega_o t} + e^{-3i\omega_o t})]. \tag{C.22}$$

Because ω_o is the central frequency of the band-pass filter and $\Delta < \omega_o$, I can assume that terms of frequency $\omega = 3\omega_o$ lie outside of the bandwidth of this dynamical system. Therefore, I approximate that these terms are negligible such that

$$\alpha\beta^3\left(\frac{e^{i\omega_o t}+e^{-i\omega_o t}}{2}\right)^3 \sim \alpha\beta^3\left(\frac{3(e^{i\omega_o t}+e^{-i\omega_o t})}{8}\right), \tag{C.23}$$

and therefore

$$F\left[\beta\left(\frac{e^{i\omega_o t}+e^{-i\omega_o t}}{2}\right)\right] \sim \beta\left(\frac{e^{i\omega_o t}+e^{-i\omega_o t}}{2}\right) - \alpha\beta^3\left(\frac{3(e^{i\omega_o t}+e^{-i\omega_o t})}{8}\right). \tag{C.24}$$

I now compare Eq. (C.24) to

$$F[\beta]\left(\frac{e^{i\omega_o t}+e^{-i\omega_o t}}{2}\right) = \beta\left(\frac{e^{i\omega_o t}+e^{-i\omega_o t}}{2}\right) - \alpha\beta^3\left(\frac{e^{i\omega_o t}+e^{-i\omega_o t}}{2}\right), \tag{C.25}$$

and note that the difference between equations (C.24) and (C.25) is approximately

$$\alpha\beta^3\frac{(e^{i\omega_o t}+e^{-i\omega_o t})}{8}. \tag{C.26}$$

Because $\beta = 1$ and $\alpha = 0.5$ in the simulations of this system (experimentally, I also approximate $\beta \sim \alpha \sim 1$), (C.26) is relatively small compared to β. Thus, I use the following approximation

$$F\left[\beta\left(\frac{e^{i\omega_o t}+e^{-i\omega_o t}}{2}\right)\right] \sim F[\beta]\left(\frac{e^{i\omega_o t}+e^{-i\omega_o t}}{2}\right). \tag{C.27}$$

This final approximation allows me to justify the simplified form of Eq. (C.20).

Finally, I substitute Eq. (C.19) into Eq. (C.16) and cancel the oscillatory terms

in ω_o, which leads to

$$2D_1A(T_1) = \omega_o \left(F\left[G\sum_{i=1}^{N} g_i A(T_1 - \varepsilon\tau_i) \right] - A(T_1) \right). \tag{C.28}$$

I rescale time by $1/\varepsilon$ and substituting $\varepsilon\omega_o$ by Δ, and Eq. (C.28) becomes the amplitude equation

$$\dot{A}(t) = \frac{\Delta}{2} \left(F\left[G\sum_{i=1}^{N} g_i A(t - \tau_i) \right] - A(t) \right). \tag{C.29}$$

Though many approximations are made to generate this amplitude equation, I show in Chs. 5 - 6 that it is a powerful tool to estimate the origins and shifts to the torus bifurcation frequency Ω_T.

C.4 Linearized Amplitude Equation about the Steady State Amplitude

In order to derive Eq. (5.2), I linearize the amplitude equation about the steady state amplitude A_s. Recall that A_s satisfies the equation $F\left[G\sum_{i=1}^{N} g_i A_s\right] = F\left[\bar{G}A_s\right] = A_s$. I first assume that the solution to the amplitude equation takes on the form $A(t) = A_s + \delta A(t)$ and substitute this into Eq.(C.29) where

$$\frac{d}{dt}(A_s + \delta A(t)) = \frac{d}{dt}\delta A(t), \tag{C.30}$$

such that

$$\delta\dot{A}(t) = \frac{\Delta}{2} \left(F\left[G\sum_{i=1}^{N} g_i (A_s + \delta A_{\tau_i}) \right] - (A_s + \delta A(t)) \right), \tag{C.31}$$

where $\delta A_{\tau_i} = \delta A(t - \tau_i)$.

To linearize this equation, I Taylor expand the nonlinear function about $\delta A = 0$ such that

$$F\left[G\sum_{i=1}^{N} g_i A(t)\right] \sim F\left[\bar{G}A_s\right] + GF'\left[\bar{G}A_s\right]\sum_{i=1}^{N} g_i \delta A_{\tau_i}. \tag{C.32}$$

Substituting this back into Eq. (C.31) and canceling the equivalent terms $F[\bar{G}A_s]$ and A_s yields

$$\delta\dot{A}(t) = \frac{\Delta}{2}\left(G\sum_{i=1}^{N} d_i \delta A(t-\tau_i) - \delta A(t)\right), \tag{C.33}$$

where $d_i = F'\left[\bar{G}A_s\right] g_i$. This concludes the derivation of the linearized amplitude equation.

C.5 Open-Loop Amplitude Equation Dynamics

In this section, I demonstrate the dynamics of the amplitude equation using simple examples of a band-pass filter and a low-pass filter in open-loop configurations using numerical simulations. As a reminder of the differences between open-loop and closed-loop configurations, see Fig. 5.2. The goal of this section is to verify that changes to an oscillatory amplitude through a linear band-pass filter can be approximated using a linear low-pass filter amplitude equation.

The equation for an open-loop linear band-pass filter is

$$\frac{\dot{\mathrm{v}}(t)}{\Delta} + \mathrm{v}(t) + \frac{\omega_\mathrm{o}^2}{\Delta}\int_{-\infty}^{t} \mathrm{v}(t')\,\mathrm{d}t' = \mathrm{v}_\mathrm{in}(t), \tag{C.34}$$

where $\mathrm{v}_\mathrm{in}(t)$ is an input driving signal at frequency $\omega = \omega_\mathrm{o}$ (the central frequency of the band-pass filter) and $\mathrm{v}(t)$ is the filtered output. As a reminder, Δ is the bandwidth of the band-pass filter. Alternatively, the equation for an open-loop linear low-pass filter is

$$\dot{A}(t) = \frac{\Delta}{2}\left(A_\mathrm{in}(t) - A(t)\right), \tag{C.35}$$

where $A_{\text{in}}(t)$ is a input driving signal at a frequency $\omega << \omega_{\text{o}}$ and $A(t)$ is the filtered output. For this particular low-pass filter, the bandwidth is $\Delta/2$, which is half that of the band-pass filter in Eq. C.34. Note that Eq. C.35 is equal to Eq. C.29 with the nonlinear feedback removed.

In this section, I simulate Eq. (C.34) and Eq. (C.35) using driving signals $\text{v}_{\text{in}}(t)$ and $A_{\text{in}}(t)$, where $A_{\text{in}}(t)$ describes the approximate envelope of oscillations in $\text{v}_{\text{in}}(t)$. For example, consider the driving signals $\text{v}_{\text{in}}(t)$ and $A_{\text{in}}(t)$ shown in Figs. C.4a-b. In this case, $\text{v}_{\text{in}}(t) = \sin(\omega_{\text{o}} t)$ and thus I use $A_{\text{in}}(t) = 1$ (constant in time) to describe the envelope of oscillations (local maxima) in $\text{v}_{\text{in}}(t)$. Using these driving signals, I separately integrate Eqs. (C.34) and (C.35) to simulate each filter output, as shown by $\text{v}(t)$ and $A(t)$ in Figs. C.4a-b. The results of these simulations show that the output amplitudes of $\text{v}(t)$ and $A(t)$ are constant. Thus, in this simple case, the dynamics of the envelope of $\text{v}(t)$ can be modeled as the output of a low-pass filter driven by a waveform that follows the envelope of $\text{v}_{\text{in}}(t)$.

Next, I consider a more interesting example where a rectangular function describes the envelope of oscillations in $\text{v}_{\text{in}}(t)$ and thus $\text{A}_{\text{in}}(t)$ is a square wave, as shown in Figs. C.4c-d. Note that the duration ΔT of the square wave is chosen such that $\Delta T > 2\pi/\omega_{\text{o}}$ to guarantee a separation in time scales between the fast and slow variations in $\text{v}_{\text{in}}(t)$ and $\text{A}_{\text{in}}(t)$, respectively. Using these two input driving signals, the outputs $\text{v}(t)$ and $A(t)$ of Eqs. (C.34) - (C.35) are shown in Figs. C.4c-d, respectively. In Fig. C.4c, the envelope of oscillations in $\text{v}(t)$ is no longer a square wave, but rather a slowly ramped function. This ramped function is is similar to the low-pass filter response of the square wave, as demonstrated by the output $A(t)$ in Fig. C.4d.

For this case, I quantify the similarities between $A(t)$ and the envelope of $\text{v}(t)$. To do so, I first sample $A(t)$ at the times t_n where $\text{v}(t_n)$ are the local maxima of $\text{v}(t)$.

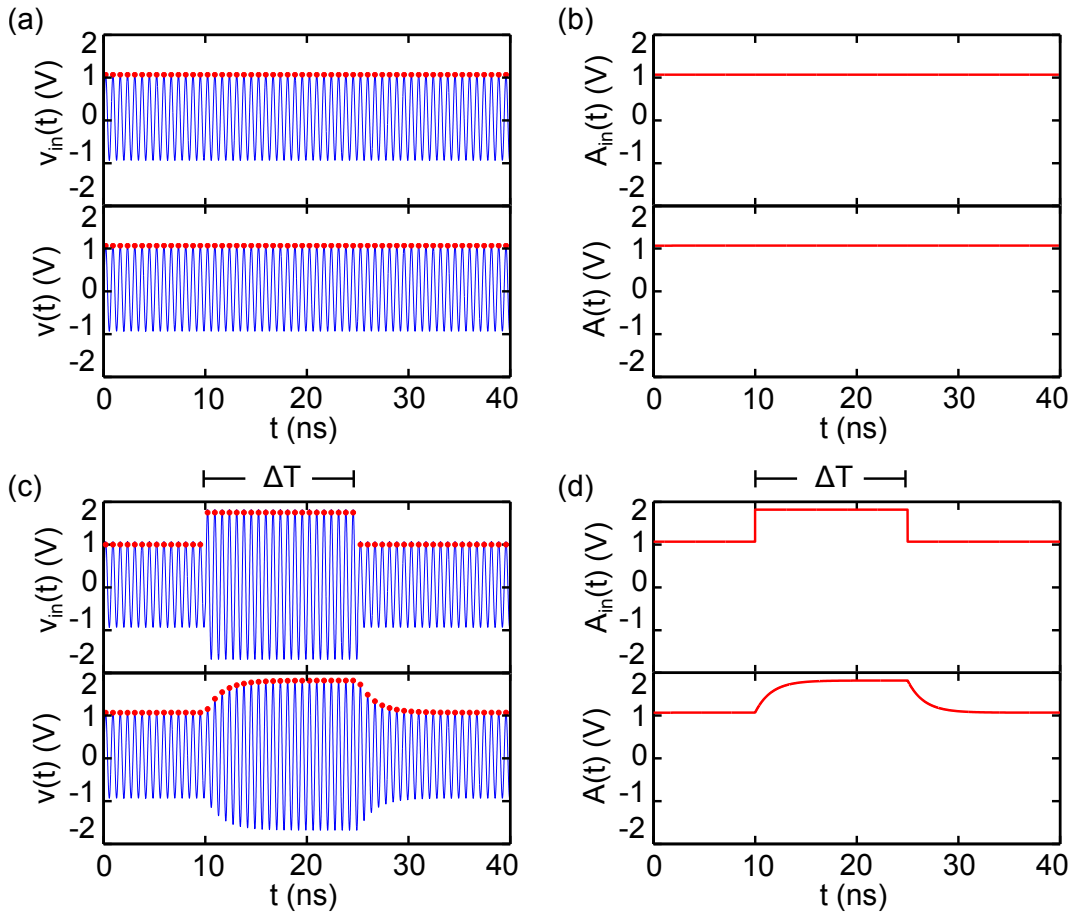

Figure C.4: Example of the dynamics from the amplitude equation in an open-loop configuration. (a) The oscillatory waveform $v_{in}(t)$ with constant amplitude drives an open-loop band-pass filter (Eq. C.34) with parameters $\omega^{(-)} = 8.2$ rad/ns, $\omega^{(+)} = 9.4$ rad/ns and central frequency $\omega_o = 8.8$ rad/ns. The output of the band-pass filter shows an oscillatory $v(t)$ with a constant amplitude. (b) A constant input waveform $A_{in}(t)$ drives an open loop low-pass filter (Eq. C.35) with bandwidth $\Delta/2$, where $\Delta = \omega^{(+)} - \omega^{(-)} = 1.3$ rad/ns to produce a constant output $A(t)$. (c) Input waveform $v_{in}(t)$ drives the band-pass filter with a square wave amplitude (of width ΔT) to produce the response $v(t)$. (d) The square wave $A_{in}(t)$ drives the low-pass filter to produce the response $A(t)$. The local maxima in $v_{in}(t)$ and $v(t)$ are labeled with red dots.

The sampled points $v(t_n)$ and $A(t_n)$ are shown in Fig. C.5a, and the differences $(v(t_n) - A(t_n))$ are shown in Fig. C.5b. As shown in the figures, the two waveforms differ most near the times that the amplitudes change. The spread in the differ-

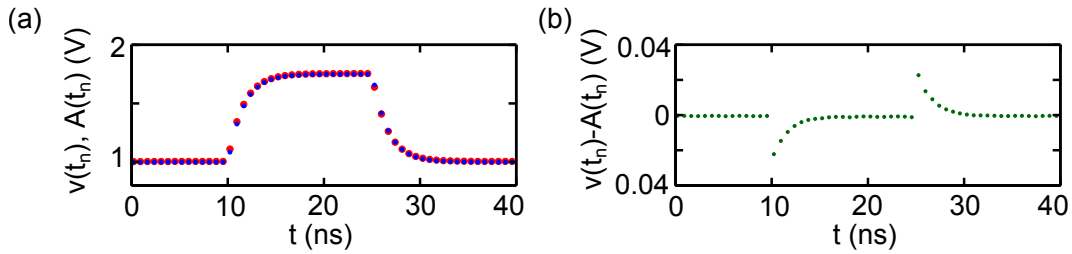

Figure C.5: **Comparison of band-pass filter and low-pass filter outputs.** (a) Sampled points v(t_n) (blue) and $A(t_n)$ (red) at times t_n, where v(t_n) are the local maxima of v(t). (b) The differences (v(t_n)$-A(t_n)$) at each of the times t_n. Note the vertical axis change from (a) to (b).

ences in Fig. C.5b is approximately ±0.025 V, which is ∼7% of the observed range in v(t_n). Furthermore, the cross-correlation coefficient $C(\text{v}(t_n),A(t_n)) = 0.99$ (calculated using Eq. (2.14)). Thus, this example shows that, when a slowly modulated waveform with a carrier frequency ω_o drives a band-pass filter with bandwidth Δ and central frequency ω_o, the output amplitude dynamics of the filter is governed approximately by a low-pass filter with bandwidth $\Delta/2$.

C.6 Special Cases of the Prediction Methods

In this last section, I examine frequency estimations from Ch. 5 which deviate from the simulated quasiperiodic frequencies. More specifically, I show example plots of the closed-loop transfer function magnitudes $|H_{\text{R}}(\omega)|$, $|H_{\text{AM}}(\omega)|$, and $|H_{\text{SR}}(\omega)|$ (associated with the R, AM, and SR methods) where the global maxima for $G = 0.95$ do not correspond to Ω_{H}, Ω_{T}, or $\Omega_{\text{H}} \pm \Omega_{\text{T}}$, respectively. These cases represent points with large fluctuations for $N = 4$ time delays in Fig. 5.5 and $N = 10$ time delays in the Fig. 5.11.

In these three special cases, the global maxima of the transfer function magnitudes do correspond to the correct frequencies. As shown in Fig. C.6a, the transfer

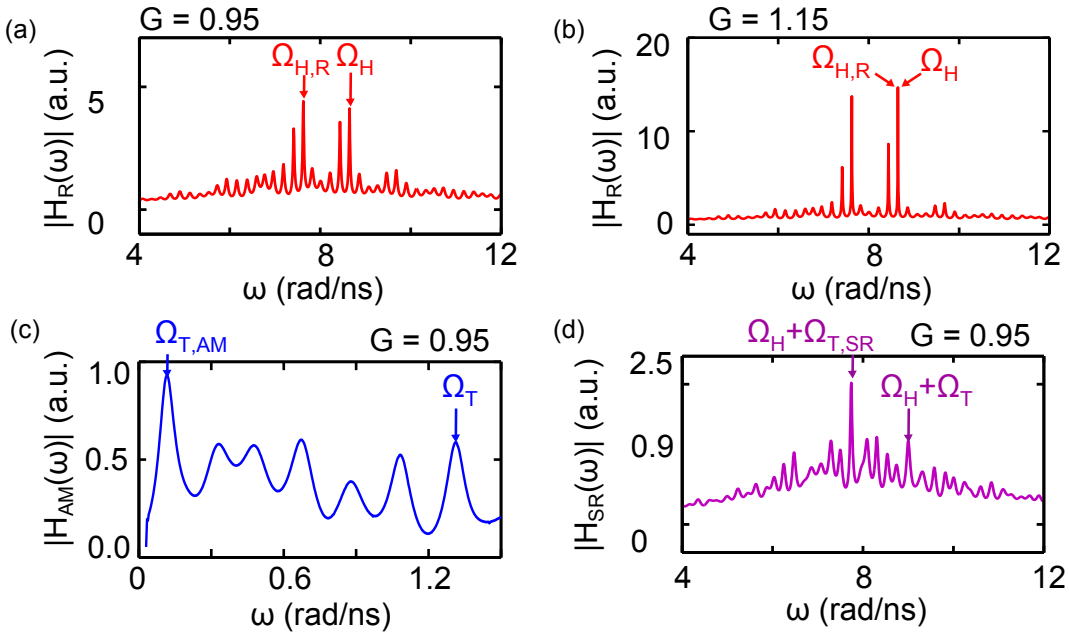

Figure C.6: **Special cases of the frequency estimation methods.** (a) $|H_R(\omega)|$ for $N = 4$ and $G = 0.95$ where $\Omega_{H,R} \sim 7.6$ rad/ns and $\Omega_H = 8.6$ rad/ns. (b) $|H_R(\omega)|$ for $N = 4$ and $G = 1.15$ where $\Omega_{H,R} \sim \Omega_H \sim 8.6$ rad/ns. (c) $|H_{AM}(\omega)|$ for $N = 10$ and $G = 0.95$ where $\Omega_{T,AM} \sim 0.1$ rad/ns and $\Omega_T \sim 1.4$ rad/ns. (c) $|H_{SR}(\omega)|$ for $N = 10$ and $G = 0.95$ where $\Omega_H + \Omega_{T,SR} \sim 7.7$ rad/ns and $\Omega_H + \Omega_T \sim 9.0$ rad/ns.

function magnitude $|H_R(\omega)|$ is plotted for an $N = 4$ case with $G = 0.95$. The frequency produced by the simulation of the $N = 4$ simplified model is labeled by Ω_H, whereas the global maximum of the closed-loop transfer function is labeled by $\Omega_{H,R}$. This discrepancy is caused by the assumption that the global maximum does not move significantly with respect to ω as G is tuned to the Hopf bifurcation point. In order to correct for this false assumption, I calculate numerically the solution to Eq. (5.5) for this case to obtain $G \sim 1.2$ as the correct gain for the Hopf bifurcation. Thus, I replot $|H_R(\omega)|$ for the $N = 4$ in Fig. C.6b case but now with G tuned closer to the bifurcation point ($G = 1.15$). In the figure, the global maximum (the estimation $\Omega_{H,R}$) now corresponds approximately to the correct value of Ω_H. This example demonstrates the limitations of the resonance method.

Similar cases are shown for $|H_{\mathrm{AM}}(\omega)|$ and $|H_{\mathrm{SR}}(\omega)|$ in Figs. C.6c-d for a case with $N = 10$. However, In these two cases, I cannot verify that the frequencies of the global maxima ($\Omega_{T,AM}$ and $\Omega_{T,SR}$) change near the torus bifurcation point. As mentioned in Ch. 5, this is because the torus bifurcation point is beyond the Hopf bifurcation point. Thus G cannot be tuned arbitrary close to the torus bifurcation without the system self-oscillating and, as a result, exhibiting nonlinear dynamics (violating the assumptions of the linear transfer function).

The cases shown in Fig. C.6 demonstrate that it is possible to select delay-gain distributions (τ_i, g_i) from a uniform distribution such that simulations oscillate at different frequencies from the predictions made using my methods. Further theory is necessary to establish strict conditions on the delay-gain distribution such that the variation in the predictive power is removed. However, based on the experimental results, the delay-gain distributions in the single-feedback, dual-feedback, and cavity-feedback system allow for the resonance, shifted-resonance, and amplitude modulation methods to predict approximately the quasiperiodic frequencies with errors below the observed variations in the simulated cases.

Appendix D

Laser-Feedback System: Calibration and Details

This appendix provides details of the two-delay optical feedback system presented in Ch. 7. In particular, the polarization of the feedback is shown to be coherent (matching the polarization of the laser), the experimental calibration of the piezoelectric transducers with respect to applied voltages is shown, and the coefficients of the numerical fits for the quasiperiodic frequency shifts are provided.

D.1 Laser Feedback Polarization

A semiconductor laser outputs an optical field with a polarization. In a feedback configuration, the components of the feedback loop, such as optical fibers and attenuators, can alter the polarization of the light such that the input and output polarizations of the laser cavity are mismatched. Depending on the type of polarization in the feedback, there are different effects on the dynamics in the feedback system. One of the most famous models for studying semiconductors with optical feedback is the Lang-Kobayashi model, which describes a laser subject to coherent optical feedback with matched input and output polarizations [94]. The Lang-Kobayashi model has also been shown to exhibit quasiperiodicity in a simulated two-delay configuration [89]. Therefore, in order to study (eventually) the laser system in a numerical model and search for quasiperiodicity in the experiment, I choose to use coherent optical feedback with a matched polarization in the two-delay optical system of Ch. 7.

In the experiment, there are several different techniques to measure the polariza-

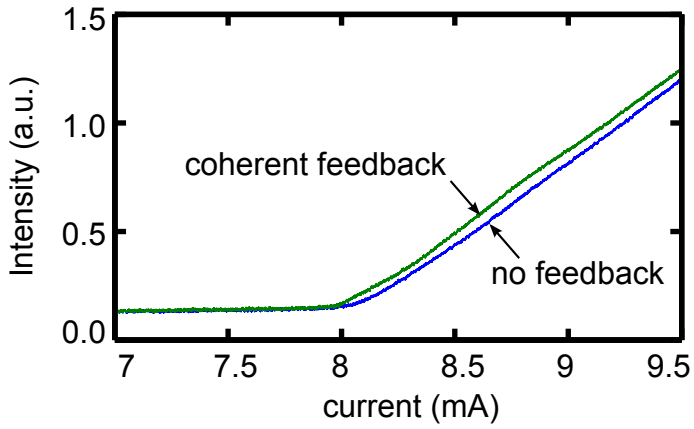

Figure D.1: **Laser threshold with coherent feedback.** Output intensity of the laser as a function of input current near the laser threshold with (green curve) and without (blue curve) coherent feedback.

tion of an optical field. One of the simplest experiments to verify that the feedback polarization is aligned involves measuring the laser threshold as a function of the applied current of the laser diode's power source. The laser threshold represents the point where the output power from the laser is no longer approximately zero. As shown in Fig. D.1, when there is no feedback to the laser, the lasing threshold of the diode occurs at around 8.05 mA (blue curve). However, when there is feedback to the laser cavity, the laser threshold occurs at a lower value of 7.95 mA. This shift is consistent with a feedback that is coherent such that its polarization matches the output polarization of the laser [94]. For incoherent feedback (unaligned polarization), the laser threshold occurs for larger current values [94].

Therefore, in the two-delay optical feedback experiment, the optical field fed back to the laser cavity is of a coherent polarization, and based on the results of Ch. 7, quasiperiodicity is achieved in this configuration.

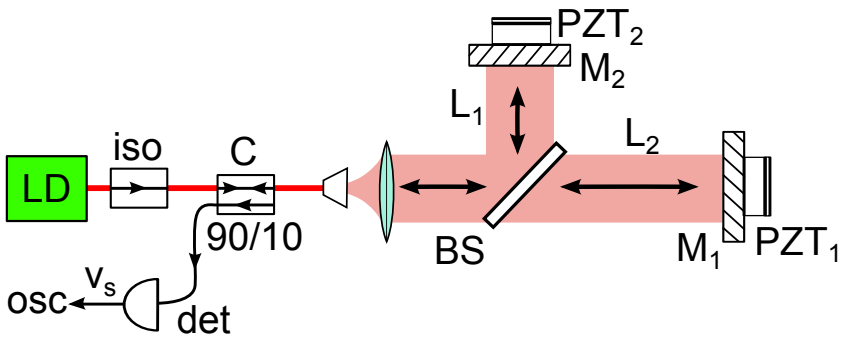

Figure D.2: **Interferometer for calibrating the piezoelectric transducers.**The output of the laser diode (LD) is fed through a unidirectional isolator (iso) that prevents feedback to the laser cavity. The optical signal is coupled to free space where it is directed along two paths via a beam splitter (BS), where it is reflected of of mirrors (M_1 and M_2) that are attached to the piezoelectric transducers (PZT_1 and PZT_2). The reflected signals interfere along a common path and are coupled (C) to a detector (det), where the voltage v_s is measured on an oscilloscope (osc).

D.2 Piezoelectric Transducers

To approximate the distances traveled by the piezoelectric transducers (PZTs) as a function of the applied voltages, I perform an experiment using an interferometer to calibrate them. Using the setup shown in Fig. D.2, the output power of a Michelson interferometer is measured as a function of the applied voltage to each PZT. In the figure, the output of a laser diode (of average wavelength $\lambda \sim 1550$ nm) is fed through an isolator that prevents the optical signals from feeding back into the laser cavity. Thus, in this configuration, the system can only exhibit a constant (steady-state) intensity. Similar to the setup in Fig. 7.2, the optical signal is coupled to free space where it is split using a beam-splitter (BS) along two separate paths of lengths L_1 and L_2 and then reflected off of mirrors M_1 and M_2 that are connected to PZT_1 and PZT_2, respectively. The reflected signals recombine along a common path and interfere. Using a coupler (C), the interfering signals are measured on a detector, which reports a voltage v_s that is proportional to the resulting interference intensity.

Based on the interference of the optical signals along the interferometer arms, the intensity measured on the detector follows from [6]

$$I = I_1 + I_2 + \sqrt{2I_1 I_2}\cos(2\pi D/\lambda), \tag{D.1}$$

where I_1 and I_2 are the intensities of the light along each path $\lambda \sim 1550$ nm is the wavelength of the light, and $D = 2\Delta L$, where $\Delta L = |L_1 - L_2|$ is the path length difference of interferometer's arms. In the calibration of PZT_1, an applied voltage ranging from 0 V to 25 V is applied while PZT_2 is held at a fixed position (and vice versa for the calibration of PZT_2). As shown in Figs. D.3a-b, the measured intensities on the detector for each PZT calibration is fitted with the function

$$I = C_1 + C_2\cos(C_3(V + C_4)), \tag{D.2}$$

where C_i are the free parameters of the fit and V is the applied voltage to the PZT. In the calibration for PZT_1 (Fig. D.3a), the fitted coefficients are $C_1 = 0.0186 \pm 0.0003$, $C_2 = 0.2365 \pm 0.00028$, $C_3 = 0.2479 \pm 0.0003$, and $C_4 = -4.3132 \pm 0.1367$, and in the calibration of PZT_2 (Fig. D.3b), the fitted coefficients are $C_1 = 0.0179 \pm 0.0002$, $C_2 = 0.3713 \pm 0.0013$, $C_3 = 0.2435 \pm 0.001$, and $C_4 = -0.0173 \pm 0.053$ (errors represents the 90% confidence intervals of the fitting parameters). To calculate the total translation of the PZTs, I use the following conversion

$$\Delta L = \frac{\lambda C_3}{4\pi}(V_{\max} + C_4), \tag{D.3}$$

where $V_{\max} = 25$ V now ΔL represents the total distance covered by PZTs. Lastly, I create the conversion factor $K = \Delta L/V_{\max}$ for each of the two PZTs. This factor allows me to convert between an applied voltage to the PZT and a translation of the

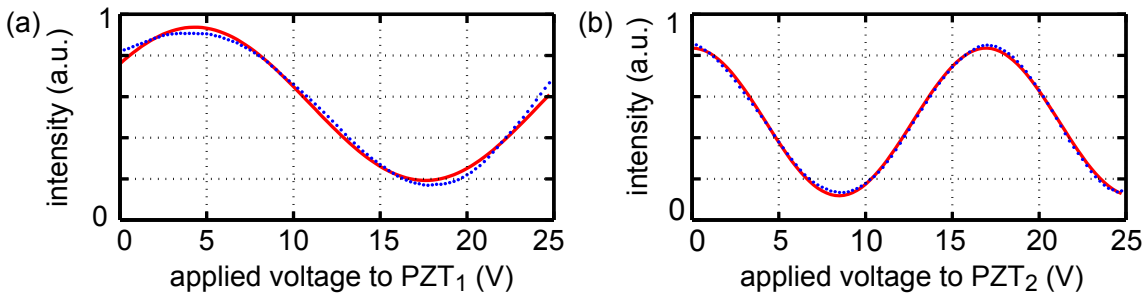

Figure D.3: **Piezoelectric transducer calibration.** (a) Output intensity of the interferometer (a) for a fixed PZT_2 while a voltage is applied to PZT_1 and (b) for a fixed PZT_1 while a voltage is applied to PZT_2. The experimental data (blue dots) are fitted (red curves) to yield conversion factors of $K_1 = 29.2 \pm 0.1$ nm/V for PZT_1 and $K_2 = 45.8 \pm 0.2$ nm/V for PZT_2.

respective mirrors. For PZT_1 and PZT_2, the conversion factors are $K_1 = 29.2 \pm 0.1$ nm/V and $K_2 = 45.8 \pm 0.2$ nm/V, respectively. Thus, using K_1 and K_2, I calculate the quantities Δx_1 and Δx_2 in the axes of Fig. 7.4.

I note that this calibration does not include the hysteresis of the PZTs under applied voltages and it also assumes a linear relationship between translations of the PZTs and the applied voltages. Therefore this calibration just provides the order of magnitude for translations of the PZTs in order to approximate the resolution of the all-optical dual-delay sensing system.

D.3 Coefficients of the Frequency-Shift Fits

In order to create a of map between $(\Delta f_2, \Delta f_4)$ and $(\Delta x_1,\ \Delta x_2)$, I fit the experimental data in Figs. 7.4a-b with the multivariate functions

$$\Delta f_2(\Delta x_1, \Delta x_2) = \sum_{i=1}^{i=2} \left(a_i \Delta x_1^i + b_i \Delta x_2^i \right) + \sum_{j=0}^{j=1} A_j \Delta x_1^j \Delta x_2^j, \tag{D.4}$$

$$\Delta f_4(\Delta x_1, \Delta x_2) = \sum_{i=1}^{i=2} \left(c_i \Delta x_1^i + d_i \Delta x_2^i \right) + \sum_{j=0}^{j=1} B_j \Delta x_1^j \Delta x_2^j, \tag{D.5}$$

where the fitted coefficients are listed in Table D.1.

Table D.1: Coefficients of the optical frequency-shift fits

Coefficient	Fitted Value
a_1	1.2458 ± 0.0562 kHz nm^{-1}
a_2	-0.0095 ± 0.0009 kHz nm^{-2}
b_1	-0.0691 ± 0.0358 kHz nm^{-1}
b_2	-0.0041 ± 0.0003 kHz nm^{-2}
A_o	-17.3784 ± 1.0834 kHz
A_1	0.0058 ± 0.0005 kHz nm^{-2}
c_1	1.8789 ± 0.1694 kHz nm^{-1}
c_2	-0.0140 ± 0.0026 kHz nm^{-2}
d_1	1.2050 ± 0.1079 kHz nm^{-1}
d_2	-0.0127 ± 0.0010 kHz nm^{-2}
B_o	-67.7941 ± 3.2683 kHz
B_1	0.0093 ± 0.0014 kHz nm^{-2}

Bibliography

[1] H. C. Ohanian. *Physics, Volume 2*. Penguin Books Canada Ltd., 1989.

[2] Z. Chen and A. Taflove. *Optics Express*, 12:1214–1220, 2004.

[3] R. D. Knight. *Physics for Scientists and Engineers: A Strategic Approach*. Pearson Education, Inc., 2013.

[4] D. C. Giancoli. *Physics for Scientists and Engineers, Volume II*. Prentice Hall, 2000.

[5] X. Michalet and S. Weiss. *PNAS*, 103:4797–4798, 2006.

[6] B. E. A. Saleh and M. C. Teich. *Fundamentals of Photonics*. John Wily and Sons, Inc., 2007.

[7] P. Hariharan. *Basics of Interferometry*. Elsevier, 2007.

[8] M. Born and E. Wolf. *Principles of Optics*. Pergamon Press, 1987.

[9] M. J. Rust, M. Bates, and X. Zhuang. *Nature Methods*, 3:793–795, 2006.

[10] E. Rittweger, K. Y. Han, S. E. Irvine, C. Eggeling, and S. W. Hell. *Nature Photon.*, 3:144–147, 2099.

[11] X. Zhuang. *Nature Photon.*, 3:365–367, 2008.

[12] M. G. L. Gustafsson. *PNAS*, 102:13081–13086, 2005.

[13] R. Heintzmann and M. G. L. Gustafsson. *Nature Photon.*, 3:362–364, 2009.

[14] S. van de Linde, R. Kasper, M. Heilemann, and M. Sauer. *Appl. Phys. B*, 93:725âĂŞ731, 2008.

[15] B. Huang, M. Bates, and X. Zhuang. *Annu. Rev. Biochem.*, 78:998–1016, 2009.

[16] X. Zhang and L. Zhaowei. *Nature Mat.*, 7:435–441, 2008.

[17] J. Zhu, S. K. Özdemir, L. He, D.-R. Chen, and L. Yang. *Optics Express*, 19:16195–16206, 2011.

[18] F. M. Huang, C. Yifang, F. J. G. Abajo, and N. I. J. Zheludev. *Opt. A: Pure Appl. Opt.*, 9:S285, 2007.

[19] W. L. Barnes, A. Dereux, and T. W. Ebbesen. *Nature*, 424:824–830, 2003.

[20] J. N. Anker, W. P. Hall, O. Lyandres, N. C. Shah, J. Zhao, and R. P. Van Duyneand. *Nature Mat.*, 7:442–453, 2008.

[21] S. D. Cohen, H. L. D. S. Cavalcante, and D. J. Gauthier. *Phys. Rev. Lett.*, 107:254103, 2011.

[22] L. Illing and D. J. Gauthier. *Chaos*, 16:033119, 2006.

[23] S. H. Strogatz. *Nonlinear Dynamics And Chaos*. Perseus Books Publishing, 2001.

[24] F. Sagués and I. R. Epstein. *Dalton Trans.*, 0:1201–1217, 2003.

[25] M.C. Mackey and L. Glass. *Science*, 197:287–289, 1977.

[26] E. N. Lorenz. *J. Atmos. Sci.*, 20:130–141, 1963.

[27] J. A. Greenberg and D. J. Gauthier. *Phys. Rev. A*, 86:013823, 2012.

[28] M. B. Elowitz and S. Leibler. *Nature*, 403:335–338, 2000.

[29] X. S. Yao and L. Maleki. *J. Opt. Soc. Am. B*, 13:8, 1996.

[30] S. Donati, G. Giuliani, and S. Merlo. *IEEE J. Quantum Elect.*, 31:113–119, 1995.

[31] R. Zhang, H. L. D. S. Cavalcante, Z. Gao, D. J. Gauthier, J. E. S. Socolar, M. M. Adams, and D. P. Lathrop. *Phy. Rev. E.*, 80:045202(R), 2009.

[32] L. Illing and D. J. Gauthier. *Physica D: Nonlinear Phenomena*, 210:180, 2005.

[33] H. Froehling, J. P. Crutchfield, J. D. Farmer, N. H. Packard, and R. Shaw. 1981.

[34] J. D. Farmer. *Physica D*, 4:366–393, 1982.

[35] K. E. Callan, L. Illing, Z. Gao, D. J. Gauthier, and E. Schöll. *Phys. Rev. Lett.*, 104:113901, 2010.

[36] T. Erneux, L. Larger, M. W. Leeb, and J.-P. Goedgebuer. *Physica D: Nonlinear Phenomena*, 194:49, 2004.

[37] S. D. Cohen, D. Rontani, and D. J. Gauthier. *Chaos*, 22:043112, 2012.

[38] H. Kantz and T. Schreiber. *Nonlinear Time Series Analysis*. Cambridge University Press, 2003.

[39] N. L. Duy, B. Journet, I. Ledoux-Rak, J. Zyss, L. V. H. Nam, and V. V. Luc. *Microwave photonics, 2008. jointly held with the 2008 asia-pacific microwave photonics conference*, page 131, 2008.

[40] S. D. Cohen, D. Rontani, and D. J. Gauthier. *To be submitted in Phys. Rev. E*, 2013.

[41] Y. Ikuma and J. Ohtsubo. *IEEE J. Quant. Elec.*, 34:1240–1246, 1998.

[42] A. Bearden, M. P. O'Neill, L. C. Osborne, and T. L. Wong. *Optics Letters*, 18:238–240, 1993.

[43] T. L. Carroll. *Chaos*, 21:023128, 2011.

[44] A. R. Sloboda and B.I. Epureanu. *Phys. Rev. E*, 87:022903, 2013.

[45] L. Moniz, J. Nichols, S. Trickey, M. Seaver, D. Pecora, and L. Pecora. 2005.

[46] M. C. Gutzwiller. *Chaos in Classical and Quantum Mechanics*. Springer-Verlag New York Inc., 1990.

[47] P. B. Wilkinson, T. M. Fromhold, R. P. Taylor, and A. P. Micolich. *Phys. Rev. E.*, 64:026203, 2001.

[48] J. U. Nöckel and A. D. Stone. *Nature*, 385:45–47, 1997.

[49] F. Haake and G. Lenz. *Phys. Rev. A*, 44:6161–6164, 1991.

[50] H. Alt, H.-D. Gräf, H. L. Harney, R. Hofferbert, H. Lengeler, A. Richter, P. Schardt, and H. A. Weidenmüller. *Phy. Rev. Lett.*, 74:62–65, 1995.

[51] A. D. Stone. *Physics Today*, 58:37–43, 2005.

[52] T. Gensty, K. Becker, I. Fischer, W. Elsässer, C. Degen, P. Debernardi, and G. P. Bava. *Phy. Rev. Lett.*, 94:233901, 2005.

[53] A. Gokirmak, D.-H. Wu, J. S. A. Bridgewater, and S. M. Anlage. *Rev. Sci. Instrum.*, 69:3410–3417, 1998.

[54] B. Taddese, J. T. Hart, T. M. Antonsen, E. Ott, and S. M. Anlage. *Appl. Phys. Lett.*, 95:114103, 2009.

[55] H.-D. Gräf, H. L. Harney, H. Lengeler, C. H. Lewenkopf, C. Rangacharyulu, A. Richter, P. Schardt, and H. A. Weidenmüller. *Phys. Rev. Lett.*, 69:1296, 1992.

[56] A. Molitor, M. Blazek, and W. Elsässe. *Optics Lett.*, 36:3777–3779, 2011.

[57] H.-J. Stöckmann. *Quantum Chaos*. Cambridge University Press, 1999.

[58] P. H. Tuan, Y. T. Yu, P. Y. Chiang, H. C. Liang, K. F. Huang, and Y. F. Chen. *Phys. Rev. E*, 85:026202, 2012.

[59] J. D. Jackson. *Classical Electrodynamics*. John Wiley and Sons, Inc., 1999.

[60] B. Taddese, J. T. Hart, T. M. Antonsen, E. Ott, and S. M. Anlage. *J. Appl. Phys.*, 108:114911, 2010.

[61] R. K. Ing and N. Quieffin. *Appl. Phys. Lett.*, 87:204104, 2005.

[62] Y. K. Chembo, P. Colet, L. Larger, and N. Gastaud. *Phy. Rev. Lett.*, 95:203903, 2005.

[63] J. M. Nichols, M. D. Todd, M. Seaver, and L. N. Virgin. *Phys. Rev. E*, 67:016209, 2003.

[64] L. Pecora, L. Moniz, J. Nichols, and T. L. Carroll. *Chaos*, 17:013110, 2007.

[65] H. Sakaguchi. *Phys. Rev. E*, 65:027201, 2002.

[66] J. Zamora-Munt, B. Garbin, S. Barland, M. Giudici, J. R. R. Leite, C. Masoller, and J. R. Tredicce. *Phys. Rev. A*, 87:035802, 2013.

[67] R. L. Weaver and O. I. Lobkis. *J. Acoust. Soc. Am.*, 120(1):102–109, 2006.

[68] D. A. McQuarrie. *Mathematical Methods for Scientists and Engineers*. University Science Books, 2003.

[69] M. Tabib-Azar, D.-P. Su, A. Pohar, S. R. LeClair, and G. Ponchak. *Rev. of Sc. Inst.*, 70:1725–1730, 1999.

[70] O. I. Lobkis and R. L. Weaver. *J. Acoust. Soc. Am.*, 125:1894, 2009.

[71] K. Ikeda, H. Daido, and O. Akimoto. *Phy. Rev. Lett.*, 45:709–712, 1980.

[72] J. Mørk, J. Mark, and B. Tromborg. *Phy. Rev. Lett.*, 65:1999–2002, 1990.

[73] I. Fischer, O. Hess, W. Elsässer, and E. Göbel. *Phy. Rev. Lett.*, 73:2188–2191, 1994.

[74] C. Gmachl, F. Capasso, E. E. Narimanov, J. Nöckel, A. D. Stone, J. Faist, D. L. Sivco, and A. Y. Cho. *Science*, 280:1556–1564, 1998.

[75] Y. K. Chembo, L. Larger, and P. Colet. *IEEE Quant. Elec.*, 44:9, 2008.

[76] A. V. Oppenheim and R. W. Schafer. *Digital Signal Processing*. Prentice Hall, 1975.

[77] MATLAB. *version 7.10.0 (R2010a)*. The MathWorks Inc., Natick, Massachusetts, 2010.

[78] S. D. Cohen, D. Rontani, and D. J. Gauthier. *Chaos*, 22:043112, 2012.

[79] R. N. Bracewell. *The Fourier Transform and Its Applications*. McGraw-Hill, Inc., 1986.

[80] V. S. Udaltsov, L. Larger, J.-P. Goedgebuer, M. W. Lee, E. Genin, and W. T. Rhodesr. *IEEE Circuits Sys.*, 49:1006, 2006.

[81] X. S. Yao and L. Maleki. *IEEE Quant. Elec.*, 36:1, 2000.

[82] T. Bánky, B. Horváth, and T. Berceli. *J. Opt. Soc. Am. B.*, 23:1371–1380, 2008.

[83] Y. K. Chembo, L. Larger, H. Tavernier, R. Bendoula, E. Rubiola, and P. Colet. *Optics Letters*, 32:17, 2007.

[84] L. Weicker, T. Erneux, M. Jacquot, Y. K. Chembo, and L. Larger. *Phys. Rev. E*, 85:026206, 2012.

[85] S. D. Cohen, D. Rontani, and D. J. Gauthier. *Chaos*, 22:043112, 2012.

[86] E. Shumaker and G. Einstein. *IEEE Photonic. Tech. L.*, 20:1881–1883, 2008.

[87] Y.-M. Wu, L. Vivien, E. Cassan, V. H. N. Luong, L. D. Nguyen, and B. Jounret. *Proc. of SPIE Optical Components and Materials VII*, 7598:7598F–1, 2010.

[88] J. N. Munday and W. M. Robertson. *Appl. Phys. Lett.*, 83:1053–1055, 2003.

[89] A. N. Pisarchik and F. R. Ruiz-Oliveras. *PIERS Online*, 3:452–456, 2007.

[90] S. D. Hemmady. *A Wave-Chaotic Approach to Predicting and Measuring Electromagnetic Field Quantities in Complicated Enclosures*. PhD thesis, University of Maryland- College Park, 2006.

[91] T.-Y. Li and J. A. Yorke. *The American Mathematical Monthly*, 82:985, 1975.

[92] M. Frazier, B. Taddese, T. Antonsen, and S. M. Anlage. *Phys. Rev. Lett.*, 110:063902, 2013.

[93] M. C. Soriano, J. Garcia-Ojalvo, C. R. Mirasso, and I. Fischer. *Rev. Mod. Phys.*, 85:1, 2013.

[94] J. Ohtsubo. *Semiconductor Lasers: Stability, Instability and Chaos*. Springer, 2006.

[95] K. Vahala. *Semiconductor Lasers: Stability, Instability and Chaos*. World Scientific Publishing Co. Pte. Ltd., 2004.

[96] K. J. Vahala. *Nature*, 424:839–846, 2003.

[97] N. Jokerst, M. Royal, S. Palit, L. Luan, S. Dhar, and T. Tyler. *J. Biophoton.*, 2:212–226, 2009.

[98] F. Vollmer and S. Arnold. *Nature Methods*, 5:591–596, 2008.

[99] C. Qiu, J. Chen, and Q. Xu. *Optics Letters*, 37:5012–5014, 2012.

[100] A.l S. Sedra and K. C. Smith. *Microelectronic Circuits*. Holt, Rinehart and Winston, Inc., 1987.

[101] Y. Chen, K. Mouthaan, and B.-L. Ooi. *IEEE Trans. Circuits and Systems*, 55:1114–1118, 2008.

[102] G. M. Maggio, M. di Bernardo, and M. P. Kennedy. *IEEE Trans. Circuits and Systems*, 47:1160–1177, 2000.

Biography

Seth Cohen was born in Silver Spring, MD on April 4, 1985 and has had homes in Bethesda, MD, Portland, OR, Needham, MA, and Pittsfield, MA. In high school, he was voted most artistic and was a captain of the track and field team. Seth attended the University of Rochester to pursue a Bachelor of Science degree in Physics and a Bachelor of Arts degree in Mathematics as well as a minor in Studio Arts. In 2005, Seth was awarded the Annual Honors Physics Prize, and in 2006 he was elected into the Sigma Pi Sigma Physics Honor Society and Phi Beta Kappa. In 2006, he also studied physics and math abroad at Queen Mary College in London.

During the summers in between college semesters, Seth returned home to the Berkshires each year to work for Lightning Technologies, an electrical engineering firm that specializes in the protection of aircrafts during a lightning strike. While working, Seth was able to travel to New Mexico and California enjoying the warm weather in both states. In 2007, Seth graduated from college magna cum laude and decided to pursue his doctorate in physics.

In the Fall of 2007, Seth moved to Durham, NC and began his graduate school career at Duke University. Following a presentation on chaotic circuits by Dr. Daniel Gauthier, Seth joined the Quantum Electronics Lab under Dr. Gauthier's advisement. During his time at Duke, he worked on several projects with nonlinear dynamics in electronic circuits ranging from synchronization in chaotic systems to chaos-based radars and nonlinear sensing techniques. In addition, while at Duke, Seth taught recitations for introductory physics students, received the AAPT Outstanding Teaching Assistant Award, and served as an elected class representative in the Duke Physics graduate student organization. In 2009, Seth received his Master of Arts degree in Physics and met his wife Caroline Yoder at the Duke gym.

Publications

S.D. Cohen, D. Rontani, D. J. Gauthier, "Multi-parametric sensing in a time-delayed nonlinear feedback system," to submitted for publication (2013)

S.D. Cohen, D. Rontani, D. J. Gauthier, "Experimental methods for predicting the frequencies associated with Hopf and torus bifurcations in a time-delayed nonlinear feedback system," to be submitted for publication (2013)

S.D. Cohen, D. Rontani, D. J. Gauthier, "Ultra-high-frequency piecewise-linear chaos using delayed feedback loops," Chaos: An Interdisciplinary Journal of Nonlinear Science, vol. 22 no. 043112 (2012)

G. M. Hall, E. J. Holder, S. D. Cohen, D. J. Gauthier, "Low-cost chaotic radar design," Proc. SPIE 8361, Radar Sensor Technology XVI, 836112 (2012)

S.D. Cohen, D. J. Gauthier, "A pseudo-matched filter for chaos," Chaos: An Interdisciplinary Journal of Nonlinear Science, vol. 22 no. 033148 (2012)

Seth D. Cohen, Hugo L. D. de S. Cavalcante, and Daniel J. Gauthier, "Subwavelength Position Sensing Using Nonlinear Feedback and Wave Chaos", Physical Review Letters, vol. 107 no. 25 (2011)

Presentations

S. D. Cohen, H. L. D. de S. Cavalcante, and D. J. Gauthier, Sub-wavelength position sensing using chaos, Invited talk presented at the 2012 Experimental Chaos and Complexity Conference, University of Michigan, May 16-19, 2012.

S. D. Cohen and D. J. Gauthier, Chaos in a Variable-Gain Amplifier Oscillator, Poster presented at Dynamics Days 2012, Baltimore, Maryland, Jan. 4-7, 2009.

S. D. Cohen, H. L. D. de S. Cavalcante, and D. J. Gauthier, Sub-wavelength position sensing using chaos, Invited talk presented at Aviation and Missile Research Development and Engineering Center (AMRDEC), Redstone Arsenal, AL, July 27, 2011.

S. D. Cohen and H. L. D. de S. Cavalcante, Delayed Nonlinear Feedback through Wave Chaotic Cavities. Invited talk presented at University of Maryland MURI Lunch in the Institute for Research in Electronics and Applied Physics, College Park, Maryland, October 2010.

S. D. Cohen, H. L. D. de S. Cavalcante, and D. J. Gauthier, Bifurcations from subwavelength changes in a wave-chaotic cavity with nonlinear feedback. Poster presented at the Dynamics Days 2011 in Chapel Hill, NC.

S. D. Cohen, H. L. D. de S. Cavalcante, R. Zhang, and D. J. Gauthier, Ultra-Wideband Antenna Design for Transmission of a Digital Chaotic Signal, Poster presented at Dynamics Days 2009, San Diego, CA, Jan. 8-11, 2009.